



University of Bremen



FB 1

Institute for Theoretical Physics

Optical and Electronic Properties of InGaAs and Nitride Quantum Dots

by Norman Baer, June 2006

Optical and Electronic Properties of InGaAs and Nitride Quantum Dots

Dem Fachbereich für Physik und Elektrotechnik

der Universität Bremen

zur Erlangung des akademischen Grades

Doktor der Naturwissenschaften (Dr. rer. nat.)

genehmigte Dissertation

von

Dipl. Phys. Norman Baer

aus Köln

1. Gutachter:

Prof. Dr. rer. nat. F. Jahnke

2. Gutachter:

Prof. Dr. rer. nat. G. Czycholl

Eingereicht am:

15.06.2006

Tag des Promotionskolloquiums: 21.07.2006

Abstract

In recent years, semiconductor quantum dots (QDs) have attracted considerable attention due to their potential for fundamental studies as well as device applications. In the present thesis, the electronic and optical properties of such nanostructures have been investigated for the well established III-V and the new group-III nitride material system.

The influence of Coulomb correlations on the optical spectra of InGaAs QDs are studied using a full configuration interaction approach. The resulting multi-exciton spectra for up to twelve excitons are investigated in detail. Characteristic features of the spectra are explained using simplified Hamiltonians that are derived taking into account the relative importance of various interaction contributions. In this way, the strong red-shift observed in the emission of the energetically lower shells with increasing number of electron-hole pairs as well as the remarkable stability of the emission of partly unoccupied shells is explained. Based on our theoretical work, recent experiments involving charged exciton complexes are analyzed.

Additionally, we study the electronic and optical properties of self-assembled InN/GaN quantum dots. The one-particle states of these low-dimensional heterostructures are provided by a tight-binding model that fully includes the wurtzite crystal structure on an atomistic level. The existence of an exactly degenerate p -shell is discussed in detail. Dipole and Coulomb matrix elements are calculated from these one-particle wave functions and serve as an input for configuration interaction calculations. We present multi-exciton emission spectra and investigate how Coulomb correlations and oscillator strengths are altered by the built-in electrostatic fields present in these structures. From our results, we predict vanishing exciton and biexciton ground state emission for small lens-shaped dots, which is explained by a careful analysis of the underlying symmetry group. For larger structures, a level reordering can lead to a bright exciton ground state. In both cases a semi-analytic discussion of the emission spectra is possible and provides deeper insight into the involved configurations.

To study the photoluminescence dynamics of an initially excited QD system, we employ a microscopic semiconductor theory. Carrier-carrier correlations beyond the Hartree-Fock level are included within a cluster expansion truncation scheme up to the singlet-doublet level. The influence of these correlations on the spectrum and the photoluminescence dynamics is investigated for the emission into free space as well as for QDs embedded in an optical microcavity. The two limiting cases of fully correlated and uncorrelated carriers are discussed. Our analysis shows that the lack of full correlation leads to a non-exponential and excitation-intensity dependent decay of the photoluminescence signal, indicating that approaches based on atomic models can fail to describe the photoluminescence dynamics and that a full semiconductor treatment is required. A detailed comparison with recent experiments is made.

Contents

Prologue

v

Part I Multi-Exciton Spectra in InGaAs Quantum Dots

Introduction to Part I	1
1 Model System and Theoretical Background	3
1.1 Single-Particle States	3
1.2 Many-Body Hamiltonian	6
1.3 Full Configuration Interaction Scheme	9
2 Full Configuration Interaction Results for the Optical Spectra	11
2.1 Basic Considerations	11
2.2 Excitonic Absorption and Emission	12
2.3 The Biexciton Problem	15
2.4 Multi-Exciton Emission Spectra	16
3 Approximation Schemes	19
3.1 Diagonal Hamiltonian	19
3.2 Adiabatic Hamiltonian	24
4 Charged Excitons	31
4.1 Experimental Findings	31
4.2 Theoretical Analysis	35
5 Influence of higher shells	41
5.1 Absorption	41
5.2 Multi-Exciton Emission	46

Part II Multi-Exciton Spectra in Nitride Quantum Dots

Introduction to Part II	57
6 Tight-Binding Single-Particle States in Nitride Quantum Dots	61
6.1 Basic Idea of a Tight-Binding Model	62
6.2 Tight-Binding Model for the InN/GaN Quantum Dot	64
6.3 Evaluation of Dipole- and Interaction Matrix Elements	68
7 Symmetry Considerations	69
7.1 Energy Spectrum	72
7.2 Single-Particle States	73
7.3 Dipole Matrix Elements	77
7.4 Coulomb Matrix Elements	79
8 Optical Properties	83
8.1 Summary of Single-Particle Properties and Selection Rules	83
8.2 Excitonic and Biexcitonic Properties	85
8.3 Configuration Interaction Results for Multi-Exciton Emission Spectra .	88
8.4 Diagonal Approximation	89
8.5 Semi-Analytic Discussion of the Multi-Exciton Spectra	92
8.5.1 $3X \rightarrow 2X$ Emission Spectrum	92
8.5.2 $4X \rightarrow 3X$ Emission Spectrum	93
8.5.3 $5X \rightarrow 4X$ Emission Spectrum	96
8.5.4 $6X \rightarrow 5X$ Emission Spectrum	101
8.6 Influence of the Built-In Fields	102
8.7 Multi-Exciton Emission for a Larger Quantum Dot	103

Part III Semiconductor Luminescence Equations

Introduction to Part III	109
9 Hamiltonian and Consistent Truncation Scheme	113
9.1 Hamiltonian	113
9.2 Hierarchy Problem and Cluster Expansion	115
10 Semiconductor Luminescence Equations	121
10.1 Formulation of the Relevant Equations of Motion	121
10.2 Specialization to a Quantum Dot Model	127
10.2.1 The Light-Matter Interaction Matrix Elements $g_{ij\xi}$	127
10.2.2 Symmetry Considerations	129
10.2.3 Formulation of the SLE for the Quantum Dot Model	130

11 Photoluminescence	135
11.1 Definition of the Spectrum	135
11.2 Adiabatic Approximation in Hartree-Fock	137
11.3 Results for Luminescence Spectra	139
11.4 Results of the Time-Resolved PL	144
12 Photoluminescence in a Microcavity	151
12.1 Basic Considerations	151
12.2 Ensemble of Identical QDs Coupled to a Single Mode	154
12.3 Inhomogeneously Broadened Ensemble of QDs Coupled to Several Cavity Modes	157
12.4 Experimental Results	161

Part IV

Summary and Outlook	167
Appendix	171
A Construction of the Hamiltonian Matrix	171
B Spin and Band Symmetries	174
C Rotation and Time-Reversal	176
D Leaky Modes	177
E Numerical Methods	179
Bibliography	194

Prologue

Over the last decade nanostructures in general and semiconductor quantum dots (QDs) in particular have shifted more and more into the focus of the research community. The keyword ‘quantum dots’ yields almost 3000 hits in the data base ‘Web of Science’ even if the search is restricted only to the year 2005 and research proposals containing the word ‘nano’ seem to flourish [1]. The great topical interest in this field is motivated partly by the wide range of possible applications, ranging from new [2–4] and/or extremely efficient light sources [5] to building blocks for quantum information technology [6–8]. Further motivation is provided by the possibility to see fundamental quantum mechanics at work and to study the effects of reduced dimensionality on carrier transport [9] and optical properties [10–12].

The confinement of the carriers in all three dimensions on a nanometer scale is achieved by, for example, embedding islands of a material with a smaller bandgap into a wider bandgap material. A widespread method of creating such QDs is the Stranski-Krastanow growth mode [13–15]: On top of an epitaxial layer of one material another material with a smaller bandgap and a different lattice constant is grown. Due to the lattice mismatch, a strain field builds up, and at a certain critical thickness it is energetically favorable to change the morphology from a flat, homogeneous layer to a thinner two-dimensional wetting layer that is decorated with randomly distributed three-dimensional islands. Finally overgrowing these nano-islands with substrate material forms the actual QDs. Due to the bandgap mismatch the carriers are confined within the QD, which leads to a full quantization of the possible eigenenergies and results in a δ -like density of states. In this respect QDs are very similar to atoms. However, the great advantage of these ‘artificial atoms’ is that one is not restricted to the periodic system of elements. Instead one can, at least to some extend, tailor the properties as needed [15, 16].

From an experimental point of view, an advantage of QDs over atoms is the fact that no expensive trapping of the ‘atoms’ is needed. Once a particular well suited QD is identified, one can analyze it in detail for weeks and is not restrained due to a limited trapping time. To date a drawback of the ‘artificial atoms’ lies in the difficulty to produce QDs with desired properties in a reliable manner. A major hindrance is the size fluctuation present in an ensemble of QDs and the corresponding fluctuation in the energy levels. Nevertheless, it is expected that this inhomogeneous broadening will be well controlled in the near future. Another difference of QDs compared to real atoms is the rather strong interaction of the carriers with their surroundings at

elevated temperatures, which complicates practical device operation. On the other hand, the environment of the QD and in particular the coupling to the continuum of wetting layer states can be utilized to continuously inject carriers into the QD states, either electrically or by off-resonant optical excitation of energetically higher states and subsequent carrier capture into the localized QD states [17, 18]. The possibility of the off-resonant pumping and of tailoring the emission energy of QDs by varying their size and composition are two important aspects that make QDs attractive for biomedical image technology [19]. First applications in this rapidly evolving sector are already commercially available [20]. Other applications, in which an entire ensemble of QDs is utilized, include QD lasers [5, 21] as well as color filters and UV-filters for sun protection [22].

In addition to the well developed InGaAs system, QDs based on group-III nitrides became a major research focus in recent years. This is in part explained by the fact that by alloying together the basic building blocks InN, GaN and AlN the optical spectrum can be covered from amber to ultraviolet [23]. Furthermore, the strong chemical bonds make this wide bandgap material system suitable for high-power devices [24]. A clear landmark in the nitride research field is Nakamura's invention of the first high-brightness GaN LED in the blue spectral region [25]. Reliable short-wavelength light sources could pave the way for fast and inexpensive high-density data storage devices [26]. Once the growth-related problems, which still constitute a major hindrance in the field of nitride research, are mastered, QDs based on this material should prove to become a cornerstone of new opto-electronic applications.

Yet another door for a variety of interesting physics opens, if one turns away from QD ensembles and enters the realm of the physics of *single* QDs. By means of single dot spectroscopy important information not only on the shell structure but also on interacting multi-exciton states is gained [11, 12, 27, 28]. Addressing of single QDs is made possible by using QD samples with very low dot density and optical focussing via a microscope objective [29], employing shadow masks [12, 28], or etching small mesas out of the samples [4]. Single QDs are furthermore discussed as ideal candidates for single-photon sources and qubits, the quantum analogue to the classical bit. The two states of the qubit could, for example, be realized by the presence or absence of an exciton in the QD [7], or they could be decoded in the spin state of an electron confined in the dot. In order to make a useful device out of such a qubit, it must be possible to (i) prepare, control and read out the qubit with high accuracy and (ii) to let one such qubit interact with other qubits in a controlled way. Only if these prerequisites are fulfilled, a realization of a quantum computer based on QDs is possible.

Single-photon sources are not only interesting from a fundamental point of view, but also because an efficient single-photon source is a key building block in many quantum cryptographical protocols. One possible realization of such a photon-source makes use of the fact that the QD emission spectra is highly sensitive to the number of carriers present in the QD. This sensitivity stems from the interaction between the charge carriers and can be used to distinguish between photons that are generated by a recombination process from, e.g., a three exciton complex and an emission process, in which only

a single exciton was present prior to emission. By tuning a frequency filter to the exciton resonance, one can therefore always expect to observe one single photon after the excitation of the system. By these means one can convert a train of classical light pulses into a pulse of single photons [2].

The efficiency of such a single-photon source is tremendously improved by embedding the QD into a microcavity. In a cavity, the photons are confined in three spatial dimensions, which leads to an altered photonic density of states [30], in analogy to the electronic density of states that is modified by confining the electrons inside a QD. Combining the QD with a microcavity, the light-matter interaction can be tailored by means of a good cavity design and the proper placement of the emitters in the cavity [31]. The realm of cavity quantum electrodynamics, which was initially only accessible using atoms in cavities, and which can now also be investigated in solid-state devices, can be divided into two regimes: the weak- and the strong-coupling regime. The latter is characterized by a reversible transfer of energy from the cavity mode to the emitter. In a solid-state device this regime was realized for the first time less than three years ago independently by three groups. It was achieved by coupling a QD to a micropillar cavity [32], a photonic crystal defect cavity [33] and a microdisk [34]. In contrast, the weak-coupling regime manifests itself in altered spontaneous emission behavior ('Purcell effect') and was first observed in atomic systems and only much later for QD systems [35–37]. While a suppression of spontaneous emission is desired in situations in which long-living exciton states are required, in many opto-electronic devices a strong enhancement of the spontaneous decay is needed. A high Purcell factor means a fast emission and can be used for high-speed LEDs, in which the switching time between 'on' and 'off' is ideally only limited by the carrier relaxation time [38]. Additionally, an enhanced Purcell factor for a certain cavity mode is used to direct a larger fraction of the spontaneously emitted light into this mode and thereby moving the laser threshold to lower current densities.

This thesis covers three different aspects of semiconductor QDs. The first part deals with the multi-exciton spectra in InGaAs/GaAs QDs, the second with those of nitride-based QDs. The third part is dedicated to the investigation of the photoluminescence dynamics in the absence and presence of a microcavity. Detailed introductions and motivations for the different topics can be found at the beginning of each part.

Instead of speculating about further development in this rapidly evolving research field, we would rather like to conclude this section with a statement sometimes attributed to Niels Bohr:

'Prediction is difficult, especially about the future.'

Part I

Multi-Exciton Spectra in InGaAs Quantum Dots

Introduction to Part I

In this part of the thesis, we focus on InGaAs/GaAs quantum dots (QDs). Later, in Part II we investigate QDs based on group-III nitrides. In contrast to the latter the former system has been experimentally thoroughly investigated over the last decades and the growth of these structures is by now well controlled so that different shapes, aspect ratios, lateral extensions and composition profiles have been realized [13, 14]. In this way, it is by now possible to tailor their electronic and optical properties to a large extend [15, 16].

Even though there exist many applications in which an entire ensemble of QDs is needed, like QD lasers [5, 21], color filters [22], or frequency selective storage devices [39], much work has been dedicated to the investigation and characterization of individual QDs. Addressing single QDs has been achieved by several means, for example by employing shadow masks [12, 28] or etching small mesas out of the samples [4]. By single-dot spectroscopy, important information not only on the single-particle shell structure but also on the interaction between different multi-exciton states is gained [11, 12, 27, 28, 40]. A deeper understanding of the underlying physical processes is of key importance for further developments in this field. For single QDs possible applications, which have partly already been demonstrated in the laboratory, include single-photon sources [3, 41] or even sources of entangled photon pairs [42]. Such sources are important ingredients for quantum information processing and quantum cryptography [6].

Apart from the experimental relevance, the possibility of studying fundamental quantum-mechanical effects of the confined interacting few-carrier systems has inspired many researchers to find an appropriate theoretical description [29, 43–49]. In the past, configuration interaction calculations for a numerically determined strain-induced confinement potential have been performed [47] and a discussion of the energy level structure and luminescence spectra in terms of density functional theory has been given [50]. Additional studies employed single-particle states based on $\mathbf{k} \cdot \mathbf{p}$ models [51, 52], pseudopotential-theory [48, 53] or tight-binding studies [49]. Furthermore electronic states and the resulting dipole transitions have been calculated in box-like confinement potentials using exact diagonalization [10, 29, 43] as well as harmonic confinement potentials [12, 44, 45] with a limited number of configurations.

As we are interested mainly in many-particle effects and the impact of Coulomb correlations on the optical spectra, we adopt in the following an effective-mass model for the single-particle states. In this way, the analysis becomes most transparent and allows for

a detailed understanding of the underlying interaction effects, which are not obscured, for example, by band-mixing effects. Furthermore, one can in this case solve the problem of few charge carriers in the discrete states of a given confinement potential without further approximations. The choice of an effective-mass model for the single-particle states is furthermore underpinned by a recent study, in which an effective-mass model was compared to a $\mathbf{k} \cdot \mathbf{p}$ approach and an effective bond orbital model [49]. A good overall agreement between all three methods was found for the investigated structure.

Based on the single-particle states, we investigate Coulomb correlations in the optical spectra of semiconductor QDs using a full configuration interaction (FCI) approach. Despite the complexity of the spectra the occurring characteristic features can be explained in terms of simplified Hamiltonians. These are obtained from the original Hamiltonian by retaining dominant terms and neglecting less important ones, such that, on the one hand, the essential spectral features are preserved and, on the other hand, analytic results can be deduced. The aim is to get a more intuitive picture of the influence of Coulomb effects and to provide an alternative to a numerically demanding full-diagonalization approach. The trade-off between accuracy and simplicity can be reached in several ways and we give two examples whose merits and shortcomings are assessed against the full calculation result.

This part of the thesis is organized as follows. In Chapter 1 the model system is introduced. In particular the choice of harmonic oscillator states for the single-particle states is motivated in Section 1.1. Subsequently, the many-body Hamiltonian is introduced and the configuration interaction approach is outlined. Following these discussions, results for the optical spectra based on this exact diagonalization scheme are presented in Chapter 2. First we analyze the excitonic and biexcitonic properties and then give the results for the emission spectra of a QD initially filled with up to six excitons. The thorough discussion of these spectra is postponed to Chapter 3, in which two different approximation schemes are derived that lead to a deeper understanding. In particular Section 3.2 will be concerned with the remarkable stability of the p -shell emission as the number of excitons in the dot is increased. Emission of charged multi-exciton complexes will be presented in Chapter 4 where they are used to interpret recent experimental findings [54]. Finally in Chapter 5 the influence of higher shells on the optical properties is investigated.

1 Model System and Theoretical Background

In this chapter, we introduce the model system that will be investigated throughout this part. Furthermore we present the basic idea of the full-configuration interaction (FCI) approach, which allows us to calculate the multi-exciton spectra presented in this and the following part of the present thesis. We start with a discussion of the single-particle states of a lens-shaped QD in Section 1.1. Then we introduce the many-body Hamiltonian for the system of interacting charge carriers in Section 1.2. The subsequent Section 1.3 deals with the FCI approach.

1.1 Single-Particle States

Before proceeding to the many-particle problem, we have to specify an appropriate single-particle basis. We will adopt the rather ubiquitous choice [12, 45, 55–64] of two-dimensional harmonic oscillator wave functions for the bound-states in the plane perpendicular to the growth direction. For the strong confinement in growth direction we use an infinite potential well to model the corresponding finite extension of the wave function and consider only the energetically lowest subband for this quantization direction.

To motivate this choice of two-dimensional harmonic oscillator wave functions, we follow the paper of Wojs et al. [57] and solve the Schrödinger equation

$$H\xi_\alpha = \varepsilon_\alpha \xi_\alpha \quad \text{with} \quad H = -\frac{\hbar^2}{2m_\lambda} \Delta + V_\lambda(\mathbf{r})$$

in envelope and effective-mass approximation for the case of flat, cylindrically symmetric QDs. We assume that the energetically lowest QD states are well approximated by the hh-states. This is motivated by the fact that the strain – which is responsible for the very existence of dots grown in the Stranski-Krastanow growth mode [13–15] – together with the dimensional reduction, leads to a lifting of the degeneracy of the light- and heavy-hole band at the Γ -point known from the bulk material by shifting the light-hole band to lower energies [65]. For the shape of the QD we assume a cap of a sphere residing on a wetting layer to model the experimentally often found lens-shaped QDs [14, 57, 66]. The QD geometry is schematically depicted in Figure 1.1. Assuming

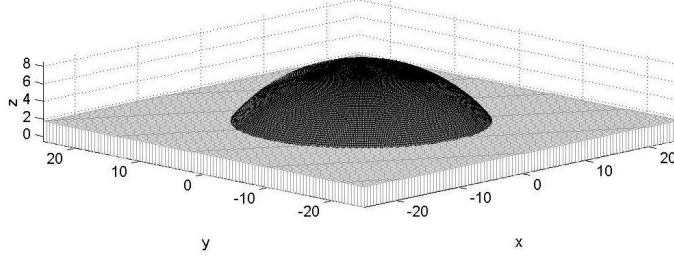


Figure 1.1: Schematic representation of a quantum dot (dark grey) residing on a wetting layer (light grey).

a constant band-offset ΔE_λ , we use for the confinement potential

$$V_\lambda(\mathbf{r}) = \begin{cases} 0 & ; \quad \mathbf{r} \text{ inside the QD and the WL,} \\ \Delta E_\lambda & ; \quad \text{otherwise.} \end{cases}$$

where $\lambda = e$ in case of electrons and $\lambda = h$ in case of holes. The rotational symmetry allows us to classify the single-particle states according to their angular momentum and to effectively reduce the three-dimensional problem to a two-dimensional one. Furthermore the flatness of the QD can be used to approximately map the two-dimensional problem on a one-dimensional problem [57], which can then be solved numerically. To check whether the proposed approximation is valid, we compare the result of the ‘adiabatic approximation’ to the solutions of the two-dimensional Schrödinger equation on a two-dimensional grid. We find that the approximation is indeed well justified for flat dots.

Using the parameters of Table 1.1, which are typical for the InGaAs/GaAs system and similar to those given in [57], we obtain the energy spectrum depicted in Figure 1.2. This spectrum resembles very much the energy spectrum of a two-dimensional harmonic

radius of quantum dot	$r_{\text{QD}} = 16 \text{ nm}$
height of quantum dot	$h = 4.0 \text{ nm}$
height of wetting layer	$z_0 = 1.6 \text{ nm}$
band off-set	$\Delta E_e = 350 \text{ meV}$
effective mass	$m_e = 0.065 m_0$

Table 1.1: Parameters defining the cylindrical symmetric QD depicted in Figure 1.1.

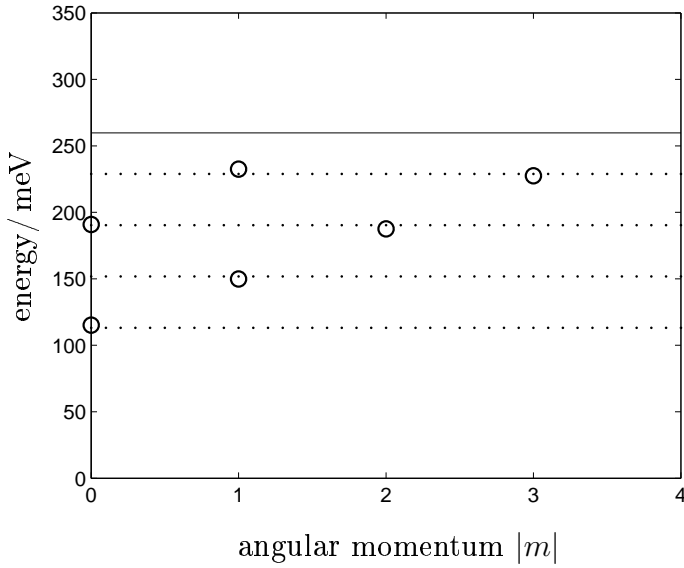


Figure 1.2: QD-energy spectrum for electrons (circles) and the equidistantly spaced energies of a two-dimensional harmonic oscillator with $\hbar\omega_0 = 38.578$ meV (dotted lines). The quasi continuum of WL states lies energetically above the solid line.

oscillator [67]. Indeed, if the circles lay exactly on the dotted line, which represent the equidistant energies of the harmonic oscillator, the energy spectrum of the bound states of the QD would fully coincide with the energy spectrum of the four energetically lowest shells of a two-dimensional harmonic oscillator.

As the form of the wave function enters the Coulomb matrix elements explicitly, we additionally check whether the good agreement between an oscillator model and the solution of the Schrödinger equation ends at the level of the energy spectrum, or if it is also valid for the wave functions, which is crucial if one aims at replacing the numerically evaluated wave functions and energies with those of a two-dimensional harmonic oscillator. A comparison of the QD wave functions and harmonic oscillator wave functions is shown in Figure 1.3. These results show that the excellent agreement is not restricted to the energy spectrum but is also found between the radial wave functions calculated for QD (solid lines) and those of a two-dimensional harmonic oscillator (dashed lines). Note that such a good agreement is not only found for the particular set of parameters of Table 1.1, but also for a wide variety of other parameters including larger and smaller QD as well as different effective masses. The dimension of the particular QD presented here is on the one hand small enough to show all the wave functions of the bound states, and, on the other hand, large enough to show that the good agreement between the harmonic oscillator states does not only hold for the lowest state.

Due to this overall good agreement, we can replace the single-particle bound-state wave functions in the plane of larger extension without hesitation by those of a two-dimensional harmonic oscillator and a box-like potential in growth direction. The as-

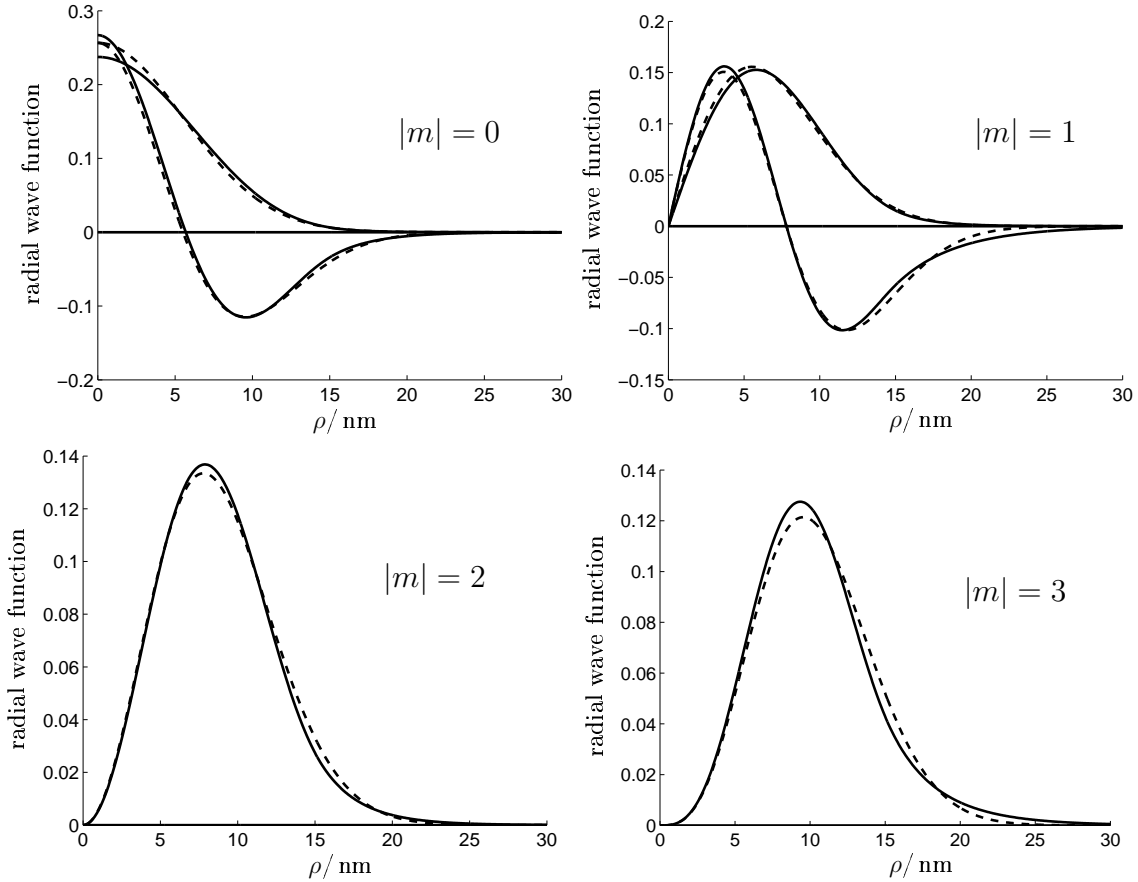


Figure 1.3: Comparison of the radial wave functions of an electron confined in the quantum dot (solid lines) with those of a two-dimensional harmonic oscillator (dashed lines) for different angular momenta.

sumption of harmonic oscillator states is furthermore underpinned by a recent publication by Sheng et al. where the effective-mass approach is compared to a $\mathbf{k}\cdot\mathbf{p}$ and a tight-binding-like calculation [49]. In the following we will adopt the so-called *symmetric case*, in which one assumes identical envelopes for the valence- and conduction-band electrons, i.e. $\xi_{i,e} = \xi_{i,h}^* = \xi_i$. This assumption, which is often employed in the literature [17, 44, 45, 56–58], holds exactly for QDs modeled by a box-like potential [10, 29, 43] and is found to be a good approximation for the oscillator potentials used here. Note that with the convention $\xi_{i,e} = \xi_{i,h}^*$ equal state indices i for electrons and holes indicate opposite angular momenta.

1.2 Many-Body Hamiltonian

In this section the Hamiltonian H of the interacting carrier system is discussed. Here we assume that the already very demanding task of realistically describing the electrons

inside a QD has been successfully solved on the single-particle level. If this has been achieved, these results can be used as input-parameters for a many-body calculation that will allow us to determine multi-exciton spectra.

The Hamiltonian that describes the system of interacting electrons and holes in a QD consists of two parts. The free part H_0 contains information about the single-particle spectrum $\varepsilon_i^{(e,h)}$ and describes a system of non-interacting charge carriers. The Coulomb interaction between the charge carriers is included in H_{Coul} . These Hamiltonians explicitly read:

$$\begin{aligned} H_0 &= \sum_{i\sigma} \varepsilon_i^e e_{i\sigma}^\dagger e_{i\sigma} + \sum_{i\sigma} \varepsilon_i^h h_{i\sigma}^\dagger h_{i\sigma} , \\ H_{\text{Coul}} &= \frac{1}{2} \sum_{\substack{ijkl \\ \sigma\sigma'}} V_{ij,kl}^{ee} e_{i\sigma}^\dagger e_{j\sigma'}^\dagger e_{k\sigma} e_{l\sigma} + \frac{1}{2} \sum_{\substack{ijkl \\ \sigma\sigma'}} V_{ij,kl}^{hh} h_{i\sigma}^\dagger h_{j\sigma'}^\dagger h_{k\sigma} h_{l\sigma} \\ &\quad - \sum_{\substack{ijkl \\ \sigma\sigma'}} V_{ij,kl}^{he} h_{i\sigma}^\dagger e_{j\sigma'}^\dagger e_{k\sigma} h_{l\sigma} . \end{aligned} \quad (1.1)$$

Here $e_{i\sigma}$ ($e_{i\sigma}^\dagger$) are annihilation (creation) operators of electrons with spin σ in the one-particle states $|i\rangle$ of energy ε_i^e . The corresponding operators and single-particle energies for holes are $h_{i\sigma}$ ($h_{i\sigma}^\dagger$) and ε_i^h , respectively. The explicit form of the single-particle wave function $\langle \mathbf{r}|i, \lambda \rangle = \psi_{i,\lambda}(\mathbf{r})$ enters the description via the Coulomb matrix elements:

$$V_{ij,kl}^{\lambda\lambda'} = \int d^3r \int d^3r' \psi_i^{\lambda*}(\mathbf{r}) \psi_j^{\lambda'*}(\mathbf{r}') V(\mathbf{r} - \mathbf{r}') \psi_k^{\lambda'}(\mathbf{r}') \psi_l^{\lambda}(\mathbf{r}) \quad (1.2)$$

with the band index $\lambda = e, h$ and the Coulomb potential $V(\mathbf{r}) = e^2/4\pi\epsilon_0\epsilon_r r$, where ϵ_r is the background dielectric constant. In envelope-function approximation ψ_i^λ is decomposed into the product $\xi_i^\lambda(\mathbf{r}) u_{\mathbf{k}=0}^\lambda(\mathbf{r})$, where $u_{\mathbf{k}}^\lambda(\mathbf{r})$ denotes the Bloch function and $\xi_i^\lambda(\mathbf{r})$ is the slowly varying envelope [68]. An additional contribution containing the electron-hole exchange terms $V_{ij,kl}^{he,\text{exch}} = \int d^3r \int d^3r' \psi_i^{h*}(\mathbf{r}) \psi_j^{e*}(\mathbf{r}) V(\mathbf{r} - \mathbf{r}') \psi_k^e(\mathbf{r}') \psi_l^h(\mathbf{r}')$ has been omitted in the Hamiltonian, as these matrix elements are strictly zero in envelope-function approximation. This is the case because Bloch functions $u_{\mathbf{k}}^\lambda(\mathbf{r})$ of different bands are orthogonal to each other. In more sophisticated approaches based on, for example, $\mathbf{k} \cdot \mathbf{p}$ [49] or tight-binding models [49, 69], these matrix elements constitute only a small perturbation, which shows once more that they can be neglected. As detailed in Appendix B, in this situation the spin of the electrons and holes are separately good quantum numbers. Please note that the electron-hole exchange matrix elements $V_{ij,kl}^{he,\text{exch}}$ should not be confused with the exchange Coulomb matrix elements $X_{ij}^{\lambda\lambda'} = V_{ij,ij}^{\lambda\lambda'}$ that can by no means be neglected and are of utmost importance for the proper description of the multi-exciton spectra.

In the symmetric case $\xi_{i,e} = \xi_{i,h}^*$ all Coulomb matrix elements are related to the electron-electron ones by

$$V_{ij,kl}^{hh} = V_{kl,ij}^{ee} \quad \text{and} \quad V_{ij,kl}^{he} = V_{lj,ki}^{ee} . \quad (1.3)$$

effective mass	$m_e = 0.065 m_0$
effective hole mass	$m_h = 0.17 m_0$
dielectric constant	$\epsilon_r = 13.69$
oscillator length	$l_{osc} = 5.4 \text{ nm}$

Table 1.2: Quantum dot parameters used in the multi-exciton calculations; m_0 denotes the vacuum electron mass.

The superscript ee will be dropped in what follows. The six-fold integral of the Coulomb-matrix elements (1.2) can be analytically reduced to a one-dimensional integral, which is evaluated numerically. Due to the cylindrical symmetry of the problem the angular momentum is conserved and one has $V_{ij,kl} \propto \delta_{m_i+m_j, m_k+m_l}$.

The many-body Hamiltonian is fully determined by the parameters listed in Table 1.2. From these values we obtain the single-particle energies with constant spacing $\hbar\omega_e = \hbar^2/m_e l_{osc}^2 = 40.20 \text{ meV}$ and $\hbar\omega_h = 15.37 \text{ meV}$, as well as the energy scale of the Coulomb matrix elements $E_c = e^2/4\pi\epsilon_0\epsilon_r l_{osc} = 19.48 \text{ meV}$. In the first part of the following chapters we will restrict ourselves to a QD containing an s - and a p -shell for both electrons and holes. In this case the orbital part of the single-particle state $|i\rangle$ can be uniquely identified by its angular-momentum, $m = 0$ for the s -shell and $m = \pm 1$ for the two p -states. All non-zero Coulomb matrix elements for this case are listed in Table 1.3. In Chapter 5 we will then investigate a QD with three shells for each type of carrier.

$(\alpha_i, \alpha_j, \alpha_k, \alpha_l)$	$V_{\alpha_i \alpha_j, \alpha_k \alpha_l}/E_c$
(0, 0, 0, 0)	1.1197
(0, 1, 1, 0), (1, 0, 0, 1)	0.8690
(0, -1, -1, 0), (-1, 0, 0, -1)	0.8690
(1, 1, 1, 1)	0.7935
(1, -1, -1, 1), (-1, 1, 1, -1)	0.7935
(-1, -1, -1, -1)	0.7935
(0, 0, 1, -1), (0, 0, -1, 1), (1, -1, 0, 0), (-1, 1, 0, 0)	0.2507
(0, 1, 0, 1), (1, 0, 1, 0)	0.2507
(0, -1, 0, -1), (-1, 0, -1, 0)	0.2507
(1, -1, 1, -1), (-1, 1, -1, 1)	0.1753

Table 1.3: Non-zero Coulomb matrix elements in units of $E_c = e^2/4\pi\epsilon_0\epsilon_r l_{osc}$. The indices refer to the z -component of the angular momentum: $m = 0$ for the s -shell and $m = \pm 1$ for the p -shell. The horizontal lines divide the matrix elements into three groups: direct- (top), exchange- (bottom) and other terms.

1.3 Full Configuration Interaction Scheme

In a semiconductor QD the finite height of the confinement potential leads to a finite number of localized states as well as to a continuum of energetically higher delocalized states. When the influence of the delocalized states on the discrete QD spectrum is neglected, the eigenvalue problem has a finite (albeit large) dimension and can be solved without further approximations. In this way the Coulomb interaction between the different possible configurations of carriers in the available bound states is fully taken into account. In this section we first outline the general idea of the ‘full configuration interaction scheme’ (FCI), which is also called ‘exact diagonalization approach’. Then we describe how optical properties can be obtained from the Coulomb-correlated few-particle states and discuss the simplification entailed by the assumption of identical envelopes.

As the Hamiltonian conserves the total number of electrons N_e and holes N_h , the Hamiltonian matrix falls into subblocks with basis states corresponding to uncorrelated many-particle states of the form

$$|\phi\rangle = \prod_{\sum_i n_i^e = N_e} (e_i^\dagger)^{n_i^e} \prod_{\sum_j n_j^h = N_h} (h_j^\dagger)^{n_j^h} |0\rangle . \quad (1.4)$$

In spatial representation the set of uncorrelated basis states $\{|\phi_i\rangle\}$ corresponds to the construction of all possible Slater states for a given number of electrons and holes. In order to find the eigenvalues and eigenfunctions of the interacting problem, the Hamiltonian $H = H_0 + H_{\text{Coul}}$ as given by Eq. (1.1) is expressed in terms of the uncorrelated basis (1.4). The resulting Hamiltonian matrix $\langle\phi_i|H|\phi_j\rangle$ is then diagonalized. For details of how to construct the Hamiltonian matrix and evaluate the matrix elements the reader is referred to Appendix A. By diagonalization, one obtains an expansion of the interacting few-particle eigenstates $|\psi\rangle$ of the system for a given number of electrons and holes in terms of the uncorrelated basis states $|\psi\rangle = \sum_i \alpha_i |\phi_i\rangle$. Such an expansion is desired as it allows one to calculate matrix elements between correlated states relatively easily, once the corresponding matrix elements for the uncorrelated basis states are determined.

As soon as the correlated eigenstates are determined, one can use them to calculate, for example, the interband emission or absorption spectra between the Coulomb-correlated eigenstates of the QD system. The corresponding *emission* intensity is calculated using Fermi’s golden rule [44, 70, 71]:

$$I(\omega) = \frac{2\pi}{\hbar} \sum_f |\langle\psi_f|H_{\text{dipole}}|\psi_i\rangle|^2 \delta(E_i - E_f - \hbar\omega) . \quad (1.5)$$

Here $|\psi_i\rangle$ denotes the initial many-particle state in the presence of Coulomb interaction with energy E_i . The corresponding quantities of the final states are $|\psi_f\rangle$ and E_f .

A similar expression is found for the absorption spectrum. The Hamiltonian H_{dipole} describes the light-matter interaction in dipole approximation and is given by

$$H_{\text{dipole}} = - \sum_{n,m} (\mathbf{E} \mathbf{d}_{nm}^{eh}) e_{n,-\sigma}^\dagger h_{m,\sigma}^\dagger + \text{h.c.} \quad (1.6)$$

In this expression \mathbf{d}_{nm}^{eh} denotes the matrix element $\langle n|e\mathbf{r}|m\rangle$ with the single-particle states $|n\rangle$ and $|m\rangle$ for the electron and hole, respectively. In envelope function approximation this can be evaluated to $\mathbf{d}_{cv}\langle n|m\rangle$ with the bulk interband matrix element \mathbf{d}_{cv} [68]. The quantity \mathbf{E} is the electric field at the position of the QD and e is the elementary charge. As the wavelength of the optical field is typically at least one order of magnitude larger than the extension of the QD, variations of the optical field over the QD can safely be neglected. Equation (1.6) shows that the optical field always creates or destroys electron-hole pairs. From this we can conclude that the only non-zero transition in Fermi's golden rule, will stem from situations in which the initial and final many-particle states differ by exactly one electron-hole pair.

In the special case of identical envelopes the dipole-matrix elements \mathbf{d}_{nm}^{eh} become diagonal, i.e. $\langle n|e\mathbf{r}|m\rangle \propto \delta_{nm}$. Therefore, the coupling of the QD to the optical field is conveniently described by the interband dipole operator

$$\mathcal{P} = \sum_{\sigma} \mathcal{P}_{\sigma} = d \sum_{i,\sigma} h_{i,\sigma} e_{i,-\sigma} \quad (1.7)$$

and its hermitian conjugate, where d is the modulus of the interband dipole matrix element. The operator \mathcal{P} describes the recombination of ‘mirror-symmetric’ pairs, that is pairs having opposite z -components of the angular momentum and spin. The hermitian conjugate operator \mathcal{P}^\dagger creates mirror-symmetric pairs and appears in the description of light absorption.

Throughout the following sections we will use the outlined FCI procedure to calculate the optical spectra for different situations. While the principle idea of the FCI approach is explained relatively easy, the numerical implementation and the resulting spectra are quite involved. Therefore a detailed discussion and interpretation of the numerically determined spectra is desirable and constitutes an integral part of the following chapters.

2 Full Configuration Interaction Results for the Optical Spectra

In this chapter we analyze the multi-exciton spectra calculated using the FCI method for a QD that provides an s - and a p -shell for electrons and holes. After some general remarks about the symmetries of the system and the initial states, we focus on the excitonic absorption and emission properties. The problem with only one electron-hole pair allows for an analytic discussion of the optical properties and illustrates the general procedure. After this, Section 2.3 deals with the biexcitonic problem, i.e., the investigation of two interacting electron-hole pairs and their optical properties. In Section 2.4 the spectra for an initial filling with up to six excitons are presented. The detailed analysis of the striking features observed in these spectra is postponed to Chapter 3.

2.1 Basic Considerations

Because the single-particle states are eigenstates of the z -component of the angular momentum operator, the classification of the uncorrelated Slater states in terms of the total angular momentum $l_z^e + l_z^h$ is straightforward. Furthermore, the states can easily be classified according to the total spin z -component separately for the electrons and the holes. Moreover, the Hamiltonian (1.1) commutes with the total spin of the electrons, \mathbf{S}_e^2 , as well as with the total spin of the holes, \mathbf{S}_h^2 , as discussed in Appendix B. However, the explicit classification of the Slater states in terms of the total spin is not straightforward. While it is relatively simple to find the linear combination of the Slater states that diagonalizes the spin operator in the case of two carriers, it is a rather tedious task in a more general situation. Instead, a numerical scheme was employed for this purpose.

The rather rich symmetry of the problem can be exploited to separate smaller Hamiltonian subblocks and to predict degeneracies. A list of good quantum numbers in this system includes $N_e, N_h, l_z^e + l_z^h, \mathbf{S}_e^2, \mathbf{S}_h^2, S_e^z, S_h^z$. The eigenstates are degenerate with respect to S_e^z and S_h^z . By numerical diagonalization of these subblocks, one obtains the Coulomb-correlated states and the corresponding eigenvalues, classified according to the above-mentioned quantum numbers.

Once the Coulomb-correlated eigenstates are determined, the absorption and emission spectra can be calculated using Fermi's golden rule. To do so one has to specify the

initial states. In the following sections we restrict ourselves to situations where the optical excitation leads to the same number of electrons and holes in the QD, i.e., $N_e = N_h = N^X$, where N^X stands for the number of electron-hole pairs (in the following loosely called excitons). Here it is further assumed that energy relaxation of carriers within the QD is considerably faster than the carrier recombination, so that the initial state for the recombination process with given N^X is the corresponding multi-exciton state with the lowest energy (N^X exciton ground state). Moreover, changes of the carrier spin during relaxation are neglected [72]. Since an optical excitation only creates multi-exciton states in which electrons and holes have opposite S_z values, only states with vanishing total z -component of the spin are considered as initial states. When considering an emission spectrum, the final state can be any (ground or excited) state of the system with one exciton removed. The same holds for an absorption spectrum, only that in this case one exciton is added to the final state. Later on in Chapter 4, we will analyze charged exciton complexes and spectra resulting from excited states.

2.2 Excitonic Absorption and Emission

As a first and most simple example we consider the absorption of an initially empty QD [44]. A schematic representation of the single-particle energy spectrum for a QD with two shells is given in Figure 2.1 a).

In part b) the energy spectrum of a QD filled with one electron-hole pair is shown in the absence (left part) and presence (right part) of Coulomb interaction. These energies belong to the possible final states in an absorption experiment. The different energy levels are classified in terms of the total angular momentum z -component $l_z^{\text{tot}} = l_z^{\text{tot},e} + l_z^{\text{tot},h}$ and their degeneracy. Without Coulomb interaction there are four different eigenenergies: The lowest energy corresponds to the case in which both electron and hole are in the s -shell. The highest energy belongs to a situation in which both carriers occupy the p -shell. For the two states energetically in the middle, one of the carriers occupies the s - and one the p -shell. The two energies are different because the energetic spacing of the single-particle states for electrons and holes are not the same, as indicated in part a) of the figure. The influence of the Coulomb interaction on the energy spectrum is two-fold: First it shifts the spectrum to lower energies due to the attractive interaction between electron and hole, and second it lifts some of the degeneracies.

In part c) of Figure 2.1 the actual absorption spectrum with (solid) and without (dashed) Coulomb interaction is shown. Bearing the harmonic oscillator model in mind, in the absence of Coulomb interaction one expects two lines: one at $\hbar\omega_e + \hbar\omega_h$ for the s -shell and one at $2(\hbar\omega_e + \hbar\omega_h)$ for the p -shell (measured relative to the bandgap). The ratio of the heights of the lines, here 2 : 1, reflects the degeneracy of the corresponding shells. Including Coulomb interaction, the absorption lines shift to lower energies due to the attractive interaction between electron and hole. Furthermore a transfer of oscillator strength from the p -shell to the s -shell emission line can be observed in the

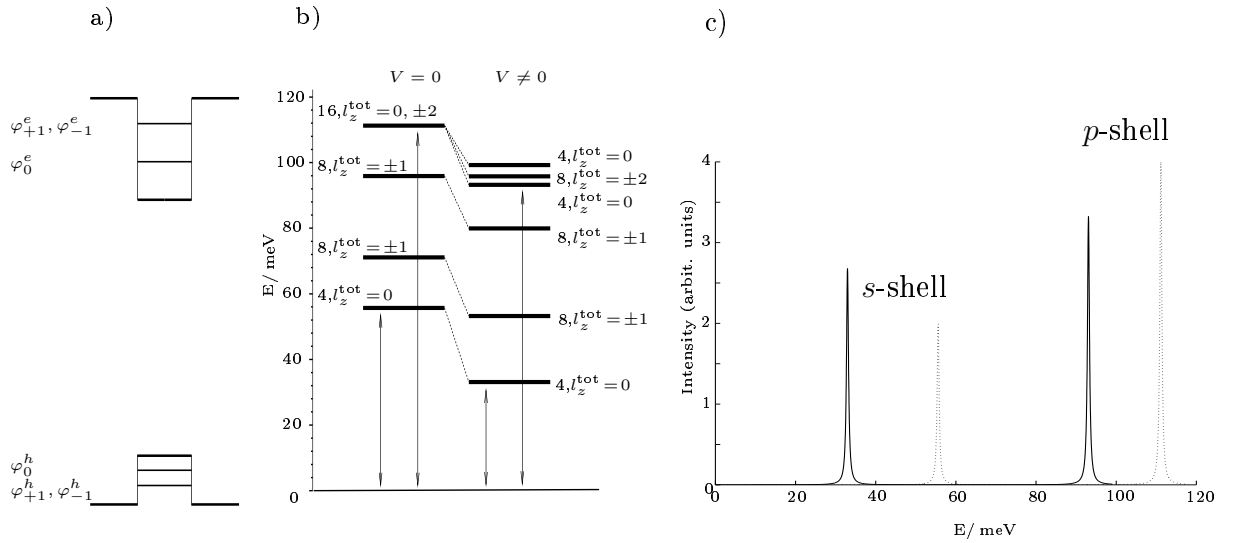


Figure 2.1: Part a) gives a schematic representation of the single-particle energy spectrum. In part b) the energy spectrum of one electron-hole pair with (right) and without (left) Coulomb interaction is shown. Additionally the classification in terms of the total angular momentum z -component $l_z^{\text{tot}} = l_z^{\text{tot},e} + l_z^{\text{tot},h}$ and the degeneracy of the energies is given. Vertical arrows denote transitions with non-vanishing oscillator strength. In part c) an absorption spectrum for an empty QD is shown. The s - and p -shell are clearly visible in the presence (solid line) and absence (dotted line) of the attractive Coulomb interaction between the carriers.

figure. Note that this transfer takes place while keeping the sum of the peak heights unchanged.

Whether a certain eigenstate $|f\rangle$ with one electron-hole pair (which we will conveniently denote in the following as $1X$ state) is visible in an absorption experiment depends on the matrix element $|\langle 0 | \mathcal{P} | f \rangle|^2$. If it is zero, the state $|f\rangle$ will be dark, otherwise it will be bright and can be observed. In the present example the initial state is the vacuum state $|0\rangle$ with no electron and no hole present. As already mentioned, the operator \mathcal{P} destroys electron-hole pairs with total angular momentum z -component and spin z -component equal to zero. Therefore, only final states with $S_z^{\text{tot},e} + S_z^{\text{tot},h} = 0$ and $l_z^{\text{tot},e} + l_z^{\text{tot},h} = 0$ are connected to the vacuum state. Consequently, in the absence of Coulomb interaction only two out of the four states can, even in principle, be observed. And indeed these two states are bright. According to their symmetry, the other two are necessarily dark. Including Coulomb interaction leads to a coupling of different uncorrelated states, so that three different energies could in principle be observed. However, the calculation yields only two transition lines. The corresponding states in the energy spectrum are indicated by vertical arrows in part b) of Figure 2.1. The states with the highest energy remain dark even though symmetry arguments do not predict this.

In the following paragraph, we give an analytic explanation of this behavior. Furthermore this simple example will clarify the general procedure. As already mentioned,

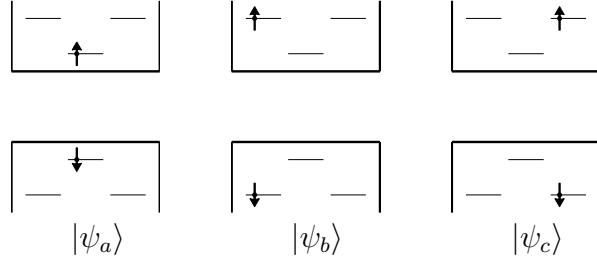


Figure 2.2: Configurations classified by $l_z^{\text{tot},e} + l_z^{\text{tot},h} = 0$ and $S_z^{\text{tot},e} + S_z^{\text{tot},h} = 0$. An additional restriction to the subspace $S_z^{\text{tot},e} = \frac{1}{2}$ and $S_z^{\text{tot},h} = -\frac{1}{2}$ is possible due spin degeneracy.

only states with $S_z^{\text{tot},e} + S_z^{\text{tot},h} = 0$ and $l_z^{\text{tot},e} + l_z^{\text{tot},h} = 0$ can be connected to the vacuum state by the dipole Hamiltonian. Therefore it is sufficient to restrict the analysis to this particular subspace. Additionally, $S_z^{\text{tot},e}$ and $S_z^{\text{tot},h}$ are good quantum numbers of the problem, so that the Hamiltonian matrix can be separated into subblocks with constant spin z -component. Therefore we can restrict ourselves to the block with $S_z^{\text{tot},e} = \frac{1}{2}$ and $S_z^{\text{tot},h} = -\frac{1}{2}$ [44]. The corresponding configurations are shown in Figure 2.2. All three states can directly be created from the vacuum by the action of \mathcal{P}^\dagger and are therefore called bright. These are the states seen in the spectrum in Figure 2.1 in the absence of Coulomb interaction. In the presence of Coulomb interaction, these states become mixed. The Hamiltonian matrix that describes this mixing contains only the non-interacting energies and the electron-hole interaction, because the contributions from electron-electron and hole-hole interaction vanish in a situation in which only one carrier of each type is present. Then the Hamiltonian matrix in the basis of Figure 2.2 is given by

$$\underline{\underline{H}} = \begin{pmatrix} \varepsilon_s^e + \varepsilon_s^h - D_{ss} & -X_{sp} & -X_{sp} \\ -X_{sp} & \varepsilon_p^e + \varepsilon_p^h - D_{pp} & -X_{pp} \\ -X_{sp} & -X_{pp} & \varepsilon_p^e + \varepsilon_p^h - D_{pp} \end{pmatrix}. \quad (2.1)$$

Here $X_{ij} = V_{ijij}$ denotes the exchange and $D_{ij} = V_{ijji}$ the direct Coulomb interaction terms. Due to the simple structure of this matrix, the eigenvalues and eigenvectors can be determined analytically. The eigenvector with the highest eigenenergy, namely $\varepsilon_p^e + \varepsilon_p^h - D_{pp} + X_{pp}$ is proportional to the transposed vector $(0, -1, 1)^t$. The other states are slightly more complicated and therefore here omitted. In order to determine the absorption spectrum, the transition matrix elements $|\langle 0 | \mathcal{P} | f \rangle|^2 = |\langle f | \mathcal{P}^\dagger | 0 \rangle|^2$ have to be evaluated. Because the configurations in Figure 2.2 are bright, one has $\mathcal{P}^\dagger |0\rangle = |\psi_a\rangle + |\psi_b\rangle + |\psi_c\rangle + |\psi_R\rangle$, where $|\psi_R\rangle$ denotes other states that are orthogonal on the set $\{|\psi_a\rangle, |\psi_b\rangle, |\psi_c\rangle\}$. More precisely $|\psi_R\rangle$ consists of the states that are generated from $\{|\psi_a\rangle, |\psi_b\rangle, |\psi_c\rangle\}$ by flipping all the spins. For an arbitrary linear combination of the possible final configurations of Figure 2.2 $|\tilde{f}\rangle = \alpha|\psi_a\rangle + \beta|\psi_b\rangle + \gamma|\psi_c\rangle$, one obtains $|\langle f | \mathcal{P}^\dagger | 0 \rangle|^2 = |\alpha + \beta + \gamma|^2$. This shows in particular that the eigenvector proportional to $(\alpha, \beta, \gamma)^t = (0, -1, 1)^t$ is not observable in an absorption spectrum, which provides the explanation of the aforementioned result of the dark third eigenstate.

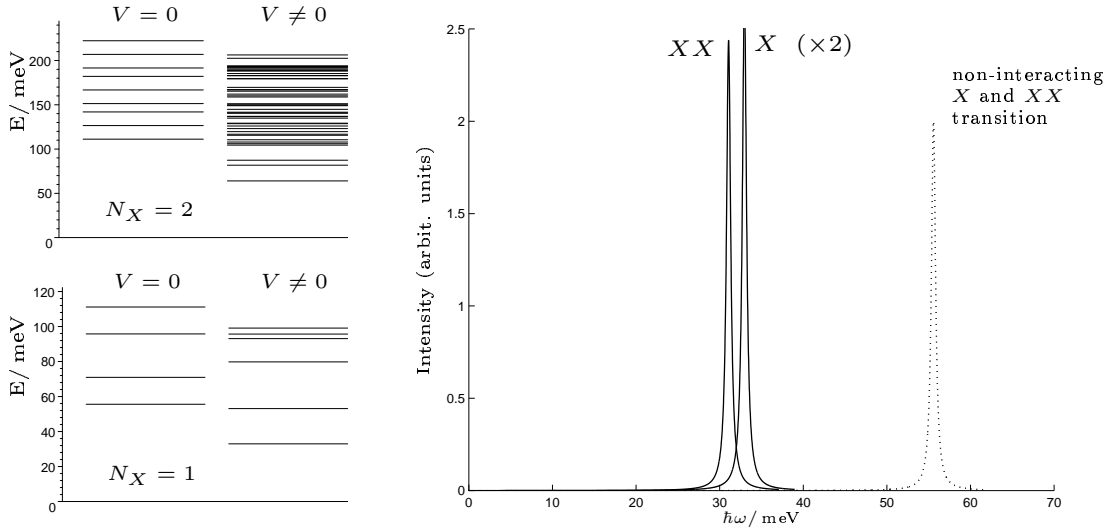


Figure 2.3: Excitonic and biexcitonic energy spectrum with and without Coulomb interaction (left). Right: Ground state emission spectra for an exciton and a biexciton. In the presence of Coulomb interaction an overall shift to lower energies is visible both in the energy spectrum and the emission lines. Furthermore a negative biexciton binding energy can be inferred. For better comparison the height of the excitonic line is doubled.

If one considers now the ground state *emission* spectrum from a QD with an initial filling of $1X$, exactly one line is found both with and without Coulomb interaction, and in both cases the lines are exactly the low-energy lines found in the absorption spectrum in Figure 2.1 c).

2.3 The Biexciton Problem

As a second example for the calculation of multi-exciton spectra, the excitonic and biexcitonic energy spectrum in the presence and absence of Coulomb interaction is shown in the left part of Figure 2.3. Again, the effect of Coulomb interaction is an overall shift to lower energies together with a reduction of degeneracies. The corresponding emission spectra are depicted on the right hand side of Figure 2.3. In the absence of Coulomb interaction the exciton and biexcitonic line coincide energetically and can be found at $\hbar\omega_e + \hbar\omega_h$. Including the interaction, the ground state emission spectrum of the biexciton lies energetically below the excitonic line. From this, a biexciton binding energy, defined by

$$B_{XX} = E_{\text{gs}}(2X) - 2E_{\text{gs}}(1X) , \quad (2.2)$$

of -1.90 meV can be deduced. Here $E_{\text{gs}}(1X)$ and $E_{\text{gs}}(2X)$ denote the ground state energy of the exciton and biexciton, respectively. A negative binding energy shows that it is energetically favorable to build a combined state out of the two electrons and the two holes.

Our value for the binding energy is in excellent agreement with recent measurements of $B_{XX} = -1.96$ meV reported in Ref. [42] and the calculated value of approximately -2 meV given in Ref. [73]. Such a good agreement is rather surprising if one bears in mind that the shape, composition and strain are neither precisely known nor accounted for in our model. Other groups [74–76] report for III-V systems somewhat larger values around -3 meV, which is – again due to the many unknown parameters – still a very satisfying result.

Considering the huge number of different configurations that interact in the biexciton problem and the fact that in this situation Coulomb interaction between equal carriers plays a role, it is not surprising that no simple analytic expression for the biexciton binding energy can be given. In order to understand the smallness of the biexciton binding energy it is illuminating to compare the QD biexciton problem with the hydrogen molecule (Heitler-London) theory. In the latter, the positive charges keep an optimal distance from one another and allow the negative ones to take the space between. In the QD, due to the discrete one-particle spectrum, no such geometrical flexibility is allowed: The carriers take preferentially the lowest available states, in which all the charges are superimposed. In the limiting case of identical envelopes the exciton is not only globally but also locally neutral, so that the two excitons do not interact at all, which would lead to a vanishing biexciton binding energy. The corrections to this picture stem from contributions of higher-state configurations that allow for a rearrangement of the charges. However, due to the large single-particle shell splitting, the energetic price to be paid keeps these admixtures small, and with it the biexciton binding energy.

2.4 Multi-Exciton Emission Spectra

After this investigation of the exciton and biexciton problem, let us consider the more general case, in which the number of excitons is step by step increased between one and the maximum number of excitons that the QD can confine. For the ground state, the analysis of Coulomb-correlated multi-exciton states shows that for an even number of excitons N^X , the spin-symmetry is singlet-singlet (ss), i.e., $S_e = S_h = 0$. These states are non-degenerate. In contrast, for odd N^X one has doublet-doublet (dd) ground states with $S_e = S_h = 1/2$ that are four times degenerate. For the choice of the initial states discussed in Section 2.1 only two states contribute as initial states to the emission formula with a weighting factor of $1/2$ each. The other two states are also dipole-allowed, but are eliminated from the emission formula Eq. (1.5) because their total spin z -component $S_z^{\text{tot},e} + S_z^{\text{tot},h}$ is nonzero. (By the same arguments one may be concerned about eliminating the states not having total angular momentum zero, but, as expected, no such ground states occur.) Note that if one would include these additional ground states only the height of some peaks is changed but no additional lines were introduced.

The results for the multi-exciton spectra are shown in Figure 2.4 for increasing population. First one observes the excitonic emission line, then the biexcitonic line, which

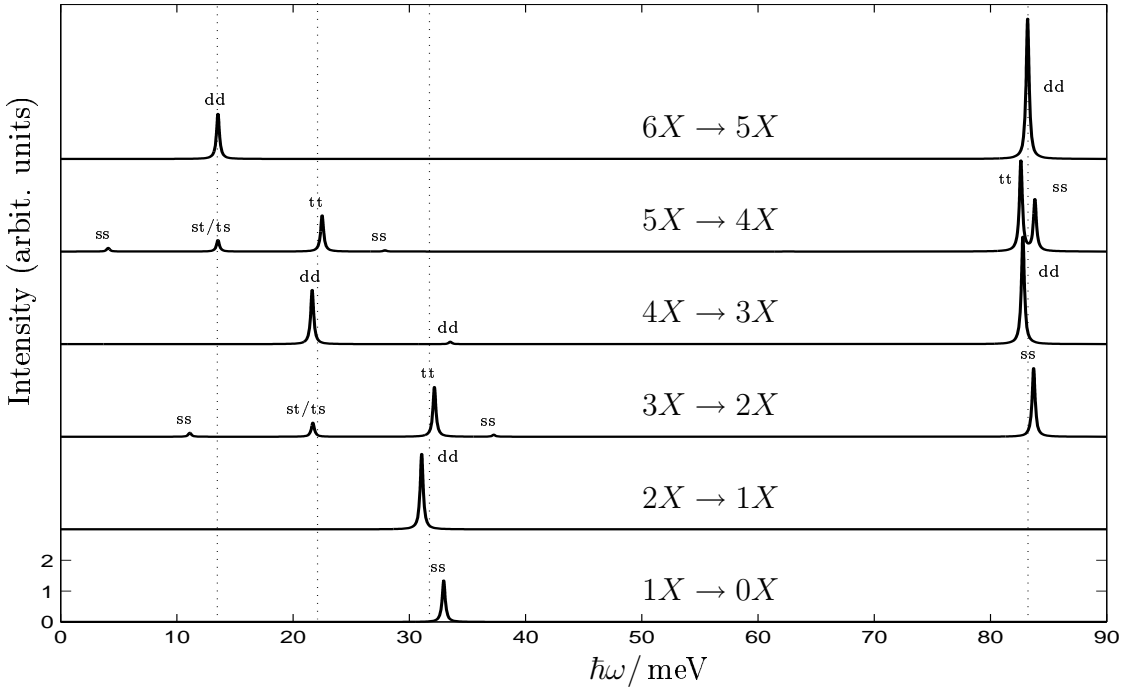


Figure 2.4: Ground state emission spectra for a QD with different number of excitons. The labels indicate the total spin of the *final* state for electrons and holes, respectively: s-singlet, d-doublet, t-triplet. The total angular momentum z -component is always zero. In the case of an odd number of excitons the spectrum is averaged over the two different $S_z^{\text{tot},e} + S_z^{\text{tot},h} = 0$ ground states. All energies are measured relative to the band-gap. The dotted lines are guides for the eye.

is shifted to lower energies due to the binding energy. Both lines stem from recombination processes that mainly involve configurations in which an exciton from the s -shell is removed. For a filling with three or more excitons, there are, in addition to the s -shell lines ($\hbar\omega < 35$ meV), peaks that stem from recombinations, in which mainly an electron-hole pair of the p -shell is removed. We therefore call the signature with $\hbar\omega > 80$ meV p -shell emission. Note that such a spectral separation of about 50 meV between the energetically lower and the energetically higher side of a multi-exciton spectrum is also observed in typical experiments [29, 40]. A closer look at the low-energy side reveals that the s -lines are arranged approximately in a descending ladder. In contrast to that, the energies of the p -lines show a remarkable stability. This stability was attributed to a 'hidden symmetry' property, which will be discussed in detail in Section 3.2.

The dipole operator \mathcal{P} has no simple commutation relation with the spin operators $\mathbf{S}_e^2, \mathbf{S}_h^2$ and therefore the spin symmetry of the final state is not determined by that of the initial state. This is why we encounter as final states all possible spin symmetries (ss, dd, tt, st, ts), as indicated in the figure.

By restricting the present discussion to an s - and a p -shell, the Hamiltonian (1.1) is identical, up to nonessential differences in the parameters, to the case analyzed in Ref. [44]. Nevertheless, the full diagonalization procedure used here leads to different relative line intensities and, more importantly, to the appearance of new emission lines. Namely, the st- and ts-lines that are altogether missing in Ref. [44].

After the investigation of the exciton and biexciton problem, we have presented in this chapter FCI results for an initially filling of the QD with up to six excitons and pointed out some of the intriguing regularities in these spectra. The next chapter is devoted to an explanation of these features. To this end, we will employ approximate Hamiltonians that retain the overall features and allow for a simpler analysis.

3 Approximation Schemes

The interaction between different configurations, as given by the FCI method, shows a quite high degree of complexity and therefore the results are not immediately intuitive. Even though we have considered electron-hole pairs that are optically created in ‘mirror-symmetric’ states, the Coulomb interaction mixes them strongly with configurations in which the electrons and holes are *not* arranged symmetrically. For instance, promoting two holes from the *s*-shell to the *p*-shell is energetically less costly than promoting one electron and one hole. The second case is more symmetric, but the first produces a state which is energetically closer to the original state and therefore it is the second state that will participate stronger in the exact interacting eigenstate. This may explain the disagreement with the line intensities found in Ref. [44], where only symmetric states are considered.

On the other hand, the relatively regular structure of the emission lines seems to indicate that an intuitive picture should be possible. This is achieved by turning to simpler, approximate Hamiltonians that allow analytic solutions and at the same time retain the essential features of the full problem. In the following section we consider a Hamiltonian that is diagonal in the free states. As we will see, this Hamiltonian is already able to explain the main features of the multi-exciton spectra. However, it overestimates the splitting observed for the *p*-shell emission and does not reproduce its stability as the number of excitons is increased in the QD. This ‘hidden symmetry’ property will be discussed in detail in Section 3.2. There we introduce the ‘adiabatic Hamiltonian’ that is able to explain both the ladder-like structure observed for the *s*-shell emission and the remarkable stability of the *p*-shell emission lines.

3.1 Diagonal Hamiltonian

In this section we derive a Hamiltonian that is diagonal in the uncorrelated many-particle basis states. The derivation is based on the relative importance of various interaction matrix elements. With the help of this Hamiltonian, it is possible to give an intuitive explanation for the main trends observed in the multi-exciton emission spectra shown in Figure 2.4 in the previous chapter. To this end we examine the list of all Coulomb matrix elements in Table 1.3 on page 8. There it can be seen that the largest Coulomb matrix elements are the direct ones, $V_{ij,ji} = D_{ij} = D_{ji}$. Their contribution to H_{Coul} can be expressed solely in terms of the occupation number operators, $\hat{n}_{i\sigma}^e = e_{i\sigma}^\dagger e_{i\sigma}$ and $\hat{n}_{i\sigma}^h = h_{i\sigma}^\dagger h_{i\sigma}$. Therefore this part is diagonal in the non-interacting basis states

given in Eq. (1.4) on page 9. The same is true for the exchange matrix elements $V_{ij,ij} = X_{ij} = X_{ji}$ with $i \neq j$ provided one includes their contribution only in the $e\text{-}e$ and $h\text{-}h$ interaction terms involving the same spin ($\sigma = \sigma'$). In this way, one obtains a Hamiltonian that is diagonal in the free states:

$$\begin{aligned} H_{\text{diag}} &= \sum_i \left(\varepsilon_i^e - \frac{1}{2} D_{ii} \right) \hat{n}_i^e + \sum_i \left(\varepsilon_i^h - \frac{1}{2} D_{ii} \right) \hat{n}_i^h \\ &+ \frac{1}{2} \sum_{i,j} D_{ij} (\hat{n}_i^e - \hat{n}_i^h) (\hat{n}_j^e - \hat{n}_j^h) \\ &- \frac{1}{2} \sum'_{i,j,\sigma} X_{ij} (\hat{n}_{i,\sigma}^e \hat{n}_{j,\sigma}^e + \hat{n}_{i,\sigma}^h \hat{n}_{j,\sigma}^h) . \end{aligned} \quad (3.1)$$

The prime in the last summation indicates that the $i = j$ terms have to be omitted and \hat{n}_i^e denotes $\hat{n}_{i\uparrow}^e + \hat{n}_{i\downarrow}^e$. Similarly \hat{n}_i^h stands for $\hat{n}_{i\uparrow}^h + \hat{n}_{i\downarrow}^h$. Of course, for this Hamiltonian there is no configuration interaction. The non-correlated states are eigenstates and the eigenvalues are derived from the formula above by inserting the corresponding occupation numbers.

If we now consider only ‘symmetric’ basis states¹, that is, only Slater states from Eq. (1.4), in which the same single-particle states are occupied by the electrons and holes ($n_{i\sigma}^e = n_{i,-\sigma}^h = n_{i\sigma}^X$) we obtain for the eigenenergies of these states:

$$E = \sum_i (\varepsilon_i^e + \varepsilon_i^h - D_{ii}) n_i^X - 2 \sum_{i < j} \sum_{\sigma} X_{ij} n_{i,\sigma}^X n_{j,\sigma}^X . \quad (3.2)$$

Here $n_{i,\sigma}^X$ is one, if the single-particle state $|i, \sigma\rangle$ is occupied by an electron (and thus a hole as we consider only symmetric states) and zero otherwise. The spin index was explicitly used to underline that the exchange interaction acts only between equal spins. Note that the second sum runs only over pairs of excitons.

In this model, the exciton energy is $E_i^X = \varepsilon_i^e + \varepsilon_i^h - D_{ii}$ where the binding energy results from the direct electron-hole Coulomb attraction. When the electron and hole envelope functions are identical, the excitons are not only globally but also locally neutral and the direct electrostatic interaction between different excitons vanishes. To better understand the physical reason for this, let us take a look at Figure 3.1. There, a typical symmetric state with two electrons and two holes is depicted. If we now consider, for example, the s -electron, the Coulomb interaction for this electron consists of three terms: The interaction with the p -electron and the interaction with the s - and p -hole. As we assumed identical envelopes the repulsive contribution of the p -electron and the attractive contribution of the p -hole on the s -electron exactly cancel each other and we are left with the attractive interaction of the s -hole. A similar argument applies for

¹ Only these states are optically active in the non-interacting case, so that one expects them to yield the main contribution to the spectrum.

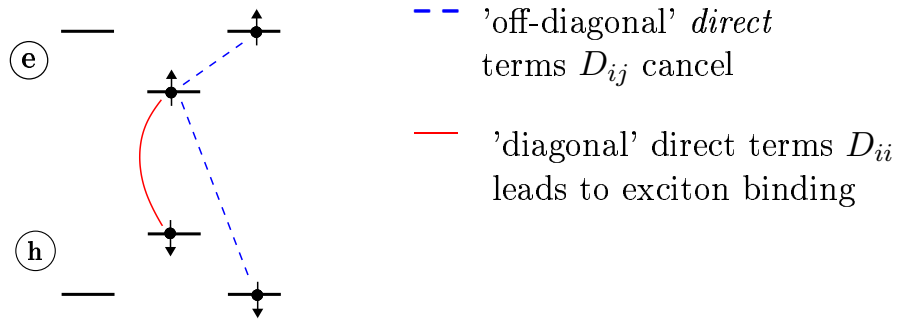


Figure 3.1: (color online) For symmetric population, only the *diagonal* direct term D_{ii} enters the approximate energy because the off-diagonal direct terms D_{ij} cancel exactly in the considered case of identical envelopes.

all the charge carriers. Therefore only the diagonal direct terms D_{ii} contribute. In the approximate Hamiltonian (3.2) the only interaction between different excitons is due to the exchange terms and takes place between excitons with the same spin structure². Consequently, the biexciton binding energy is zero in this approximation. In the case of a dot with only two shells the exciton energy E_i^X depends only on the shell and not on the state $|i\rangle$. Furthermore the exchange-interaction X_{ij} is completely described by the two numbers X_{sp} and X_{pp} as one has:

$$\left(V_{ijij} \right)_{i,j} = \begin{pmatrix} D_{ss} & X_{sp} & X_{sp} \\ X_{sp} & D_{pp} & X_{pp} \\ X_{sp} & X_{pp} & D_{pp} \end{pmatrix}, \quad (3.3)$$

and only exchange terms with $i \neq j$ enter Eq. (3.2). As a consequence, only four numbers describe the QD in terms of the diagonal Hamiltonian: E_s^X , E_p^X , X_{sp} and X_{pp} . For example, using this notation, the state in Figure 3.1 has the energy: $E_s^X + E_p^X - 2X_{sp}$.

A comparison of the results from the diagonal model with those from the full Hamiltonian is given in Figure 3.2. The approximate Hamiltonian indeed reproduces the dominant features of the multi-exciton emission spectra. It shows a ladder-like structure of the s -lines, with the corresponding spacing in good agreement with the full calculation. However, it overestimates the splitting in the p -shell and blue-shifts the s -shell transitions. Furthermore, there is a discrepancy in the peak height as the oscillator strength in the simplified picture takes only integer values. This is the case because any allowed transition between Slater states enters with an oscillator strength of one. Since we have a good overall agreement between the full calculation and the

² Since we only consider electron-hole pairs with opposite z -components of the spin, the exciton spin is always zero. Exchange interaction between two excitons is possible when the z -components of the spin for the two electrons agree, which is then also true for the holes.

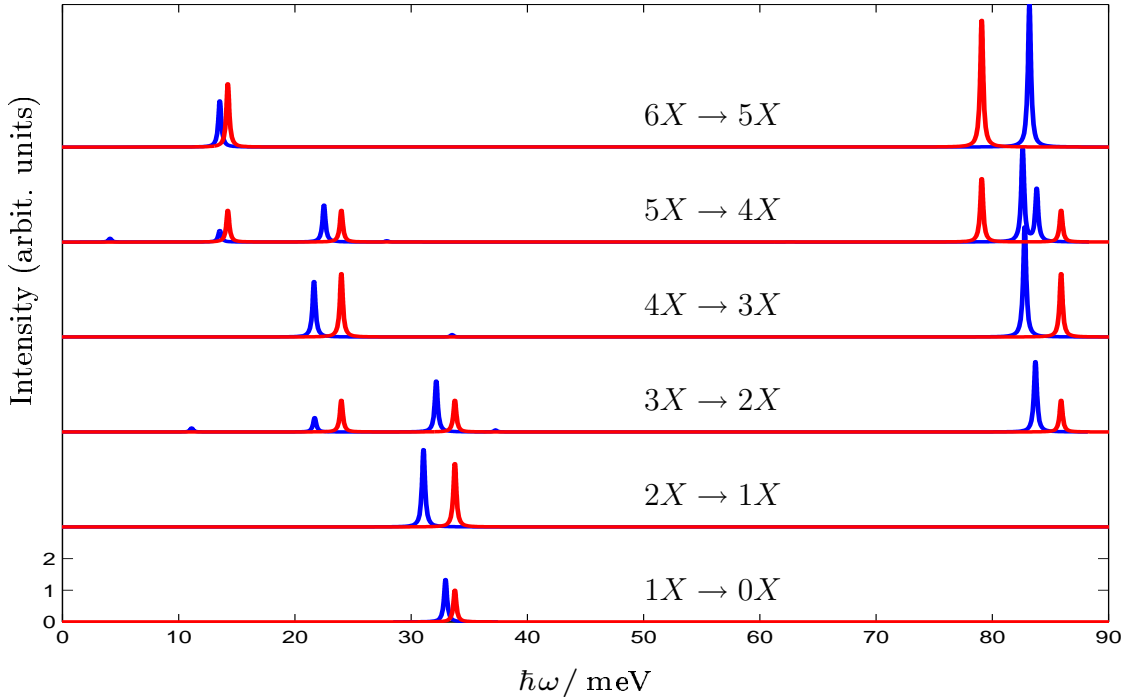


Figure 3.2: (color online) Comparison of results from the diagonal Hamiltonian (red) and the full diagonalization (blue) for ground state emission spectra with increasing number of excitons. The dominant features are well reproduced by the approximate scheme.

simplified model and the latter is diagonal in the uncorrelated states, we can use these non-interacting states to discuss the features of the excitonic emission spectrum.

For example, starting from the ground state of the QD filled with three excitons (see Figure 3.3) either the p -electron recombines with the p -hole, which results in the high-energy line, or one of the s -electrons recombines with an s -hole, resulting in the low energy lines. The splitting of the latter is due to the exchange terms X_{ij} [29, 53]. Depending on which of the two s -shell electrons recombine, the remaining electron can or cannot lower its energy by exchange. In the approximate scheme the splitting is given by the exchange interaction between carriers in the s - and p -shell: According to Eq. (3.2) the energy change for the removal of one s -exciton with a given spin structure is proportional to the number of p -excitons having the same spin structure. Adding equal contributions from electrons and holes, the coefficient is $2X_{sp}$. A similar splitting can be observed for an initial filling with five excitons. In addition to the main peaks, which can be explained in the approximate picture, there are smaller peaks in the spectrum that stem from admixtures of more complicated configurations.

As the exchange terms are responsible for the s -shell splitting in the three and five exciton emission spectrum it is easy to understand why there is no splitting in the case of four and six excitons: In this case, no matter which of the s -electrons recombines, it always has an exchange partner, so that there is no energy difference between these configurations, as depicted in Figure 3.4.

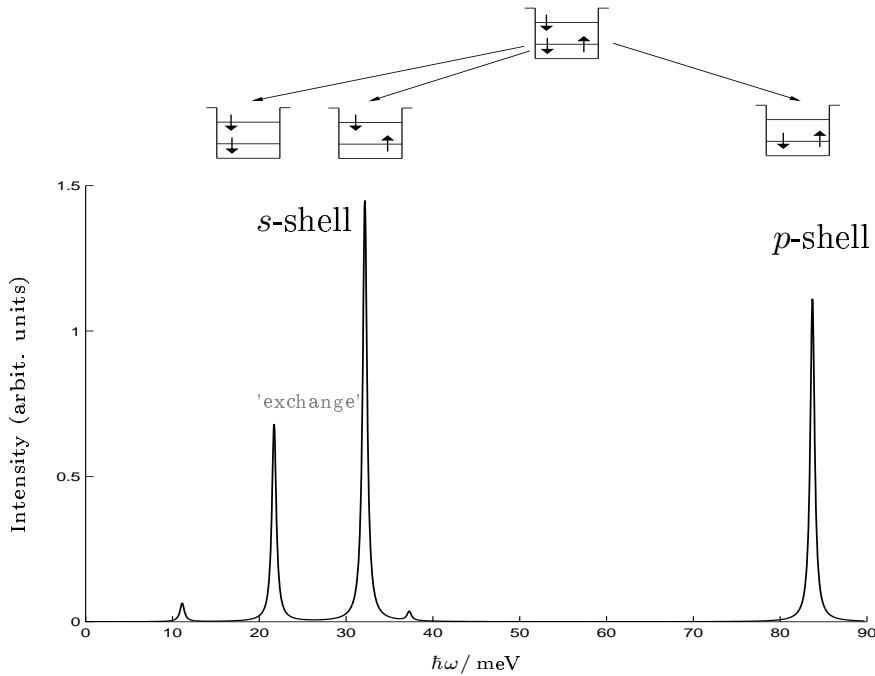


Figure 3.3: $3X \rightarrow 2X$ emission spectra obtained from the full calculation and interpretation of the main peaks using the diagonal Hamiltonian. The exchange integrals are responsible for the splitting of the major s -shell lines. As we consider only symmetrically populated states in the approximate description, it is sufficient to depict only the electronic configurations.

Even though the diagonal Hamiltonian gives an intuitive picture of the main features in terms of uncorrelated states, the following shortcomings of this model need to be discussed: The ground state of the four exciton problem is inaccurately given by the diagonal model as a triplet-triplet state, as predicted by Hund's rule. It is known that Hund's rule does not always apply in QDs and this is such a case. The true ground state with an energy slightly below this triplet-triplet state has a singlet-singlet spin symmetry, as mentioned in the previous section. It is this singlet-singlet state that is used as initial state in the emission spectrum obtained from the diagonal Hamiltonian, red line in Figure 3.2, in order to make the comparison meaningful. Additionally the diagonal Hamiltonian entails a ladder-like structure for the p -lines too, with a spacing of $2X_{pp}$, which is not confirmed by the full calculation. As explained in the next section, this stems from neglecting important contributions from the interaction.

These spectral features have been described previously [10, 29]. Here we show which terms of the full Hamiltonian are responsible for them and that these terms can be included in an exactly solvable approximate Hamiltonian H_{diag} . Note that the eigenenergies of the diagonal Hamiltonian coincide exactly with those obtained by evaluation of the matrix elements $\langle \psi_i | H | \psi_i \rangle$ with $|\psi_i\rangle$ being a Slater state, or by a non-self-consistent HF-theory. Therefore the resulting approximate eigenenergies are sometimes referred to as the HF-eigenenergies, see, e.g., Ref. [46, 53, 77]. Here we have presented an independent derivation of these approximate eigenenergies based on an analysis of

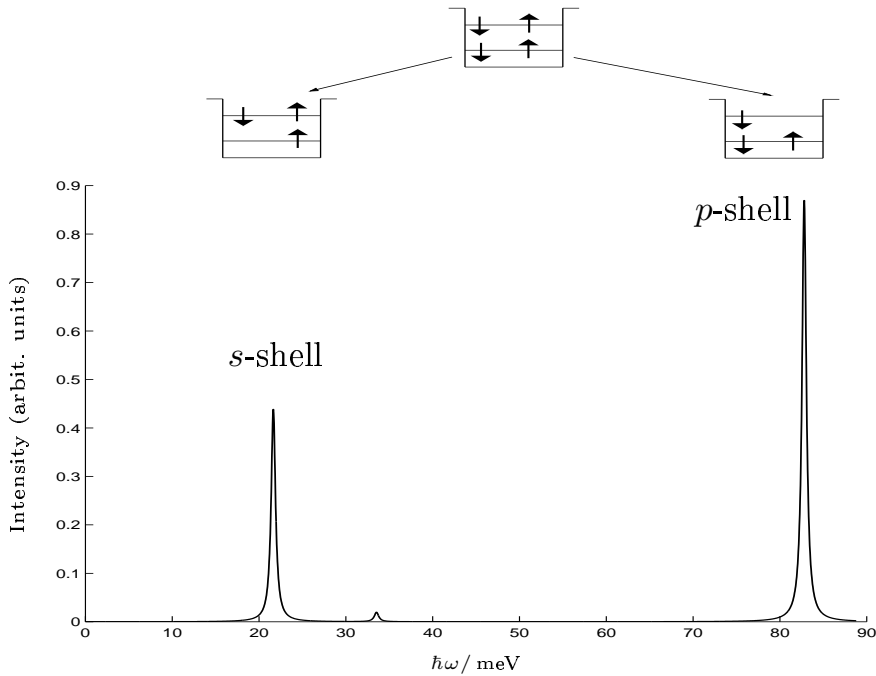


Figure 3.4: $4X \rightarrow 3X$ emission spectra obtained from the full calculation and interpretation of the main peak using the diagonal Hamiltonian. Only the electronic configurations and one possible decay path is shown.

the importance of the different Coulomb matrix elements. Furthermore the derived Hamiltonian H_{diag} is formally richer than a HF-Hamiltonian because H_{diag} is a genuine two-particle Hamiltonian while a HF-Hamiltonian is always an effective one-particle Hamiltonian [71].

3.2 Adiabatic Hamiltonian

Clearly, the diagonal Hamiltonian discussed above allows for an intuitive picture of the most important features in terms of uncorrelated states. The main drawback, however, is that it predicts a ladder-like structure for the p -shell emission lines as a function of the number of excitons in this shell. In contrast, the full calculation does not yield such a ladder structure but a remarkable energetic stability of the p -shell emission, see Figure 3.2.

Before we move on to study an approximate Hamiltonian not entailing such a ladder structure for the p -shell and therefore accounting more accurately for the emission spectra, we will briefly review the argument for the stable p -shell emission as presented in the literature. This stability is the topic of a series of papers published by P. Hawrylak and co-workers [12, 49, 57, 78, 79] who introduced the phrase ‘hidden symmetry’ for this intriguing property to the QD community. Their analysis assumes a *single, degenerate shell*, which means assuming that there exists only one shell, or in case of several shells,

that these shells are completely decoupled from each other. The central point is now to *assume* that one has to a good approximation $[H_{\text{shell}}, \mathcal{P}_{\text{shell}}] = -\tilde{E}_{\text{shell}}^X \mathcal{P}_{\text{shell}}$, where H_{shell} is the Hamiltonian in Eq. (1.1) restricted to a single shell and $\mathcal{P}_{\text{shell}}$ denotes $\sum_{i,\sigma} h_{i\sigma} e_{i,-\sigma}$ with i running over the states of this single shell. If the aforementioned commutator indeed holds and if $|\psi, N_X + 1\rangle$ is an eigenstate of H_{shell} with energy $E_{|\psi, N_X + 1\rangle}$ containing $N_X + 1$ excitons, then $\mathcal{P}_{\text{shell}}|\psi, N_X + 1\rangle$ is also an eigenstate of H_{shell} , with eigenenergy $E_{|\psi, N_X\rangle} = E_{|\psi, N_X + 1\rangle} - \tilde{E}_{\text{shell}}^X$ and one electron-hole pair less than the original state. The proof of this statement runs in close analogy to the case of the algebraic solution of the harmonic oscillator known from elementary quantum mechanics [67, 70], in which the annihilation operator \hat{a} obeys the equation $[H_{\text{HO}}, \hat{a}] = -\hat{a}$, and is given here for completeness:

$$\begin{aligned} H_{\text{shell}} (\mathcal{P}_{\text{shell}}|\psi, N_X + 1\rangle) &= ([H_{\text{shell}}, \mathcal{P}_{\text{shell}}] + \mathcal{P}_{\text{shell}}H_{\text{shell}}) |\psi, N_X + 1\rangle \\ &= (-\tilde{E}_{\text{shell}}^X + E_{|\psi, N_X + 1\rangle}) (\mathcal{P}_{\text{shell}}|\psi, N_X + 1\rangle) . \end{aligned} \quad (3.4)$$

As the new state is created by the action of $\mathcal{P}_{\text{shell}}$, the transition matrix element $|\langle\psi, N_X | \mathcal{P}_{\text{shell}} | \psi, N_X + 1\rangle|^2$ is non-zero. Consequently, a line at the energy difference $\tilde{E}_{\text{shell}}^X$ will be observable in an emission spectrum irrespective of the initial number of electron-hole pairs in the system. This is at the heart of ‘hidden symmetry’.

In other words, the energetic stability of the emission line with increasing number of excitons means that the energy increases linearly with the number of excitons in the system. This idea is borrowed from a completely different research field, namely, from the community of ultra-high magnetic fields in two-dimensional electron gases, see, for example, Ref. [80, 81], where similar results were found. In a strong magnetic field directed perpendicular to the two-dimensional electron gas, the energy bands for the electrons and holes split into discrete and highly degenerate Landau levels [71]. In the strong-field limit all carriers are confined in the lowest of these levels. It is exactly in this limit that the linear increase of the total energy with increasing number of excitons is found. The connection to the case of a QD is made if one realizes that this lowest Landau level provides exactly the single-degenerate shell discussed above.

Unfortunately, the aforementioned commutator does not hold in general. In particular, the proof of the argument makes use of the assumption that one deals with a single degenerate shell, while in fact several, not weakly interacting shells are always present. Therefore, it is by no means clear if the ‘hidden symmetry’ result holds, and, if it does, why and in what form. We show that in the adiabatic approach, and due to certain peculiarities of the problem, the ‘hidden symmetry’ can be recovered, albeit with the parameters renormalized by the interaction between the shells. The adiabatic Hamiltonian is more realistic than the assumption of a single, degenerate shell because it captures the essential part of the inter-shell interaction, as we will see from a comparison of the multi-exciton spectrum of this adiabatic Hamiltonian and the full calculation. The discussion of the conditions in which the ‘hidden-symmetry’ commutator holds sheds light on the limits of validity of the ‘hidden symmetry’ argument.

Refinement of the approximate Hamiltonian

Now we turn to the refinement of the approximate Hamiltonian regarding the p -shell emission. This can be achieved in the following way: An examination of the ground states for a situation with three or more excitons, calculated with the full diagonalization procedure, shows that it is safe to assume that in such states the s -shell is completely filled. The states with full s -shell configurations appear with a weighting factor of at least 0.95. Therefore, as far as the ground states and the lower excited states are concerned, it is possible to construct an approximate Hamiltonian that describes the fully interacting p -states following 'adiabatically' an external field provided by the 'frozen' s -carriers. Practically, this is obtained from the full interacting Hamiltonian (1.1) along the same lines as before, but this time one enforces diagonality *only with respect to the s-occupation numbers*. In other words, one discards only those terms that contain s -state creation or annihilation operators but cannot be expressed in terms of s -state occupation numbers. In this way, fully correlated p -states at given s -orbital fillings are obtained. The resulting Hamiltonian is called 'adiabatic', because we use some degrees of freedom, namely the s -shell excitons, as parameters. This is in principle like the Born-Oppenheimer approximation, in which the nuclei are taken out of the dynamics and their positions are used as parameters.

In the resulting 'adiabatic' Hamiltonian $H_{ad} = H_{ad}^{(s)} + H_{ad}^{(p)} + H_{ad}^{(sp)}$ we have separated the terms describing the s - and p -shell as well as the s - p -interaction. The p -shell part retains the form of Eq. (1.1) with the summation restricted to the p -orbitals. Therefore, in the following equations, the indices i, j, k, l label only p -states while for the s -states the explicit subscript s is taken. Using the symmetry relations of the Coulomb matrix elements, Eq. (1.3), and bringing close the operators with the same spin, $H_{ad}^{(p)}$ can be rewritten as

$$H_{ad}^{(p)} = \sum_{i\sigma} \varepsilon_i^e \hat{n}_{i\sigma}^e - \frac{1}{2} \sum_{ijk\sigma} V_{ij,kj} e_{i\sigma}^\dagger e_{k\sigma} + \sum_{i\sigma} \varepsilon_i^e \hat{n}_{i\sigma}^h - \frac{1}{2} \sum_{ijk\sigma} V_{ij,kj} h_{i\sigma}^\dagger h_{k\sigma} \\ + \frac{1}{2} \sum_{\substack{ijkl \\ \sigma\sigma'}} V_{ij,kl} \left(e_{i,\sigma}^\dagger e_{l,\sigma} - h_{l,\sigma}^\dagger h_{i,\sigma} \right) \left(e_{j,\sigma'}^\dagger e_{k,\sigma'} - h_{k,\sigma'}^\dagger h_{j,\sigma'} \right) , \quad (3.5)$$

where the new one-particle Coulomb terms (the second and fourth term in Eq. (3.5)) result from the reordering of operators and the resulting Kronecker delta. The s -shell part and the s - p -interaction are similar to the diagonal Hamiltonian, Eq. (3.1),

$$H_{ad}^{(s)} = \left(\varepsilon_s^e - \frac{1}{2} D_{ss} \right) \hat{n}_s^e + \left(\varepsilon_s^h - \frac{1}{2} D_{ss} \right) \hat{n}_s^h + \frac{1}{2} D_{ss} (\hat{n}_s^e - \hat{n}_s^h)^2 , \quad (3.6)$$

$$H_{ad}^{(sp)} = D_{sp} (\hat{n}_s^e - \hat{n}_s^h) (\hat{n}_p^e - \hat{n}_p^h) - X_{sp} \sum_{\sigma} (\hat{n}_{s,\sigma}^e \hat{n}_{p,\sigma}^e + \hat{n}_{s,\sigma}^h \hat{n}_{p,\sigma}^h) , \quad (3.7)$$

where $\hat{n}_{s,p}^{e,h}$ is the *total* population of electrons or holes in the s - or p -shell, respectively. Note that the first line collapses to $(\varepsilon_s^e + \varepsilon_s^h - D_{ss}) n_{s,\sigma}^X$ in the case of symmetric population and the second one yields in this case $-2X_{sp} \sum_{\sigma} \hat{n}_{s,\sigma}^X \hat{n}_{p,\sigma}^X$.

It is important to note that – with the Coulomb matrix elements listed in Table 1.3 on page 8 – in the one-particle Coulomb terms in the first line of Eq. (3.5) only contributions with $i = k$ appear. This can be traced back to the angular momentum conservation which leads to $V_{ijkj} \propto \delta_{m_i+m_j, m_k+m_j} = \delta_{m_i, m_k}$ in the circular symmetric system and the fact that in the present case the states are uniquely identified by their angular momentum. Therefore one has $V_{ijkj} \propto \delta_{i,k}$ and the one-particle Coulomb terms in Eq. (3.5) describe a renormalization of the one-particle energies $\varepsilon_i^{e,h}$. Moreover, these renormalized energies do not depend on the index i within the p -shell, so that $H_{ad}^{(p)}$ describes a 'single degenerate shell' [44, 56, 78], and can be rewritten as

$$H_{ad}^{(p)} = \left(\varepsilon_p^e - \frac{1}{2}D_{pp} - \frac{1}{2}X_{pp} \right) \hat{n}_p^e + \left(\varepsilon_p^h - \frac{1}{2}D_{pp} - \frac{1}{2}X_{pp} \right) \hat{n}_p^h + \frac{1}{2} \sum_{\substack{ijkl \\ \sigma\sigma'}} V_{ij,kl} \left(e_{i,\sigma}^\dagger e_{l,\sigma} - h_{l,\sigma}^\dagger h_{i,\sigma} \right) \left(e_{j,\sigma'}^\dagger e_{k,\sigma'} - h_{k,\sigma'}^\dagger h_{j,\sigma'} \right) . \quad (3.8)$$

Consequences for the spectra

With the help of the adiabatic Hamiltonian H_{ad} the full emission spectrum depicted in Figure 2.4 can be explained as follows: For the s -lines the arguments showing the formation of a ladder with the spacing of $2X_{sp}$ are as in the case of the diagonal Hamiltonian H_{diag} . The energetic position of the p -shell emission can be deduced from the commutation relation of H_{ad} with the p -shell dipole-transition operator \mathcal{P}_p , defined as in Eq. (1.7) but this time with the sum restricted only to p -states. It is readily verified, that

$$\left[e_{i,\sigma}^\dagger e_{j,\sigma} - h_{j,\sigma}^\dagger h_{i,\sigma}, \mathcal{P}_p \right] = 0 \quad (3.9)$$

and therefore \mathcal{P}_p commutes with the second line of Eq. (3.8). As explained at the beginning of this section, this is the core of the 'hidden symmetry' property [56, 78] showing that the interaction part plays no role in this argument. The commutation of \mathcal{P}_p with the occupation number operators of the shells is rather obvious, because the application of \mathcal{P}_p corresponds to a population reduction by one electron-hole pair in the p -states and no change in the s -states. Correspondingly, one can verify $[\hat{n}_p^{e,h}, \mathcal{P}_p] = -\mathcal{P}_p$ and $[\hat{n}_s^{e,h}, \mathcal{P}_p] = 0$. Such simple relations arise only when commuting \mathcal{P}_p with the *total* number operator of the p -shell, not with individual number operators. This is why it is important to have a degenerate shell.

Assuming that the s -states are fully occupied ($n_{s,\sigma}^{e,h} = 1$), one obtains from these results

$$[H_{ad}, \mathcal{P}_p] = -(\varepsilon_p^e + \varepsilon_p^h - D_{pp} - X_{pp} - 2X_{sp}) \mathcal{P}_p . \quad (3.10)$$

As detailed in the beginning of this section, this shows that the removal of one p -exciton is accompanied by an energy decrease that does not depend on the number of excitons.

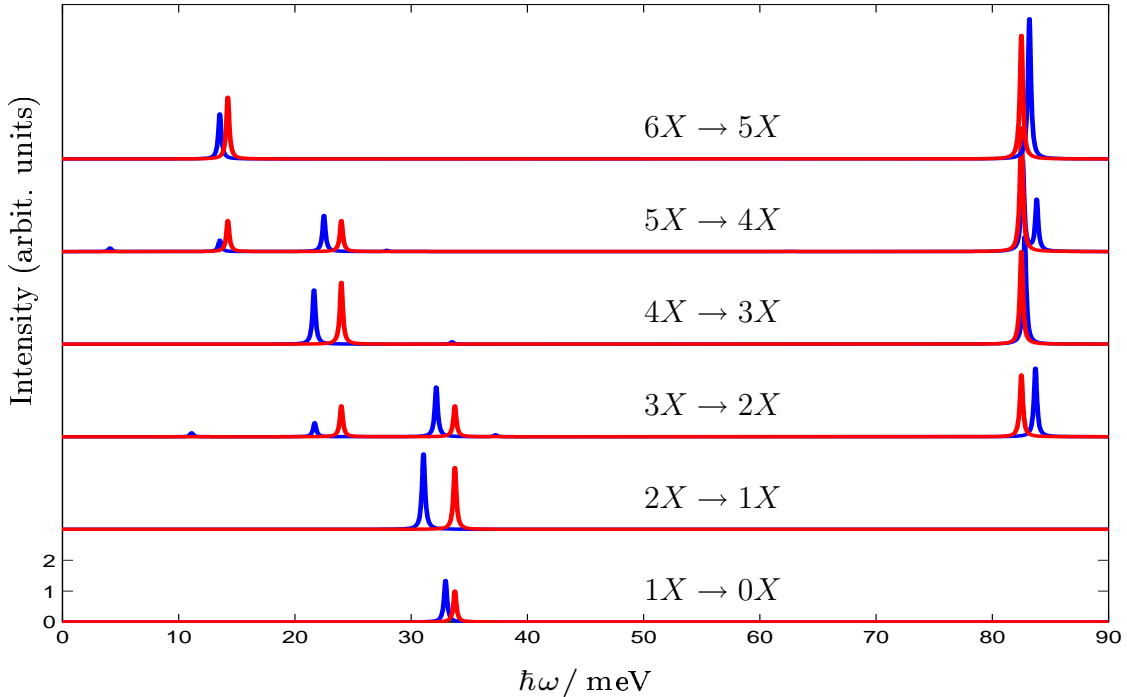


Figure 3.5: (color online) Comparison of results from the adiabatic Hamiltonian (red) and the full diagonalization (blue) for QD emission spectra with increasing number of excitons.

The value of this energy,

$$\begin{aligned}\mathcal{E}_p^X &= \varepsilon_p^e + \varepsilon_p^h - D_{pp} - X_{pp} - 2X_{sp} \\ &= E_p^X - X_{pp} - 2X_{sp} ,\end{aligned}\quad (3.11)$$

is in excellent agreement with the exact diagonalization result, see Figure 3.5. Indeed, using the values in Table 1.3 one obtains $\mathcal{E}_p^X = 82.5$ meV. The emission spectrum associated with the adiabatic Hamiltonian is shown in Figure 3.5 and consists of p -lines having all this common value, while the s -line ladder remains the same as given by the diagonal Hamiltonian.

Connection to the literature

The 'hidden symmetry' argument, as discussed by Wojs and Hawrylak [44, 56, 78], is based on the assumptions that (i) one has identical envelopes for the electrons and holes and (ii) the one-particle levels form 'a single degenerate shell'. In these hypotheses, one gets approximately a constant energy value at the removal of each exciton, and this value depends only on the parameters of this shell. To see this, let us start with the

Hamiltonian

$$\begin{aligned} H_{\text{shell}} = & \varepsilon_{\text{shell}}^e \hat{n}_{\text{shell}}^e - \frac{1}{2} \sum_i W_i \hat{n}_i^e + \varepsilon_{\text{shell}}^h \hat{n}_{\text{shell}}^h - \frac{1}{2} \sum_i W_i \hat{n}_i^h \\ & + \frac{1}{2} \sum_{\substack{ijkl \\ \sigma\sigma'}} V_{ij,kl} (e_{i,\sigma}^\dagger e_{l,\sigma} - h_{l,\sigma}^\dagger h_{i,\sigma}) (e_{j,\sigma'}^\dagger e_{k,\sigma'} - h_{k,\sigma'}^\dagger h_{j,\sigma'}) \end{aligned} \quad (3.12)$$

that can be deduced for any single, degenerate shell and not only for the p -shell, as it was done in Eq. (3.8). In this Hamiltonian \hat{n}_{shell}^e denotes the total number operator for the electron in this shell, \hat{n}_i^e is defined via $\hat{n}_{i,\uparrow}^e + \hat{n}_{i,\downarrow}^e$ and W_i is given by $\sum_j V_{ij,ij}$. If the commutator $[\mathcal{P}_{\text{shell}}, H_{\text{shell}}]$ is evaluated, one finds again that the last line in Eq. (3.12) plays no role and one is left with $(\varepsilon_{\text{shell}}^e + \varepsilon_{\text{shell}}^h) \mathcal{P}_{\text{shell}} - \sum_i W_i e_i^\dagger h_i^\dagger$. While W_i does not depend on the state index i in the case of a p -shell, in general it will, so that it is *impossible* to recast the expression into the form of $\tilde{E}_{\text{shell}}^X \mathcal{P}_{\text{shell}}$. Nevertheless the desired form can be reached in an approximation, in which W_i is replaced by its average value $\bar{W}_{\text{shell}} = \frac{1}{N_{\text{shell}}} \sum_i W_i$ [56, 78], where the quantity N_{shell} denotes the number of degenerate states within the shell. Using this approximation yields

$$\tilde{E}_{\text{shell}} \approx \varepsilon_{\text{shell}}^e + \varepsilon_{\text{shell}}^h - \bar{W}_{\text{shell}} . \quad (3.13)$$

If the ‘hidden-symmetry’ argument is applied to the s -shell one obtains $\bar{W}_{\text{shell}} = D_{ss}$ and therefore transition energies in accordance with the diagonal Hamiltonian. Evaluating this expression, however, for the p -shell yields $\bar{W}_{\text{shell}} = D_{pp} - X_{pp}$ and shows a discrepancy with the result of the adiabatic Hamiltonian of $-2X_{sp}$. This missing contribution $-2X_{sp}$ stems from the important interaction between the s and the p -shell that is completely neglected in the argument by Hawrylak and coworkers [44, 56, 78]. But it is only the corrected value obtained from the adiabatic Hamiltonian that is in very good agreement with the full result.

The ‘hidden symmetry’ argument is always analyzed for a single, degenerate shell. In contrast, the Hamiltonian under discussion and generally used in the literature, is rather describing several interacting shells, so that is not obvious why (if at all) the argument holds. In the present case the answer is contained in the adiabatic Hamiltonian. In it the p -shell is the ‘single degenerate shell’ because (i) the s -shell is ‘frozen’ and higher shells are absent in the considered situation and (ii) the field created by the s -shell carriers does not remove the degeneracy of the p -shell. Under such conditions the adiabatic Hamiltonian obeys the ‘hidden symmetry’ commutation relations exactly. In this picture the energy for the removal of a p -exciton, Eq. (3.11), contains also terms coming from the s - p -interaction, and it is this value that is in agreement with the full diagonalization.

This analysis also shows the validity range of the ‘hidden symmetry’. For instance, the presence of higher shells (but also depending on the actual model parameters) may spoil the argument. This seems to be the case described in Ref. [29], where the p -lines are not independent of the exciton number, but are arranged in a descending ladder

too. Also, the field of the 'frozen' states may remove some of the degeneracy of the shell in question. For example if the outer shell is a d -shell, the state with zero angular momentum and those with angular momentum ± 2 will experience the field created by the s -shell carriers differently. Nevertheless, if these differences are small compared to the non-interacting energies, one may still observe a stable d -shell emission, as we will see in Section 5.

It may be argued that by approximating the full Hamiltonian, Eq. (1.1), with the adiabatic one, Eqs. (3.5)-(3.7), the interaction inside the p -shell is still too complicated to allow analytic diagonalization, i.e., the 'hidden symmetry' property is a simple relation between otherwise complex, strongly correlated states. Nevertheless, the Fock subspace generated by the p -orbitals is significantly smaller and this is in itself a numerical simplification. Symmetry arguments also can be used to reduce the blocks to be diagonalized and at least the ground states can be obtained analytically. A procedure for obtaining analytic eigenstates is the repeated application of the raising operator \mathcal{P}_p^\dagger on the 'vacuum' (full s -shell, empty p -shell) state as detailed earlier in this chapter and in Ref. [44, 56, 78].

As a concluding remark we would like to point out that the 'hidden symmetry' commutator holds *exactly* for an arbitrary single, degenerate shell in the cv -picture. That is, the whole argument holds if the $\{\varepsilon_i^c\}_i$ and $\{\varepsilon_i^v\}_i$ rather than the $\{\varepsilon_i^e\}_i$ and $\{\varepsilon_i^h\}_i$ are each degenerate within one band. The proof of this strong statement relies on the formal equivalency of the interband operator \mathcal{P} and the spin-operator S_- and is given in Appendix B. In the e - h picture the single-particle energies are renormalized due to the Hartree-Fock terms originating from the full valence band. These renormalizations can be different for different individual states of a given shell and can therefore spoil the symmetry as outlined in the discussion of Eq. (3.13).

In summary, an explanation for the formation of the s -shell ladder was given in this chapter. Additionally, we discussed in detail the 'hidden symmetry' property. Motivated by recent experiments, the next chapter deals with charged exciton complexes and the emission from excited states.

4 Charged Excitons

So far we have investigated neutral multi-exciton complexes. But of course one can additionally study the emission properties of charged complexes [43, 45, 53, 59, 82–85] as they might be observed due to background doping [73], electrical charging of the system [86] or resonant excitation of acceptor levels [28]. These complexes consist of multi-exciton configurations in which the number of electrons and holes is not equal. We were led to investigate these complexes in more detail by the results of a series of intriguing experiments performed jointly by Sven Ulrich et al. in the group of Prof. Peter Michler, University of Stuttgart, and by Matthias Schwab and coworkers in the group of Prof. Manfred Bayer, University of Dortmund. More information about the experiments can be found in [54, 87]. In the following we first report on the experimental findings and give the interpretation of those results that were rather well understood from other experiments. Then new and more surprising experimental results are discussed that led to a vivid exchange between the two experimental groups and our group as we accounted for these findings.

4.1 Experimental Findings

The experiments were performed on self-assembled InAs QDs grown on a n -doped GaAs substrate. In order to enable studies on individual QDs, an array of mesa structures was fabricated in a post-growth step by electron beam lithography and wet chemical etching. The experiments were then performed using a combined low-temperature (4 K) micro-photoluminescence (μ -PL) system and a Hanbury Brown and Twiss-type photon correlation setup [88]. A tunable Ti:sapphire laser was used to allow either for quasi-resonant pumping of the p -shell or off-resonant excitation energetically above the GaAs barrier.

In the upper left part of Figure 4.1 the μ -PL spectrum as obtained for off-resonant excitation is shown. Apart from an almost unstructured small PL background the spectral window of interest is dominated by a pair of intense narrow lines at 1.3414 eV and 1.3372 eV, which exhibit nearly resolution-limited linewidths. As is depicted in the upper right part of Figure 4.1, the PL of the two lines reveals a linear (slope = 1) and super-linear (slope = 2.3) increase of intensity with excitation density over almost two orders of magnitude.

The different dependence of the PL on the excitation power can, at least qualitatively, be understood by a somewhat hand-wavy argument. In this spirit one may expect

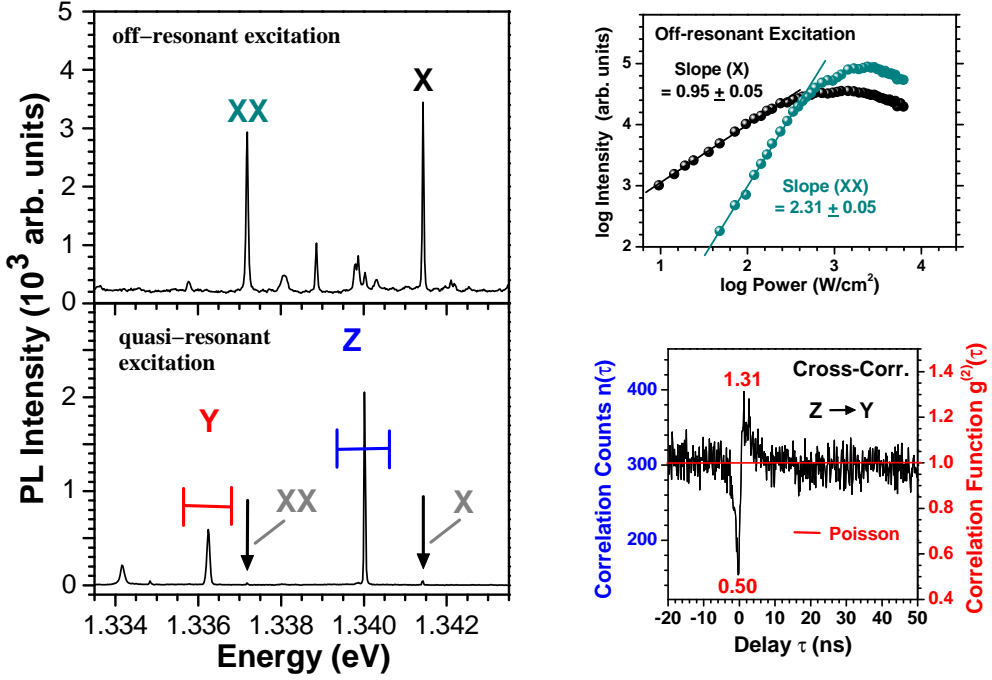


Figure 4.1:(color online) Left panel: μ -PL spectrum from a single (In,Ga)As QD as observed for off-resonant (i.e. above barrier) laser excitation (upper part) and spectrum taken on the same QD under quasi-resonant (p -shell) excitation (lower part). Horizontal markers: filter bandpass for photon correlation experiments. Upper figure on the right: power-dependence of the neutral exciton and biexcitonic line under off-resonant excitation. Lower figure: Cross-correlation trace obtained from the 1.3400 eV (Z: ‘start’) and 1.3362 eV (Y: ‘stop’) PL lines. Conclusions about the assignment of X and Y lines to specific configurations will be drawn in the text.

the intensity of the PL line of an exciton to be proportional to the probability of creating an exciton. This probability is then assumed to be proportional to the pump intensity. Therefore one would expect a slope of one in a log-log plot of the PL intensity versus excitation power. The PL intensity of the biexcitonic line is in this oversimplified picture proportional to the joint probability of creating a second exciton if a first exciton is already present. If we assume the probability of creating a second exciton to be independent of the presence of the first one, we approximate the joint probability by the square of the probability to create a single exciton. Then we get $I_{XX} \propto I_{\text{pump}}^2$, from which we would expect a slope of two in the log-log plot. The measured slopes are close to the values obtained from this simple argument, which, for example, does not take any kind of saturation into account. Maybe even more important than the plausibility considerations given above is the fact that the slopes are in good agreement to those typically found in an experiment for the pump-power dependence of the PL intensity of an excitonic and biexcitonic line [28, 76].

Additionally, it can be seen in Figure 4.1 that the line with the larger slope starts at higher excitation power and saturates later than the one with the smaller slope. This, too, fits into the picture of an exciton-biexciton cascade. Further evidence is obtained from time-resolved spectroscopy providing a radiative lifetime $\tau_X \approx 1.0$ ns and $\tau_{XX} \approx 500$ ps for these lines. That the decay-time for a biexciton is faster by almost a factor of two [89] can be understood by the fact that the biexciton has two decay channels (either of the two excitons forming the biexciton complex may decay), whereas the exciton has only one decay channel. The assignment of both peaks to the same QD is moreover supported by the observed line spacing of $\Delta E_{X-XX} = 4.2 \pm 0.1$ meV, which is consistent with the biexciton-binding energy range reported for such dots.

The observed PL spectrum changes dramatically if the pumping condition is varied for the same QD from off-resonant to resonant excitation into the p -shell at 1.4068 eV. In this case, which is shown in the lower part of the left panel in Figure 4.1, one finds a new set of almost background-free narrow intense lines at 1.3400 eV and 1.3362 eV and a weak third signature at 1.3342 eV. These lines appear shifted to lower energies with respect to the strongly suppressed excitonic and biexcitonic PL (marked by arrows in Figure 4.1).

In order to obtain information about the temporal ordering of the emission events, a modified Hanbury Brown & Twiss setup, schematically shown in Figure 4.2, was used. In such an experiment light from the QD is sent to a 50/50 beamsplitter. Then each of the two beams is sent through a narrow band filter and is focussed onto a photo detector. By tuning the transmission of one of the filters to the energy of transition line ‘Y’ and the other to the energy of the line ‘Z’, it is possible to use the photon with energy $\hbar\omega_Y$ as the ‘start’ and the photon with energy $\hbar\omega_Z$ as the ‘stop’ signal and measure the time delay τ between the start and the stop signal.

In a large number of repeated experiments, one obtains in this way the correlation distribution $n(\tau)$ between photons of type ‘Z’ that reach the stop detector with a time delay τ after the photon of type ‘Y’ has triggered the start photo detector. In other words, one obtains a measure of the conditional probability that a photon from the emission event ‘Z’ will be emitted at a time τ *after* the recombination process ‘Y’ has occurred. By inserting a time delay into the detector path of the stop-detector it is also possible to measure negative delay times: If one puts a time-delay of, e.g., 20 ns into the path and measures a time delay of 5 ns one can conclude that emission signal that is detected at the stop-detector was emitted 15 ns *prior* to the emission event to which the start-detector is tuned. This is conveniently expressed as $\tau = -15$ ns.

The result of such a so-called *cross-correlation* measurement is shown in the lower right part of Figure 4.1. For positive delay times, one observes a bunching-like behavior, i.e., an increased number of correlation counts, whereas for negative delay times an anti-bunching behavior, i.e., a reduced number of correlation counts, is observed. This clearly indicates that one deals here with a cascaded emission of ‘Y’ and ‘Z’, that is, the emission ‘Z’ is only possible after the emission ‘Y’ has occurred. The same behavior is found in a biexciton-exciton cascade, where it is only possible to observe

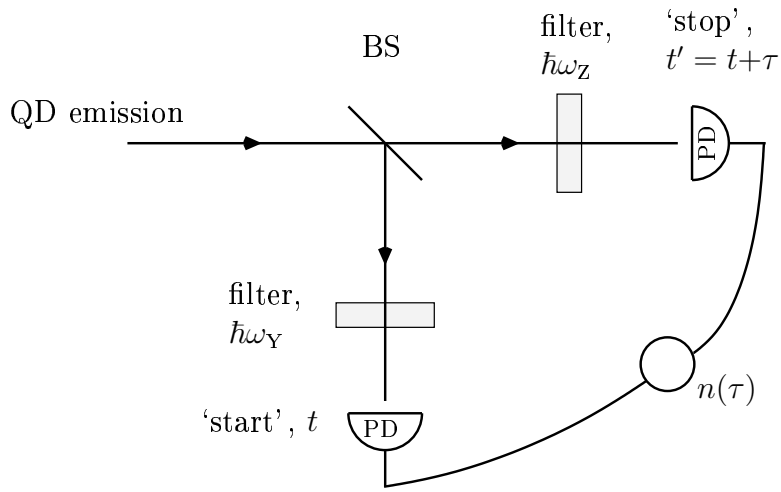


Figure 4.2: Modified Hanbury Brown & Twiss setup for cross-correlation measurements. The incoming beam is split by a non-polarizing 50/50 beamsplitter (BS). Each of the two beams pass a tunable narrow bandpass filter and is focused onto a photo detector (PD). The number of detection events $n(\tau)$ as a function of the time-delay τ between the ‘start’ and ‘stop’ signal is recorded.

the excitonic emission *after* the biexcitonic recombination process has already taken place. Additionally, the cross-correlation measurement leads to the conclusion that the two lines originate from the same QD, as such a strong temporal correlation is not expected for statistically independent emission events from different QDs. It is quite noteworthy that in a biexciton-exciton cascade for this type of QDs the photon with lower energy comes first and is followed by a photon with higher energy, whereas in this new cascade the high-energy photon comes first and is followed by a photon with lower energy. This surprising observation and the fact that an n -doped GaAs substrate was used, led us to investigate whether charged excitons could be responsible for the observed cascade.

The possibility that the observed PL under quasi-resonant excitation originates from charged QD carrier complexes whereas neutral complexes are responsible for the PL under off-resonant excitation is supported by a simple model scheme: In the absence of laser excitation a doping-related or intrinsic (i.e., donor-type) impurity in the vicinity of an individual QD enables an excess electron to relax into the QD ground state. In this way one is initially left with a charged dot and a nearby ionized impurity. Under p -shell excitation, electrons and holes are injected pairwise into the QD and can consecutively relax into available lower s -states. Therefore, the creation of charged complexes ($e\text{-}h$ pairs plus an extra electron) should be favored. In contrast to this, for above-barrier pumping the effect of *photo-depletion* [73, 90] is expected: The dissociation of hot $e\text{-}h$ pairs through the Coulomb field of the local QD-impurity leads to the attraction of holes into the QD, whereas excess electrons are partly trapped by the impurity centers. Under these conditions, the radiative decay of neutral X and XX complexes is expected.

4.2 Theoretical Analysis

In our first attempt to assign multi-exciton complexes to the observed PL lines, we considered ground-state emission of charged excitons and biexcitons. We used the full diagonalization approach including an s - and a p -shell for both the electrons and the holes. Results for the exciton and biexciton as well as the corresponding negatively and, for completeness, positively charged complexes (X^- , XX^- and X^+ , XX^+) are shown in Figure 4.3. The left part corresponds to the case of equal envelopes with the parameters discussed in Chapter 1 whereas the right panel shows a case in which the envelopes of

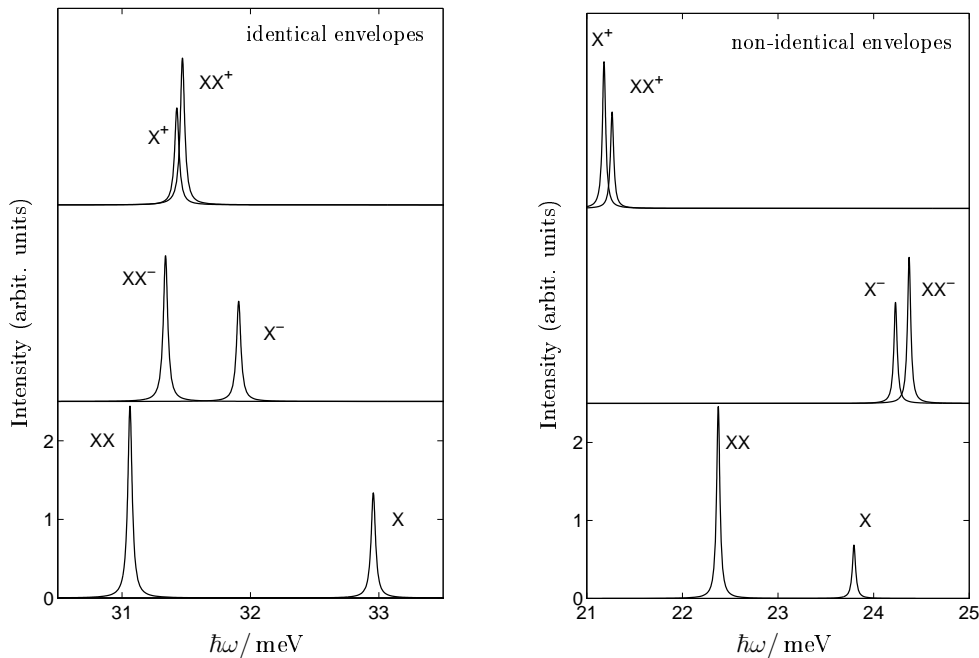


Figure 4.3: Ground state emission lines of the neutral exciton (X) and biexciton (XX) and the corresponding negatively and positively charged complexes. Left: identical envelopes, right: non-identical envelopes.

the holes have larger extension than those of the electrons ($l_{\text{osc}}^e = 6 \text{ nm}$, $l_{\text{osc}}^h = 7 \text{ nm}$). In case of equal envelopes, the emission lines of the charged exciton complex are all in-between those of the neutral ones. In this case, the e - h -pairs are not only *globally* but also *locally* neutral. On the other hand, in case of non-identical envelopes the exciton is locally charged and should – as a consequence – be more sensitive to the presence of an additional charge. Indeed, the relative position of the emission stemming from charged exciton complexes are changed with respect to the neutral ones in the case of non-equal envelopes, as shown in the right panel of Figure 4.3. However, it is – by changing the parameters in a reasonable regime – not possible to increase the splitting between lines of equally charged complexes significantly. As it seems impossible to reproduce the

order and the large splitting of the lines as it is observed in the experiment, we focus in what follows on emission involving *excited* states.

In Figure 4.4 the emission line corresponding to the ground state emission of the negatively charged biexciton is shown. The recombination process leads to an *excited* negatively charged exciton or excited trion state. It is this state that was used to calculate the subsequent emission shown as the X^{-*} line in Figure 4.4. Additionally the figure contains the emission lines of the neutral complexes as a reference.

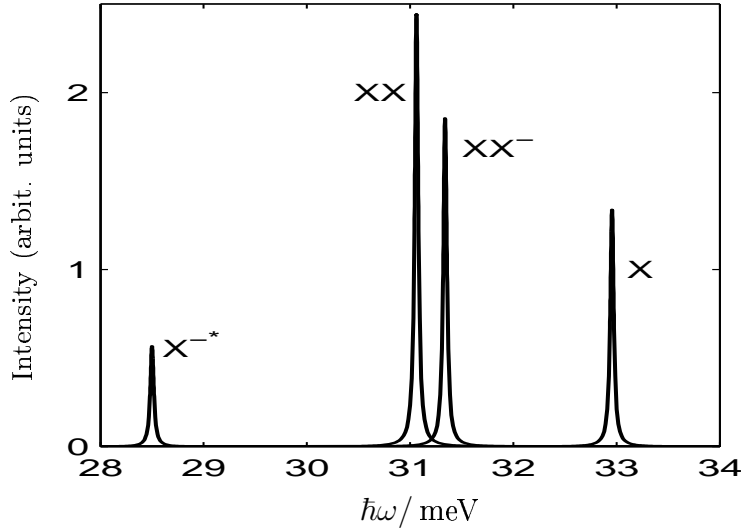


Figure 4.4: Configuration interaction results for the two emission lines of the $XX^- \rightarrow X^{-*} \rightarrow e$ cascade, schematically depicted in Figure 4.5. The emission lines of the neutral exciton and biexciton are included as a reference. The cascaded emission involving the excited trion state explains clearly both the large splitting and the energetic order found in the experiment.

By comparing the ground-state emission of the negatively charged complexes in the left panel of Figure 4.3 one can observe that the charged biexciton PL is shifted below the charged exciton ground state emission line. This is due to the (charged) biexciton binding energy. As will become clearer in what follows, in the case of the *excited* trionic line the exchange interaction between the *s*-shell and *p*-shell carriers overcomes the small biexcitonic binding energy and reverses the order of the lines as depicted in Figure 4.4. It is this order and the large splitting between the two lines that agrees with the experimental findings.

The eigenstates provided by the CI calculations are combinations of many configurations. In Figure 4.5 only the dominant configurations of the states taking part in the cascade are shown. Their high participation ratio (> 96%) allows us to estimate the corresponding energies according to the approximation scheme discussed in Chapter 3. For the energy of the initial charged biexciton configuration *A* this leads to $E_A = 2E_s^X + \varepsilon_p^e - X_{sp}$, i.e., the sum of two *s*-exciton energies E_s^X , the one-particle *p*-shell electronic energy ε_p^e and the (attractive) exchange energy X_{sp} between *s* and *p* electrons

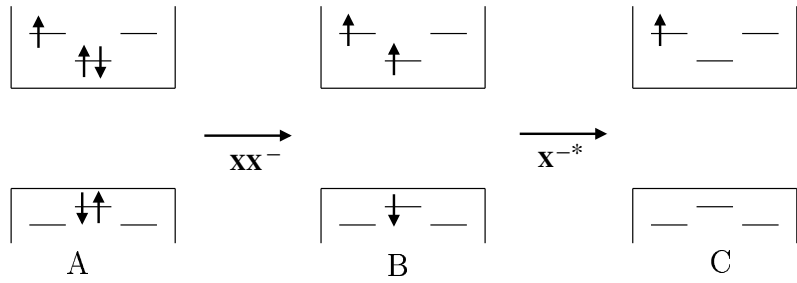


Figure 4.5: Schematic representation of one possible $XX^- \rightarrow X^{-*} \rightarrow e$ cascade: Starting from the charged biexciton ground state A , an excited triion state B is reached by a $e\text{-}h$ recombination process. The subsequent recombination step leads to an excited dot state C with only one electron. Here only the dominant configurations are shown.

with parallel spin. Similarly, $E_B = E_s^X + \varepsilon_p^e - X_{sp}$ and $E_C = \varepsilon_p^e$. Strictly speaking, the additivity of different energy contributions leaves out some configuration-interaction effects. One of them is the biexcitonic binding energy, which can be accounted for only by the interaction of the configurations of Figure 4.5 with the other possible arrangements of the carriers in the available states. Considering only the s - and p -shells and based on the material parameters of Chapter 1, we obtain from FCI calculations a biexciton binding energy of ≈ 2 meV for the neutral biexciton and ≈ 1.2 meV for the charged one. Including this configuration-interaction effect, the energy of configuration A reads $E_A = 2E_s^X - \Delta + \varepsilon_p^e - X_{sp}$ with the charged biexciton binding energy Δ . As a result, one finds the following emission energies:

$$\begin{aligned} E_{XX^-} &= E_A - E_B = E_s^X - \Delta \\ E_{X^{-*}} &= E_B - E_C = E_s^X - X_{sp} . \end{aligned} \quad (4.1)$$

The difference in the positions of the two lines is given by $X_{sp} - \Delta$. The exchange integral X_{sp} (in our case ≈ 4.9 meV) is significantly larger than the charged biexcitonic binding energy Δ , which explains the energetic order $E_{X^{-*}} < E_{XX^-}$.

We would like to point out that the charged biexciton binding energy being smaller than the $s\text{-}p$ exchange energy is not a matter of special parameters. While our explicit example used the material parameters of Chapter 1, there are more general arguments showing that the discussed situation is expected rather than coincidental. In Section 2.3 we compared the QD biexciton problem with the Heitler-London theory of the hydrogen molecule and found that the biexciton binding energy is small, because a binding can only occur if contributions of higher-state configurations allow for a rearrangement of the charges. But the energetic price to be paid for this rearrangement is quite large in zero-dimensional systems and keeps these admixtures small. This results in a small biexciton binding energy. This picture applies even more to the case of the charged biexciton, because the presence of the additional carrier in the p -shell limits the available higher states. This explains the numerical results that the charged biexciton binding

energy is smaller than the binding energy of the neutral biexciton. Therefore it is not a numerical accident but rather a physical fact that one obtains, for a whole range of reasonable parameters, the same conclusion: the $s\text{-}p$ exchange energy overtakes the (charged) biexciton binding energy and the X^{-*} line appears therefore at an appreciably lower energy.

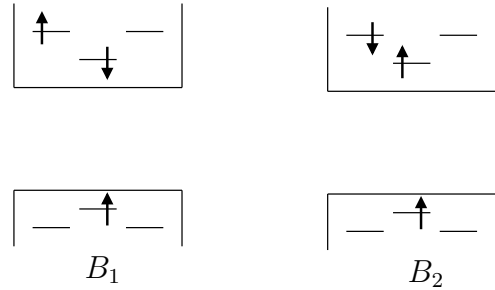


Figure 4.6: Additional to the configuration B in Figure 4.5 the trion configurations B_1 with opposite spins for the s and p electrons can occur in a final state configuration of an emission process. Due to Coulomb interaction, B_1 is mixed with B_2 , a configuration that cannot be reached directly from the charged biexciton state A .

So far we have considered only the possible decay channel depicted in Figure 4.5. However, for the recombination of the first electron-hole pair in the cascade there are in fact two possible decay paths. The one discussed so far leads to a final charged exciton state in which the two electrons have identical spin orientations (see Figure 4.5). Additionally, the other $e\text{-}h$ -pair can recombine, which then leads to two electrons with opposite spins as depicted in configuration B_1 in Figure 4.6. In this case, the above argument seems to fail, since the exchange integral apparently plays no role any more. However, the FCI calculation shows that this is *not* the case. Actually, the configuration B_1 alone is not an eigenstate of the problem. It gets mixed with the configuration B_2 (which cannot directly be obtained from the radiative decay of configuration A in Figure 4.5) and results in a state with exactly the same energy as state B . This is by no means a coincidence: The electrons in the configuration B have the spin state $S^e = 1, S_z^e = 1$ and the sum of B_1 and B_2 corresponds to $S^e = 1, S_z^e = 0$. These states are necessarily degenerate in an eigenvalue problem which conserves both the electron and hole spin. Additionally, the admixture of B_1 and B_2 can produce an electronic singlet state ($S^e = 0$), which is energetically higher by roughly twice the $s\text{-}p$ exchange integral. Consequently, the transition from the charged biexciton complex to this state falls outside the energy range of interest. To complete the discussion, we point out that the initial charged biexciton state is actually fourfold degenerate, since four states are available to the p -electron. As these four states all produce the same emission spectrum, a separate analysis of the individual cases is not necessary.

If the symmetry of the problem is reduced, some of the degeneracies are removed and additional lines may appear in PL. For example, if it is the rotation symmetry that is broken, the two p -states are not equivalent any more. One then expects different single-particle energies for the 'left' and 'right' p -states and also the exchange integral would take two different values. By examining Eq. (4.1), one sees that both emission energies are insensitive to the position of the p -level while only the X^{-*} line is sensitive to the change in the X_{sp} integral. In this case it is only the lower line which becomes split by the symmetry lowering. This might be a possible explanation for the appearance of a third line below X^{-*} . However, since it was currently not possible to use the weak signal of this line for correlation measurements, its identification has to be left for future investigations.

By combining all this evidence, we conclude that the emission lines observed under quasi-resonant excitation conditions stem from charged exciton and biexciton carrier complexes. Furthermore we found clear indications for a predominant recombination of an excited trion state, which reflects a long-lived excess electron spin configuration. As a result, we assign the 'Z'-line in Figure 4.1 to the charged biexciton emission and the 'Y' line to the *excited* trion emission.

In this chapter we presented results for charged exciton complexes. We showed how our theoretical analysis could be used to assign multi-exciton configurations to the different emission lines found in recent experiments. In the next and final chapter of Part I, we investigate the influence of higher shells on the emission spectra.

5 Influence of higher shells

In the previous chapters, we have investigated the optical properties of a QD with two shells per carrier type. Such a situation is often encountered for small QDs. For larger dots, however, additional shells may be present. Here, we restrict ourselves to a situation where an additional d -shell is provided by the confinement potential. As a d -shell can accommodate up to six carriers the total number of confined states is doubled by this additional shell. This factor of two translates into a factor of $2^4 = 16$ for the number of involved Coulomb matrix elements. More important, the dimension of the largest Hilbert space occurring in the calculation of the multi-exciton energy spectra is more than three orders of magnitude larger than the corresponding one for a QD with two shells. This leads to an enormous need of computer memory that is necessary to store and handle the involved matrices. Therefore, the analysis of the multi-exciton spectra was only possible at the supercomputer ‘JUMP’ at the Forschungszentrum Jülich with its huge shared-memory architecture [91]. The main problem that cannot be circumvented is the fact that one needs to calculate *all* the eigenstates of the $N_X - 1$ -exciton problem for the final states and not just a couple of the energetically lowest. Therefore the extremely fast and less memory consuming algorithms that are established for the latter purpose cannot be used. Due to the huge number of states involved, a detailed analysis of each peak is not feasible. However, the knowledge gained by our studies of a dot with two shells will be of great help for the discussion of the complicated emission spectra.

This chapter is organized as follows: In Section 5.1 we start with the investigation of the absorption spectrum of an initially empty QD. This is the most simple situation and even though an analytic treatment is not possible, some general statements about the spectrum can be derived. In particular we compare our results with those found in Ref. [83] and explain the origin of the differences. Then we present in Section 5.2 the multi-exciton emission spectra for up to twelve excitons and study the main features and trends.

5.1 Absorption

In the absence of Coulomb interaction the absorption spectrum consists of three distinct lines: the s -shell absorption at $\hbar\omega_e + \hbar\omega_h$, the p -shell absorption at $2(\hbar\omega_e + \hbar\omega_h)$, and, finally, the d -shell absorption at $3(\hbar\omega_e + \hbar\omega_h)$. The ratio of the peak heights is $1 : 2 : 3$ and reflects the degeneracy of the different shells. In Figure 5.1 the corresponding

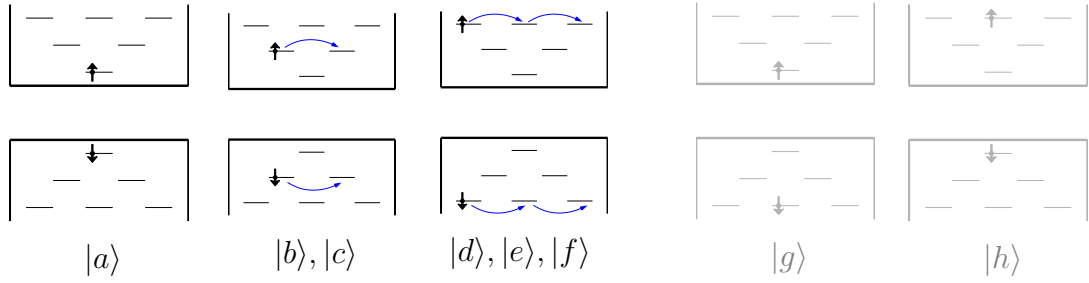


Figure 5.1: Six bright exciton states $|a\rangle$ to $|f\rangle$ together with the two dark exciton states $|g\rangle$ and $|h\rangle$. Moving the electron and hole in the second and third configuration according to the blue arrows, generates the other states in this subspace. All states are classified by $l_z^{\text{tot},e} + l_z^{\text{tot},h} = 0$, $S_z^{\text{tot},e} = \frac{1}{2}$ and $S_z^{\text{tot},h} = -\frac{1}{2}$, and become mixed by Coulomb interaction.

final state configurations are depicted as the states $|a\rangle$ to $|f\rangle$. Additionally, two ‘dark’ configurations, $|g\rangle$ and $|h\rangle$, are shown that are mixed to the ‘bright’ configurations $|a\rangle$ to $|f\rangle$ by Coulomb interaction.

In the presence of Coulomb interaction, the resulting absorption spectrum is shown in Figure 5.2. One can observe three main peaks that we refer to as *s*-, *p*-, and *d*-line as well as three smaller peaks: one between the *s*- and *p*-line, one at the tail of the *d*-peak, and additionally a tiny third peak between the *p*- and *d*-peak at around 120 meV that is only visible on the logarithmic scale in the inset of Figure 5.2. Moreover, a clear transfer of oscillator strength from the energetically higher to the energetically lower emission lines can be inferred.

When we compared this result with those given in Ref. [83] we were at first left somewhat irritated. In this reference the authors state that the 8×8 block, generated by the states

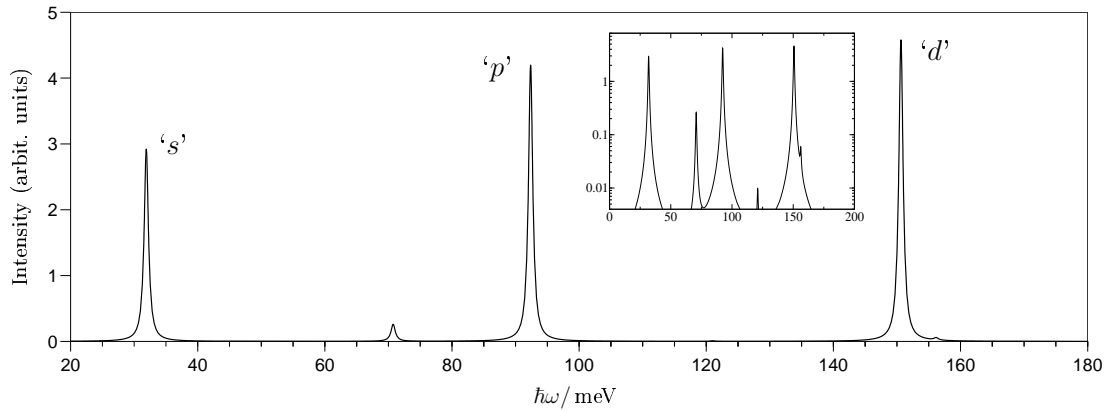


Figure 5.2: Absorption spectrum of an initially empty QD confining three shells. Different regions that are characterized mainly by the creation of an *s*-, *p*-, or *d*-exciton can be identified. Besides the three major peaks, there are three additional peaks. The smallest is only visible on the logarithmic scale in the inset.

$|a\rangle$ to $|h\rangle$ of Figure 5.1, can analytically be separated into a block of dimension five, containing dark and bright exciton states, and a 3×3 block, containing solely dark exciton states. If such a decomposition were valid, one could observe at *most* five lines in the absorption spectrum. However, the close inspection of our absorption spectrum shows a tiny sixth peak, which should – if the statement in Ref. [83] were true – not be there at all. To see where this discrepancy stems from, we follow here the arguments given in Ref. [83]. We find that the discussed separation is in general *not* possible. Instead, one stays with a six by six block containing bright exciton states, and will therefore in general observe six lines in the spectrum.

In terms of the basis states depicted in Figure 5.1 the free part of the Hamiltonian (1.1) contains along its diagonal the elements:

$$(\hbar\omega_e + \hbar\omega_h), 2(\hbar\omega_e + \hbar\omega_h), 2(\hbar\omega_e + \hbar\omega_h), 3(\hbar\omega_e + \hbar\omega_h), \\ 3(\hbar\omega_e + \hbar\omega_h), 3(\hbar\omega_e + \hbar\omega_h), \hbar\omega_e + 3\hbar\omega_h, 3\hbar\omega_e + \hbar\omega_h .$$

All off-diagonal matrix elements vanish. In order to have a one-to-one comparison between our results and those of Ref. [83], we adopt in this section their notation and introduce $V_0 = \sqrt{\frac{\pi}{2}}E_c = \sqrt{\frac{\pi}{2}}\frac{e^2}{4\pi\varepsilon_r\varepsilon_0l_k}$, the kinetic energy $t = \hbar\omega_e + \hbar\omega_h$ and evaluate the Coulomb matrix elements in the pure two-dimensional limit. In this case the Coulomb matrix elements can be evaluated analytically and the interacting part reads:

$$H_{\text{Coul}} = -V_0 \begin{bmatrix} 1 & \frac{1}{4} & \frac{1}{4} & \frac{3}{32} & \frac{3}{32} & \frac{3}{16} & -\frac{1}{4} & -\frac{1}{4} \\ \frac{1}{4} & \frac{11}{16} & \frac{3}{16} & \frac{31}{128} & \frac{15}{128} & \frac{7}{64} & \frac{1}{16} & \frac{1}{16} \\ \frac{1}{4} & \frac{3}{16} & \frac{11}{16} & \frac{15}{128} & \frac{31}{128} & \frac{7}{64} & \frac{1}{16} & \frac{1}{16} \\ \frac{3}{32} & \frac{31}{128} & \frac{15}{128} & \frac{585}{1024} & \frac{105}{1024} & \frac{57}{512} & \frac{9}{128} & \frac{9}{128} \\ \frac{3}{32} & \frac{15}{128} & \frac{31}{128} & \frac{105}{1024} & \frac{585}{1024} & \frac{57}{512} & \frac{9}{128} & \frac{9}{128} \\ \frac{3}{16} & \frac{7}{64} & \frac{7}{64} & \frac{57}{512} & \frac{57}{512} & \frac{153}{256} & -\frac{7}{64} & -\frac{7}{64} \\ -\frac{1}{4} & \frac{1}{16} & \frac{1}{16} & \frac{9}{128} & \frac{9}{128} & -\frac{7}{64} & \frac{11}{16} & \frac{3}{16} \\ -\frac{1}{4} & \frac{1}{16} & \frac{1}{16} & \frac{9}{128} & \frac{9}{128} & -\frac{7}{64} & \frac{3}{16} & \frac{11}{16} \end{bmatrix} .$$

Now we can calculate the absorption spectrum by diagonalizing the 8×8 matrix and evaluating the oscillator strength $|\langle\phi_n|\mathcal{P}^+|0\rangle|^2$ for the numerically determined eigen-

states $|\phi_n\rangle$. Instead of doing so, we follow Ref. [83] by introducing the new basis set:

$$\begin{aligned} |A\rangle &= |a\rangle, \\ |B\rangle &= \frac{1}{\sqrt{2}}(|b\rangle + |c\rangle), \\ |C\rangle &= \frac{1}{\sqrt{2}}(|b\rangle - |c\rangle), \\ |D\rangle &= \frac{1}{\sqrt{3}}(|d\rangle + |e\rangle + |f\rangle), \\ |E\rangle &= \frac{1}{\sqrt{2}}(|d\rangle - |e\rangle), \\ |F\rangle &= \frac{1}{\sqrt{6}}(|d\rangle + |e\rangle - 2|f\rangle), \\ |G\rangle &= \frac{1}{\sqrt{2}}(|g\rangle - |h\rangle), \\ |H\rangle &= \frac{1}{\sqrt{2}}(|g\rangle + |h\rangle). \end{aligned}$$

If we now sort the basis as $[A, B, H, D, F, G, C, E]$ the Hamiltonian transforms into

$$H = \begin{bmatrix} t - 1 & -\frac{\sqrt{2}}{4} & \frac{\sqrt{2}}{4} & -\frac{\sqrt{3}}{8} & \frac{\sqrt{6}}{32} & 0 & 0 & 0 \\ -\frac{\sqrt{2}}{4} & 2t - \frac{7}{8} & -\frac{1}{8} & -\frac{5\sqrt{6}}{32} & -\frac{3\sqrt{3}}{64} & 0 & 0 & 0 \\ \frac{\sqrt{2}}{4} & -\frac{1}{8} & 2t - \frac{7}{8} & -\frac{\sqrt{6}}{96} & -\frac{23\sqrt{3}}{192} & \Delta E & 0 & 0 \\ -\frac{\sqrt{3}}{8} & -\frac{5\sqrt{6}}{32} & -\frac{\sqrt{6}}{96} & 3t - \frac{51}{64} & \frac{3\sqrt{2}}{256} & 0 & 0 & 0 \\ \frac{\sqrt{6}}{32} & -\frac{3\sqrt{3}}{64} & -\frac{23\sqrt{3}}{192} & \frac{3\sqrt{2}}{256} & 3t - \frac{243}{512} & 0 & 0 & 0 \\ 0 & 0 & \Delta E & 0 & 0 & 2t - \frac{1}{2} & 0 & 0 \\ 0 & 0 & 0 & 0 & 0 & 0 & 2t - \frac{1}{2} & -\frac{1}{8} \\ 0 & 0 & 0 & 0 & 0 & 0 & -\frac{1}{8} & 3t - \frac{15}{32} \end{bmatrix},$$

where we have introduced $\Delta E = \hbar\omega_h - \hbar\omega_e$ and measured all elements in units of V_0 . In this new basis the matrix separates into a 6×6 and a 2×2 block. Only in the special case of $\Delta E = 0$ the 6×6 -block further separates into a 5×5 and a 1×1 -block.

Note that the 2×2 block does not need to be considered for an absorption spectrum, because these states are always dark. This can be seen by expressing $\mathcal{P}^+|0\rangle$ in terms of the new basis: $\mathcal{P}^+|0\rangle = |A\rangle + \sqrt{2}|B\rangle + \sqrt{3}|D\rangle$, see Ref. [83]. As the eigenstates from the 2×2 -block are linear combinations of $|C\rangle$ and $|E\rangle$, they always have a vanishing oscillator strength. In the absence of Coulomb interaction, the states $|A\rangle, |B\rangle$, and

$|D\rangle$ are eigenstates of the Hamiltonian and occur as final states $|f\rangle$. The resulting oscillator strengths $|\langle f|\mathcal{P}^+|0\rangle|^2$ for the transitions are 1, 2 and 3 in accordance with the degeneracy of the respective shells.

It is interesting to note that the claimed separation into a 5×5 and a 3×3 -block is not spoiled by the Coulomb interaction, but by the free part of the Hamiltonian, because the non-interacting part is *not* diagonal in the new basis:

$$\begin{aligned}\langle G|H_0|H\rangle &= \frac{1}{2} [\langle g|H_0|g\rangle + \langle g|H_0|h\rangle - \langle h|H_0|g\rangle - \langle h|H_0|h\rangle] \\ &= \frac{1}{2} [\langle g|H_0|g\rangle - \langle h|H_0|h\rangle] \\ &= \frac{1}{2} [(3\hbar\omega_h + \hbar\omega_e) - (\hbar\omega_h + 3\hbar\omega_e)] = \hbar\omega_h - \hbar\omega_e = \Delta E .\end{aligned}$$

It is exactly this matrix element that couples the upper 5×5 -block to one state of the lower 3×3 -block and that is responsible for the origin of a sixth, albeit tiny, line in the spectrum.

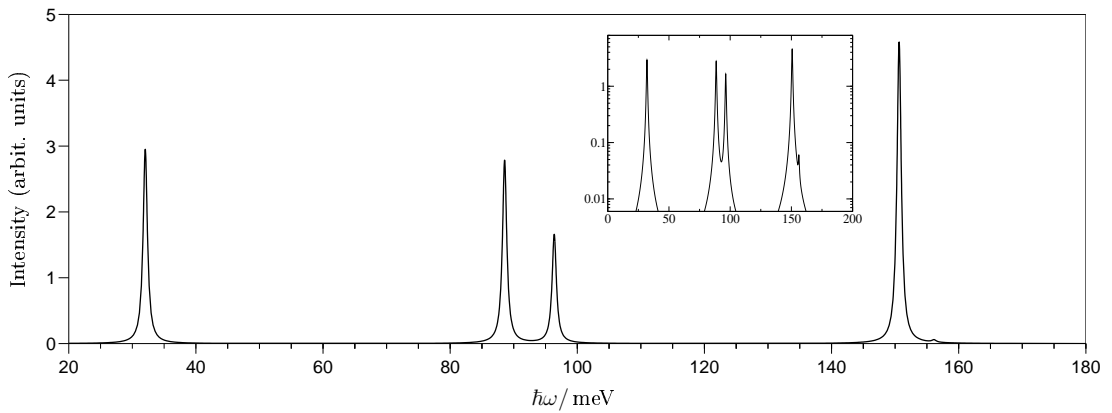


Figure 5.3: Same as Figure 5.2 but with a kinetic energy, which is distributed equally over the level spacings ($\hbar\omega_h = \hbar\omega_e = t/2$). In this particular case even on the logarithmic scale in the inset only five lines can be observed.

To further support this result and test our programs we artificially distributed the kinetic energy t in equal parts on the level spacings $\hbar\omega_h$ and $\hbar\omega_e$, which leads to $\Delta E = 0$. For this case the result of the full calculation is depicted in Figure 5.3 and shows indeed only five lines. While the peaks at the low- and at the high-energy side are almost unaffected by the redistribution of the single-particle energy, a strong transfer of oscillator strength is observed for the mid-energy region. This can mainly be attributed to the fact that the non-interacting states with, say, the electron in the s - and the hole in the d -shell is energetically degenerate with the state where both carriers are in the p -shell. As a consequence of this degeneracy in the absence of Coulomb interaction, the states $|g\rangle$ and $|h\rangle$ will intermix strongly with the states $|b\rangle$ and $|c\rangle$ in the presence of Coulomb interaction.

5.2 Multi-Exciton Emission

The multi-exciton emission spectrum of a QD containing three shells is depicted in Figure 5.4. As initial states the ground states with $S_z^{\text{tot}} = 0$ are chosen. One can clearly separate three energetic regions: A low-energetic region ($\hbar\omega < 40 \text{ meV}$), in which the emission is dominated by the s -exciton, a mid-energy range (roughly between 50 and 90 meV), which is characterized by p -shell emission, and an high-energy side ($\hbar\omega > 130 \text{ meV}$) that stems from d -shell emission. For an initial filling with one and two excitons, we observe solely one line, namely, the excitonic and the biexcitonic line. The latter line is redshifted with respect to the former and reveals the biexciton binding energy. For more than two excitons the p -shell is populated and can henceforth be observed in an emission spectrum. When more than six excitons occupy the QD yet another set of lines appears that can be attributed to emission of the d -shell.

There are several interesting features in the spectrum. Let us first concentrate on the low-energy side. By starting to populate the p -shell, the s -shell emission starts to redshift due to the possibility of lowering the energy by acquiring exchange matrix elements as the number of carriers is increased. This was already discussed in Section 2 and further explained in Section 3.1 for a QD with two shells. Additionally, the peak heights become less pronounced as the number of carriers in the p - and later in the d -shell is increased. This can mainly be attributed to the increased number of peaks over which the oscillator strength is distributed and only to a small part to an overall change of oscillator strength in the different energetic regions. In the range of seven to nine excitons the s -shell emission lines are barely visible, but for ten and more excitons the peaks recover oscillator strength again.

The p -shell starts with an occupation of three excitons and shows a rather stable transition energy for up to six excitons. The origin of the remarkable stability was detailed in Section 3.2. If the number of excitons is further increased, we can clearly observe a redshift in the p -shell emission which, again due to additional exchange matrix elements, forms a ladder-like structure.

For more than six excitons the additional emission from the d -shell enriches the spectrum. Here one observes, exactly as in the case of the p -shell for lower exciton numbers, that the energetic position of the emission is quite stable and does only slightly change with increasing number of excitons. This is in particular intriguing as the arguments for the ‘hidden symmetry’ fail in this situation as already indicated in Section 3.2.

In order to gain further insight into the multi-exciton spectra in the presence of an additional d -shell, we first compare the spectra with those obtained when only two shells are confined. This comparison is shown in Figure 5.5. On the high energy side a redshift of the emission lines due to the presence of the d -shell can be observed. Furthermore, one may notice that the oscillator strength of the transition lines in case of three shells is slightly enhanced. Qualitatively, however, the high energy side does not change. In contrast to that, one observes qualitative changes on the low-energy side for more than two excitons. These changes will be discussed in the following paragraphs.

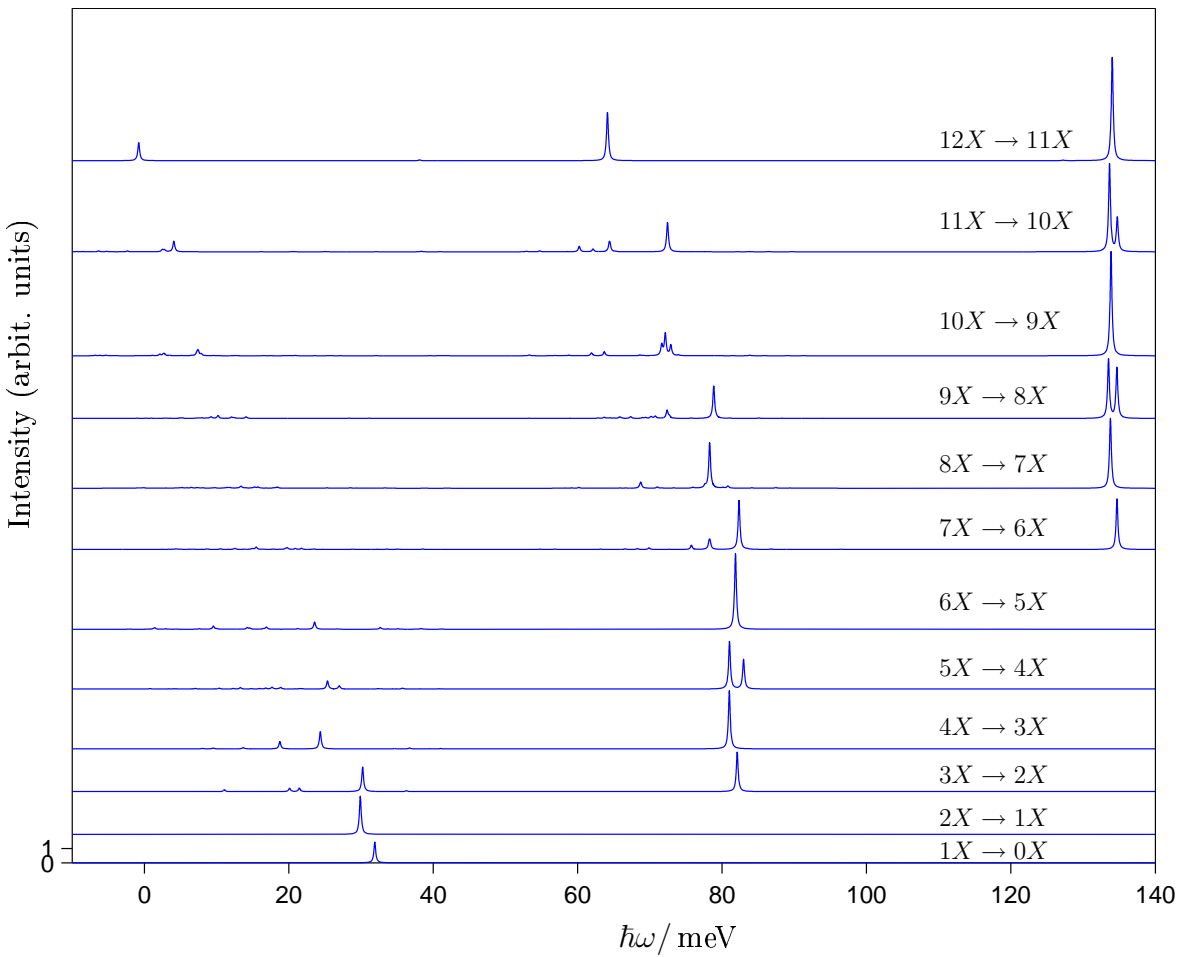


Figure 5.4: Ground state emission spectrum of a quantum dot that confines an s -, p -, and a d -shell. The initial filling varies from one to twelve excitons and the ground states with $S_z^{\text{tot}} = 0$ were selected. Three energetic regions, corresponding mainly to the recombination of an s -, a p - and a d -shell excitons, can be distinguished.

s -Shell Emission

For one and two excitons we observe in Figure 5.5 a redshift of the lines that are influenced by the d -shell. The red shift of the ground state excitonic emission can easily be explained by noting that the ground state energy of a system is always reduced when the Hilbert space, out of which the wave function can be constructed, is enlarged. The increased biexciton binding energy reveals that this lowering of the ground state energy is even more effective in the case of two electron-hole pairs. This can be attributed to the increased number of configurations that are available for the redistribution of the charge carriers, see the discussion of the biexciton binding energy in Section 2.3. The reader should be warned, however, that the observed redshift of the p -shell cannot

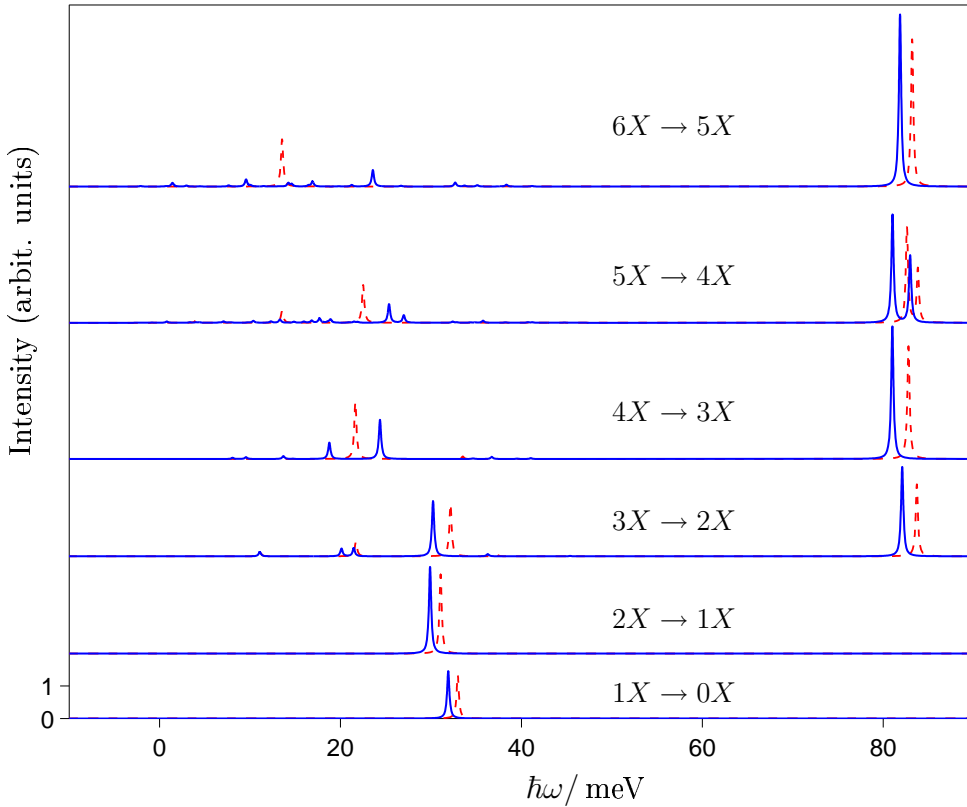


Figure 5.5: (color online) Ground state emission spectrum for an initial filling of one to six excitons. Blue solid lines correspond to a QD confining three shells. The dotted red line corresponds to a calculation including only two shells.

directly be linked to the lowering of the ground state energies. Such a conclusion is not possible as a transition spectrum always shows energy differences.

Comparing the $3X$ emission in the presence and absence of a d -shell in Figure 5.5, one additional line (the second from the left) at the low-energy side of the spectrum can be seen. Note that the left-most transition line of the ' sp '-QD overlaps exactly with the one of the ' spd '-QD. The new line in the $3X$ spectrum stems from a splitting in the energies of the final triplet-singlet (ts) and singlet-triplet (st) spin-states, which were degenerate in the case of two shells. In order to understand how an additional shell can lead to this splitting, let us first recall why the st and ts-transition are degenerate in the case of two shells. To this end we consider first only the electrons. The dominant configurations that occur as final states of the low-energy transitions are depicted in Figure 5.6. In the case of two shells only the state $|\psi_a\rangle$ together with the one generated by flipping all spins exist. These can either form a spin singlet or a spin triplet-state.

The Hamiltonian matrix for these two states is given by:

$$\underline{H}_{s/t}^e = \begin{pmatrix} \varepsilon_s^e + \varepsilon_p^e + D_{sp}^{ee} & -X_{sp}^{ee} \\ -X_{sp}^{ee} & \varepsilon_s^e + \varepsilon_p^e + D_{sp}^{ee} \end{pmatrix} = (\varepsilon_s^e + \varepsilon_p^e + D_{sp}^{ee}) \underline{1} - X_{sp}^{ee} \begin{pmatrix} 0 & 1 \\ 1 & 0 \end{pmatrix}. \quad (5.1)$$

The eigenvalues are $E_{s/t} = \varepsilon_s^e + \varepsilon_p^e + D_{sp}^{ee} \pm X_{sp}^{ee}$ which reveals a splitting of $2X_{sp}^{ee}$, with the singlet state being higher in energy. For the holes, one finds a similar matrix and deduces a splitting of $2X_{sp}^{hh}$. Therefore one gains by going from an ts - to an st -spin state the energy $2X_{sp}^{ee}$ and loses $2X_{sp}^{hh}$. In case of identical envelopes the net change is zero and we find a degenerate transition line in the case of two shells.

It is important to note that the singlet-triplet splitting for each type of carrier does not depend on the single-particle energies only because the two involved configurations have identical energies in the diagonal approximation. Therefore the interaction between the two configurations depends only on X_{sp}^{ee} while the diagonal contribution leads to an overall shift of the energies. In the presence of a d -shell, the states $|\psi_b\rangle$ and $|\psi_c\rangle$ become mixed to the configuration $|\psi_a\rangle$ of Figure 5.6 and their counterparts that are obtained by flipping all the spins simultaneously. As these configurations involve a d -shell carrier, already the non-interacting energies differ and it is not possible to write the Hamiltonian in the form $E^{\text{diag}} \underline{1} + \underline{A}$ where \underline{A} includes only off-diagonal terms. Consequently, the splitting between the singlet and the triplet state will be influenced by the single-particle energies. Because the single-particle energies for electrons and holes are different, the singlet-triplet splitting differs for electrons and holes. This leads to a splitting of the st and ts transitions even in the case of identical envelopes.

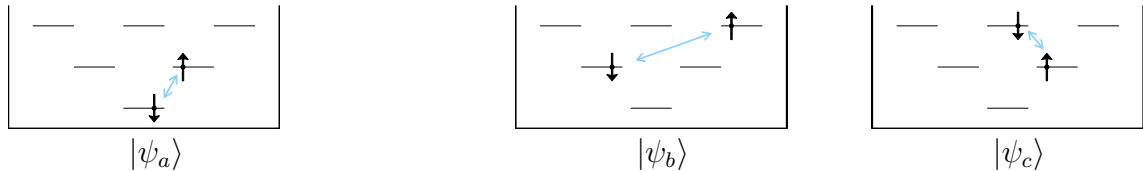


Figure 5.6:(color online) Configuration $|\psi_a\rangle$ is one of the typical electronic configurations one encounters in a final state of the $3X \rightarrow 2X$ low-energy transition. The blue arrow indicates that states in which all the spins are flipped lie in the same symmetry class. In the presence of a d -shell, the states $|\psi_b\rangle$ and $|\psi_c\rangle$ are also in this symmetry class and are coupled to $|\psi_a\rangle$ via Coulomb interaction. This coupling will lead to a singlet-triplet splitting.

Without a d -shell, the $4X$ emission spectrum is dominated by one line at the high and one line at the low-energy side. By including an additional shell, the s -shell emission line is split into two larger and a couple of smaller lines. Unfortunately there is no simple explanation for this splitting in terms of a couple of contributing states. Instead, the distribution of the oscillator strength over many peaks is a result of an interplay of many different interacting states. The existence of an entire series of different transition lines at the low-energy side of the spectrum is common for an initial filling of four to ten excitons and is worth analyzing in some more detail.

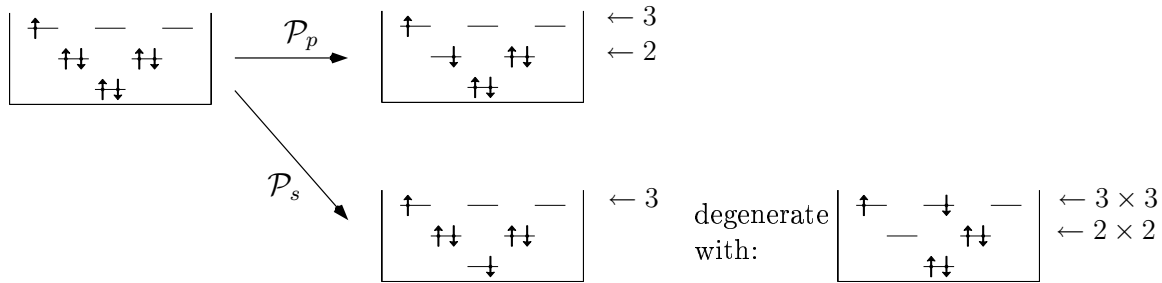


Figure 5.7: Typical configuration with seven excitons together with a typical configuration that is created by removing one p or one s -exciton. For clarity only the electronic configuration is shown and a symmetric configuration for the holes is assumed. By moving the carriers inside the shell, new states can be created with the same non-interacting energy. The number of states that can be created in this way is indicated next to the shell. If an s -shell carrier is removed there are additional qualitatively different degenerate states, which are depicted in the figure. All in all one finds for the case of a removed p -shell carrier $2 \times 3 = 6$ and for an s -shell carrier $3 + 3 \times 3 \times 4 = 39$ degenerate symmetric configurations within this subblock.

In the absence of Coulomb interaction, the low-energy transition is produced by removing an electron-hole pair from the s -shell. Coulomb interaction mixes these states with other configurations that have the same symmetry properties. Within these states, a particular strong interaction is expected for those states that have the same non-interacting energy. In the presence of a d -shell, a new class of configurations is possible, which does not exist in the case of two shells: These configurations are created by replacing an electron pair from the p -shell by one electron in the s - and one electron in the d -shell and either doing the same for the holes or leaving them unaffected. By changing the configurations for the electrons and holes in a symmetric way, one makes automatically sure that a certain symmetry subspace is not left. In Figure 5.7 an example of these new states and the number of degenerate configurations, which can be created out of this state, is given. Obviously, one may only move a carrier from the p -shell into the d -shell, if a site with the right spin is unoccupied in the latter shell. Unless the d -shell is highly populated, there are many different states within this new class. Henceforth there are – in general – many more degenerate configurations for the s -shell transition than for the p -shell transition. This explains why the s -shell transition splits in general into more different peaks than the p -shell transitions. As the shell population approaches the maximum filling of twelve carriers for both the electrons and holes, the number of possible configurations decreases and less lines are observed in the spectrum. In the extreme case of twelve excitons there are three strong lines and two smaller lines visible in the spectrum. Actually, in analogy to the absorption spectrum, there is even a third tiny line with extremely small oscillator strength, that cannot be discerned in the presented figure.

p-Shell Emission

As long as the d -shell is not occupied, one observes a remarkable stable p -shell emission from three to six excitons. For a QD with two shells, this was already discussed in Section 3.2. The presence of the additional shell has only slight impact on the position of the lines for the studied set of parameters.

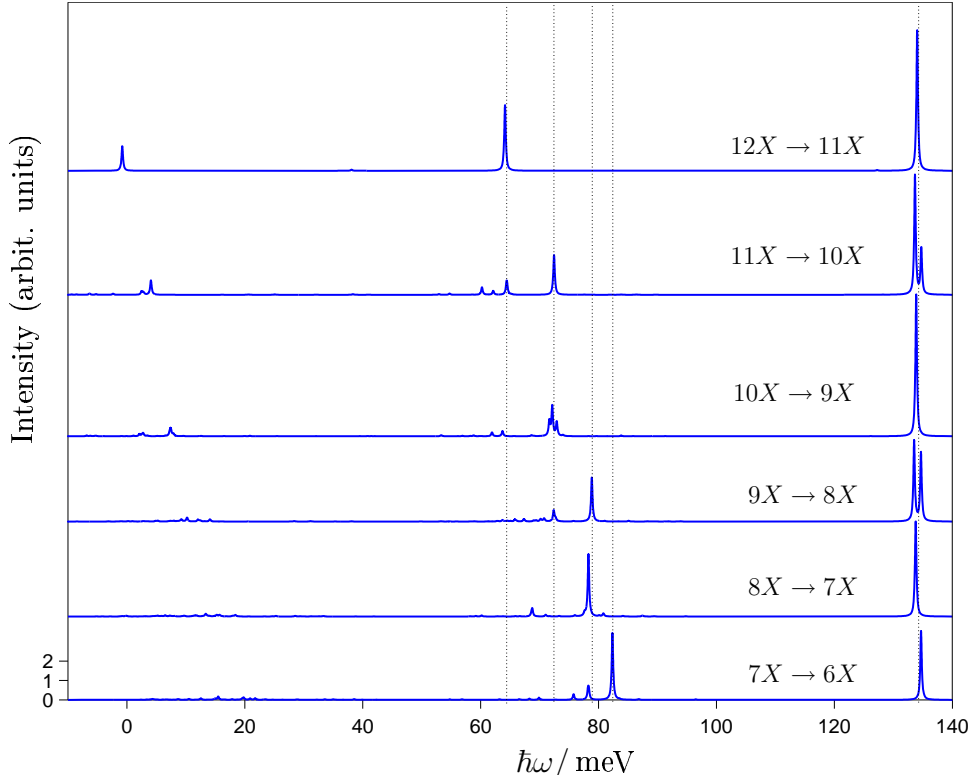


Figure 5.8: Ground state emission spectrum for an initial filling of seven to twelve excitons for a QD confining three shells. Ground states with $S_z^{\text{tot}} = 0$ are chosen. The dotted lines are included as a guide for the eye. A three-step ladder in the p -shell emission can be inferred.

For more than six excitons, that is when the d -shell starts to be populated, one can witness the formation of a ladder-like structure in the p -shell emission. This is in analogy to the formation of a ladder in the s -shell as soon as carriers are filled into the p -shell. As the ground state for seven to twelve excitons is a doublet state for an odd number of excitons and a singlet state for an even number of excitons, one expects – in full analogy of the explanation of the s -ladder in Section 3.1 – a formation of a ladder with three steps. Each step is formed by the possibility of the final configuration to reduce its energy by means of an additional exchange integral. Even though the ladder is not as pronounced as the s -shell ladder in the case of a QD with two shells, this three-step ladder of the p -shell emission with increasing number of excitons can

indeed be found in the spectrum in Figure 5.8. While the spacing in the s -shell was to a good approximation given by $2X_{sp}$, one cannot find a similar simple expression for the p -ladder, because there is not just one exchange matrix element ' X_{pd} ' but three different ones, namely, X_{p+d_-} , X_{p+d_0} and X_{p+d_+} (and identical ones for the combination involving the state p_-). Here we explicitly give the angular-momentum z -component as $+, 0, -$ for $l_z = +2, 0, -2$ for the d -shell and $+, -$ for $l_z = +1, -1$ for the p -shell. In addition to the different exchange matrix elements, the ground states themselves show that the different sites are non-equivalent when the interaction is introduced, as the $m = 0$ and $m = \pm 2$ states of the d -shell are differently populated. All this hampers a simple expression of the step size. However, the total distance spanned by all three steps is to a very good approximation given by $2X_{p+d_-} + 2X_{p+d_0} + 2X_{p+d_+} = 18.16$ meV.

d-Shell Emission

For more than six excitons the d -shell becomes populated. This results in the appearance of a strong high-energy transition line. One can see from Figure 5.4 that these transition lines are quite stable as the number of excitons is increased, exactly as in the case of the p -shell emission for lower population. This is somewhat surprising because the ‘hidden symmetry’ argument, which relied on the commutation of $[H, \mathcal{P}_p]$ being proportional to \mathcal{P}_p and was exact in the adiabatic treatment of a QD with an s - and a p -shell, is spoiled in the presence of a d -shell as already indicated at the end of Section 3.2. As the full calculation shows nevertheless this intriguing stability, we try to approximately determine the energetic position of this emission. For this, we follow the derivation of the stable p -shell emission analyzed in Section 3.2. Then we see whether the argument fails badly for the d -shell or can be recovered using additional approximations.

In analogy to the discussion presented in Section 3.2 we obtain the adiabatic Hamiltonian $H_{ad} = H_{ad}^{(s)} + H_{ad}^{(p)} + H_{ad}^{(sd)} + H_{ad}^{(pd)} + H_{ad}^{(d)}$ from the full interacting Hamiltonian (1.1) by enforcing diagonality with respect to the s - and p -occupation numbers. As we are interested only in the energetic position of the d -shell emission line, which is closely connected to the commutator $[H_{ad}, \mathcal{P}_d]$, we do not need to consider the contributions $H_{ad}^{(s)}$ and $H_{ad}^{(p)}$, which contain only s - and p -shell operators and therefore commute with \mathcal{P}_d , the dipole-transition operator restricted to the d -shell.

The contribution $H_{ad}^{(sd)}$ describes the interaction between the ‘frozen’ s -shell and the d -shell carriers. Its explicit form is given by

$$H_{ad}^{(sd)} = \sum_{j \in \{+, 0, -\}} D_{sd_j} (\hat{n}_s^e - \hat{n}_s^h) (\hat{n}_{d_j}^e - \hat{n}_{d_j}^h) - \sum_{j \in \{+, 0, -\}, \sigma} X_{sd_j} (\hat{n}_{s,\sigma}^e \hat{n}_{d_j,\sigma}^e + \hat{n}_{s,\sigma}^h \hat{n}_{d_j,\sigma}^h) . \quad (5.2)$$

As the first term contains the total s -shell population operator \hat{n}_s^e , which commutes with \mathcal{P}_d , it plays no role in the argument. Because one has $X_{s,d_+} = X_{s,d_-} \neq X_{s,d_0}$, the matrix element X_{sd_j} in the second term cannot be pulled in front of the sum. Consequently, one cannot rewrite the second term in the form $\bar{X}_{sd} \sum_{\sigma} (\hat{n}_{s,\sigma}^e \hat{n}_{d,\sigma}^e + \hat{n}_{s,\sigma}^h \hat{n}_{d,\sigma}^h)$. But this

would be necessary for the ‘hidden symmetry’ argument as \mathcal{P}_d is the lowering operator for the total population. Therefore the fact that different d -shell states experience the influence of the ‘frozen’ s -shell differently, spoils the ‘hidden symmetry’ argument. In the same way, the interaction of the d -shell carriers with the ‘frozen’ p -shell – described by the Hamiltonian of the form Eq. (5.2), in which all s labels are replaced by p – spoils the commutation relation, because X_{p_i,d_j} takes different values for different $i \in \{+, -\}$ and $j \in \{+, 0, -\}$.

In the adiabatic description, the correlation between the d -shell carriers is fully taken into account. Therefore the Hamiltonian for the part $H_{ad}^{(d)}$ retains the form of the general Hamiltonian (1.1) but now with the indices restricted to the d -shell. Along the lines discussed in Section 3.2 the Hamiltonian can then be rewritten as

$$H_{ad}^{(d)} = \varepsilon_d^e \hat{n}_d^e - \frac{1}{2} \sum_i W_i \hat{n}_i^e + \varepsilon_d^h \hat{n}_d^h - \frac{1}{2} \sum_i W_i \hat{n}_i^h + \frac{1}{2} \sum_{\substack{ijkl \\ \sigma\sigma'}} V_{ij,kl} (e_{i,\sigma}^\dagger e_{l,\sigma} - h_{l,\sigma}^\dagger h_{i,\sigma}) (e_{j,\sigma'}^\dagger e_{k,\sigma'} - h_{k,\sigma'}^\dagger h_{j,\sigma'}) \quad (5.3)$$

where W_i is given by $\sum_j V_{ij,ij}$. If one evaluates now the commutator $[\mathcal{P}_d, H_{ad}^{(d)}]$ one finds again that the last line in Eq. (5.3) plays no role and one is left with $(\varepsilon_d^e + \varepsilon_d^h)\mathcal{P}_d - \sum_i W_i e_i^\dagger h_i^\dagger$. In the case of the d -shell, we have $W_+ = W_- \neq W_0$, so that it is impossible to recast the expression into the form of ‘constant $\times \mathcal{P}_d$ ’. To summarize, the interaction of the d -shell carriers with the ‘frozen’ s - and p -shell as well as the interaction of the d -shell carriers among each other spoils the ‘hidden symmetry’ argument.

To obtain nevertheless an approximate expression for the position of the d -shell, one can proceed as follows: (i) replace X_{sd_j} with $j \in \{+, 0, -\}$ by its average value \bar{X}_{sd} , (ii) similarly approximate X_{p_i,d_j} by \bar{X}_{pd} and (iii) replace W_i as well by its average \bar{W} . In this way, one obtains for the position of the d -shell emission

$$\mathcal{E}_d^X \approx \varepsilon_d^e + \varepsilon_d^h - \bar{W} - 2(\bar{X}_{sd} + 2\bar{X}_{pd}) \quad (5.4)$$

where the term $-2(\bar{X}_{sd} + 2\bar{X}_{pd})$ stems from the interaction with the ‘frozen’ s - and p -shell. Evaluating the expression leads to $\mathcal{E}_d^X \approx 133$ meV, which is in very good agreement with the full result and shows that replacing the different matrix elements by its averages does – for the present set of parameters – not produce too much of an error. This can be attributed to the fact that while the different matrix elements that are replaced in the steps (i) to (iii) by an averaged value differ by more than a factor of two from each other, the deviations are small compared to the energy scale defined by the non-interacting energies $\hbar\omega_e + \hbar\omega_h$.

We investigated in this chapter the influence of higher shells on the emission and absorption spectra. The huge number of interacting configurations leads to manifold splittings of lines, which are degenerate in the absence of the additional shell. This greatly complicates the interpretation of the series of multi-exciton spectra as the number of excitons in the QD is increased. Nevertheless, major trends, like, the formation of a p -shell ladder and the stability of the emission of open shells can be observed.

5 Influence of higher shells

This discussion concludes the analysis of multi-exciton spectra in conventional III-V semiconductor QDs. The next part is dedicated to the multi-exciton spectra of QDs based on group-III nitrides. As we will see, the resulting spectra deviate strongly from those of the InGaAs system.

Part II

Multi-Exciton Spectra in Nitride Quantum Dots

Introduction to Part II

In the fast evolving research field of semiconductor nanostructures, there was in recent years an increasing level of interest in quantum dots based on group-III nitrides, i.e., AlN, GaN, and InN. Compared to conventional group-III arsenide semiconductor materials, nitride-based nanostructures have the huge advantage that it is in principle possible to span the spectrum from amber to ultraviolet. This is achieved by properly alloying together the three building blocks AlN, GaN, and InN and thereby engineering the direct band gap of these materials [23]. Furthermore the strong chemical bonds in the nitride system make them mechanically more stable and therefore suitable for high-power devices [24] as the generated heat has only a smaller impact on the device. Nevertheless and despite the intense research on nitride QDs over the last decade the understanding of this material system is – compared to other III-V materials – still in its infancy. From an experimental point of view this is mainly due to the fact that it remains difficult to grow QDs with a precision similar to the one routinely achieved in more conventional group-III arsenide dots. This has, at least in part, to be attributed to the lack of a proper substrate for these systems in terms of lattice constants and thermal expansion coefficients [24, 92] in particular as bulk nitrides are very hard to synthesize. Furthermore the spontaneous polarization fields in nitrides are much larger than those in conventional group-III arsenide systems [92, 93], which leads to a reduction in oscillator strength for opto-electronic applications. Another curious point about the nitride system is the fact that the band gap of InN is still controversial in the literature. For a long time the value of about 2 eV was widely accepted [94]. Only recently this value shifted to about 0.7 eV [23, 95].

From the theoretical point of view, one challenge is the proper inclusion of effects that stem from the altered microscopic structure of the underlying lattice. While most of the nitrides can crystallize both in the zinc-blende and the wurtzite phase, the latter is by far more stable [94]. Additionally the strong built-in field needs to be accounted for. Furthermore, and in contrast to many other III-V semiconductors, the spin-orbit coupling in the nitrides is rather weak [23] so that the calculation of the electronic states in terms of a simple effective-mass approximation is not possible due to strong valence-band mixing effects. Instead, a microscopic description of the single-particle states based on, for example, a tight-binding model or pseudo-potential calculation is necessary. Another difference to InGaAs QDs is the background dielectric constant, which is typically smaller in nitride structures. Therefore effects of Coulomb interaction become even more pronounced in these systems.

In the past a large amount of experimental and theoretical work was dedicated to the optical properties of III-V and II-VI semiconductor QD structures based on, amongst others, InGaAs/GaAs or CdSe/ZnSe. One important aspect concerned the analysis of absorption and emission spectra of QDs as a function of the excitation density. A large bulk of literature deals with this problem [10, 12, 39, 43–45, 48, 78, 84, 96]. A common result is that the transitions mainly involve ‘diagonal’ transitions, i.e., transitions connecting, for example, s -shell electrons with s -shell holes or p -shell electrons with p -shell holes. This is due to the fact that the dipole matrix elements $\mathbf{d}_{ij} = \langle \psi_i^e | e\mathbf{r} | \psi_j^h \rangle$ are to a good approximation shell diagonal: In envelope-function approximation the dipole-matrix elements are proportional to the overlap of the electron and hole wave function. In the case of identical envelopes one obtains in particular $\mathbf{d}_{ij} \propto \delta_{i,j}$. This picture has been proven to be very fruitful for conventional III-V materials and is oftentimes carried over to the nitride system where emission spectra are then calculated using these ‘diagonal’ excitons [97–102]. Our analysis shows, however, that such an approach is in general not adequate for the description of nitride QDs.

In particular, we find for the nitrides that the emission is dominated by recombination of ‘skew’ excitons. These excitons consist of one s -shell carrier of one band and a p -shell carrier from the other band. This selection rule cannot be explained in a simple effective-mass picture but necessitates a microscopic, multi-band approach for the electronic single-particle states that properly accounts for the underlying atomic lattice. These new selection rules, which are dictated by the altered dipole-matrix elements, are the main reason for dramatically different optical spectra in nitrides. For *small* lens-shaped QDs, they lead to the prediction of dark exciton and biexciton ground states. Additionally, the transitions that occur in systems with a higher population of excitons (three or more excitons) differ strongly from those known from the InGaAs/GaAs system. For large nitride QDs the energetic order of the s -shell and p -shell is interchanged, with the p -shell being lowest in energy. This results in an optical active exciton and biexciton ground state. However, as it is known from the quantum confined Stark effect (QCSE), the corresponding dipole matrix elements decrease rapidly [69, 99, 103] with increasing height of the QD due to the separation of the electron and hole wave functions in the strong internal electric fields. This may turn out to be the real limiting factor for opto-electronic device applications.

In this thesis we study the multi-exciton emission spectra of nitride QDs and discuss the resulting complicated peak structure in detail. Restricting ourselves to the two lowest shells allows even a semi-analytic description of the problem. The single-particle states are deduced from a microscopic theory based on a tight-binding model. But also without the microscopically determined single-particle states that initially led us to the intriguing selection rules, it is quite interesting to investigate the impact of the changed symmetry on the dipole-matrix elements and thereby on the multi-exciton spectra.

This part of the thesis is divided into three chapters. Chapter 6 starts with a general introduction to the calculation of electronic properties within the framework of a tight-binding treatment. Then Section 6.2 gives details about the actually implemented TB-approach and presents results for single-particle wave function as they have been

calculated by Stefan Schulz in the group of Prof. Gerd Czycholl [69]. This is followed by a short discussion of how Coulomb and dipole-matrix elements can be obtained from these single-particle states.

At the beginning of Chapter 7 some of the most important aspects of the symmetry group of the wurtzite lattice structure are introduced and contrasted to those of the zinc-blende lattice. Section 7.1 deals with degeneracies that can be predicted from these symmetry groups. The following Section 7.2 is devoted to the transformation properties of the single-particle wave functions, which are used in Section 7.3 for the derivation of selection rules for the dipole matrix elements. In particular we will find that the dipole-matrix elements are dominated by off-diagonal contributions. These will lead to the aforementioned ‘skew’ excitons.

In the first part of Chapter 8 the symmetry properties of the single-particle wave functions and the resulting optical selection rules are briefly summarized. Then the absorption spectrum of an initially empty QD is discussed, followed by a brief analysis of the exciton and biexciton emission spectrum. Results for an initial filling with up to six excitons are provided in Section 8.3 and major trends are described in Section 8.4 in terms of an approximate Hamiltonian. This is proceeded by a detailed, semi-analytic discussion of the observed multi-exciton spectra. In the subsequent Section 8.6 the influence of the strong built-in field is investigated. Finally, the spectra for a larger nitride QD is presented in Section 8.7 and compared to those found for the smaller structure.

6 Tight-Binding Approach for the Single-Particle States in Nitride Quantum Dots

Even though our ultimate goal is the investigation of the many-body effects on the optical spectra, a proper description of the single-particle states is needed. In particular we find that by just carrying over the intuition gained by the analysis of InGaAs/GaAs QDs to the nitride system one obtains wrong results, even qualitatively. This is at least in part due to the fact that the spin-orbit coupling in nitrides is quite small compared to conventional III-V systems¹. Therefore at least a two-band treatment of the valence band structure is needed. So far, most of the theoretical work concerning InN QD structures is based on effective-mass [97–102, 104] and $\mathbf{k} \cdot \mathbf{p}$ calculations [105]. As both approaches constitute in effect a continuum description of the quantum dot, important parts of the microscopic structure of the underlying lattice is neglected. Therefore a microscopic description in terms of more sophisticated models, like a tight-binding (TB) model, is desirable and we are in the fortunate situation of having a vivid cooperation with the group of Prof. Gerd Czycholl, University of Bremen. In his group the actual calculation of the single-particle wave function and energies in the framework of a TB model have been performed by Stefan Schulz. Starting from these single-particle states the Coulomb and dipole-matrix elements have been jointly evaluated by S. Schulz and Stefan Schumacher [69]. The details of the TB-approach and the calculation of the matrix elements are beyond the scope of the present thesis and can be found in [69, 106]. Once the interaction and dipole-matrix elements are determined, they are used as input data for the configuration interaction (CI) calculation presented in Section 8.

In a first motivating step, the general idea behind the TB-approach is outlined in Section 6.1. To give a faint flavor of this sophisticated and computationally intense approach, the description is extremely simplified. For the avid reader Ref. [107, 108] are recommended for details of this research field. In a second step, we will present in Section 6.2 the method employed by S. Schulz for the calculation and give results for the one-particle states. Within this method, it is in particular possible to study the influence of the internal electrostatic fields on the wave functions by artificially turning the fields on and off [69]. A brief discussion of how dipole- and interaction matrix elements can be determined from the TB single-particle states concludes the present chapter.

¹ Here we denote as conventional III-V semiconductors those composed from In, Ga, Al, and As.

6.1 Basic Idea of a Tight-Binding Model

In this Section we present the basic idea behind a microscopic tight-binding description of the electronic properties in solids. To this end an ideal infinitely extended one-dimensional structure and its generalization to a heterostructure is discussed. Furthermore the necessary changes for the description of a realistic structure are addressed.

The starting point for this description are wave functions that are each mainly localized around a certain atom and represent the wave functions of the electrons of the outer shell(s) of the lattice atoms. Using this basis set one has to find the linear combinations that are the eigenstates of an electron moving in the potential V_{Ion} generated by all the core-ions. If $|\alpha, \mathbf{R}\rangle$ denotes an orbital α , which is located around the lattice point \mathbf{R} , it is at least plausible that the matrix elements $\langle \mathbf{R}', \alpha' | -\frac{\hbar^2}{2m} \Delta^2 + V_{\text{Ion}}(r) | \mathbf{R}, \alpha \rangle$ are largest for nearby lattice points. This should be the case as the wave functions are well localized. Indeed, it turns out that it is often sufficient to consider hopping to just

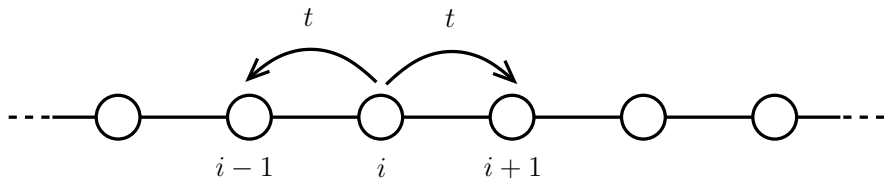


Figure 6.1: Schematic representation of a one-dimensional crystal and a nearest neighbor hoping matrix elements t .

a few neighbors. In order to understand how such a model can lead to the formation of a band structure, let us consider the one-dimensional chain of atoms depicted in Figure 6.1 and assume for simplicity that only one orbital α is present at each lattice site. In this case the states $|\mathbf{R}\alpha\rangle$ can be characterized solely by the site index i . For the sake of a simplified discussion we further assume that $\langle \mathbf{R}_i, \alpha_i | -\frac{\hbar^2}{2m} \Delta^2 + V_{\text{Ion}}(r) | \mathbf{R}_j, \alpha_j \rangle$ can be written as $\varepsilon \delta_{ij} + t \delta_{i,j\pm 1}$. The quantity t is the so-called *hopping matrix element*, which connects nearest neighbors and is related to the probability of an electron moving from one site to another [71]. The onsite matrix element ε is connected to the orbital energies. The corresponding TB-Hamiltonian then reads

$$H = \sum_i \varepsilon |i\rangle \langle i| + t \sum_i (|i+1\rangle \langle i| + |i-1\rangle \langle i|) \quad (6.1)$$

and has the eigenvectors $|\psi_l\rangle$ and energies E_l given by

$$|\psi_l\rangle = \sum_m e^{i \frac{2\pi l}{N} m} |m\rangle \quad , \quad E_l = \varepsilon + 2t \cos\left(\frac{2\pi}{N} l\right) . \quad (6.2)$$

Here l labels the eigenstates and N denotes the number of lattice sites and the integer m runs from 0 to $N - 1$. For the diagonalization of the Hamiltonian periodic boundary conditions have been assumed. The corresponding energy spectrum is depicted in

Figure 6.2. For $N \rightarrow \infty$ the energy spectrum forms a continuum. By identifying the quantity $\frac{2\pi}{N}l$ with the wave vector k and expanding the expression around $k = 0$ one finds $E_l \approx \varepsilon + 2t - 2tk^2$. From this it is possible to infer that the hopping matrix element t is, in this simplified model, basically determined by the effective mass.

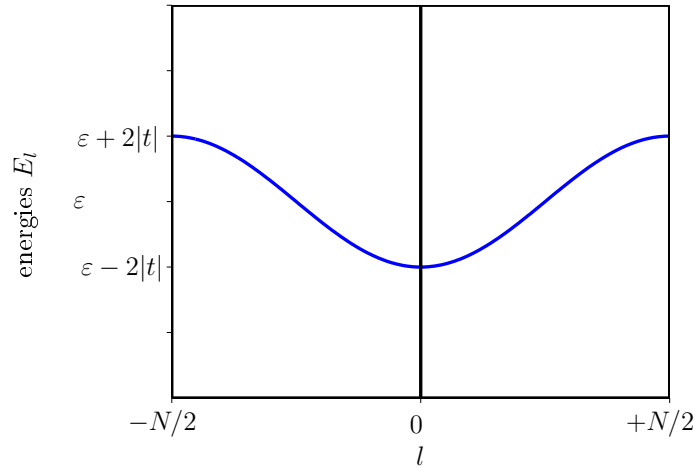


Figure 6.2: Eigenvalue spectrum of the one-dimensional chain depicted in Figure 6.1. A hopping matrix element $t < 0$ was assumed.

So far we have considered the case of just one hopping matrix element at each lattice site. This matrix element could for example originate from the overlap between adjunct s -orbitals. If we consider instead various hopping matrix elements connecting neighboring lattice sites, as they could, for example, originate from additionally including p -orbitals, one obtains further energy bands. Note that the assumed periodicity in the above example allowed us to map the N -dimensional matrix problem onto a scalar problem via a Fourier transform. In the general case of a bulk material it is Bloch's theorem that allows us to reduce the matrix dimension from $N_{\text{unit cells}} \times N_{\text{atom per unit cell}} \times N_{\text{orbitals per atom}}$ to $N_{\text{atom per unit cell}} \times N_{\text{orbitals per atom}}$ – a gigantic simplification. Unfortunately in the case of a heterostructure the translational symmetry is broken, so that one can no longer apply Bloch's theorem. Instead one is left with a matrix problem of extremely high dimension that can only be tackled with today's supercomputers.

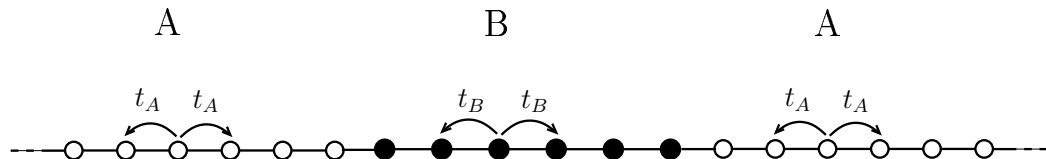


Figure 6.3: Schematic representation of a one-dimensional heterostructure, together with some nearest neighbor hopping matrix elements for the two materials A and B.

A very appealing point of the description of a heterostructure within the TB-approach is that its principle idea is very simple. One just assigns the hopping matrix element at each site according to the material of the occupying atom and its neighboring site, which is connected by this hopping matrix element. This is illustrated in Figure 6.3 for a simple one-dimensional model consisting of a material B sandwiched between materials of type A. This example includes only hopping to nearest neighbors, one atom per unit cell and one orbital per atom. The two materials differ not only in the hopping matrix elements, that is, to first approximation, in their effective masses, but also in their onsite energies ε_i . The difference $\varepsilon_A - \varepsilon_B$ is similar to the potential step ΔV used in the effective mass calculation in Chapter 1.1 and is mainly responsible for the confinement of the carriers in the QD. Of course all the simplifying assumption of hopping only to nearest neighbors, one atom per unit cell and one orbital per atom can in general not be used in a realistic description of a QD, as outlined in the next section.

6.2 Tight-Binding Model for the InN/GaN Quantum Dot

So far we have presented the general idea of a tight-binding model. In this section we briefly discuss the TB-model actually utilized for the calculation of the single-particle energies and wave function for nitride QDs and present results obtained from this approach.

Before we can start the modeling of a nanostructure we have to determine the tight-binding parameters for the involved bulk materials. To this end we use for the nitride system a TB-model with an sp^3 basis $|\alpha, \mathbf{R}\rangle$. That means that we consider one s -state ($\alpha = s$) and three p -states ($\alpha = p_x, p_y, p_z$) per spin direction at each lattice site \mathbf{R} . In this basis set the TB matrix elements are given by:

$$E_{\alpha\mathbf{R},\alpha'\mathbf{R}'} = \langle \alpha\mathbf{R} | H^{\text{bulk}} | \alpha'\mathbf{R}' \rangle. \quad (6.3)$$

We include non-diagonal elements of the TB Hamiltonian matrix up to nearest neighbors and use the two-center approximation of Slater and Koster [109] to evaluate the overlap matrix elements with the bulk Hamiltonian H^{bulk} . This yields nine independent TB-parameters $E_{\alpha\mathbf{R},\alpha'\mathbf{R}'}$. In contrast to most other III-V and II-VI semiconductors, one can neglect spin-orbit coupling and crystal-field splitting in InN and GaN, which are of the order of ~ 10 meV [23, 110]. Using Bloch's theorem the electronic properties of the pure bulk materials is contained in a 16×16 matrix $\underline{\underline{H}}^{\text{bulk}}(\mathbf{k})$ for each \mathbf{k} point [111]. The matrix dimension is given by $N_{\text{atoms per unit cell}} \times N_{\text{orbitals per atom}} = 4 \times 4 = 16$. The matrix elements depend on the different TB-parameters $E_{\alpha\mathbf{R},\alpha'\mathbf{R}'}$, which are empirically determined by adjusting the TB-parameter such that the characteristic properties of the bulk band structure [112, 113] in the vicinity of the Γ point are reproduced.

Once the bulk TB-parameters are determined, one can model the QD on an atomistic level. For this, the TB wave function $\psi_i(\mathbf{r})$ is expressed as a linear combination of the

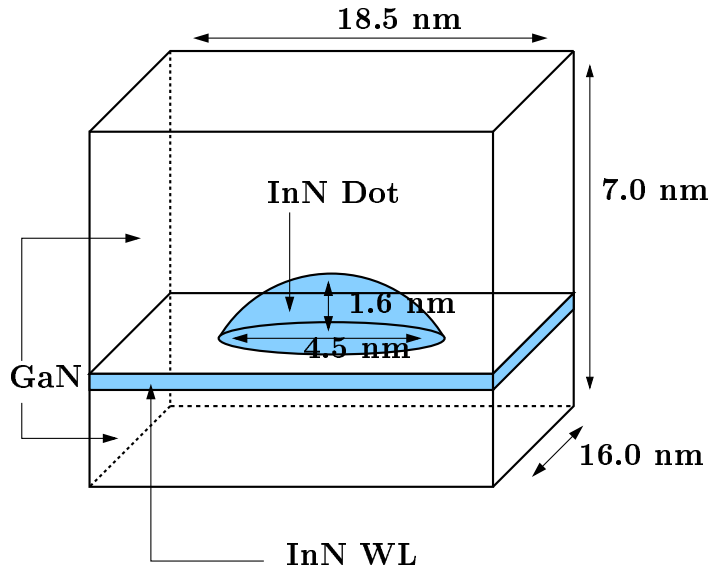


Figure 6.4: Illustration of the finite-size supercell in which the QD geometry is modeled (not to scale). The investigated lens-shaped InN QD is placed on top of an InN wetting layer (WL) and has circular symmetry around the z -axis. The InN QD-WL-system is embedded in a GaN matrix. The actual numbers refer to the small dot investigated here. (Figure adopted from [69].)

orbitals $\phi_{\alpha\mathbf{R}}(\mathbf{r}) = \langle \mathbf{r} | \alpha, \mathbf{R} \rangle$ localized at lattice site \mathbf{R} using the TB coefficients $c_{\mathbf{R}\alpha}^i$:

$$\psi_i(\mathbf{r}) = \sum_{\mathbf{R}\alpha} c_{\mathbf{R}\alpha}^i \phi_{\alpha\mathbf{R}}(\mathbf{r}). \quad (6.4)$$

The corresponding Schrödinger equation reads

$$\sum_{\mathbf{R}\alpha} \langle \alpha', \mathbf{R}' | H | \alpha, \mathbf{R} \rangle c_{\mathbf{R}\alpha}^i - E^i c_{\mathbf{R}'\alpha'}^i = 0, \quad (6.5)$$

and constitutes a huge, but finite dimensional eigenvalue problem. The quantity E^i denotes the energy and for the matrix elements $\langle \alpha', \mathbf{R}' | H | \alpha, \mathbf{R} \rangle$ the TB-parameters of the bulk materials are used. The parameters for each site are set according to the occupying atoms (N, In, Ga) in the InN/GaN heterostructure. At the InN/GaN interfaces averages of the TB-parameters are used [106] to take into account that the Nitrogen atoms cannot unambiguously be attributed to the InN or the GaN material. The valence band offset between the two materials is included by shifting the diagonal matrix elements of the bulk system by 0.5 eV [69]. To model an InN QD embedded in a GaN matrix, a finite wurtzite lattice within a supercell with fixed boundary conditions is chosen. We use these boundary conditions to avoid artificial dot-dot coupling, which could be produced in case of periodic boundary conditions, if the boundaries are not pushed far enough from the QD, and employ a large supercell. Typically the matrix size is of the order of $10^6 \times 10^6$. Such a large supercell is necessary to avoid numerical artifacts for the localized QD states, especially due to the cubic symmetry of the boundaries.

As discussed in detail in the next chapter the cubic symmetry of the supercell could in principle destroy the symmetry of the single-particle wave functions which is determined by the underlying lattice. More specifically, we consider lens-shaped InN QDs, grown in (0001)-direction on top of an InN wetting layer (WL). The embedded QD-WL-system is schematically shown in Figure 6.4. For the WL we assume a thickness of one lattice constant c .

So far we have not addressed the electrostatic built-in fields that play in general an important role in nitride systems and can significantly modify both the electronic structure and the optical properties. In contrast to cubic III-V semiconductor heterostructures, based on InAs or GaAs and crystalized in the zinc-blende structure, the III-V wurtzite nitrides exhibit considerably larger electrostatic built-in fields for several reasons [93]: First of all the shape of the unit cell in InN and GaN differs slightly from the ideal symmetry in the wurtzite structure². This small aberration causes a polarization, which is referred to as the spontaneous polarization $\mathbf{P}^{\text{spont}}$. Additionally, a quite strong strain-induced piezoelectric polarization $\mathbf{P}^{\text{piezo}}$ occurs in InN/GaN heterostructures. In order to incorporate the electrostatic fields in the TB model, the potential ϕ_p is needed. This potential enters the description as a site-diagonal contribution $V_p(\mathbf{r}) = -e\phi_p(\mathbf{r})$ to the TB Hamiltonian. This approach has previously been applied to quantum well [114] and QD [115] structures. The electrostatic potential then follows from the solution of the Poisson equation $\Delta\phi_p = -\frac{1}{\epsilon_0\epsilon_r}\rho_p$ where the polarization charge ρ_p is deduced from $\text{div } \mathbf{P} = -\rho_p$. Small effects due to the different dielectric constants ϵ_r in the QD and the surrounding material are neglected. As already mentioned, the polarization \mathbf{P} has two contributions, the spontaneous polarization $\mathbf{P}^{\text{spont}}$ and the piezo-electric part $\mathbf{P}^{\text{piezo}}$ due to strain inside the material. The spontaneous part $\mathbf{P}^{\text{spont}}$ in the wurtzite crystal structure lies within the (0001)-direction, which we assume to be the growth direction, $\mathbf{P}^{\text{spont}} = P^{\text{spont}}\mathbf{e}_z$. For the strain contribution we use the approximation described in Ref. [97] and assume $\mathbf{P}^{\text{piezo}} \sim \mathbf{e}_z$. This is justified for the present QD geometry, as even a more sophisticated inclusion of strain effects will generate merely small lateral contributions to the piezoelectric field [115]. If one is just interested in a rough estimate for the electrostatic field strength inside the QD, a simple capacitor model can be used. Such an estimation yields a value of approximately 5.5 MV/cm.

The small QD schematically depicted in Figure 6.4 confines three bound states for the electrons. The corresponding probability densities are shown together with the three energetically lowest hole states in Figure 6.5. The influence of the built-in field was included in the calculation. For each state the atomic orbital character of the TB wave functions is given and the dominant contributions are highlighted. According to their nodal structure, the depicted electron states $\psi_{1,2,3}^e$ can be classified as s - and p -like states. Obviously such a classification based on the nodal structure is not possible for the hole states due to strong band mixing effects.

² In an ideal wurtzite structure the two lattice constants c and a have a ratio $\frac{a}{c} = \sqrt{8/3} \approx 1.633$, where the lattice constants are defined as shown, for example, in Figure 7.1 on page 70. For InN one finds a ratio 1.609 and for GaN 1.6259, see Ref. [23].

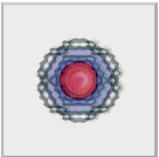
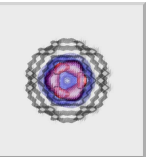
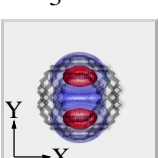
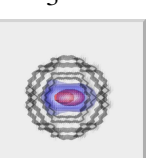
electrons	holes
$E_1^e = 1.7320\text{ eV}$  p _x : 0.051 p _y : 0.051 p _z : 0.144 s : 0.754	$E_1^h = 0.6256\text{ eV}$  p _x : 0.499 p _y : 0.499 p _z : 0.001 s : 0.000
$E_2^e = 1.9621\text{ eV}$  p _x : 0.041 p _y : 0.136 p _z : 0.118 s : 0.705	$E_2^h = 0.6158\text{ eV}$  p _x : 0.144 p _y : 0.834 p _z : 0.016 s : 0.006
$E_3^e = 1.9621\text{ eV}$  p _x : 0.136 p _y : 0.041 p _z : 0.118 s : 0.705	$E_3^h = 0.6158\text{ eV}$  p _x : 0.834 p _y : 0.144 p _z : 0.016 s : 0.006

Figure 6.5: (Color online). The QD geometry is shown from atop. The structure is visualized and isosurfaces of the charge density in the presence of the built-in field for the three energetically lowest electron (left) and hole (right) states are included for 10 % (blue) and 50 % (red) of the maximum value. For the holes the atomistic structure of the wurtzite crystal becomes most apparent for the excited p -states. The corresponding energies ($E_{1,2,3}^{e,h}$) of electron and hole states measured from the valence band maximum of bulk GaN and the atomic orbital character for each wave function are given. The dominant contributions are highlighted.(d=4.5 nm, h=1.6 nm.)

If one compares the single-particle states with and without the inclusion of the built-in field, one finds that in the presence of the fields, the electron states are squeezed into the cap of the QD, while the hole states are constraint to a few atomic layers at the bottom of the QD, near the wetting layer [69]. The influence of the electrostatic field on the one-particle densities is much more pronounced for larger QD. In this case a clear spatial separation of electron and hole probability densities is observed. This lowers the direct spatial overlap of electron and hole wave functions and leads to a strongly reduced dipole matrix elements for larger structures. Besides the influence on the oscillator strength, the additional confinement of the electrons into the cap of the QD increases the electronic Coulomb matrix elements [69]. Furthermore the single-particle energies are strongly affected by the built-in field: The electrostatic field shifts the electron single-particle states to lower energies, whereas the hole states are shifted to higher energies. Consequently, the built-in field leads to an overall red-shift in the single-particle energy-gap [69], known from the quantum confined Stark effect (QCSE).

6.3 Evaluation of Dipole- and Interaction Matrix Elements

Starting with the TB single-particle wave-functions one can determine dipole- and Coulomb matrix elements. Here we will only give the general idea of how the matrix elements are numerically determined and refer the reader to Ref. [69] for further details. General properties of these matrix elements, that can be deduced from the underlying symmetry of the system, are discussed in Chapter 7.

As emphasized above, a TB model represents an atomistic approach to describe the electronic structure of low-dimensional heterostructures. However, explicit knowledge about a basis set of the localized states is not required for the calculation of one-particle energies and wave functions. Only the basic assumptions about the localized (atomic) orbitals, i.e. symmetry, spatial orientation, and orthogonality, enter the TB Hamiltonian [109]. Nevertheless, for the calculation of dipole and Coulomb matrix elements one needs – in principle – the localized basis states. For the Coulomb matrix elements, however, which are dominated by long-range contributions, the explicit knowledge of the atomic orbitals is in practice not required. This is because the structure of the localized orbitals is of significance only for on-site and nearest-neighbor interactions, which contribute less than 5 % to the total Coulomb matrix elements. These findings are in agreement with Ref. [116]. Thus, the matrix elements are approximated by a sum over the TB coefficients at atom sites \mathbf{R}, \mathbf{R}' with orbital indices α, β :

$$V_{ijkl} \approx \sum_{\mathbf{R}\mathbf{R}'} \sum_{\alpha\beta} c_{\mathbf{R}\alpha}^{i*} c_{\mathbf{R}'\beta}^{j*} c_{\mathbf{R}'\beta}^k c_{\mathbf{R}\alpha}^l \frac{e_0^2}{4\pi\epsilon_0\epsilon_r |\mathbf{R} - \mathbf{R}'|}. \quad (6.6)$$

The labels i, j, k, l refer either to electron or to hole states in case of the repulsive electron-electron and hole-hole interaction, or i, l label electron and j, k hole states for the attractive electron-hole interaction. The considerably smaller matrix elements of the electron-hole exchange interaction are neglected. The electronic charge and the vacuum dielectric constant are denoted by e_0 and ϵ_0 , respectively. We use the InN dielectric constant $\epsilon_r = 8.4$ according to Ref. [104] since the wave functions are almost completely confined inside the QD.

For the calculation of dipole matrix elements $\mathbf{d}_{ij}^{eh} = e_0 \langle \psi_i^e | \mathbf{r} | \psi_j^h \rangle$, the explicit structure of the localized orbitals is required as the dipole-operator has mainly local character. Standard Slater orbitals [117] have been used in earlier calculations [118] within orthogonal TB models. While they include the correct symmetry properties, the missing orthogonality limits their applicability. To overcome this problem, we use numerically orthogonalized Slater orbitals.

In this chapter the TB-model and the resulting single-particle wave function have been presented. Additionally we discussed how Coulomb and dipole matrix elements can be evaluated based on these one-particle states. The next chapter is concerned with general statements about the single-particle properties and interaction matrix elements that can be deduced based on the wurtzite symmetry of the underlying atomic lattice.

7 Symmetry Considerations

In the following, the influence of symmetries on the energy spectrum, the single-particle states as well as on the dipole-matrix and Coulomb matrix elements is addressed. Symmetry considerations play an important role for the prediction of energy degeneracies and of optical selection rules [119, 120]. The overall symmetry of the QD is determined by two factors: (i) the crystal symmetry of the underlying lattice and (ii) the symmetry of the QD geometry or, in general, the geometry of the heterostructure [121]. In particular we are interested in lens-shaped QDs placed on a WL, determining the geometry, grown in the wurtzite phase, which dictates the lattice structure. Additionally we will compare these QDs to dots grown in the zinc-blende structure and disk-like QDs.

In order to illustrate the interplay of the dot geometry and the underlying lattice, let us consider a lens-shaped QD. The geometry of the QD has a $C_{\infty v}$ -symmetry. This means that the geometry is left unchanged by any rotation around the z -axis (here we choose the z -axis to be directed along the growth direction) and that one furthermore has arbitrary many vertical (perpendicular to the x - y -plane) mirror planes. Because these operations form a non-commutative group, the $C_{\infty v}$ symmetry predicts – as we will discuss in more detail later on – degeneracies in the energy spectrum. In the effective mass approximation or in the $\mathbf{k} \cdot \mathbf{p}$ -theory the underlying atomic structure is not resolved so that one obtains degenerate energies for the lens-shaped QD (see, for example, Section 1.1). If one takes the atomistic structure into account, as it is done in a TB-calculation [69, 122] or a pseudo-potential calculation [53], the symmetry will be reduced and degeneracies may be lifted [121]. For example, a lens-shaped QD grown on a wurtzite lattice has only a C_{3v} symmetry. If the same QD is grown in the zinc-blende phase, one is left with a C_{2v} symmetry. As we will see in the next section, the C_{3v} symmetry group is still rich enough for the prediction of degeneracies, while no statements about the degeneracy of states can be deduced from the C_{2v} symmetry group. Even though one needs to include the atomistic lattice for the correct description of degeneracies and selection rules, it is expected that those derived from continuum models will hold – at least approximately – for sufficiently smooth nanostructures.

The conventional group-III nitrides InN, GaN, and AlN can crystallize in principle both in the zinc-blende and in the wurtzite phase [23, 94]. Nevertheless the predominant phase for the group-III nitrides is the wurtzite structure [23] as it usually is the thermodynamically stable phase of bulk InN, GaN, and AlN [94]. The conventional unit cell of a wurtzite crystal is shown in Figure 7.1. In the case of InN the blue spheres represent the Indium atoms and the orange spheres the Nitrogen atoms. The chemical bonds are shown as thick lines. Additional thin lines are introduced as guides for the

wurtzite structure

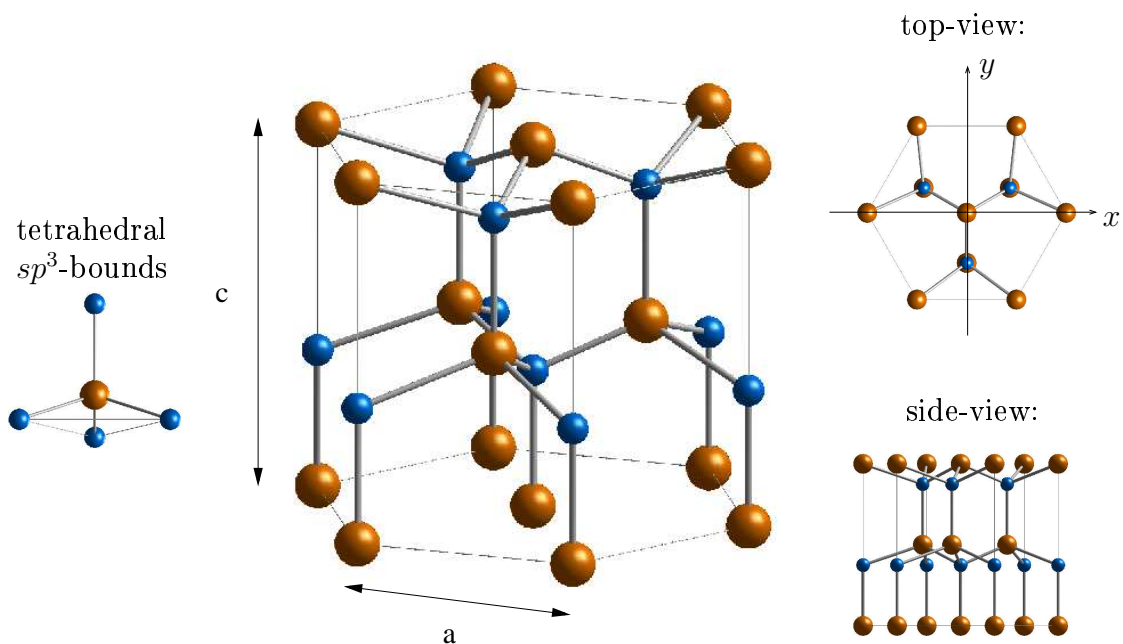


Figure 7.1: (color online) Conventional unit cell of the wurtzite crystal (middle) together with a top- and side-view (right side) and the tetrahedral atom arrangement of nearest neighbors. In the case of InN the larger orange spheres symbolize the Nitrogen atom, the smaller blue spheres the Indium atom.

eyes to clarify the relative position. As can be inferred from the side-view in Figure 7.1 the crystal is in vertical direction composed of alternating layers of Nitrogen and Indium atoms. Each atom sort alone forms a hexagonal closed packed (hcp) structure. In horizontal direction, the individual layers have a hexagonal symmetry with a six-fold axis. Nevertheless the wurtzite crystal has only a three-fold axis as adjacent layers are displaced in the horizontal direction (see Figure 7.1). That there can be at most a three-fold axis may also be inferred from the top view in Figure 7.1. The three-fold rotation around the z -axis (here we chose the z -axis along the c axis of the unit-cell) is also evident in the atomic arrangement in the sp^3 -hybridized orbitals of the Nitrogen atom shown in the left-most part of Figure 7.1. Another symmetry that can be identified is the IC_{2x} symmetry, that is, a rotation around the x -axis by π followed by an inversion or, equivalently, a mirroring across the plane normal to the x -axis defined by $(x, y, z) \rightarrow (-x, y, z)$. The wurtzite bulk material has additional, more complicated symmetries, like, a rotation followed by a non-primitive¹ translation. But all these symmetries are spoiled by the geometry of the QD and are therefore not of interest

¹ In contrast to a primitive translation, a non-primitive translation does not map the lattice onto itself.

zinc-blende structure

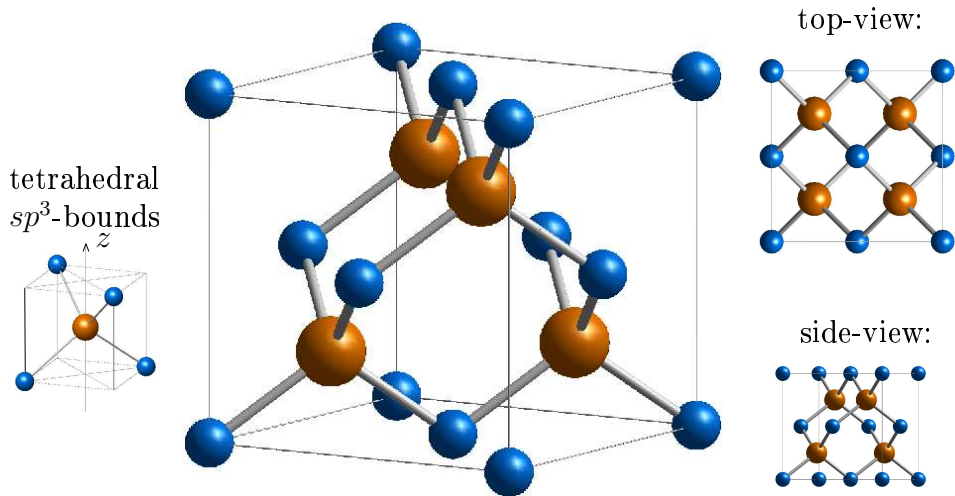


Figure 7.2: (color online) Conventional unit cell of the zinc-blende crystal (middle) together with a top- and side-view (right side) and the tetrahedral atomic arrangement. The orange spheres symbolize the Arsenide atom, the smaller blue spheres the Indium atom.

for the following discussion that concern the electronic states in a QD. In particular we considered here only symmetry operations that contain rotations around the z -axis because all other possible rotation axes will be destroyed by the geometry of a lens- or disk-like QD.

Even though group-III nitrides can also crystallize in zinc-blende, we will discuss this crystal structure using a more typical example, namely, InAs. That both phases are possible for the nitrides, relies on the sp^3 -hybridization of the atomic orbitals that are found in both structures. In this arrangement the nearest neighbors around each atom form a regular tetrahedron. Nevertheless, the different arrangement of these orbitals in the crystal structure leads to quite different symmetry properties. The conventional unit cell of zinc-blende is shown in Figure 7.2. The blue spheres represent Indium atoms, the orange spheres the Arsenide atoms. Each atom sort alone forms a face centered cubic (fcc) lattice, which has, amongst other symmetries, the z -axis as a four-fold rotation axis. For the combined system the most obvious symmetry is the C_{2z} -symmetry. But there are additional symmetries, like the IC_{4z} -improper rotation, that is a rotation around the z -axis by $\frac{\pi}{2}$ followed by an inversion. This symmetry can probably best be seen by considering the atoms that surround an Arsenide atom shown in the left part of Figure 7.2. However, this rotoinvariance will be spoiled by any geometry that does not have an inversion center, like, for example, the lens-shaped QD grown on a WL. In this case only the two-fold rotation axis remains.

7.1 Energy Spectrum

As outlined in the previous section, the symmetry group of a lens-shaped nitride QD placed on top of a WL grown in the wurtzite phase is C_{3v} . This group is generated by the rotation around the z -axis with angle $\frac{2\pi}{3}$, denoted by C_{3z} , together with a mirror plane perpendicular to the y -axis, denoted by IC_{2y} . By successively applying these operations one generates six symmetry operations. The three mirror planes are schematically depicted in Figure 7.3. Additionally, one has the three rotations around the z -axis by $\frac{2\pi}{3}$, $\frac{4\pi}{3}$, and 2π (the identity). While these operations commute with the Hamiltonian, they do not commute among themselves. To illustrate this, a simple example is shown in Figure 7.4.

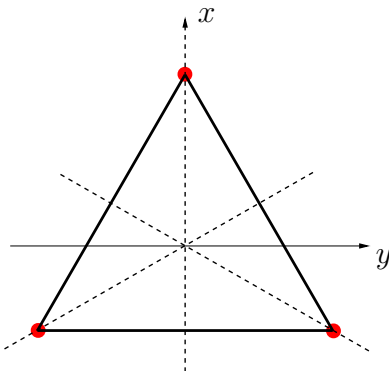


Figure 7.3: The triangle represents the C_{3v} symmetry: there are three rotations and three mirror planes that leave the triangle unchanged.

From this non-abelian character of the group we can immediately conclude that there must exist energetically *degenerate* states. Indeed, if two operators A and B commute with the Hamiltonian but not with each other then there must exist degenerate states. A simple proof of this runs as follows: Assuming that all the states were energetically non-degenerate then the choice of the eigenbasis of H is unique. The commutation of the Hamiltonian with the operator A would imply that all the eigenstates of H are as well eigenstates of A . From $[H, B] = 0$, one were led to the same conclusion for the operator B . But this would mean that these states are common eigenstates of all three operators H , A and B , which would result in $[A, B] = 0$. This is in contradiction to the assumption and completes the proof. Consequently there must exist energetically degenerate eigenstates leading to several possible choices for the eigenbasis of H : one shared with A and one shared with B . This is also the case for the wurtzite QD under consideration. One example of such degenerate states are the p -shell states given in Figure 6.5 on page 67. Probably the best-known elementary example of degeneracies produced by non-commuting operators is provided by the angular momentum operators [70]. The operator \mathbf{J}^2 commutes with J_x , J_y , and J_z , but the components do not commute with each other. As a consequence the subspaces characterized by the eigen-

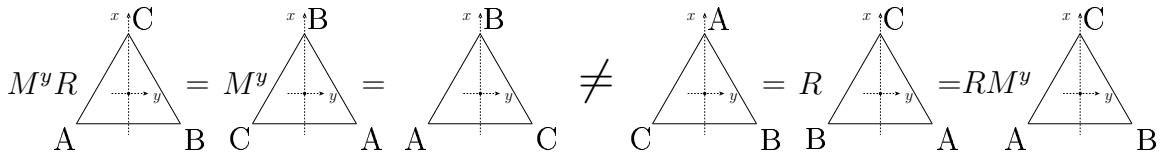


Figure 7.4: Illustration of the fact that the rotation R around the center and mirroring M^y , defined by $(x, y, z) \rightarrow (x, -y, z)$, do not commute.

value $\hbar^2 j(j+1)$ of \mathbf{J}^2 are $(2j+1)$ -times degenerate. A systematic use of these ideas is developed by the methods of group theory [120, 123]. Here, due to the simplicity of the symmetry group involved, some elementary considerations are sufficient.

The degeneracy of the p -shell states in the wurtzite structure is in particular intriguing as a recent paper by Bester and Zunger underlined that the p -shell in a zinc-blende structure must split into two states if a microscopic description for the single-particle states is used [121]. This seems to be at odds with our results as the bulk crystal structure of zinc-blende has a symmetry group that is much richer than the one of the wurtzite crystal. This situation underscores that it is not the symmetry of either the lattice or the geometry of the QD alone that is responsible for the degeneracies of the states, but the symmetry group of the combined system. For a lens-shaped QD grown in the wurtzite phase this is the C_{3v} symmetry, which is a non-abelian group as mirroring and rotation do not commute. This leads to degenerate states. In the zinc-blende phase the overall symmetry group is only C_{2v} . As this is an abelian group, one cannot derive any degeneracy from this group. If one considers instead a disk-like QD, as schematically depicted in Figure 7.5, one has both in the wurtzite and in the zinc-blende structure non-abelian symmetry groups and henceforth necessarily degenerate eigenstates. In Appendix C we give an additional proof of the presence/absence of degeneracies based only on the so-called order of the rotation axis combined with the time-reversal. The p -shell splitting that has been predicted for a QD on a wurtzite lattice in previous publications [124, 125] must be attributed to the rectangular boundary condition and/or the rectangular discretization used in their calculations. Such a numerical treatment destroys the C_{3z} symmetry of the underlying lattice and with it the symmetry properties.

In summary, one can expect degeneracies in a disk-like QD in both the wurtzite and zinc-blende phase, whereas for a lens-shape QD degeneracies are only to be expected in the wurtzite phase and not in a zinc-blende structure.

7.2 Single-Particle States

So far we discussed rotations in the three-dimensional space, which leave the system invariant. In order to make statements about how symmetries affect the properties of the wave function, we need to define the action of the symmetry operations on the elements of the Hilbert space. In spatial representation the action of any symmetry

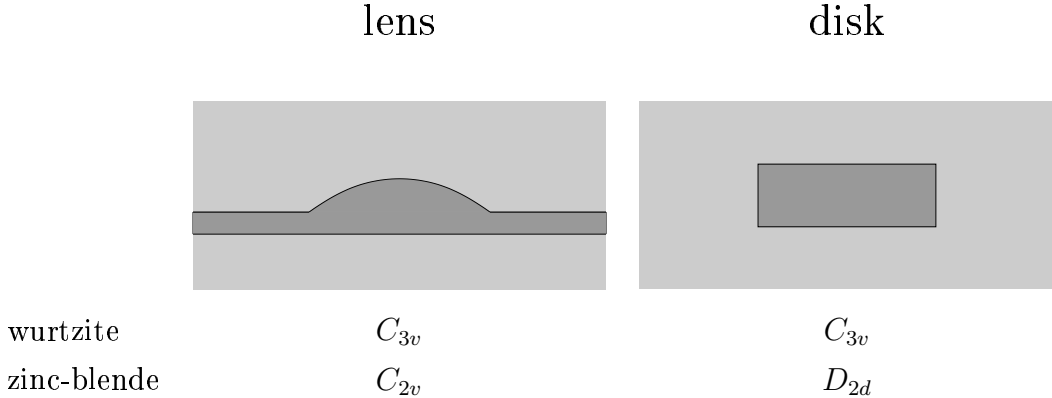


Figure 7.5: Symmetry group in different QD geometries and crystal structures (Schönflies notation was used to identify the groups [123]). The non-abelian group D_{2d} contains the improper rotation IC_{4z} . Cuts through the QDs are shown as dark grey areas.

operation T is defined via $(T\psi)(\mathbf{r}) = \psi(T^{-1}\mathbf{r})$, see for example Refs. [120, 123]. In the case of the rotation one has, for example, $(R\psi)(\mathbf{r}) = \psi(R^{-1}\mathbf{r})$. This means that by rotating the entire system the new function $R\psi$ (after this rotation) takes at point \mathbf{r} the value of the old function ψ at position $R^{-1}\mathbf{r}$ prior to rotation. So, loosely speaking, one can say that each point simply keeps its functional value while it undergoes the rotation from the point $R^{-1}\mathbf{r}$ to the point \mathbf{r} . In the case of a tight-binding wave function this amounts to a simultaneous transformation of the orbitals and their centers. In the remaining part of this section we concentrate on the consequences of the spatial symmetry of the QD geometry and the underlying lattice on the single-particle wave functions.

As mentioned previously in Chapter 6 we use in the tight-binding description of the eigenstates one s -orbital and three p -orbitals at each lattice point \mathbf{R} . Then the expansion of an eigenstate can be written as

$$|\phi\rangle = \sum_{\mathbf{R}} |s\rangle_{\mathbf{R}} a(\mathbf{R}) + \sum_{\mathbf{R},j} |p_j\rangle_{\mathbf{R}} b_j(\mathbf{R}) , \quad (7.1)$$

where $\langle \mathbf{r}|s\rangle_{\mathbf{R}} = \psi_s(\mathbf{r} - \mathbf{R})$ denotes the atomic s -orbital centered around the site \mathbf{R} . Similarly $\langle \mathbf{r}|p_i\rangle_{\mathbf{R}} = \psi_{p_i}(\mathbf{r} - \mathbf{R})$ with $i \in \{x, y, z\}$ denotes a p -orbital around \mathbf{R} . Instead of using the real-valued p -orbitals, which are advantageous for the numerical determination of the TB wave functions, it is more convenient for an analysis of the symmetry properties to work with the linear combinations $p_{\pm} = \frac{1}{\sqrt{2}}(p_x \pm ip_y)$ of the atomic orbitals. These linear combinations transform under a rotation R around their center and mirroring $M_{\mathbf{R}}^y$, like

$$\begin{aligned} R|p_+\rangle &= e^{-i\frac{2\pi}{3}}|p_+\rangle , & M^y|p_+\rangle &= |p_-\rangle , \\ R|p_-\rangle &= e^{+i\frac{2\pi}{3}}|p_-\rangle , & M^y|p_-\rangle &= |p_+\rangle . \end{aligned} \quad (7.2)$$

More interesting is how the *total* wave function (7.1) and not just some local orbital changes under the symmetry operation of the C_{3v} group. If the single-particle state is invariant under all the operations of the group, we call it an s -state and denote it $|\phi_s(\mathbf{r})\rangle$. This notation is somewhat abusive as in this notation a p_z -orbital is also an s -state. Nevertheless we use this notation for the sake of simplicity. If a wave function transforms under rotation and mirroring like the local orbitals in Eq. (7.2), we call the wave functions an p_{\pm} -state and write $|\phi_{p_{\pm}}(\mathbf{r})\rangle$. The probability density of $|\phi_{p_{\pm}}(\mathbf{r})\rangle$ is shown in Figure 7.6. The corresponding real-valued linear combinations, shown in Figure 6.5 on page 67, are called p_x - and p_y -states and are denoted as $|\phi_{p_x}(\mathbf{r})\rangle$ and $|\phi_{p_y}(\mathbf{r})\rangle$, respectively.

In order to access the transformation properties of the eigenstates, one has to study how the overall wave-function transforms under rotation. The rotation of atomic orbitals that are not situated in the origin leads to rotated orbitals in a rotated position or, equivalently, to transformed coefficients $a(\mathbf{R})$ and $\{b_i(\mathbf{R})\}_{i=1}^3$ taken at rotated values. In a somewhat lengthy analysis one can show that an s -state $|\phi_s(\mathbf{r})\rangle$ must be of the form:

$$|\phi_s(\mathbf{r})\rangle = \sum_{\mathbf{R}} [|s\rangle_{\mathbf{R}} \alpha(\mathbf{R}) + |p_z\rangle_{\mathbf{R}} \beta_z(\mathbf{R})] + \sum_{\mathbf{R}} [|p_+\rangle_{\mathbf{R}} \mathcal{Z}_{\mathbf{R}}^* \beta(\mathbf{R}) + |p_-\rangle_{\mathbf{R}} \mathcal{Z}_{\mathbf{R}} \beta^*(\mathbf{R})] \quad (7.3)$$

where the coefficients $\alpha(\mathbf{R})$, $\beta_z(\mathbf{R})$, and the real part of $\beta(\mathbf{R})$ are invariant under all transformation of C_{3v} , while the imaginary part of $\beta(\mathbf{R})$ is invariant under rotation of the group and changes sign under the action of the mirror operation. The quantity $\mathcal{Z}_{\mathbf{R}}$ is defined as $X_{\mathbf{R}} + iY_{\mathbf{R}}$ or in polar coordinates $\sqrt{X_{\mathbf{R}}^2 + Y_{\mathbf{R}}^2} e^{i\phi_{\mathbf{R}}}$, where $X_{\mathbf{R}}$ and $Y_{\mathbf{R}}$ denote the cartesian coordinates of the lattice site \mathbf{R} and $\phi_{\mathbf{R}}$ is the polar angle of the point \mathbf{R} in cylindrical coordinates. Without presenting all the details, one can make the identification of the state (7.3) as an s -state more plausible: the s - and p_z -orbital part are left unchanged under the action of the elements of C_{3v} because the coefficients $\alpha(\mathbf{R})$ transforms into $\alpha(\mathbf{R}') = \alpha(\mathbf{R})$, so that there is no change. The same is true for $\beta_z(\mathbf{R})$. The transformation of the $|p_+\rangle$ -part is a bit more complicated. First of all, under the C_{3z} rotation one obtains a phase factor $e^{-i\frac{2\pi}{3}}$, which stems from the transformation behavior of the atomic orbitals. This is compensated by the phase factor acquired by $\mathcal{Z}_{\mathbf{R}}^*$ under rotation: the new values of the coefficients are those of the site $\mathbf{R}' = R^{-1}\mathbf{R}$ prior to the rotation. But $\beta(\mathbf{R}') = \beta(\mathbf{R})$ and $\mathcal{Z}_{\mathbf{R}'}^* = (\sqrt{X_{\mathbf{R}'}^2 + Y_{\mathbf{R}'}^2} e^{i\phi_{\mathbf{R}'}})^* = \sqrt{X_{\mathbf{R}}^2 + Y_{\mathbf{R}}^2} e^{-i(\phi_{\mathbf{R}} - \frac{2\pi}{3})} = \mathcal{Z}_{\mathbf{R}}^* e^{+i\frac{2\pi}{3}}$. As a consequence the phase factors cancel, so that there is no net change in the state. The same is true for the part containing the $|p_-\rangle$ -orbitals. Therefore $|\phi_s(\mathbf{r})\rangle$ is indeed an invariant state.

A close inspection of the numerically determined TB coefficients for typical sets of lattice points reveals that the states with lowest energy for the electron and holes depicted in Figure 6.5 are indeed s -states. In this figure the sum of the modulus squared of the coefficients of the orbitals are displayed. For the electrons, the state looks as one would expect for an s -state in the effective mass approximation: it is symmetric under

rotation², has a single maximum at the center and decays to the boundaries. In contrast, the shape of the s -state of the holes does not show this behavior. It has the rotational symmetry, but has a node at the center. The rotational symmetry can be understood by recalling that Figure 6.5 displays the sum of the modulus squared of the orbital-coefficients. Because the contribution of the $|s\rangle$ - and $|p_z\rangle$ -orbitals to the QD s -state is only small, they can be neglected for the discussion of the shape. Then we find from Eq. (7.3) for the probability density $2|\mathcal{Z}_\mathbf{R}^* \beta(\mathbf{R})|^2 = 2(X_\mathbf{R}^2 + Y_\mathbf{R}^2)|\beta(\mathbf{R})|^2$, which reveals the rotational symmetry. The coefficient $\mathcal{Z}_\mathbf{R}^* \beta(\mathbf{R})$ of $|p_+\rangle$ is zero at the origin and assuming that $\beta(\mathbf{R})$ is smooth, they vanish gradually for $\mathbf{R} \rightarrow 0$. This explains the unexpected node at the center for the hole.

A similar analysis of the coefficients can be carried out for the $|\phi_{p\pm}(\mathbf{r})\rangle$ states. By comparing the properties of the coefficients as they are deduced from this analysis with those numerically determined in the TB-approach, one can infer that the states 2 and 3 in Figure 6.5 are indeed p_x and p_y states. The symmetry properties of the p -states become more obvious if instead of the real-valued functions, $|\phi_{p_x}(\mathbf{r})\rangle$ and $|\phi_{p_y}(\mathbf{r})\rangle$, which are selected by the numerical diagonalization procedure, the linear combinations $|\phi_{p\pm}(\mathbf{r})\rangle \propto (|\phi_{p_x}(\mathbf{r})\rangle \pm i|\phi_{p_y}(\mathbf{r})\rangle)$ are plotted. The resulting probability densities are depicted in Figure 7.6.

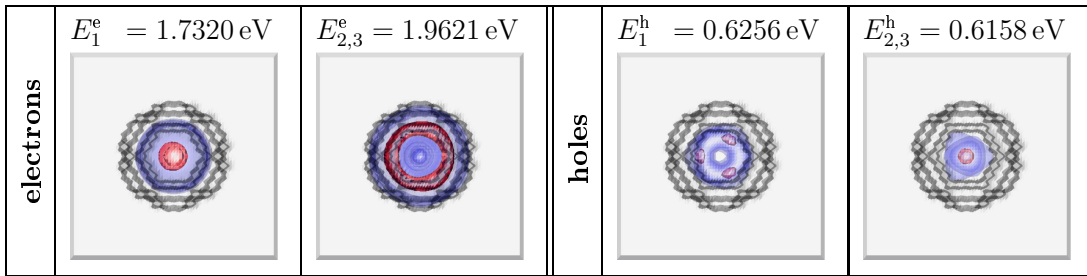


Figure 7.6:(color online) Same as Figure 6.5, with the only difference that here the probability densities for the linear combination $\frac{1}{\sqrt{2}}(|\phi_{p_x}(\mathbf{r})\rangle + i|\phi_{p_y}(\mathbf{r})\rangle)$ is shown as the second state for the electrons and holes instead of $|\phi_{p_x}(\mathbf{r})\rangle$ and $|\phi_{p_y}(\mathbf{r})\rangle$. The probability density of the additional combination $\frac{1}{\sqrt{2}}(|\phi_{p_x}(\mathbf{r})\rangle - i|\phi_{p_y}(\mathbf{r})\rangle)$ is not included, as it is identical. For all wave functions the rotational C_{3z} -symmetry is obvious.

In the previous Section we have pointed out that there must exist energetically degenerate states in the wurtzite QD. Here, we additionally explain why the p -states are those that are degenerate. This can best be seen using the $|\phi_{p_x}(\mathbf{r})\rangle$ and $|\phi_{p_y}(\mathbf{r})\rangle$ functions. If $|\phi_{p_x}(\mathbf{r})\rangle$ has the energy E_{p_x} then we have on the one hand

$$H(R|\phi_{p_x}(\mathbf{r})\rangle) = H(\cos \theta |\phi_{p_x}(\mathbf{r})\rangle + \sin \theta |\phi_{p_y}(\mathbf{r})\rangle) = E_{p_x} \cos \theta |\phi_{p_x}(\mathbf{r})\rangle + \sin \theta H|\phi_{p_y}(\mathbf{r})\rangle$$

and on the other hand

$$H(R|\phi_{p_x}(\mathbf{r})\rangle) = R(H|\phi_{p_x}(\mathbf{r})\rangle) = E_{p_x} (\cos \theta |\phi_{p_x}(\mathbf{r})\rangle + \sin \theta |\phi_{p_y}(\mathbf{r})\rangle) .$$

² Of course, due to the lattice structure only the rotation by $\frac{2\pi}{3}$ is a symmetry operation and not an arbitrary rotation, as one would expect from an effective mass model.

By comparing these two expressions we see that $H|\phi_{p_y}(\mathbf{r})\rangle = E_{p_x}|\phi_{p_y}(\mathbf{r})\rangle$, so that one has indeed $E_{p_x} = E_{p_y}$. Note that this line of argumentation does not work in case of a C_{2z} -symmetry. In this case the action of the rotation is solely given by $R|\phi_{p_x}(\mathbf{r})\rangle = -|\phi_{p_x}(\mathbf{r})\rangle$ with no admixture of $|\phi_{p_y}(\mathbf{r})\rangle$. Therefore no relationship between E_{p_x} and E_{p_y} can be deduced.

7.3 Dipole Matrix Elements

The numerical evaluation of the dipole-matrix elements shows that the non-zero values of the in-plane dipole matrix elements $\mathbf{e}d_{ij}^{eh}$ with \mathbf{e} in the x - y -plane are much larger than those with \mathbf{e} in z -direction. Therefore we consider here only the in-plane matrix elements with $\mathbf{e} = 1/\sqrt{2}(1, 1, 0)$ and denote the corresponding dipole-matrix elements by d_{ij}^{eh} . When comparing the resulting elements with those known from the InGaAs-system, the probably most surprising fact is that the matrix element d_{ss}^{eh} vanishes. As an immediate consequence we find a dark exciton ground-state for the small QD discussed in Figure 7.6. This is due to the fact that the ground state contains mainly configurations in which both carriers are in their s -shells, so that an emission is not possible. Furthermore the matrix elements $d_{p_ip_j}^{eh}$, with $i, j \in \{x, y\}$ are more than one order of magnitude smaller than the other non-vanishing matrix elements. As a consequence, these contribution can safely be neglected in the calculation of optical spectra, in which the absolute value of the dipole-matrix elements enters even quadratically. If we restrict the analysis to the two energetically lowest shells for the electrons and holes we are, to a good approximation, left with the following dipole-matrix elements:

$$d_{ij}^{eh} = \begin{pmatrix} 0 & d_{sp+}^{eh} & d_{sp-}^{eh} \\ d_{p+s}^{eh} & 0 & 0 \\ d_{p-s}^{eh} & 0 & 0 \end{pmatrix}. \quad (7.4)$$

Can we understand these selection rules for the dipole matrix elements, or do they stay as a mere numerical result? It turns out that in terms of the symmetry of the wave functions the selection rules can indeed be understood in case of the s to s transition and made plausible for the p to p transitions. To this end we consider the matrix elements $\langle \lambda_z | x \pm iy | \lambda'_z \rangle$, where we denoted the states by the phase factor $e^{-i\lambda_z \frac{2\pi}{3}}$ they acquire under rotation of $\frac{2\pi}{3}$, i.e., $\lambda_z = 0$ for the s -state and $\lambda_z = \pm 1$ for the p_{\pm} -state. Then we write:

$$\begin{aligned} \langle \lambda_z | x + iy | \lambda'_z \rangle &= \langle \lambda_z | R_+^{-1} R_+(x + iy) R_+^{-1} R_+ | \lambda'_z \rangle \\ &= e^{+i(\lambda_z - \lambda'_z)\theta} \langle \lambda_z | R_+(x + iy) R_+^{-1} | \lambda'_z \rangle \\ &= e^{+i(\lambda_z - \lambda'_z - 1)\theta} \langle \lambda_z | x + iy | \lambda'_z \rangle , \end{aligned} \quad (7.5)$$

where R_+ denotes the rotation by $\theta = \frac{2\pi}{3}$. In the first step we used the transformation properties of the wave-function under the rotation, then we used $R_+(x + iy)R_+^{-1} =$

$e^{i\phi}(x+iy)$. From Eq. (7.5), one can read off that the dipole matrix element $\langle \lambda_z | x + iy | \lambda'_z \rangle$ must be zero unless $(\lambda_z - \lambda'_z - 1)\theta$ is an integer multiple of 2π . If the symmetry group would support the rotation around the z -axis by an arbitrary angle θ it could be deduced that for $\lambda_z - \lambda'_z + 1 \neq 0$ the dipole matrix element must be zero. By considering the matrix element $\langle \lambda_z | x - iy | \lambda'_z \rangle$ one would find that this matrix element is zero if $\lambda_z - \lambda'_z - 1 \neq 0$. Therefore, if $|\lambda_z - \lambda'_z| \neq 1$ one would obtain $\langle \lambda_z | x \pm iy | \lambda'_z \rangle = 0$ and from this it could directly be inferred that the matrix element $d_{\lambda_z, \lambda'_z}^{eh}$ must vanish. Consequently, it could be concluded that the elements d_{ss}^{eh} , d_{p_i, p_j}^{eh} with $i, j \in \{\pm\}$ vanish and that only d_{s, p_i}^{eh} and $d_{p_i, s}^{eh}$ are non-zero. However, this statement is not true, because one has only a C_{3z} symmetry. The reduced symmetry opens additional transition channels. Indeed, only for $|\lambda_z - \lambda'_z|$ modulo 3 $\neq 1$ zero dipole-matrix elements d_{ij}^{eh} are obtained. From this we still obtain $d_{ss}^{eh} = d_{p_+, p_+}^{eh} = d_{p_-, p_-}^{eh} = 0$, but in addition to the non-zero matrix elements $d_{p_\pm, s}^{eh}$ and d_{s, p_\pm}^{eh} one has $d_{p_+, p_-}^{eh} \neq 0$ and $d_{p_-, p_+}^{eh} \neq 0$. Nevertheless, as the latter two are zero in case of a continuous rotation symmetry, it is quite plausible that they remain small, even in the case of only a three-fold axis. And indeed the numerically determined matrix elements show exactly this behavior.

Comparison to the Selection Rules used in Part I

Before proceeding to discuss the symmetry properties of the Coulomb matrix elements, a comment on the selection rules found here in the case of nitrides in comparison to those used throughout Part I is in order. There seems to be a contradiction related to the following facts: (i) in both the nitride case and the InGaAs system the electron and holes QD ground states (gs) are, including the spin degree of freedom, double degenerate. This suggests an s -type symmetry, that is, an invariance with respect to the particular symmetry group that characterizes the QD. (ii) The s -type character is confirmed by a solution of the Schrödinger equation in the effective mass approximation for the InGaAs system as outlined in Section 1.1. In this way, one finds s -type envelope functions (invariant to the $C_{\infty v}$ operations) for the gs eigenfunctions in both bands. (iii) despite these facts, which suggest the same symmetry in the nitride and the InGaAs system one has $d_{gs, gs}^{eh} = 0$ in the former and $d_{gs, gs}^{eh} \neq 0$ in the latter case.

This seems to be a symmetry-related contradiction and the answer should therefore be mainly based on symmetry considerations. In conventional III-V structures the spin-orbit coupling is much stronger than in nitrides and can by no means be neglected. Consequently, one cannot argue in terms of the orbital and spin angular momentum separately (as for group-III nitride case) but only in terms of the total angular momentum J . It is known that the wave function for the holes in a heterostructure is oftentimes to high accuracy described using only the heavy-hole (hh) subband [49], characterized by spin quantum numbers $j = \frac{3}{2}$ and $m_j = \pm\frac{3}{2}$. The dominant character of the heavy-hole band is due to two facts: (i) one has on the one hand a clear separation of the so-called split-off band from the light-hole (lh) and the hh-band due to the spin-orbit interaction and (ii) a splitting between the lh- and hh-band due to the confinement in growth direction and the difference in the effective masses. Therefore

the energetically lowest subband is the hh one and in an effective mass approach the s -envelope function is modulating a hh-Bloch function. In terms of a TB description this is equivalent to

$$|\phi_+^h(\mathbf{r})\rangle = \sum_{\mathbf{R}} |p_+ \uparrow\rangle_{\mathbf{R}} \beta(\mathbf{R}) , \quad (7.6)$$

where the coefficient $\beta(\mathbf{R})$ is invariant. The spin degeneracy is in this case replaced by the Kramers degeneracy [126], so that the state

$$|\phi_-^h(\mathbf{r})\rangle = \sum_{\mathbf{R}} |p_- \downarrow\rangle_{\mathbf{R}} \beta^*(\mathbf{R}) , \quad (7.7)$$

has the same energy. If we consider only the spatial part we see from the combination of the atomic orbitals and the coefficients that the ground states in this system are what we would call a p -state: Under a rotation of an angle θ the coefficients are unchanged, but the atomic orbitals pick up a phase factor $e^{\pm i\theta}$. But the dipole-matrix elements of the hole states (7.6) and (7.7), with the electronic ground state remain non-zero, exactly as in the case of the nitride system. In terms of angular momenta the difference between the electronic ground state ($j = \frac{1}{2}$) and the hole ground state ($j = \frac{3}{2}$) is $\Delta j = 1$, so that the transition is dipole-allowed.

Is it correct to call the pair of states (7.6) and (7.7) s -states in spite of their being a linear combination of p -states? Here one should be careful with the terminology. In spin $\frac{1}{2}$ systems there are no non-degenerate states, the minimal degeneracy is two (Kramers doublets [126]). If the Hamiltonian is spin-independent, as it is the case for negligible spin-orbit interaction, one considers only the orbital degeneracy. A non-degenerate state, like an s -state, becomes a doublet due to the spin and thus its degeneracy is minimal. Similarly, the pairs of states (7.6) and (7.7) form a Kramers pair: the action of the $C_{\infty v}$ group leaves the subspace spanned by these two states invariant. In order to see this, one has to bear in mind that we deal in the case of the two states (7.6) and (7.7) with a so-called *double group* [123], in which every space rotation is accompanied by a spin rotation. It can be shown that the operations of the $C_{\infty v}$ double group, which transforms $|p_+\rangle$ into $|p_-\rangle$ also changes \uparrow into \downarrow . In the sense of minimal degeneracy they can therefore be called s -states in agreement with the spatial symmetry of their envelopes in the effective mass approximation or their $\beta(\mathbf{R})$ coefficients in the tight-binding formulation.

7.4 Coulomb Matrix Elements

It is not only possible to use the symmetry properties of the wave functions to predict selection rules for the dipole-matrix elements, but also for the Coulomb matrix elements. Exactly as in the case of the dipole-matrix elements, we find that a three-fold symmetry axis allows for more non-zero elements than a $C_{\infty z}$ -axis. Nevertheless, these additional matrix elements are rather small.

$(\mathbf{i}, \mathbf{j}, \mathbf{k}, \mathbf{l})$	$\mathbf{V}_{ijkl}^{cc}/\text{meV}$
(0, 0, 0, 0)	93.8459
(0, +, +, 0), (0, -, -, 0)	81.6389
(+, 0, 0, +), (-, 0, 0, -)	81.6389
(+, +, +, +)	75.8542
(+, -, -, +), (-, +, +, -)	75.8542
(-, -, -, -)	75.8542
(0, 0, +, -), (0, 0, -, +), (+, -, 0, 0), (-, +, 0, 0)	17.0949
(0, +, 0, +), (+, 0, +, 0)	17.0949
(0, -, 0, -), (-, 0, -, 0)	17.0949
(+, -, +, -), (-, +, -, +)	9.3997
(+, 0, -, -), (+, +, 0, -), (-, 0, +, +), (-, -, 0, +)	-0.1972
(0, +, -, -), (+, +, -, 0), (0, -, +, +), (-, -, +, 0)	-0.1972

Table 7.1: All non-zero electron-electron Coulomb matrix determined numerically from the TB-wave function. The index 0 denotes the state $|\phi_s(\mathbf{r})\rangle$ and \pm denote the states $|\phi_{p\pm}(\mathbf{r})\rangle$. The horizontal single lines group elements together that are degenerate due to symmetry. The matrix elements below the horizontal double line are states that are zero in the case of a $C_{\infty v}$ - symmetry. Explicit numbers are given for the QD discussed in Figure 7.6 but without the inclusion of the internal electrostatic field.

If the entire system is rotated by an angle $\theta = \frac{2\pi}{3}$, then each single-particle wave function acquires a phase factor, but the distance $|\mathbf{r} - \mathbf{r}'|$ is not affected by this rotation. Therefore we find for the electron-electron interaction matrix elements

$$V_{ijkl}^{ee} = e^{i(\lambda_i^z + \lambda_j^z - \lambda_k^z - \lambda_l^z)\theta} V_{ijkl}^{ee} . \quad (7.8)$$

From this we deduce that V_{ijkl} must be zero if $(\lambda_i^z + \lambda_j^z - \lambda_k^z - \lambda_l^z)$ modulo 3 $\neq 0$. If one would have a full rotation axis $C_{\infty z}$ then one would recover the selection rules of Section 1.3 that correspond to full angular momentum conservation. But with only a three-fold axis, additional matrix elements occur. These are separated in table 7.1 from those also present in case of a full rotation by a double line. The explicit numbers are obtained from those calculated by Schulz et al. in (s, p_x, p_y) -representation by a transformation to (s, p_+, p_-) -representation. Clearly these additional matrix elements are rather small. This is in accordance with our expectations about matrix elements that would altogether vanish in a system with a higher symmetry.

This chapter was devoted to statements about the single-particle properties and interaction matrix elements that can be deduced by a careful analysis of the symmetry properties of the wurtzite QDs. The results were contrasted to those of zinc-blende QDs. In the following chapter, we analyze the multi-exciton spectra of wurtzite InN/GaN dots. We find dramatic differences to the spectra known from conventional III-V systems as they were discussed in Part I.

8 Optical Properties

In Chapter 6 we have presented the TB-model used to calculate the single-particle states in nitride QDs. Subsequent to this, the symmetry properties of the resulting wave-functions, dipole and Coulomb matrix elements have been studied in the last chapter. In this Chapter we address the optical properties of these QDs. Of particular importance, and in clear contrast to the case of an InGaAs system analyzed in the first part of this thesis, are the altered selection rules in the nitride case and the fact that the wave functions for electrons and holes are far from being identical. A consequence of the former is the prediction of dark exciton and biexciton states in the case of small lens-shaped QDs. The latter will lead to strong blue shifts as the number of excitons in the QD is increased. Additionally we present results for larger nitride QDs for which the shell structure for the holes is changed, leading to bright exciton states. For both types of QDs a detailed semi-analytic discussion will be given in addition to the results obtained numerically from a configuration interaction (CI) calculation. Before we start the analysis of the multi-exciton spectra we will summarize in the next section the most important properties of the single-particle states and the resulting selection rules for the dipole-matrix elements. For a general introduction to the configuration interaction method and the many-body Hamiltonian employed, the reader is referred to Part I of this thesis.

8.1 Summary of Single-Particle Properties and Selection Rules

In this section we summarize the single-particle properties and selection rules that are of major importance for the following discussion of the multi-exciton spectra. For more details see Chapters 6 and 7.

Due to strong band-mixing effects in the valence band a simple effective mass approach is not applicable and the single-particle properties were determined using a tight-binding model. As the problem is essentially spin-independent the Hamiltonian matrix is real and the numerical diagonalization procedure yields real eigenvectors. For the small QD analyzed throughout Chapter 6 the single-particle ground state is non-degenerate for both electrons and holes and has an almost cylindrically symmetric form, see Figure 6.5 on page 67. In the following we denote these states as the *s*-states. The two first excited states are oriented preferentially in *x*- and *y*-direction, respectively, see again Figure 6.5 on page 67. As these two states are energetically degenerate, one is free

to choose linear combinations of these states and obtain eigenfunctions that make the symmetry properties of the wave function more transparent, compare Figure 7.6 on page 76. These two linear combinations are called p_+ and p_- and form the 'p-shell'. Due to the underlying wurtzite crystal symmetry the angular momentum is not a good quantum number and henceforth p_+, p_- cannot be identified with angular-momentum eigenstates $\propto e^{im\phi}$. Instead, they can be identified by their behavior under rotation around the growth direction by an angle of $\frac{2\pi}{3}$ as follows:

$$\begin{aligned} R|s\rangle &= |s\rangle, \\ R|p_+\rangle &= e^{+i\frac{2\pi}{3}}|p_+\rangle, \\ R|p_-\rangle &= e^{-i\frac{2\pi}{3}}|p_-\rangle. \end{aligned} \quad (8.1)$$

Note that in a system with full cylindrical symmetry the function with angular momentum z -component $0, +1, -1$ would show the same transformation behavior under this discrete rotation. This motivates the notion of the states having angular quasi-momentum $\lambda_z = 0, +1, -1$. The reader should be warned, however, that only λ_z modulo 3 and not λ_z itself is a good quantum number in a system with C_{3v} symmetry. Based on the angular quasi-momentum conservation, we deduced selection rules for the dipole matrix elements in Section 7.3 and for the Coulomb matrix elements in Section 7.4. For the latter we found some non-vanishing matrix elements that would be strictly zero in a system with $C_{\infty v}$ symmetry. However, the inspection of the numerically determined values revealed that angular momentum is approximately a good quantum number. This is due to the fact that the system is rotationally symmetric on a mesoscopic scale and the lower C_{3v} -symmetry becomes only apparent on the microscopic level.

Of greater impact are the new selection rules obtained for the dipole-matrix elements. For light polarization along the $(1, 1, 0)$ direction, one finds that only the matrix elements d_{s,p_\pm}^{eh} and $d_{p_\pm,s}^{eh}$ are important. This means for the QD discussed in Section 6.2 that neither the ground states nor the first excited states are connected by the optical field. Note that an effective mass approximation, which is oftentimes successfully applied in InGaAs systems and quite commonly carried over to nitride based systems [97–102], cannot explain these selection rules. To fully account for these selection rules a microscopic treatment using, for example, a TB model is needed. For qualitative arguments at least a two-component $\mathbf{k} \cdot \mathbf{p}$ treatment is necessary.

If we express the dipole Hamiltonian in terms of the interband polarization operator \mathcal{P} , as outlined in Chapter 1.3 in Part I, we find the following convenient splitting of the different contributions

$$\mathcal{P} = \mathcal{P}_{\text{low}} + \mathcal{P}_{\text{high}} ,$$

with

$$\begin{aligned} \mathcal{P}_{\text{high}} &= \sum_{\sigma} \left(d_{ps}^{eh} e_{p_+, \sigma} h_{s, -\sigma} + d_{ps}^{eh*} e_{p_-, \sigma} h_{s, -\sigma} \right), \\ \mathcal{P}_{\text{low}} &= \sum_{\sigma} \left(d_{sp}^{eh} e_{s, \sigma} h_{p_+, -\sigma} + d_{sp}^{eh*} e_{s, \sigma} h_{p_-, -\sigma} \right). \end{aligned} \quad (8.2)$$

As the energetic separation between s - and p -shell for the electrons is much larger than the spacing for holes, one may roughly characterize the transitions as high-energy or low-energy transitions according to the involved electron state. If an electron from the p -shell is dominantly involved in the transition, one obtains a high-energy transition, otherwise a transition on the low-energy side. To illustrate the possible transitions, Figure 8.1 displays the electron-hole pairs that can be removed by \mathcal{P}_{low} in the case of a four excitons configuration.

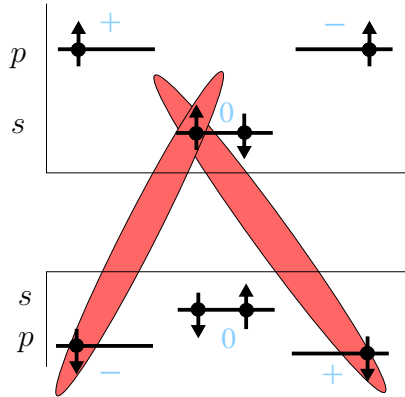


Figure 8.1: (color online) Typical configuration with four excitons in the small QD. The shaded red areas connect the electron-hole pair that can be removed by \mathcal{P}_{low} . The light blue labels 0, +, – refer to the angular quasi-momentum z -component of the single-particle states.

Exactly as in the case of the InGaAs QDs, we will restrict our analysis of the ground-state emission spectra to initial states with total spin z -component zero. By considering the two energetically lowest shells per carrier, a semi-analytic analysis is possible.

8.2 Excitonic and Biexcitonic Properties

In the following sections we analyze the absorption spectrum and the multi-exciton emission spectra for the QD of Section 6.2 in detail. To be able to distinguish between effects originating from the altered symmetry group of the QD from those additionally introduced by the internal electric fields, we will first present the results for a QD for which we artificially switch off the internal fields. Later, in a second step, we will analyze the influence of these fields on the multi-exciton spectra. In Section 8.7 we will then turn to larger QDs for which the energetic order of the two lowest hole shells is reversed in the presence of the internal electric fields. The consequences of this level reordering will be studied.

Absorption Spectra

The absorption spectrum of an initially empty nitride QD with two shells shows the two lines depicted in Figure 8.2, one at the high-energy side and one at the low-energy side. Qualitatively this is the same as in the case of the InGaAs system. In the nitride case, however, the transitions do not originate from 'diagonal' ss - and pp -excitons, but from 'skew' excitons, namely sp - and ps -excitons. Here an $\alpha\beta$ -exciton denotes an electron-hole pair, in which the electron has mainly α and the hole mainly β character. Because of the large energetic splitting between the s - and the p -shell of the electrons, the ps -excitonic transition is well separated from the sp transition. Without Coulomb interaction, these transition can be found at the sum of the single-particle energies $\varepsilon_p^e + \varepsilon_s^h$ and $\varepsilon_s^e + \varepsilon_p^h$, respectively.

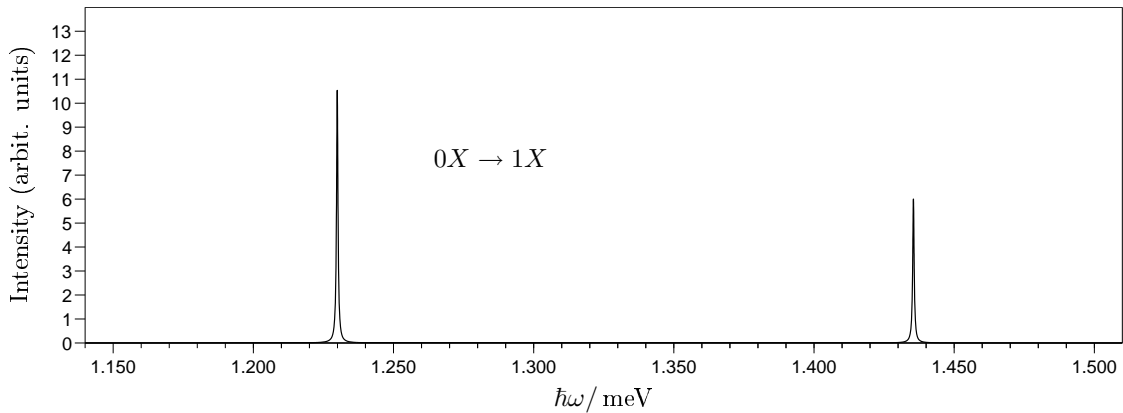


Figure 8.2: Absorption spectrum of the initially empty nitride QD with level structure schematically depicted in Figure 8.1. The high-energy side stems from a transition in which mainly the s -shell of the hole and the p -shell of the electrons becomes occupied. For the low-energy side, the s -shell of the electrons and the p -shell of the holes yield the main contribution.

To understand the impact of Coulomb correlation on the absorption spectrum, one needs to analyze how the different non-interacting states containing one exciton are mixed by the interaction. As the spin of the electrons and holes is separately a good quantum number, we can restrict the discussion to the subspace with $S_z^e = +\frac{1}{2}$ and $S_z^h = -\frac{1}{2}$. Furthermore, the vacuum state has a vanishing *total* angular quasi-momentum z -component, $\Lambda_z = 0$, which means that optical transitions are only possible to states with Λ_z modulo 3 = ± 1 . In the following we will consider only the subspace with Λ_z modulo 3 = +1. The results for Λ_z modulo 3 = -1 are obtained along the same lines. The former subspace contains the three states depicted in Figure 8.3. Even though only two of the states, namely $|\psi_a\rangle$ and $|\psi_b\rangle$, can be reached by the action of \mathcal{P}^\dagger on the vacuum state, one can expect to see three lines in absorption as all three states in Figure 8.3 are mixed by Coulomb interaction. In what follows we will call configurations that are connected with the initial state via the action of \mathcal{P}^\dagger 'bright' and

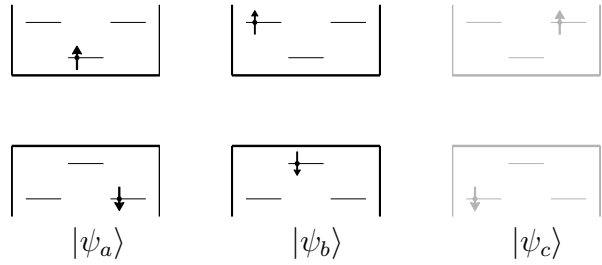


Figure 8.3: Configurations involved in the absorption spectrum. While the configurations $|\psi_a\rangle$ and $|\psi_b\rangle$ are bright, the dark configuration $|\psi_c\rangle$ (light grey) is mixed to them via Coulomb interaction. According to Eq. (8.1) the depicted states are characterized from left to right by $\Lambda_z = +1, +1$ and -2 .

those that are not connected 'dark'. In the basis depicted in Figure 8.3, the Hamiltonian has the form

$$\underline{\underline{H}} = \begin{pmatrix} \varepsilon_s^e + \varepsilon_p^h - D_{sp}^{eh} & V_{ss,-+}^{eh} & V_{s+,-}^{eh} \\ V_{ss,-+}^{eh} & \varepsilon_p^e + \varepsilon_s^h - D_{ps}^{eh} & V_{++s-}^{eh} \\ V_{s+,-}^{eh} & V_{++s-}^{eh} & \varepsilon_p^e + \varepsilon_p^h - D_{pp}^{eh} \end{pmatrix}. \quad (8.3)$$

Here V_{ijkl}^{eh} are the electron-hole Coulomb matrix elements as defined in Section 1.2 in Part I. In particular D_{ij}^{eh} denotes the direct interaction matrix element V_{ijji}^{eh} . For the present QD, the matrix elements $V_{s+,-}^{eh}$ and V_{++s-}^{eh} , which couple the bright $\Lambda_z = 1$ states with the dark $\Lambda_z = -2$ state, are quite small. Consequently the admixture of the bright states to the dark state is very weak so that $|\psi_c\rangle$ remains to a good approximation an eigenstate of the interacting Hamiltonian and the corresponding transition remains dark. As a consequence only the transitions stemming from the mixture of the two bright states $|\psi_a\rangle$ and $|\psi_b\rangle$, which couple as described by the upper left 2×2 block of the Hamiltonian matrix (8.3), will be observable in the absorption spectrum. That the mixture of the two subspaces with different angular quasi-momentum Λ_z is so small, is a consequence of the cylindrical symmetry of the system on a mesoscopic scale.

The interpretation of the multi-exciton spectra becomes more transparent if we neglect the small mixture of blocks with different angular quasi-momentum and assume for the following discussion that Λ_z itself and not Λ_z modulo 3 is conserved. In the case of strong confinement, in which the energy scale defined by the non-interacting energies dominates over the Coulomb interaction, the Hamiltonian matrix (8.3) approximately becomes diagonal and one finds the transitions at $\varepsilon_s^e + \varepsilon_p^h - D_{sp}^{eh}$ and $\varepsilon_p^e + \varepsilon_s^h - D_{ps}^{eh}$ with oscillator strengths $|d_{sp}^{eh}|^2$ and $|d_{ps}^{eh}|^2$ respectively.

Excitonic and Biexcitonic Emission

The excitonic and biexcitonic ground states are dominated by those configurations where all the carriers are in their energetically lowest shell. As a consequence of this and the fact that the dipole-matrix element d_{ss}^{eh} vanishes, the excitonic and biexcitonic emission remains dark for the small QD. As we will see in detail in Section 8.7, the energetic order of s - and the p -shell is reversed for the holes in larger QDs so that the ground state for the holes is p -like. This level reordering will lead to a bright exciton and biexciton state. However, the corresponding oscillator strengths are small. The dipole-matrix elements are strongly reduced, compared to those of the smaller dot, due to the strong spatial separation of the single-particle wave functions of electron and hole in the presence of the internal electric field [69, 115].

8.3 Configuration Interaction Results for Multi-Exciton Emission Spectra

After the analysis of the absorption spectrum of an empty QD and the discussion of the excitonic and biexcitonic ground state emission, we will investigate in the next sections the emission spectra for an initial filling with up to six excitons.

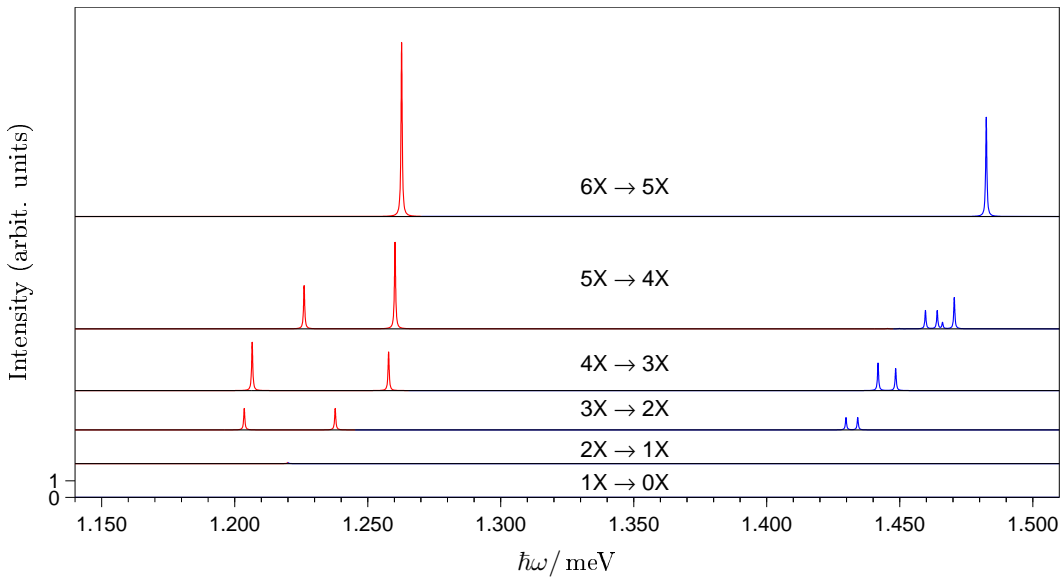


Figure 8.4: (color online) Ground state emission spectra for a QD with different number of excitons. The high-energy side is shown in blue, the low-energy side in red. For the studied system almost no ground state emission is observed for exciton and biexciton. As initial states the ground states with $S_z^{tot} = 0$ are chosen and the internal electric fields is switched off.

An overview of the resulting multi-exciton emission spectra is shown in Figure 8.4. As already explained, the excitonic and biexcitonic emission remains dark. Only for more than two excitons a clear signal can be observed because only then the p -shell for both the electrons and the holes is to a significant amount populated. And it is only then that an emission process involving the ‘skew’ excitons can take place. As mentioned earlier, the low- and high-energy side of the spectrum can be attributed, respectively, to processes where a p -hole or p -electron recombines. This is depicted in Figure 8.5. In contrast to the case analyzed in the first part of this thesis, the spectra

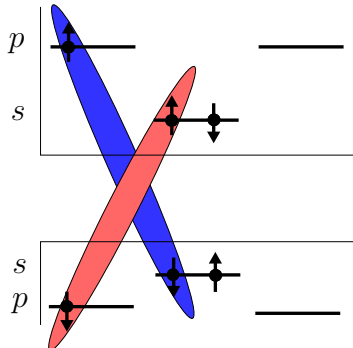


Figure 8.5: (color online) Schematic representation of one of the excitonic configuration involved in a three exciton state. The red and blue shaded areas connect the carriers that will lead to a emission at the low- and high-energy side of the spectrum, respectively.

show blue-shifts as the number of excitons is increased. As we will see in Section 8.6 these shifts become even more pronounced in the presence of the internal electric fields. As detailed in the next section, this feature can already be explained in terms of the diagonal Hamiltonian and the fact that the envelopes for the electrons and holes differ strongly. Another feature is striking: with the exception of the $5X \rightarrow 4X$ -emission spectrum all the spectra are rather symmetric if one compares the line structure of the low- and high-energy side. On the other hand, the oscillator strengths on the high-energy side are all weaker than the corresponding ones at the low-energy side. All these aspects will be addressed in the following.

8.4 Diagonal Approximation

As discussed in Chapter 3 in Part I an approximate description using a Hamiltonian that is diagonal in the free states can be motivated by inspecting the relative importance of the various Coulomb matrix elements. The eigenvalues of this approximate Hamiltonian are then the non-selfconsistent Hartree-Fock energies. This approximation

has successfully been used to describe the dominant trends in multi-exciton spectra in conventional III-V systems [46, 53, 54, 77].

In the absence of Coulomb interaction, one line at the high-energy side at $\varepsilon_p^e + \varepsilon_s^h$ and one at $\varepsilon_s^e + \varepsilon_p^h$ on the low-energy side would be observable in a ground state emission spectrum for an initial filling from three to six excitons. In the presence of Coulomb interaction, one observes instead of a single line at the low- and high-energy side two cluster of peaks, see Figure 8.4. These clusters blue-shift as the number of excitons is increased. The approximate position of the clusters can already be explained by considering only the diagonal elements of the Hamiltonian matrix. The major difference to the case of an InGaAs system assuming identical envelopes, which was analyzed in Part I, is that we clearly have non-identical envelopes for electrons and holes in the nitride system. This leads to additional interaction terms that would at least partly cancel in the case of identical envelopes. In the diagonal approximation, the transition energy $\Delta E_{A \rightarrow B}^{\text{diag}}$ from a many-particle configuration $|A\rangle$ to a configuration $|B\rangle$ is given by

$$\begin{aligned} \Delta E_{A \rightarrow B}^{\text{diag}} = & \varepsilon_{\bar{e}}^e + \varepsilon_{\bar{h}}^h - D_{\bar{e}\bar{h}}^{eh} + \sum_{i \neq \bar{e}, \bar{h}} (D_{\bar{e}i}^{ee} n_i^e - D_{\bar{e}i}^{eh} n_i^h - X_{\bar{e}i}^{ee} n_i^e) \\ & + \sum_{i \neq \bar{e}, \bar{h}} (D_{i\bar{h}}^{hh} n_i^h - D_{i\bar{h}}^{eh} n_i^e - X_{i\bar{h}}^{hh} n_i^h) . \end{aligned} \quad (8.4)$$

Here \bar{e} and \bar{h} denote, respectively, the single-particle states of the electrons and holes that are depopulated in the emission process. The index i runs over all single-particle states except the states \bar{e} and \bar{h} . The quantity $D_{ij}^{\lambda\lambda'}$ stands for the direct Coulomb matrix elements $V_{ijji}^{\lambda\lambda'}$, while the exchange Coulomb matrix elements $X_{ij}^{\lambda\lambda'}$ are given by $V_{ijij}^{\lambda\lambda'}$. Of course these exchange terms contribute only if the spin of \bar{e} or \bar{h} agrees with the electron or hole in state i . The first line of Eq. (8.4) contains the free particle energies $\varepsilon_{\bar{e}}^e$ and $\varepsilon_{\bar{h}}^h$ of the recombining carriers together with the attractive Coulomb interaction matrix element $-D_{\bar{e}\bar{h}}^{eh}$. Additionally, all terms that stem from the interaction of the electron in state \bar{e} with all the other electrons and holes have been grouped in the first line. Similarly the second line contains the interaction between the hole labeled with \bar{h} and all the other carriers. Explicitly, one obtains for the high-energy transition of the $3X$ configuration shown in Figure 8.5

$$E_{3X \rightarrow 2X}^{\text{diag}} = \varepsilon_p^e + \varepsilon_s^h - D_{ps}^{eh} - X_{sp}^{hh} - X_{sp}^{ee} + 2D_{sp}^{ee} - D_{ps}^{eh} + D_{ps}^{hh} - D_{pp}^{eh} + D_{ss}^{hh} - 2D_{ss}^{eh} . \quad (8.5)$$

If identical envelopes for the electrons and holes are assumed, one can deduce from the above equation the expression $E_{3X \rightarrow 2X}^{\text{diag}} = \varepsilon_p^e + \varepsilon_s^h + D_{sp} - D_{pp} - D_{ss} - 2X_{sp}$. From this, it can be seen that there is, in addition to the Fock term, a further Hartree contribution that is not present in the cases studied in Part I. These additional contributions stem from the fact that the interband operator \mathcal{P} connects in the case of nitrides carriers from different shells.

Similarly, one finds from Eq. (8.4) for the ground state transitions on the high-energy side for more than three excitons:

$$\begin{aligned} E_{4X \rightarrow 3X}^{\text{diag}} &= E_{3X \rightarrow 2X}^{\text{diag}} + \Delta E_{\text{Hartree}} - X_{pp}^{ee} - X_{sp}^{hh}, \\ E_{5X \rightarrow 4X}^{\text{diag}} &= E_{4X \rightarrow 3X}^{\text{diag}} + \Delta E_{\text{Hartree}}, \\ E_{6X \rightarrow 5X}^{\text{diag}} &= E_{5X \rightarrow 4X}^{\text{diag}} + \Delta E_{\text{Hartree}}. \end{aligned} \quad (8.6)$$

Note that the Hartree-shift $\Delta E_{\text{Hartree}}$, defined by $(D_{pp}^{ee} - D_{pp}^{eh}) + (D_{ps}^{hh} - D_{ps}^{eh})$, would be zero for identical envelopes of electrons and holes. Note further that the matrix element X_{pp}^{ee} denotes $V_{p+p-p+p-}^{ee}$. The peaks obtained from the diagonal description gives the approximate position of the cluster calculated by the CI approach, see Figure 8.6. In particular the smaller shift of $4X$ spectrum relative to the $3X$ spectrum as compared to the shifts involving more excitons is well described in terms of the exchange matrix elements in the first line of Eq. (8.6). The transition energies of the low-energy side can be found by changing $e \leftrightarrow h$ in the above equation.

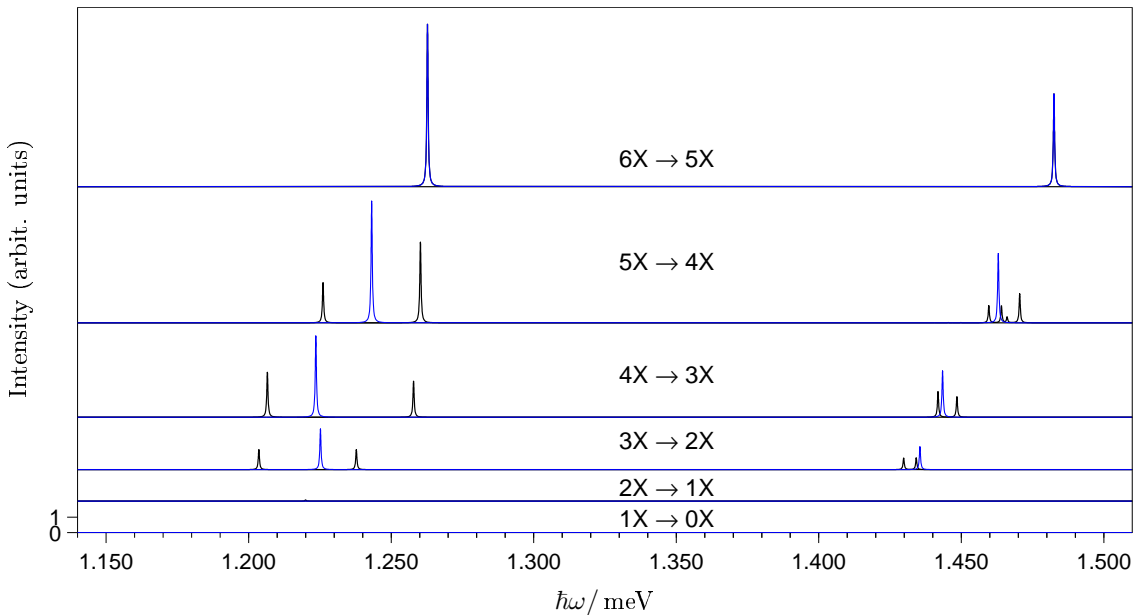


Figure 8.6: (color online) Comparison of ground state emission spectra of the QD using the CI-approach (black) and the diagonal Hamiltonian (blue). Where the full calculation gives a cluster of lines, the approximate result gives only single lines. Note that in the case of six excitons the two results practically coincide. All data are calculated in the absence of the piezo electric field.

While the central position of the clusters is well reproduced by the diagonal treatment, the splittings within each cluster are not explained. A thorough analysis of the states involved in the different emission processes shows that a semi-analytic description of the spectrum is possible. Such a description will be given in the following sections.

8.5 Semi-Analytic Discussion of the Multi-Exciton Spectra

In the case of the InGaAs system presented in Part I, the diagonal treatment was already sufficient to produce the major trends observed in the multi-exciton spectra. Therefore and because this system has been extensively investigated in the past, we did not present a semi-analytic treatment for this system. In the case of nitride QDs, however, optical spectra have only seldom been discussed and if so only with selection rules carried over from the InGaAs system [97, 98, 101]. Additionally, the diagonal treatment can reproduce only the overall position of the clusters, but is by no means sufficient to explain the multiplets. Therefore we will investigate in the following the different multi-exciton spectra in detail.

8.5.1 $3X \rightarrow 2X$ Emission Spectrum

In this section we analyze the ground state emission spectrum with an initial filling of three excitons. The corresponding spectrum is shown in Figure 8.7. It is dominated by two strong lines on the high- and on the low-energy side. The splitting on the low-energy side is considerably larger than the one on the high-energy side. Here we will analyze only the low-energy side, as the same line of argumentation applies to the high-energy side.

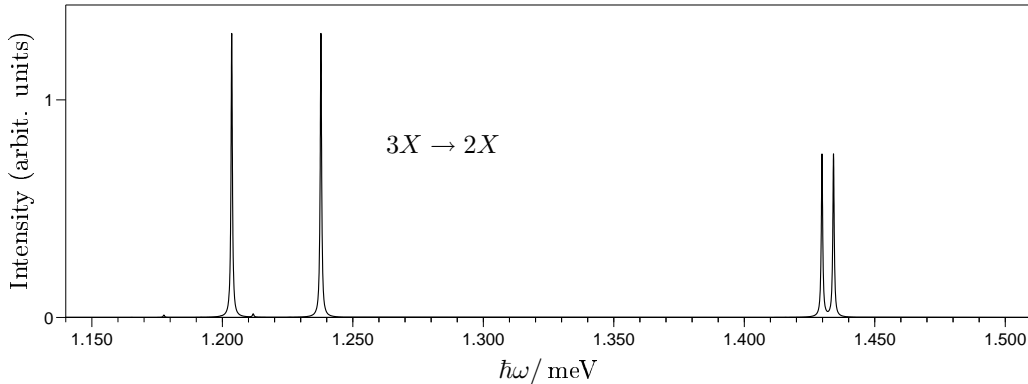


Figure 8.7: Ground state emission spectrum for an initial filling of three excitons. As initial states the ground states with $S_z^{tot} = 0$ are chosen.

Due to the spin symmetry we can again restrict ourselves to one of the two possible ground states. In Figure 8.8 the dominant contribution to the $3X$ ground state is shown. It contains the configuration $|A\rangle$ together with the configuration $|B\rangle$ that is obtained from $|A\rangle$ by moving the p -shell carriers simultaneously according to $p_+ \leftrightarrow p_-$. These two states enter the $3X$ -ground state with the same amplitude but opposite sign. Nevertheless, one can restrict the discussion to one part of the configuration.

This is due to two facts: (i) one can convince oneself that both $|A\rangle$ and $|B\rangle$ individually produce the same spectrum. (ii) The state $\mathcal{P}_{\text{low}}|A\rangle$ and $\mathcal{P}_{\text{low}}|B\rangle$ have different angular quasi-momentum Λ_z . Therefore the interference terms of the form $\langle 2X, i|\mathcal{P}_{\text{low}}|A\rangle\langle 2X, i|\mathcal{P}_{\text{low}}|B\rangle^*$, with $|2X, i\rangle$ being the i -th two exciton state, that occur in the expansion of $|\langle 2X, i|\mathcal{P}_{\text{low}}(|A\rangle + |B\rangle)|^2$ and reveals whether a certain transition is visible, are zero for any eigenstate $|2X, i\rangle$. Of course, the same line of arguments holds for $\mathcal{P}_{\text{high}}$.¹

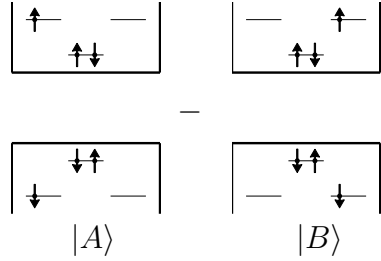


Figure 8.8: Dominant configuration of one out of two $3X$ ground states with $S_z^{\text{tot}} = 0$.

In Figure 8.9 configuration $|A\rangle$ is shown together with the $2X$ -configuration (in black) that can be reached via the action of \mathcal{P}_{low} . Note that the latter is not an eigenstate of the Hamiltonian. Instead it will be mixed with other states by Coulomb interaction. The predominant contribution to this mixture is shown in Figure 8.9 in light grey. Together these two states either form a spin triplet state for the electrons and a spin singlet state for the holes (ts) or a singlet-singlet (ss) state. These two states are split by the exchange Coulomb matrix element $2X_{sp}^{ee}$ and can both be observed in the spectrum. The oscillator strengths of the corresponding transitions are approximately equal since both final states contain the bright $2X$ -exciton state with the same probability amplitude. Along the same line one finds for the high-energy side an approximate splitting of $2X_{sp}^{hh}$. Both splittings are in good agreement with the CI result and explain the dominant peak structure in Figure 8.7. The ratio of the peak heights on the low- and the high-energy side is given by d_{sp}^{eh}/d_{ps}^{eh} . Additional tiny peaks, which the alert reader may have spotted in Figure 8.7, are caused by a extremely weak coupling of the bright state to other dark states.

8.5.2 $4X \rightarrow 3X$ Emission Spectrum

The $4X \rightarrow 3X$ ground state emission spectrum is depicted in Figure 8.10. As in the case of the $3X \rightarrow 2X$ emission discussed in the previous paragraph, the spectrum is

¹ Note that this argument holds only in the case of ‘skew’ excitons. If we denote the interband operator that removes ‘diagonal’ excitons with $\mathcal{P}_{\text{diag}}$, then we find that the states $\mathcal{P}_{\text{diag}}|A\rangle$ and $\mathcal{P}_{\text{diag}}|B\rangle$ have the same angular (quasi-)momentum z -component. Consequently the interference terms are important in the case of ‘diagonal’ excitons discussed in Part I.

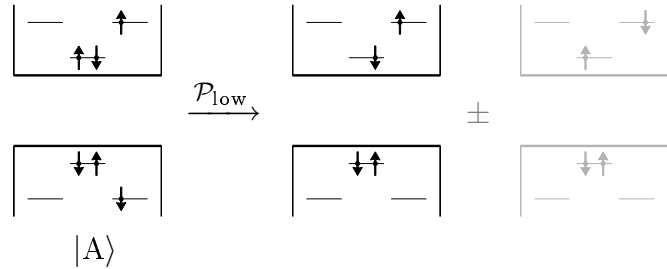


Figure 8.9: One part of the dominant configuration of the $3X$ -ground state together with the $2X$ configuration (in black) that is created by removing the sp -exciton via the action of \mathcal{P}_{low} . Additionally the most important dark configuration to which the bright $2X$ -state couples via Coulomb interaction is shown in light grey.

dominated by two lines at the low-energy side and two lines at the high-energy side. Again the splitting at the right side of the spectrum is larger than the corresponding one at the left side and the oscillator strengths on the low-energy side are again larger. However, the splitting between the lines on both sides is larger than in the case of $3X \rightarrow 2X$ emission.

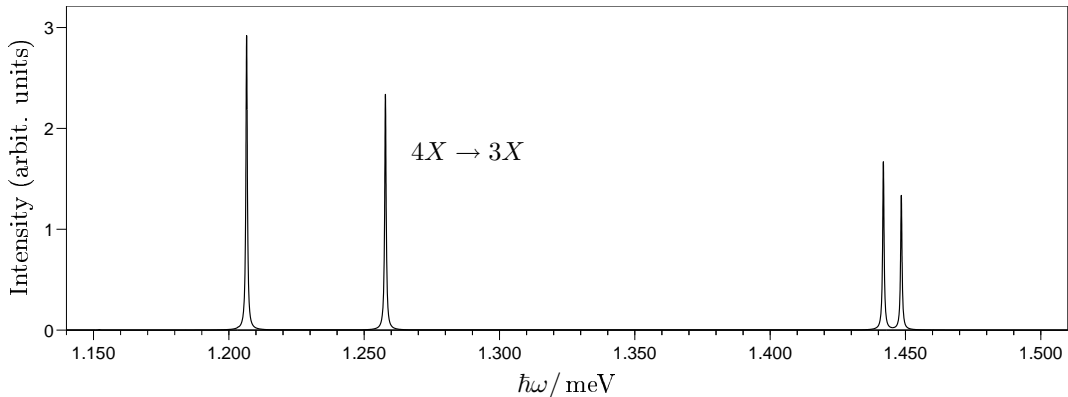


Figure 8.10: Ground state emission spectrum for an initial filling of four excitons. As initial states the ground states with $S_z^{\text{tot}} = 0$ are chosen.

There are three triplet-triplet $4X$ -ground states. One of them together with the $3X$ states connected via \mathcal{P}_{low} is depicted in Figure 8.11. The two $3X$ -states are not coupled to each other via Coulomb-interaction as they belong to subspaces characterized by the angular quasi-momentum quantum number $\Lambda_z = +1$ and $\Lambda_z = -1$, respectively. Therefore there are, not even modulo 3, within the same symmetry class. However, they will individually be coupled to other states with Λ_z modulo 3 = ± 1 , $S_z^e = +\frac{1}{2}$, $S_z^h = -\frac{1}{2}$. Picking the first $3X$ state of Figure 8.11 and additionally restricting ourselves to those states with the same non-interacting energy – which should give rise to the largest corrections – we find that the electrons mix with the two configurations depicted in Figure 8.12. In contrast, for the holes no mixing with other configuration having the

same non-interacting energy is possible because such states lie in a different symmetry class.

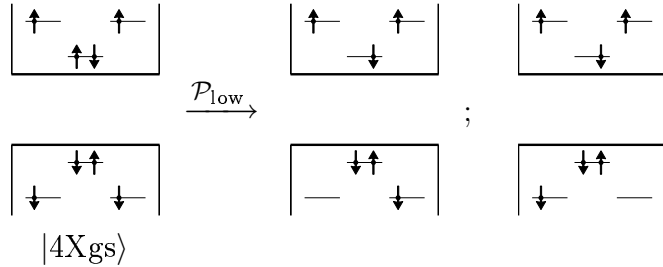


Figure 8.11: Dominant configuration of one of the three triplet-triplet $4X$ -ground states together with the $3X$ configurations that are created by removing a sp -exciton.

In writing down the Hamiltonian matrix $\underline{\underline{H}}$ that couples the uncorrelated states of Figure 8.12 involving only electrons, one finds:

$$\underline{\underline{H}} = E^{\text{diag}} \underline{\underline{1}} - \begin{bmatrix} X_{pp}^{ee} & X_{sp}^{ee} & X_{sp}^{ee} \\ X_{sp}^{ee} & X_{sp}^{ee} & X_{pp}^{ee} \\ X_{sp}^{ee} & X_{pp}^{ee} & X_{sp}^{ee} \end{bmatrix}. \quad (8.7)$$

Here E^{diag} denotes the diagonal contribution, which is the same for all the configurations. Diagonalization of the Hamiltonian matrix yields the eigenvectors and eigenvalues

$$\begin{aligned} E_\alpha &= E^{\text{diag}} - (X_{sp}^{ee} - X_{pp}^{ee}), & |\alpha\rangle &= (-2, 1, 1)^t, \\ E_\beta &= E^{\text{diag}} + (2X_{sp}^{ee} + X_{pp}^{ee}), & |\beta\rangle &= (1, 1, 1)^t, \\ E_\gamma &= E^{\text{diag}} + (X_{sp}^{ee} - X_{pp}^{ee}), & |\gamma\rangle &= (0, 1, -1)^t. \end{aligned} \quad (8.8)$$

The states $|\alpha\rangle$ and $|\beta\rangle$ contain the first configuration of Figure 8.12 – and therefore the final states depicted in Figure 8.11 – with a non-zero amplitude and can henceforth be seen in an emission spectrum. In contrast, the state $|\gamma\rangle$ will be dark as it does not contain any contribution of the ‘bright’ state. By applying the spin operator ($S^{\text{tot},e}$)² on these states, one can check that the state $|\alpha\rangle$ belongs to a doublet ($S^e = \frac{1}{2}$) and

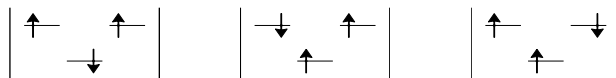


Figure 8.12: All three electronic configurations have the same non-interacting energy and the same symmetry Λ_z , S_z^e , and S_z^h . Consequently they will strongly be mixed via Coulomb interaction. Together with the hole configurations of Figure 8.11 they will form the final states of the $4X \rightarrow 3X$ transition.

the state $|\beta\rangle$ to a quadruplet ($S^e = \frac{3}{2}$). The estimated doublet-quadruplet splitting $E_\beta - E_\alpha$ is $3X_{pp}^{ee}$ and in good agreement with the values found by the CI approach. For the high-energy side one finds a doublet-quadruplet splitting of $3X_{pp}^{hh}$, which is much smaller than the $3X_{pp}^{ee}$ and explains the smaller line splitting on the high-energy side. Again, the ratio of the peak heights on the low- and the high-energy side is given by d_{sp}^{eh}/d_{ps}^{eh} . The peak heights within one cluster can be obtained by calculating the different contribution from the final states in Eq. (8.8) and a similar analysis for the other two possible ground states with $S_z^{\text{tot}} = 0$. Doing so, one obtains a ratio of 5 to 4 in good agreement with the full result.

8.5.3 $5X \rightarrow 4X$ Emission Spectrum

In this section we present details of the emission spectrum shown in Figure 8.13 of a nitride QD with initial filling with $5X$. As it turns out this spectrum is the most complicated one. This is due to the fact that the splittings cannot be described to a good approximation in terms of an integer multiple of some exchange matrix element as it was the case for three or four excitons. Instead the splittings and oscillator strength are determined by a subtle interplay of quite different configurations and henceforth Coulomb matrix elements.

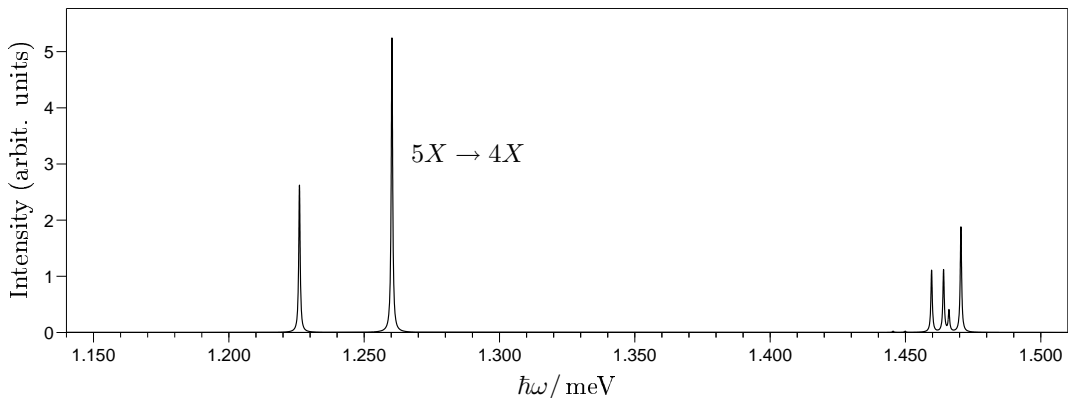


Figure 8.13: Ground state emission spectrum for an initial filling of five excitons. As initial states the ground states with $S_z^{\text{tot}} = 0$ are chosen.

A striking difference to all the other multi-exciton spectra is the fact that in the present case there is a strong asymmetry between the left and right side of the spectrum shown in Figure 8.13. In order to explain this, let us have a closer look at the configurations involved. To simplify the analysis, we assume full angular momentum conservation. As the initial $5X$ ground state depicted in Figure 8.14 has in this approximation angular momentum $l_z^{\text{tot}} = 0$ and $S_z^{\text{tot}} = 0$, the final states will have angular momentum ± 1 . Picking one of them, namely, $l_z^{\text{tot}} = -1$, one finds for the final $4X$ states a 16×16 block with $S_z^e = 0$ and $S_z^h = 0$. However, for the high-energy side, the main contribution

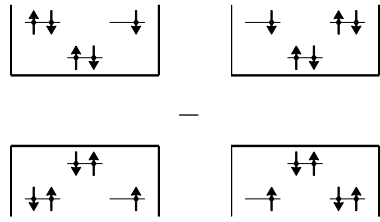


Figure 8.14: Dominant ground state configuration for five excitons with $S_z^{tot} = 0$. By flipping all spins a second, degenerate ground state is produced.

stems from the 6×6 block generated by the configurations schematically represented in Figure 8.15. These states have the lowest non-interacting energy amongst those states that can be reached by a removal of one ps -exciton from the configurations shown in Figure 8.14. Their electronic configuration is given by $2e_s 2e_p 1h_s 3h_p$. A similar block with configurations $1e_s 3e_p 2h_s 2h_p$ is found for the low-energy transitions. Due to this symmetry one would expect the same number of lines on the high- and on the low-energy side of the spectrum. Note that the expectation of a symmetric peak structure on the high- and low-energy side of the spectrum is fulfilled for all but the $5X \rightarrow 4X$ transitions, compare Figure 8.4 on page 88.

By combining the first four states in Figure 8.15 properly, one can form ss, st, ts and tt spin states. Here the first letter denotes the electron, the second the hole configuration and s stands for a singlet and t denotes a triplet spin state. The last two states in Figure 8.15 allow the formation of a st and ss state. While the electrons of the first four states always occupy both p_+ and p_- they occupy only the p_- state in the last two configurations. Therefore one expects that the energy of the ss state formed by

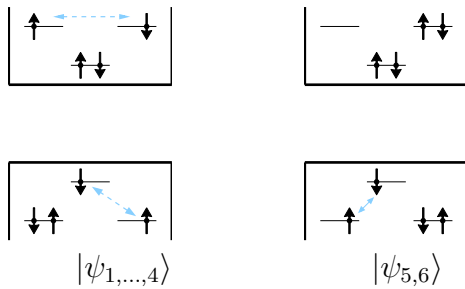


Figure 8.15: (color online) Main contribution to the final states of the high-energy side of the $5X \rightarrow 4X$ transition with classification $S_z^{tot} = 0$ and, assuming full angular momentum conservation, $l_z^{tot} = 0$. The arrow between electrons or holes indicates that additional states can be derived from the displayed configuration by flipping the spins of the connected carriers simultaneously. This way one can create four different states from the first configuration and two from the second one.

the states ψ_1 to ψ_4 differs from the energy of the eigenstate created by combining ψ_5 and ψ_6 . By the same token one expects two different energies for the st -states. So all in all six different energies are expected. On the high energy side of the spectrum four lines are clearly visible and another two can be identified with the eye of love on the left side of the cluster. For the low-energy side, however, only two lines can be observed.

To obtain further insight into the situation, we construct the Hamiltonian matrix \underline{H} using the basis $\{|\psi_i\rangle\}_{i=1}^6$ of Figure 8.15:

$$\underline{H} = E^{\text{diag}} \underline{1} + \begin{bmatrix} 0 & -X_{sp}^{hh} & -X_{pp}^{ee} & 0 & X_{pp}^{eh} & 0 \\ -X_{sp}^{hh} & 0 & 0 & -X_{pp}^{ee} & 0 & X_{pp}^{eh} \\ -X_{pp}^{ee} & 0 & 0 & -X_{sp}^{hh} & -X_{pp}^{eh} & 0 \\ 0 & -X_{pp}^{ee} & -X_{sp}^{hh} & 0 & 0 & -X_{pp}^{eh} \\ X_{pp}^{eh} & 0 & -X_{pp}^{eh} & 0 & 0 & -X_{sp}^{hh} \\ 0 & X_{pp}^{eh} & 0 & -X_{pp}^{eh} & -X_{sp}^{hh} & 0 \end{bmatrix}. \quad (8.9)$$

Here, E^{diag} denotes the diagonal contribution that is identical for all configurations and is given by

$$E^{\text{diag}} = 2(\varepsilon_s^e + \varepsilon_p^e) + \varepsilon_s^h + 3\varepsilon_p^h + (D_{ss}^{ee} + D_{pp}^{ee} + 4D_{sp}^{ee} - 2X_{sp}^{ee}) + (3D_{sp}^{hh} + 3D_{pp}^{hh} - X_{sp}^{hh} - X_{pp}^{hh}) - (2D_{ss}^{eh} + 6D_{sp}^{eh} + 2D_{ps}^{eh} + 6D_{pp}^{eh}) . \quad (8.10)$$

The Hamiltonian matrix as given in Eq. (8.9) can be block-diagonalized by choosing the proper linear combinations that correspond to the spin eigenstates. This is possible as the Hamiltonian commutes individually with the total spin of both electrons and holes as discussed in Appendix B. To this end one collects the coefficients of the linear combinations that transform the basis states $\{|\psi_i\rangle\}_{i=1}^6$ into spin-eigenstates, namely, ts, ss, ss, st, st, and tt, in the columns of the transformation matrix \underline{U} :

$$\underline{U} = \begin{bmatrix} -\frac{1}{2} & 0 & -\frac{1}{2} & -\frac{1}{2} & 0 & \frac{1}{2} \\ \frac{1}{2} & 0 & \frac{1}{2} & -\frac{1}{2} & 0 & \frac{1}{2} \\ -\frac{1}{2} & 0 & \frac{1}{2} & \frac{1}{2} & 0 & \frac{1}{2} \\ \frac{1}{2} & 0 & -\frac{1}{2} & \frac{1}{2} & 0 & \frac{1}{2} \\ 0 & -\frac{1}{\sqrt{2}} & 0 & 0 & \frac{1}{\sqrt{2}} & 0 \\ 0 & \frac{1}{\sqrt{2}} & 0 & 0 & \frac{1}{\sqrt{2}} & 0 \end{bmatrix}.$$

By performing the change of basis according to $\underline{U}^\dagger \underline{H} \underline{U}$ one finds for the Hamiltonian \underline{H}

$$\begin{bmatrix} X_{sp}^{hh} - X_{pp}^{ee} & 0 & 0 & 0 & 0 & 0 \\ 0 & X_{sp}^{hh} & \sqrt{2}X_{pp}^{eh} & 0 & 0 & 0 \\ 0 & \sqrt{2}X_{pp}^{eh} & X_{sp}^{hh} + X_{pp}^{ee} & 0 & 0 & 0 \\ 0 & 0 & 0 & -X_{sp}^{hh} + X_{pp}^{ee} & -\sqrt{2}X_{pp}^{eh} & 0 \\ 0 & 0 & 0 & -\sqrt{2}X_{pp}^{eh} & -X_{sp}^{hh} & 0 \\ 0 & 0 & 0 & 0 & 0 & -X_{sp}^{hh} - X_{pp}^{ee} \end{bmatrix}.$$

The resulting blocks have the classification ts, ss, st, and tt, respectively. In order to further analyze the blocks, we introduce the two dimensionless parameters $t = 2\sqrt{2}X_{pp}^{eh}/X_{pp}^{ee}$ and $\tilde{t} = X_{sp}^{hh}/X_{pp}^{ee}$. Furthermore, we measure all energies in units of X_{pp}^{ee} relative to $E^{\text{diag}} + \tilde{t} + \frac{1}{2}$. This way one obtains for the four subblocks:

$$H_{ts} = -\frac{3}{2}, \quad \underline{H}_{ss} = \frac{1}{2} \begin{pmatrix} -1 & t \\ t & 1 \end{pmatrix},$$

$$\underline{H}_{st} = -2\tilde{t}\underline{1} - \underline{H}_{ss}, \quad H_{tt} = -2\tilde{t} - \frac{3}{2},$$

with the six eigenvalues $E_{ts} = -\frac{3}{2}$, $E_{ss} = \pm\frac{1}{2}\sqrt{1+t^2}$, $E_{st} - 2\tilde{t} \mp \frac{1}{2}\sqrt{1+t^2}$, and $E_{tt} - 2\tilde{t} - \frac{3}{2}$. From these expression one can read off that the st and tt spectrum is in dimensionless units shifted by $-2\tilde{t}$ relative to the ss and ts spectrum, respectively. In Figure 8.16 the six different eigenvalues as a function of t are shown for a fixed value of $\tilde{t} \approx 0.47$, which corresponds to the value of \tilde{t} obtained from the numerically determined Coulomb matrix elements. It is clearly evident that one has either six, five or four different energies. Only four different eigenvalues exist for $t = 2\sqrt{2}$ or, equivalently, $X_{pp}^{eh} = X_{pp}^{hh}$.

In order to obtain the corresponding oscillator strength of the transitions, one has to calculate the transition matrix elements $\langle 4X, i | \mathcal{P}_{\text{high}} | 5X, \text{gs}_j \rangle$, where $|4X, i\rangle$ denotes the i -th eigenstate of the four exciton problem and $|5X, \text{gs}_j\rangle$ labels the different ground states of the five exciton problem. Note, that each $5X$ ground state couples only to two of the six states $\{|\psi_i\rangle\}_{i=1}^6$ depicted in Figure 8.15:

$$\mathcal{P}_{\text{high}} |5X, \text{gs}_1\rangle \propto d_{ps}^{eh} |\psi_1\rangle + d_{ps}^{eh} |\psi_5\rangle + \text{other states not within } 6 \times 6 \text{ block},$$

$$\mathcal{P}_{\text{high}} |5X, \text{gs}_2\rangle \propto d_{ps}^{eh} |\psi_4\rangle - d_{ps}^{eh} |\psi_6\rangle + \text{other states not within } 6 \times 6 \text{ block}. \quad (8.11)$$

While within the one-dimensional subspaces of the ts- and tt-transition the oscillator strength does not depend on the parameter t , the heights of the ss- and st-lines depend

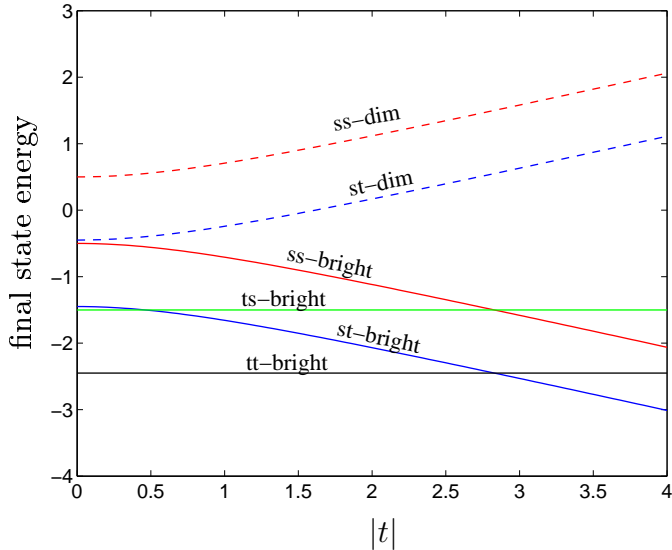


Figure 8.16: (color online) Energies of the final states involved in the high-energy transition, measured in units of X_{pp}^{ee} relative to $E^{\text{diag}} + \tilde{t} + \frac{1}{2}$, as a function of the dimensionless parameter $t = 2\sqrt{2}X_{pp}^{eh}/X_{pp}^{ee}$ for fixed $\tilde{t} \approx 0.47$. The labeling refers to the spin configuration of the final states and whether the states are 'bright' or 'dim'.

strongly on t . Denoting the eigenstates of H_{ss} with $(\alpha_i, \beta_i)^t$ the oscillator strength of the ss transition is given by

$$\text{Osc} = |d_{ps}^{eh}|^2 \left| \frac{\alpha_i}{\sqrt{2}} + \frac{\beta_i}{2} \right|^2. \quad (8.12)$$

In order to see this, one can use the expansion of $|4X, ss\rangle = \alpha_i |\tilde{\psi}_2\rangle + \beta_i |\tilde{\psi}_3\rangle$ in terms of the original basis $\{|\psi_i\rangle\}_{i=1}^6$. This expansion is given by $|4X, ss\rangle = \alpha_i \sum_j |\psi_j\rangle U_{j,2} + \beta_i \sum_j |\psi_j\rangle U_{j,3}$. Now one can investigate how the oscillator strength changes as a function of the dimensionless parameter t . The result is shown in Figure 8.17.

A similar analysis can be performed for the *st* transition. In this case one finds

$$\text{Osc} = |d_{ps}^{eh}|^2 \left| \frac{\alpha_i}{2} - \frac{\beta_i}{\sqrt{2}} \right|^2 \quad (8.13)$$

for the oscillator strength. As H_{ss} and H_{st} have the same eigenvectors and if $v = (\alpha, \beta)^t$ is an eigenvector, so is $v' = (-\beta, \alpha)^t$, one finds for the *st*-transitions again the dependency of the oscillator strength shown in Figure 8.17. For the analysis of the low-energy cluster, only the labels $e \leftrightarrow h$ have to be changed in all the derived equations.

For the parameters of the investigated dot one obtains $t \approx -1.23$ for the high-energy side and $t \approx -2.83$ for the low energy side. This, together with Figure 8.17, explains

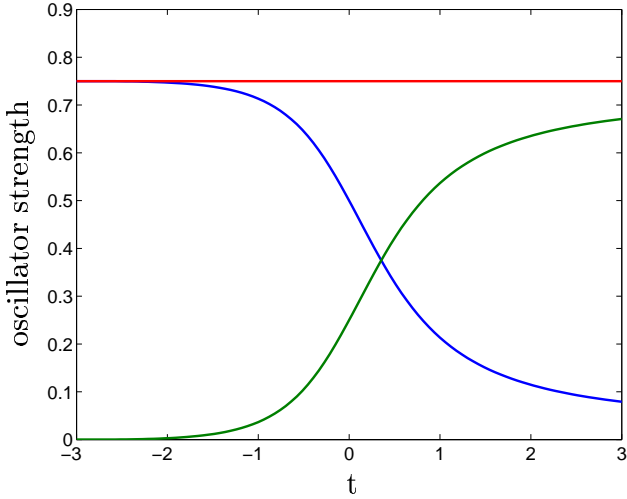


Figure 8.17: (color online) Oscillator strength (shown in green and blue) of the two ss transitions as a function of the dimensionless parameter t . A clear redistribution of oscillator strength from one to the other transition is visible. The total oscillator strength (red), however, remains unchanged. Note that one obtains $t < 0$ for the investigated dots. For $t < -2$ the spectrum is dominated by one of the two lines.

why it is possible to discern two ss as well as two st transitions in the high-energy cluster, but only one ss and one ts transition in the low-energy cluster of the $5X \rightarrow 4X$ spectrum depicted in Figure 8.13. Since furthermore $X_{pp}^{eh} \approx X_{pp}^{ee}$, the transitions ss and st as well as ts and tt have almost identical transition energies on the left-hand side of the spectrum. As a consequence, only two distinct lines can be observed on the low-energy side of the spectrum but six lines on the high-energy side.

8.5.4 $6X \rightarrow 5X$ Emission Spectrum

In the case of two shells, the QD is completely filled with six excitons and there is only one ground state possible. By removing one sp -exciton or one ps -exciton from this configuration, we find that the possible final states are exactly those shown in Figure 8.3 on page 87 for the $0X \rightarrow 1X$ transitions, only that the occupied sites in the $0X \rightarrow 1X$ problem are now the unoccupied ones. This analogy may be carried further by defining a new vacuum state in which the dot is completely filled and noting that the emission, that is the destruction of an electron-hole pair, is then equivalent to a creation of an electron-hole pair from this new vacuum. This corresponds to the introduction of new quasi-particles, namely an 'anti-electron' and an 'anti-hole' [43]. In doing so, one obtains a matrix similar to Eq. (8.3) and can follow the arguments given in Section 8.2. Therefore the $6X \rightarrow 5X$ emission spectrum is very similar to the $0X \rightarrow 1X$ absorption spectrum, with the main difference being that the lines are shifted due to the interaction with the 'background' carriers.

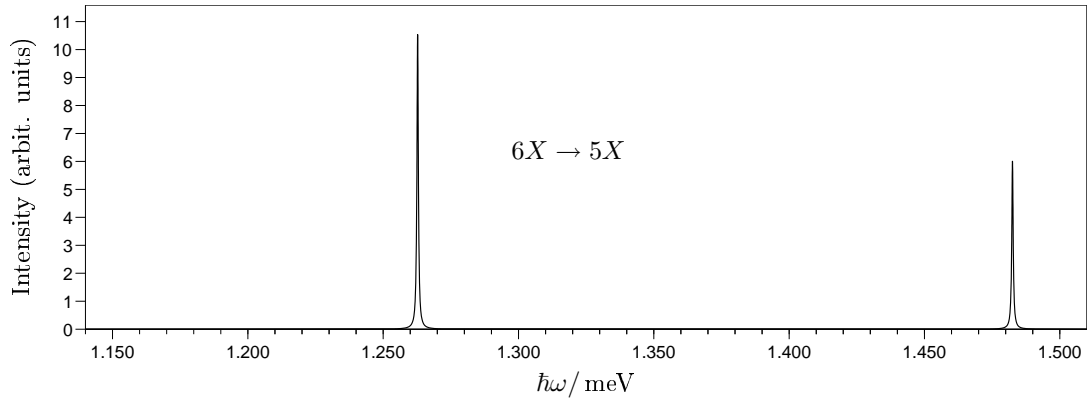


Figure 8.18: Ground state emission spectrum for an initial filling of six excitons.

8.6 Influence of the Built-In Fields

So far we have investigated a nitride QD for which we artificially switched off the internal electric fields. This allowed for a step-by-step analysis instead of analyzing all the effects at once. In this section, we investigate how these built-in fields influence the multi-exciton spectra.

The nitride QDs considered here are characterized by the presence of strong internal electrostatic fields. These fields have a component stemming from the spontaneous polarization and a part generated by strain as outlined in Section 6.2. If these fields are now included in the calculation of the single-particle properties, the electron and hole wave functions are spatially separated from each other. This leads to a reduction of the oscillator strength [69, 99, 103]. Furthermore the single-particle gap and the Coulomb matrix elements are altered. The resulting multi-exciton spectra (red) in comparison to the spectra calculated without the inclusion of the built-in fields (black) are shown in Figure 8.19.

Several features are immediately obvious. First of all the aforementioned reduction of the oscillator strength and the change of the single-particle gap that yields an overall red-shift of the spectra and is known as the quantum confined Stark effect. Furthermore the energetic shift as the number of excitons is increased is by far more pronounced in the presence of the internal fields. This is due to the strong separation of the electron and hole wave functions that is accompanied by strong Hartree-shifts in the spectrum. Indeed, if the diagonal approximation is applied as outlined in Section 8.4, one obtains again the position of the cluster to a good approximation. Another difference can be observed in the $5X \rightarrow 4X$ spectrum. In this situation the number of observable lines with the intrinsic field differs from the number observed without the field. Taking into account that for all other excitonic populations the spectra are only altered quantitatively this is a rather surprising result. But it is resolved by noting that the situation

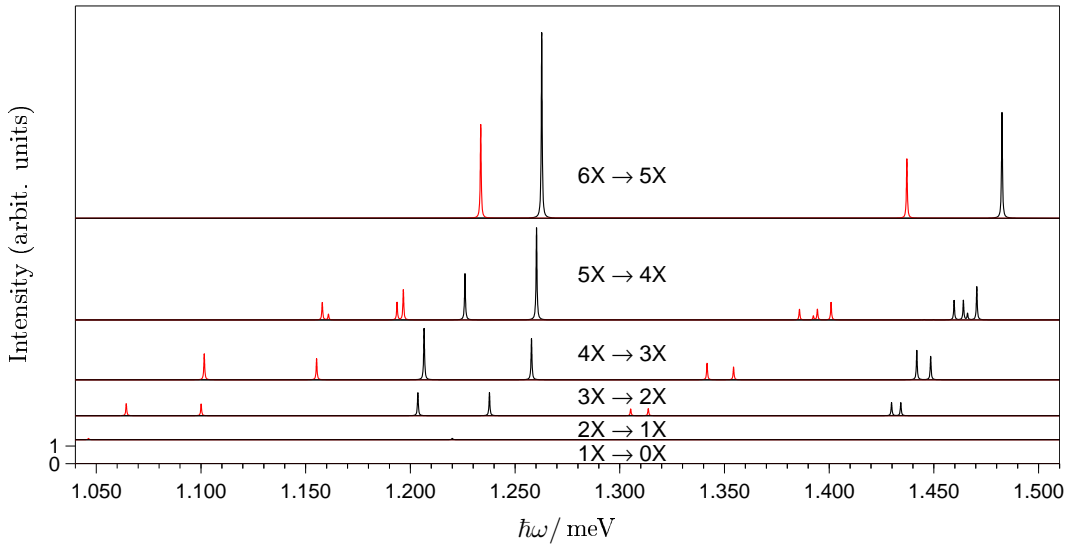


Figure 8.19:(color online) Comparison of the ground state emission with (red) and without (black) the inclusion of the internal fields for different number of excitons. For the studied system almost no ground state emission is observed for the exciton and biexciton. For all spectra the ground states with $S_z^{tot} = 0$ are chosen as initial states.

without the intrinsic field is rather special as $X_{pp}^{eh} \approx X_{pp}^{ee}$. In the present case there is a significant deviation of the two matrix elements and henceforth a clear splitting of the previously almost degenerate lines is observed.

8.7 Multi-Exciton Emission for a Larger Quantum Dot

In addition to the small QD discussed so far, we have investigated a somewhat larger QD with a diameter of $d = 5.7$ nm and height of $h = 2.3$ nm. In this case the energetic order of the two energetically lowest hole levels is reversed due to the presence of the internal electrostatic fields. In the absence of the built-in field, one still has the ‘usual’ order with the s -shell being lower in energy followed by the energetically higher p -shell. In this case the spectrum looks similar to those presented in the preceding sections of this chapter and is here therefore omitted. In the presence of the built-in field the two-fold degenerate p -shell constitute the hole ground states and has non-vanishing dipole matrix elements with the electron ground state. This is in agreement with recent $\mathbf{k} \cdot \mathbf{p}$ calculations [105] and experimental results for CdSe QDs [127] grown in the wurtzite phase. As an immediate consequence the excitonic and biexcitonic ground state is bright. However, the corresponding d_{sp}^{eh} dipole-matrix elements are strongly reduced in comparison with the smaller QD due to the stronger separation of the electron and

hole wave function in this enlarged structure. A schematic representation of the level-structure and electron-hole pairs typical involved in high- and low-energy transitions is depicted in Figure 8.20.

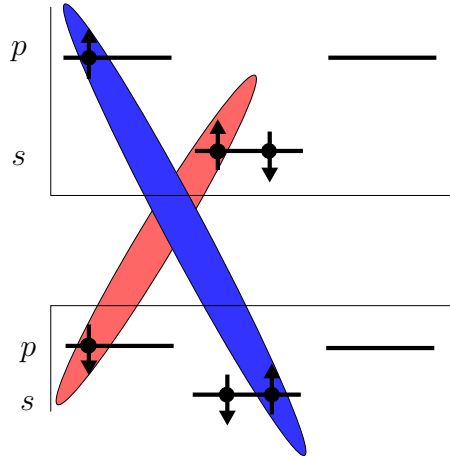


Figure 8.20: (color online) Schematic representation of a three exciton configuration. The red and blue shaded areas connect the carriers that will lead to a emission at the low- and high-energy side of the spectrum, respectively.

Equipped with the knowledge gained from the smaller QD, one can try to figure out what the spectrum should look like in this case: In the absence of Coulomb interaction one line at $\varepsilon_s^e + \varepsilon_p^h$ for a filling from one to four excitons and an additional line at $\varepsilon_p^e + \varepsilon_s^h$ for more than four excitons is expected. Furthermore, one anticipates that the oscillator strength on the low-energy side will increase linearly as the number of excitons is increased from one to four. Such an increase is expected as the number of decay channels grows linearly with the population. Including Coulomb interaction there should be strong Hartree shifts of the lines and additionally a splitting of the lines into clusters. If this expectation is compared to the spectra actually calculated, strong deviations can be observed in Figure 8.21. First of all the high-energy transitions (blue) appear already in a QD containing three excitons. Furthermore the oscillator strength of the biexciton is approximately equal to the excitonic emission and not enhanced by roughly a factor of two as expected. How can we understand these strong deviations? The answer is that our intuition once more failed in the nitride system. The ground states are by no means given by those states with lowest non-interacting energy as we anticipated in our first guess. Instead, one finds that the energetically higher hole s -shell is significantly populated if more than one electron-hole pair is present in the QD.

In a free particle picture the energies of the $2X$ states $|a\rangle$, $|b\rangle$, $|c\rangle$, and $|d\rangle$ schematically depicted in Figure 8.22 obey $E_a = E_b < E_c < E_d$. With Coulomb interaction one would expect the state $|a\rangle$ to participate strongly in the ground state as it can lower its energy

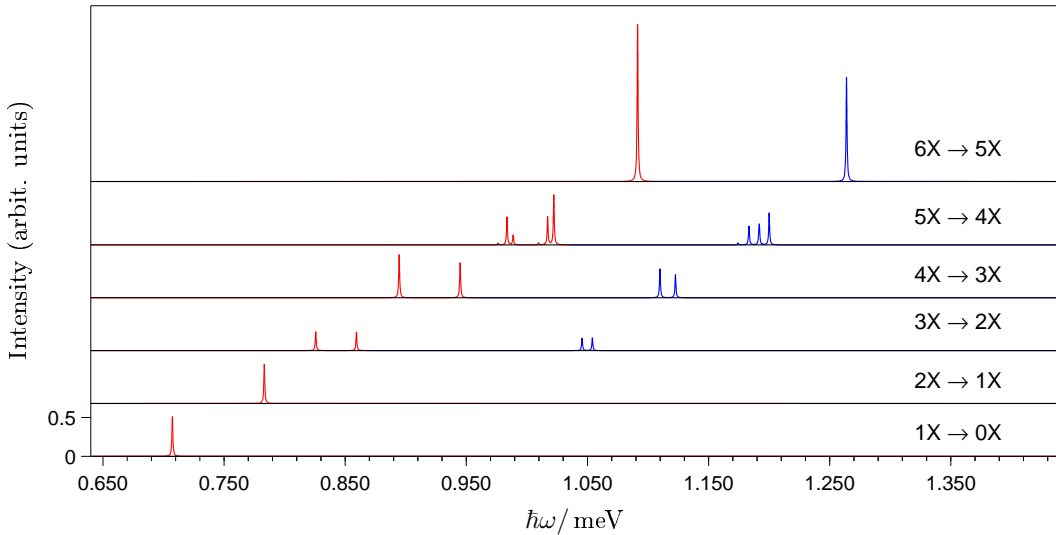


Figure 8.21: (color online) Ground state emission spectra for a larger QD ($d = 5.7\text{ nm}$ and $h = 2.3\text{ nm}$) with different number of excitons and in the presence of the internal fields. The high-energy side is shown in blue, the low-energy side in red. Due to the reversed level structure for the holes a ground state emission is observed for exciton and biexciton. As initial states the ground states with $S_z^{tot} = 0$ are chosen.

in a linear combination with the state $|a'\rangle$, in which all the spins are flipped. However configuration $|c\rangle$ constitutes the main contribution to the ground state. This is already confirmed by a calculation that contains only the Hartree Coulomb terms. This is the case, because the attraction between the electron and hole being in their respective s -shells is stronger than the attraction in the case of s - and p -shell carriers. Therefore it compensates the higher single-particle energy of the hole in the s -shell. An additional promotion of the other hole, leading to state $|d\rangle$, however, is not favored because the increase in energy due to the stronger repulsive interaction between the holes in their s -shell is higher than the energy reduction due to the stronger attraction between s -

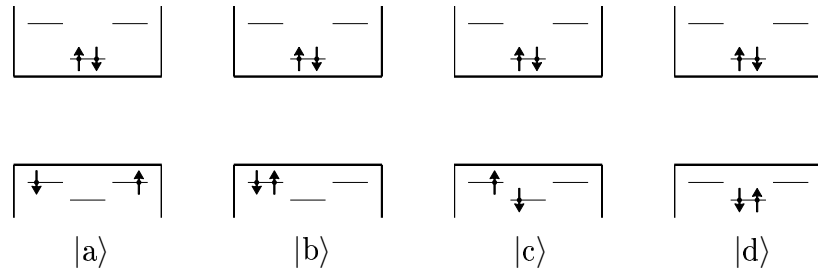


Figure 8.22: Different configurations containing two excitons. While one has $E_a = E_b < E_c < E_d$ in the absence of Coulomb interaction the configuration $|c\rangle$ is the dominant configuration in the presence of Coulomb interaction.

electrons and s -holes. The ground state configuration $|c\rangle$ explains why the oscillator strength of the exciton and biexciton emission are almost identical: no additional decay channel is opened by this configuration.

If one considers the three excitons configuration shown in Figure 8.23 one finds in the absence of Coulomb interaction $E_A < E_B < E_C$. But already by including only Hartree terms, it can be deduced along the lines discussed above that configuration $|C\rangle$ has the lowest energy and therefore constitutes the dominant part of the ground state in a CI calculation.

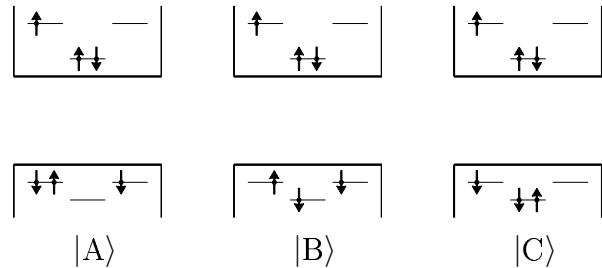


Figure 8.23: Different configurations containing three excitons. While one has $E_A < E_B < E_C$ in the absence of Coulomb interaction the configuration $|C\rangle$ is the dominant configuration in the presence of Coulomb interaction.

In summary, for the larger QD the multi-exciton spectra can be explained as follows: Due to the reversed energetic ordering of the two energetically lowest hole levels in the presence of the built-in field, a bright exciton ground state can be observed. In contrast to the intuitive picture in which first the configurations with lowest single-particle energy are occupied, a strong population of the hole s -shell for more than one exciton is found. In the case of the biexciton, no further decay channel is opened by the additional charge carriers in the system. Therefore the biexcitonic line has approximately the same oscillator strength as the excitonic one. From three excitons on, the ground states are dominated by configurations in which both the s -shell for electrons and the s -shell for holes are fully populated. As a consequence, one obtains qualitatively the same spectra as in the case of the smaller dot with the ‘normal’ energetic order of the shells. If it comes to numbers, however, one finds that the oscillator strengths are, as expected, strongly reduced in the larger system and that the Hartree shifts are even more pronounced.

In this chapter we presented a detailed analysis of the multi-exciton spectra in wurtzite InN/GaN QDs. We found strong differences compared to the more conventional InGaAs system discussed in Part I. In particular dark exciton and biexciton ground states for small, lens-shaped InN/GaN QD together with strong blue shifts for the higher multi-exciton spectra are predicted.

The next and final part of this thesis is devoted to the spontaneous emission *dynamics* of QDs embedded either in free space or in a microcavity. A central point will be the investigation of the influence of correlations on the spectrum and on the decay dynamics.

Part III

Semiconductor Luminescence Equations

Introduction to Part III

The influence of Coulomb-correlated multi-exciton states on optical spectra of QDs has been investigated by several groups [29, 43, 44, 47, 84] and was discussed in Part I of this thesis for InGaAs QDs and in Part II for nitride-based systems. Much less is known about the influence of correlations on the spontaneous recombination *dynamics*. By studying the photoluminescence (PL) dynamics in time-resolved measurements, it is often possible to distinguish between different types of decay channels. In particular one gains direct access to the efficiency of carrier scattering processes after optical excitation with short pulses, see, for example Ref. [128].

In analogy to the way in which the electronic states can be altered by carrier confinement, it is possible to modify the photonic density of states by confining the light field in all spatial directions in a microcavity [30]. By embedding the QDs in a microcavity it is possible to tailor the light-matter interaction. An enhanced light-matter coupling is achieved by a combination of good cavity design and the proper placement and spectral tuning of the emitters [31]. For the cavity, a high Q value together with a small mode volume is desired. To achieve maximal light-matter coupling, the emitter must be placed at the field maximum with its dipole parallel or anti-parallel to the local electromagnetic field. Furthermore, the transition energy of the emitter must match the cavity resonance for an optimal coupling of the two. The manipulation of the light-matter interaction is interesting both from an applied as well as from a fundamental point of view. At first, experiments, in which the modification of the interaction between a light emitter and the optical field was achieved, were limited to Rydberg atoms in microwave cavities [129]. Only in the last few years it became possible to access the realm of cavity quantum electrodynamics with solid-state devices. These experiments can be divided into two categories: the weak- and the strong-coupling regime. The latter is characterized by a reversible transition of energy from the cavity mode to the emitter. This strong-coupling regime was realized approximately two years ago for the first time in a solid-state device by coupling a QD emitter to a micropillar cavity [32], a photonic crystal defect cavity [33], or a microdisk [34]. In contrast, the weak coupling regime manifests itself in a modification of the spontaneous emission rate [35–37], the so-called ‘Purcell effect’. The altered spontaneous emission dynamics of QDs has been demonstrated using different resonator types, such as microdisk structures [130], patterned cavity pillars [38, 131] or photonic crystal defects [132]. A strong enhancement of the spontaneous decay is needed for many opto-electronic devices, like high-speed LEDs with improved output coupling, in which the switching time between ‘on’ and

‘off’ is – in the ideal case – only limited by the carrier relaxation time into the QD [38]. Furthermore larger Purcell factors are crucial for increasing the so-called β -factor – a key parameter in the quest for a reduced laser threshold and ultimately for thresholdless lasing [133]. On the other hand, a suppression of spontaneous emission is desired in some quantum-computational applications, in which the carriers must be trapped for a long time.

The experimental verification of the Purcell effect requires time-resolved PL measurements. In order to extract a spontaneous emission lifetime from such experiments, it became a standard to use the exponential decay known from two-level emitters and to carry it over to a QD system in order to quantify the emission dynamics and in particular the Purcell effect. A closer inspection of the literature reveals, however, that in many cases a non-exponential decay of the time-resolved PL is observed for a wide variety of QD resonator systems [37, 134, 135] and even for QDs without optical cavities [136–138]. This complicates the quantification of the altered spontaneous emission in terms of a constant decay time. In a cooperation with Matthias Schwab et al. in the group of Prof. Manfred Bayer at the University of Dortmund and with Mohamed Benyoucef in the group of Prof. Peter Michler in Stuttgart we investigated the PL of self-assembled InGaAs/GaAs QDs embedded in GaAs-based micropillars [139]. In their experiments, one finds, in addition to the non-exponential character, a strong dependence of the time-resolved PL decay on the excitation intensity: Starting from the weakest possible pumping, which allows to detect the PL and is well below the laser threshold, up to the threshold, the decay rate continuously increases [139]. These two effects make it impossible to assign a single decay time in terms of a two-level atom.

On the theoretical level, semiconductor QDs with dimensions of only a few nanometers have in the past often been described as ‘artificial atoms’ and modeled by two-level atoms. Clearly a two-level atom is by no means sufficient to capture the complicated structure of the multi-exciton spectra analyzed in Part I and II of this thesis. Furthermore, the carrier *dynamics* is in the existing literature often discussed in terms of two-level systems and excitons, i.e., fully correlated electron-hole pairs. However, such a simplified picture should be treated with care since the elementary quasi-particles in semiconductors are electrons and holes. The degree of correlations depends on the many-body Coulomb interaction and on the carrier-photon interaction. A microscopical description is rather challenging, because it requires not only a computation of carrier scattering and correlations, but also a full quantum mechanical treatment of the light field. One promising approach for the description of PL is the equation of motion technique [140, 141]. It is a well-known difficulty that the equation of motion technique leads to a hierarchy of correlation functions. A systematic way to truncate this hierarchy is the cluster expansion method [142]. Based on this truncation scheme equations for the evolution of the carrier dynamics and the photon number can be derived. The resulting semiconductor luminescence equations (SLE) have previously been used to study PL spectra [143] and exciton formation [144] in a quantum-well system. Here we apply this general method to develop a microscopic theory for QD carriers interacting with the quantized light field. This allows us to study the time-resolved PL signal. We find that

the origin of the non-exponential and excitation intensity-dependent decay is the lack of full correlations between carriers in the QDs.

This part of the thesis is organized as follows: In Chapter 9 we introduce the Hamiltonian of the system and discuss the hierarchy problem, which is inherent to every many-body problem. Furthermore we explain how the introduction of correlation functions paves the way for a consistent truncation scheme. Chapter 10 is then dedicated to the derivation of semiconductor luminescence equations that go beyond the Hartree-Fock approximation and include correlation contributions up to the so-called *singlet-doublet* level. These equations are then applied in Chapter 11 to study the PL of a QD system into free space. In particular, we investigate the influence of correlations induced by Coulomb and light-matter interaction on the PL spectrum and the time dynamics. Finally, Chapter 12 deals with the decay dynamics of a QD ensemble embedded in a microcavity and gives a detailed discussion of recent experiments on such systems.

9 Hamiltonian and Consistent Truncation Scheme

We start this chapter by introducing the Hamiltonian describing the system of charge carriers that interact among themselves and with the quantized light field. In contrast to Part I and II of this thesis, we are now explicitly interested in the dynamics of the photonic field. Therefore, a fully quantum mechanical treatment of the carrier system and the electromagnetic field is necessary. In the subsequent Section 9.2, the hierarchy that is entailed on the one hand by the Coulomb interaction and on the other hand by the light-matter interaction is discussed. In particular it is explained how the introduction of correlation functions enables us to truncate this hierarchy in an unambiguous way in the framework of the cluster expansion technique. Later on, we restrict ourselves to the so-called *singlet-doublet* factorization to reach a consistent description of the carrier-carrier and carrier-photon correlations.

9.1 Hamiltonian

In order to study the PL dynamics both the carriers and the electromagnetic field are treated fully quantum mechanically. The total Hamiltonian for the system has the following contributions:

$$H = H_{\text{carr}}^0 + H_{\text{Coul}} + H_{\text{ph}}^0 + H_{\text{D}} . \quad (9.1)$$

The Hamiltonian, $H_{\text{carr}}^0 + H_{\text{Coul}}$, that describes the system of interacting charge carriers was already introduced in Section 1.2 in the electron-hole picture and is given here for completeness in the valence- and conduction-band picture, that we adopt in the following assuming identical envelopes

$$\begin{aligned} H_{\text{carr}}^0 &= \sum_i \varepsilon_i^c c_i^\dagger c_i + \sum_i \varepsilon_i^v v_i^\dagger v_i , \\ H_{\text{Coul}} &= \frac{1}{2} \sum_{ijkl} V_{ij,kl} c_i^\dagger c_j^\dagger c_k c_l + \frac{1}{2} \sum_{ijkl} V_{ij,kl} v_i^\dagger v_j^\dagger v_k v_l \\ &\quad + \sum_{ijkl} V_{ij,kl} c_i^\dagger v_j^\dagger v_k c_l . \end{aligned} \quad (9.2)$$

The electronic states are labeled by the latin characters i, j, k, l . In the case of a QD placed on a wetting layer there are two different types of states: localized bound QD states, denoted by $i = (\nu, \sigma)$, and delocalized WL states, corresponding to the quasi-free motion in the WL plane and labeled by $i = (\mathbf{k}, \sigma)$. The operator c_i (c_i^\dagger) are annihilation (creation) operators of electrons in the one-particle states $|i\rangle$ of energy ε_i^c . The corresponding quantities for the valence band are denoted by v_i (v_i^\dagger) and ε_i^v , respectively. The single-particle energy spectrum $\varepsilon_i^{(c,v)}$ consists of a discrete part for the bound states and a continuous part for the delocalized WL states. The Coulomb interaction is contained in H_{Coul} . Details on the interaction matrix elements $V_{ij,kl}^{\lambda\lambda'}$ can be found in Chapter 1.

As we are interested mainly in many-particle effects, we adopt in the following an effective-mass model for the single-particle states, as already discussed in Section 1.1. However, the inclusion of microscopically determined single-particle properties would be straightforward in the presented scheme.

The free part of the quantized light field is given by the Hamiltonian [145]

$$H_{ph}^0 = \sum_{\xi} \hbar\omega_{\xi} \left(b_{\xi}^\dagger b_{\xi} + \frac{1}{2} \right) . \quad (9.3)$$

The quantity $\hbar\omega_{\xi}$ is the energy of a photon created (destroyed) by the operator b_{ξ}^\dagger (b_{ξ}) in the mode ξ . In the case of ‘free space’, the mode label ξ contains the wave vector \mathbf{q} and the polarization vector of the electromagnetic field $\mathbf{e}_p(\mathbf{q})$, with the index $p = \pm$ labeling the two orthogonal polarization states. The mode frequencies are then given by $\omega_{\xi} = c|\mathbf{q}|$, with c being the speed of light, and the explicit form of the modes is $\mathbf{U}_{\xi}(\mathbf{r}) = \mathbf{e}_p(\mathbf{q}) e^{i\mathbf{qr}}$.

The Hamiltonian that describes the light-matter interaction in dipole approximation reads

$$H_D = -i \sum_{ij\xi} \left(g_{ij\xi} c_i^\dagger v_j b_{\xi} + g_{ij\xi} v_i^\dagger c_j b_{\xi} \right) - \text{h.c.} \quad (9.4)$$

The first term in the brackets and the corresponding one in the hermitian conjugate expression describe resonant contributions, the other two terms non-resonant contributions. The resonant elementary process associated with this Hamiltonian is the transition of an electron from the valence into the conduction band by absorption of a photon, or vice versa by emission. In contrast, the non-resonant elementary processes describe transition of an electron from the valence into the conduction band by emission of a photon or the transition of an electron from the conduction to the valence-band via absorption. These contributions clearly violate energy conservation and will therefore be neglected in the so-called rotating wave approximation (RWA).

The explicit form of the Hamiltonian (9.4) for the light-matter interaction is obtained by going from the dipole Hamiltonian in first quantization $H_{\text{dipole}} = -e\mathbf{Er}$ to second quantization and replacing the electric field \mathbf{E} by the hermitian operator $\hat{\mathbf{E}} = \hat{\mathbf{E}}^+ + \hat{\mathbf{E}}^-$. In this expression $\hat{\mathbf{E}}^+$ is given by $i \sum_{\xi} \tilde{E}_{\xi} \mathbf{U}_{\xi}(\mathbf{r}) b_{\xi}$ and describes the mode expansion of

the field. The quantity $\tilde{E}_\xi = \sqrt{\hbar\omega_\xi/2\epsilon_r\epsilon_0 V}$, with V being the normalization volume, has the dimension of an electric field and is sometimes called the ‘field per photon’ [145]. Keeping only the terms describing interband transitions, one obtains the Hamiltonian of the light-matter interaction as given by Eq. (9.4). The explicit form of the coupling matrix elements is

$$g_{ij\xi} = \tilde{E}_\xi \int d^3r \psi_i^{c*}(\mathbf{r}) e\mathbf{r} \mathbf{U}_\xi(\mathbf{r}) \psi_j^v(\mathbf{r}) . \quad (9.5)$$

They describe the coupling strength between the mode ξ of the electromagnetic field and the carrier transition involving the single-particle conduction-band states $|i\rangle$ and the valence-band state $|j\rangle$.

After this discussion of the different contributions to the total Hamiltonian (9.1) we will now analyze the hierarchy it entails.

9.2 Hierarchy Problem and Cluster Expansion

To study the dynamics of the averages of interest – like the electronic population in a certain state $f_i^e = \langle c_i^\dagger c_i \rangle$ or the number of photons $\langle b_\xi^\dagger b_\xi \rangle$ in a given mode ξ – we use Heisenberg’s equation of motion technique. In Heisenberg representation the time evolution of an operator A is determined by

$$i\hbar \frac{\partial}{\partial t} \Big|_H A = [A, H] .$$

This equation directly carries over to arbitrary operator averages $\langle \dots \rangle$, defined with the trace Tr via $\langle \dots \rangle = \text{Tr}\{\rho_0 \dots\}$, as the density matrix ρ_0 in Heisenberg representation does not evolve in time.

In order to illustrate the well-known hierarchy problem [68, 146–148] and to motivate the need for a consistent and unambiguous truncation scheme, let us take a closer look at the time evolution generated by the Coulomb Hamiltonian H_{Coul} in the case of the electronic population $f_i^e = \langle c_i^\dagger c_i \rangle$:

$$i\hbar \frac{\partial}{\partial t} \Big|_{H_{\text{Coul}}} f_i^e = i\hbar \frac{\partial}{\partial t} \Big|_{H_{\text{Coul}}} \langle c_i^\dagger c_i \rangle = \langle \left(i\hbar \frac{\partial}{\partial t} \Big|_{H_{\text{Coul}}} c_i^\dagger \right) c_i + c_i^\dagger \left(i\hbar \frac{\partial}{\partial t} \Big|_{H_{\text{Coul}}} c_i \right) \rangle .$$

The time evolution of the individual carrier operators due to the Coulomb interaction are given by

$$i\hbar \frac{\partial}{\partial t} \Big|_{H_{\text{Coul}}} c_i = \sum_{jkl} V_{ijkl} (c_j^\dagger c_k + v_j^\dagger v_k) c_l^\dagger \quad (9.6)$$

and

$$i\hbar \frac{\partial}{\partial t} \Big|_{H_{\text{Coul}}} c_i^\dagger = - \sum_{jkl} V_{ijkl}^* c_l (c_k^\dagger c_j + v_k^\dagger v_j) , \quad (9.7)$$

where the latter is easily obtained by hermitian conjugation. Using these equations, one finds for the population

$$i\hbar \frac{\partial}{\partial t} \Big|_{H_{\text{Coul}}} f_i^e = - \sum_{jkl} \{ V_{ijkl}^* \langle c_l^\dagger (c_k^\dagger c_j + v_k^\dagger v_j) c_i \rangle + V_{ijkl} \langle c_i^\dagger (c_j^\dagger c_k + v_j^\dagger v_k) c_l^\dagger \rangle \} . \quad (9.8)$$

From this example it can be inferred that the dynamics of a one-particle average (an average containing one creation and one annihilation operator, schematically denoted by $\langle 1 \rangle$) couples to two-particle averages (containing two creation and two annihilation operators, schematically $\langle 2 \rangle$). In the following, such averages are – according to the number of creation operators present in this expression – sometimes called *singlet*- and *doublet*-terms, respectively.

In order to determine the time evolution of f_i^e , one needs to derive the equations of motion for the two-particle quantities. Doing so, immediately leads to averages with six operators, that is, three-particle averages $\langle 3 \rangle$, as the time derivative of a single creation/annihilation operator has to be replaced according to Eq. (9.6) and Eq. (9.7) by a sum of three operators.

If one formulates the equation of motion for these three-particle averages, Coulomb interaction – or in fact any other two-particle Hamiltonian – will couple this to four-particle averages. Similarly the dynamics of four-particle averages are coupled to five-particle averages and so on. This is at the heart of the hierarchy problem, which can be schematically summarized as:

$$\langle 1 \rangle \xrightarrow{H} \langle 2 \rangle \xrightarrow{H} \langle 3 \rangle \xrightarrow{H} \langle 4 \rangle \xrightarrow{H} \dots$$

In this scheme $\langle N \rangle$ denotes the highest N -particle average generated by the time evolution via the Hamiltonian H and we simply write \xrightarrow{H} to symbolize this evolution.

Note that a one-particle Hamiltonian $\sum_{ij} h_{ij} a_i^\dagger a_j$ does not entail a hierarchy, because in the evolution generated by such a Hamiltonian the time derivative of one fermion operator is replaced by a sum of again single fermion operators. Therefore the number of operators in an expectation value is not changed.

Hartree-Fock Approximation

The most simple way of truncating the infinite hierarchy is the Hartree-Fock approximation, in which the two-particle averages are replaced by all possible combinations of one-particle averages

$$\langle a_i^\dagger a_j^\dagger a_k a_l \rangle \approx \langle a_i^\dagger a_j^\dagger a_k a_l \rangle_{\text{HF}} = \langle a_i^\dagger a_l \rangle \langle a_j^\dagger a_k \rangle - \langle a_j^\dagger a_l \rangle \langle a_i^\dagger a_k \rangle . \quad (9.9)$$

The sign is determined by the number of transpositions that are necessary to bring the operators from their original order in the two-particle average in Eq. (9.9) into the

order they have in the product of singlets. If the number of these transposition is odd, one obtains a minus sign, a plus sign otherwise.

For the following discussion the Hamiltonian $H = H_1 + H_2$ is divided into a one-particle part H_1 and a two-particle part H_2 . Using the HF-factorization for the two-particle averages $\langle 2 \rangle$, one can express the equation of motion of a one-particle average $\langle 1 \rangle$ schematically as

$$i\hbar \frac{\partial}{\partial t} \langle 1 \rangle = F_1\{\langle 1 \rangle\} + F_2\{\langle 2 \rangle\} \approx F_1\{\langle 1 \rangle\} + F_2\{\langle 2 \rangle_{\text{HF}}\} = F_1\{\langle 1 \rangle\} + F_2\{\langle 1 \rangle \langle 1 \rangle\} . \quad (9.10)$$

The time evolution generated by H_1 yields a dependency of $i\hbar \frac{\partial}{\partial t} \langle 1 \rangle$ on other one-particle averages and is summarized in $F_1\{\langle 1 \rangle\}$. The two-particle Hamiltonian H_2 , however, produces a coupling to two-particle averages expressed by the function F_2 . An explicit example for F_2 was given in Eq. (9.8). In the second step of Eq. (9.10), the doublets $\langle 2 \rangle$ are factorized into singlets according to the HF-approximation (9.9). In this way, the equations of motion are closed on singlet level.

Correlations

The difference between the full two-particle average $\langle 2 \rangle$ and its Hartree-Fock factorized part $\langle 2 \rangle_{\text{HF}}$ is the two-particle correlation $\delta\langle 2 \rangle$. Therefore, one may write schematically

$$\langle 2 \rangle = \langle 2 \rangle_{\text{HF}} + \delta\langle 2 \rangle = \langle 1 \rangle \langle 1 \rangle + \delta\langle 2 \rangle . \quad (9.11)$$

Similar, one can define a three-particle correlation schematically as

$$\begin{aligned} \delta\langle 3 \rangle &= \langle 3 \rangle - \text{all lower correlations} \\ &= \langle 3 \rangle - \langle 1 \rangle \delta\langle 2 \rangle - \langle 1 \rangle \langle 1 \rangle \langle 1 \rangle . \end{aligned} \quad (9.12)$$

Here the terms $\langle 1 \rangle \delta\langle 2 \rangle$ and $\langle 1 \rangle \langle 1 \rangle \langle 1 \rangle$ mean that the three-particle average $\langle 3 \rangle$ should be broken in every possible combination of doublet correlations and singlets plus all possible combinations of three singlets. Along similar lines, one can define N -particle correlations [142]. Note that $\langle 1 \rangle = \delta\langle 1 \rangle$, so that on the right hand side of Eq. (9.12) indeed only the full three-particle expectation value and correlations enter.

In terms of correlation functions the Hartree-Fock approximation is equivalent to considering only singlets and discarding all two-particle and higher-order correlations. That is sometimes called *singlet approximation*. Going beyond the singlet approximation, one keeps all correlations up to a certain order and discards all higher correlation terms. This unambiguously defines the set of equations of motion for the correlations on a certain truncation level [142].

A clear advantage of describing the system in terms of the N -particle correlations instead of the pure N -particle expectation values, is given by the following fact: Even

in the case of a non-interacting system a N -particle expectation value is in a grand-canonical ensemble in general non-zero. In contrast, all N -particle correlations with $N > 1$ are zero in this situation, because Wick's theorem applies for all the averages [142, 149]. Therefore it is reasonable to assume that in the spirit of an approximation scheme, one may indeed discard higher-order correlation terms, as they are zero in the non-interacting case. However, a similar statement directly for the expectation values is not valid. From an intuitive standpoint, neglecting higher-order correlations may be justified by realizing that an important contribution to the correlation becomes less likely as the number of involved operators increases.

Singlet-Doublet Approximation

In the so-called *singlet-doublet approximation*, which we will adopt in the following, one keeps all correlations below the three-particle correlations. In the schematic descriptions used above, the equation of motion on singlet-doublet level read

$$i\hbar \frac{\partial}{\partial t} \langle 1 \rangle = F_1 \{ \langle 1 \rangle \} + F_2 \{ \langle 2 \rangle \} = F_1 \{ \langle 1 \rangle \} + F_2 \{ \langle 1 \rangle \langle 1 \rangle, \delta \langle 2 \rangle \} \quad (9.13)$$

and

$$\begin{aligned} i\hbar \frac{\partial}{\partial t} \delta \langle 2 \rangle &= i\hbar \frac{\partial}{\partial t} (\langle 2 \rangle - \langle 1 \rangle \langle 1 \rangle) = G_1 \{ \langle 2 \rangle, \langle 1 \rangle \langle 1 \rangle \} + G_2 \{ \langle 3 \rangle, \langle 2 \rangle \langle 1 \rangle \} \\ &\approx G_1 \{ \delta \langle 2 \rangle, \langle 1 \rangle \langle 1 \rangle \} + G_2 \{ \langle 1 \rangle \delta \langle 2 \rangle, \langle 1 \rangle \langle 1 \rangle \langle 1 \rangle \} . \end{aligned} \quad (9.14)$$

As before F_1 and F_2 denote the coupling to other one- and two-particle averages, respectively. In contrast to the HF-approximation, the two-particle averages are now treated without approximation and are rewritten as $\langle 2 \rangle = \langle 1 \rangle \langle 1 \rangle + \delta \langle 2 \rangle$. The evolution of the correlation $\delta \langle 2 \rangle$ as generated by the one-particle Hamiltonian H_1 leads to the function $G_1 \{ \langle 2 \rangle, \langle 1 \rangle \langle 1 \rangle \}$ because one has schematically: $\langle 2 \rangle \xrightarrow{H_1} \langle 2 \rangle$ and $\langle 1 \rangle \langle 1 \rangle \xrightarrow{H_1} \langle 1 \rangle \langle 1 \rangle$. Similarly G_2 denotes the corresponding function for H_2 and depends on $\langle 3 \rangle$ and $\langle 2 \rangle \langle 1 \rangle$, because $\langle 2 \rangle \xrightarrow{H_2} \langle 3 \rangle$ and $\langle 1 \rangle \langle 1 \rangle \xrightarrow{H_2} \langle 2 \rangle \langle 1 \rangle$. In order to obtain a set of differential equations that is closed on the singlet-doublet level, one rewrites all occurring averages in terms of correlations and applies the singlet-doublet approximation scheme. To this end, we write $\langle 3 \rangle = \langle 1 \rangle \delta \langle 2 \rangle + \langle 1 \rangle \langle 1 \rangle \langle 1 \rangle + \delta \langle 3 \rangle$ according to Eq. (9.12) and neglect the triplet correlations $\delta \langle 3 \rangle$. This leads to the second line of Eq. (9.14) and closes the set of equations.

So far we have used only a schematic description of the singlet-doublet approximation scheme. When fully spelt out, the schematic equation $\langle 3 \rangle_{SD} = \delta \langle 2 \rangle \langle 1 \rangle + \langle 1 \rangle \langle 1 \rangle \langle 1 \rangle$ is

given by [142, 150]:

$$\begin{aligned}
 \langle a_i^\dagger a_j^\dagger a_k^\dagger a_l a_m a_n \rangle_{SD} = & + \langle a_i^\dagger a_l \rangle \delta \langle a_j^\dagger a_k^\dagger a_m a_n \rangle - \langle a_i^\dagger a_m \rangle \delta \langle a_j^\dagger a_k^\dagger a_l a_n \rangle + \langle a_i^\dagger a_n \rangle \delta \langle a_j^\dagger a_k^\dagger a_l a_m \rangle \\
 & - \langle a_j^\dagger a_l \rangle \delta \langle a_i^\dagger a_k^\dagger a_m a_n \rangle + \langle a_j^\dagger a_m \rangle \delta \langle a_i^\dagger a_k^\dagger a_l a_n \rangle - \langle a_j^\dagger a_n \rangle \delta \langle a_i^\dagger a_k^\dagger a_l a_m \rangle \\
 & + \langle a_k^\dagger a_l \rangle \delta \langle a_i^\dagger a_j^\dagger a_m a_n \rangle - \langle a_k^\dagger a_m \rangle \delta \langle a_i^\dagger a_j^\dagger a_l a_n \rangle + \langle a_k^\dagger a_n \rangle \delta \langle a_i^\dagger a_j^\dagger a_l a_m \rangle \\
 & - \langle a_i^\dagger a_l \rangle \langle a_j^\dagger a_m \rangle \langle a_k^\dagger a_n \rangle + \langle a_i^\dagger a_l \rangle \langle a_j^\dagger a_n \rangle \langle a_k^\dagger a_m \rangle - \langle a_i^\dagger a_m \rangle \langle a_k^\dagger a_l \rangle \langle a_j^\dagger a_n \rangle \\
 & + \langle a_i^\dagger a_n \rangle \langle a_j^\dagger a_m \rangle \langle a_k^\dagger a_l \rangle - \langle a_i^\dagger a_n \rangle \langle a_j^\dagger a_l \rangle \langle a_k^\dagger a_m \rangle + \langle a_i^\dagger a_m \rangle \langle a_j^\dagger a_l \rangle \langle a_k^\dagger a_n \rangle .
 \end{aligned} \tag{9.15}$$

This factorization contains nine terms of the form $\langle 1 \rangle \delta \langle 2 \rangle$ and six terms of the form $\langle 1 \rangle \langle 1 \rangle \langle 1 \rangle$. The sign is again determined by the number of transposition needed to go from the original order of the three-particle average to the order of the operators in the factorization.

In addition to expectation values containing only fermion operators, the light-matter interaction produces mixed averages with both carrier and photon operators. To understand how one must treat averages containing boson operators in the cluster expansion scheme, consider the equation of motion for the photon creation operator in rotating wave approximation

$$i\hbar \frac{\partial}{\partial t} \Big|_H b_\xi^\dagger = -\hbar\omega_\xi b_\xi^\dagger + i \sum_{ij} g_{ij\xi} c_i^\dagger v_j .$$

Integrating this differential equation yields

$$b_\xi^\dagger(t) = b_\xi^\dagger(0) e^{+i\omega_\xi t} + \frac{1}{\hbar} \sum_{ij} g_{ij\xi} \int_0^t dt' e^{+i\omega_\xi(t-t')} c_i^\dagger(t') v_j(t') . \tag{9.16}$$

This shows that a photon creation operator is formally equivalent to the product of two fermion operators [147]. From this equivalency it is rather obvious that the interaction with a quantized light field, described by the Hamiltonian (9.4), creates itself a hierarchy. This can be seen as the Hamiltonian of the light-matter interaction contains, for example, terms of the form $b^\dagger v^\dagger c$. Therefore two hierarchies need to be tackled, one from the Coulomb interaction and one from the interaction with the quantized light field¹.

In the absence of a coherent electromagnetic field, one has $\langle b_q^\dagger \rangle = 0$. In this case the singlet-doublet approximation yields

$$\begin{aligned}
 \langle b_\xi^\dagger a_i^\dagger a_j^\dagger a_k a_l \rangle_{SD} = & + \delta \langle b_\xi^\dagger a_i^\dagger a_l \rangle \langle a_j^\dagger a_k \rangle + \delta \langle b_\xi^\dagger a_j^\dagger a_k \rangle \langle a_i^\dagger a_l \rangle \\
 & - \delta \langle b_\xi^\dagger a_j^\dagger a_l \rangle \langle a_i^\dagger a_k \rangle - \delta \langle b_\xi^\dagger a_i^\dagger a_k \rangle \langle a_j^\dagger a_l \rangle .
 \end{aligned}$$

¹ Note that the interaction with a classical light-field is described by a one-particle Hamiltonian and does, consequently, not create a hierarchy.

Furthermore, one obtains in the incoherent regime $\delta\langle b_\xi^\dagger a_i^\dagger a_j \rangle = \langle b_\xi^\dagger a_i^\dagger a_j \rangle$ so that the ' δ ' for this quantity is dropped in the remainder of this thesis. Along the same lines, we find in the case of two boson and two fermion operators

$$\langle b_\xi^\dagger b_{\xi'}^\dagger a_i^\dagger a_j \rangle_{SD} = \langle b_\xi^\dagger b_{\xi'}^\dagger \rangle \langle a_i^\dagger a_j \rangle . \quad (9.17)$$

In the next chapter the general truncation procedure explained in this section will be applied to derive equations of motion for the coupled dynamics of charge carriers in the QD-WL system and the photons of the optical environment. This paves the way for a detailed investigation of the PL dynamics in Chapter 11 and 12.

10 Semiconductor Luminescence Equations

In this chapter the semiconductor luminescence equation (SLE), including correlations up to the singlet-doublet level, are derived. For this, we consider an incoherent population of carriers generated either by optical pumping high into the bands and subsequent rapid dephasing and carrier relaxation, or by direct carrier injection. In both cases coherent polarizations that contribute in pump-probe or four-wave mixing experiments and are described by the semiconductor Bloch equations, play no role. A specialized version of the SLE for the case of a quantum well is used in Refs. [144, 150, 151]. Due to the complicated structure of the relevant equations, a one-dimensional model system had to be used in these references for the actual evaluation of the equations. In the present thesis, the application of the SLE to semiconductor QDs is presented. For this purpose, the theory is formulated in a general basis and subsequently specialized to the QD-WL system. Similar work was only recently published [152] and was partly influenced by discussion between our group and these authors but is restricted only to the investigation of QDs coupled to the modes of free space. Here, we use this formalism to investigate a QD system embedded in two different photonic environments, namely, free space in Chapter 11 and a optical microcavity in Chapter 12.

10.1 Formulation of the Relevant Equations of Motion

We start our analysis with the derivation of the carrier population changes. Then we discuss how the photon number evolves in time. As both quantities depend on the so-called *photon-assisted polarization* an equation of motion for this quantity is derived. After this, the correlation functions occurring in the differential equations of the aforementioned quantities are analyzed.

Carrier Population

With the Hamiltonian described in Section 9.1 the equation of motion for the generalized population or intraband polarization $\langle c_i^\dagger c_j \rangle$ is given by

$$\begin{aligned} i\hbar \frac{\partial}{\partial t} \langle c_i^\dagger c_j \rangle &= -(\varepsilon_i^c - \varepsilon_j^c) \langle c_i^\dagger c_j \rangle \\ &\quad - i \sum_{1\xi} \left\{ g_{i1\xi}^* \langle b_\xi^\dagger v_1^\dagger c_j \rangle + (g_{j1\xi}^* \langle b_\xi^\dagger v_1^\dagger c_i \rangle)^* \right\} \\ &\quad + \sum_{234} V_{i234} \left\{ \langle c_j^\dagger c_2^\dagger c_3 c_4 \rangle - \langle c_j^\dagger v_2^\dagger c_4 v_3 \rangle \right\} \\ &\quad - \sum_{234} V_{j234}^* \left\{ \langle c_4^\dagger c_3^\dagger c_2 c_i \rangle - \langle c_4^\dagger v_3^\dagger c_i v_2 \rangle \right\} . \end{aligned} \quad (10.1)$$

In this expression the integers 1, 2, 3, and 4 refer to electronic indices that are summed over. This notation will be kept throughout this section to distinguish between outer indices (not to be summed over) and inner indices (to be summed over). The first line of Eq. (10.1) stems from the free Hamiltonian H_{carr}^0 , the second line comes from the light-matter interaction H_D , and the last two lines are due to the Coulomb interaction between the carriers. A similar equation can be derived for the valence-band electrons. The two-particle averages that occur in the above equation can now be split according to Eq. (9.11) into the Hartree-Fock contribution and the pure two-particle correlation:

$$\begin{aligned} \langle c_j^\dagger c_2^\dagger c_3 c_4 \rangle &= \underbrace{\delta \langle c_j^\dagger c_2^\dagger c_3 c_4 \rangle}_{=: C_{j234}^c} - \langle c_j^\dagger c_3 \rangle \langle c_2^\dagger c_4 \rangle + \langle c_2^\dagger c_3 \rangle \langle c_j^\dagger c_4 \rangle , \\ \langle c_j^\dagger v_2^\dagger c_3 v_4 \rangle &= \underbrace{\delta \langle c_j^\dagger v_2^\dagger c_3 v_4 \rangle}_{=: C_{j234}^X} - \langle c_j^\dagger c_3 \rangle \langle v_2^\dagger v_4 \rangle . \end{aligned} \quad (10.2)$$

Note that in the second line of Eq. (10.2) the additional term $\langle v_2^\dagger c_3 \rangle \langle c_j^\dagger v_4 \rangle$ that would occur according to the definitions (9.9) and (9.11) is zero in the incoherent regime and is therefore omitted. Note further that the photon-assisted polarization $\langle b^\dagger v^\dagger c \rangle$ is its own two-particle correlation as the HF-contribution vanishes, see discussion of Eq. (9.16). For proper populations ($i = j$) one can recast the equation of motion (10.1) into

$$\begin{aligned} i\hbar \frac{\partial}{\partial t} \langle c_i^\dagger c_i \rangle &= -2i\text{Re} \left\{ \sum_{1\xi} g_{i1\xi}^* \langle b_\xi^\dagger v_1^\dagger c_i \rangle \right\} \\ &\quad + 2i\text{Im} \left\{ \sum_{234} V_{i234} (C_{2i43}^c - C_{i243}^X - \langle c_i^\dagger c_3 \rangle \langle c_2^\dagger c_4 \rangle \right. \\ &\quad \left. + \langle c_2^\dagger c_3 \rangle \langle c_i^\dagger c_4 \rangle + \langle c_i^\dagger c_4 \rangle \langle v_2^\dagger v_3 \rangle) \right\} . \end{aligned} \quad (10.3)$$

Before deriving the differential equations for the other averages of interest, it is instructive to inspect the above equation somewhat closer. The first line describes the

population changes due to the interaction with the photonic field. This term leads to an overall decrease of the carrier density in the conduction band. This is in contrast to the second part, which gives the population changes due to Coulomb interaction. As Coulomb interaction is known to leave the total population $\sum_i f_i^\lambda$ in each band λ unchanged, it is well worth checking if the expression

$$\sum_i \text{Im} \left\{ \sum_{234} V_{i234} (C_{2i43}^c - C_{i243}^X - \langle c_i^\dagger c_3 \rangle \langle c_2^\dagger c_4 \rangle + \langle c_2^\dagger c_3 \rangle \langle c_i^\dagger c_4 \rangle + \langle c_i^\dagger c_4 \rangle \langle v_2^\dagger v_3 \rangle) \right\}$$

is indeed zero. By changing the indices $2 \leftrightarrow 3$ and $i \leftrightarrow 4$, one can verify that the above sum is equal to its complex conjugate. Therefore the imaginary part vanishes. This shows that one has indeed $i\hbar \frac{\partial}{\partial t} \Big|_{H_{\text{Coul}}} \sum_i f_i^c = 0$.

Photon Number

In the case of a photoluminescence experiment, the most interesting quantity is either the photon number $\langle b_\xi^\dagger b_\xi \rangle$, which denotes the number of photons in a given mode ξ , or the number of photons generated per unit time $\frac{d}{dt} \langle b_\xi^\dagger b_\xi \rangle$. For the more general expression $\langle b_\xi^\dagger b_{\xi'} \rangle$ one finds

$$i\hbar \frac{\partial}{\partial t} \langle b_\xi^\dagger b_{\xi'} \rangle = -(\hbar\omega_\xi - \hbar\omega_{\xi'}) \langle b_\xi^\dagger b_{\xi'} \rangle + i \sum_{12} (g_{12\xi}^* \langle b_{\xi'}^\dagger v_2^\dagger c_1 \rangle)^* + i \sum_{12} g_{12\xi'}^* \langle b_\xi^\dagger v_2^\dagger c_1 \rangle .$$

This reduces to

$$i\hbar \frac{\partial}{\partial t} \langle b_\xi^\dagger b_\xi \rangle = 2i \text{Re} \left\{ \sum_{12} g_{12\xi}^* \langle b_\xi^\dagger v_2^\dagger c_1 \rangle \right\} \quad (10.4)$$

for the diagonal terms $\xi = \xi'$. Combining this equation with Eq. (10.3) one finds

$$\frac{\partial}{\partial t} \left\{ \sum_\xi \langle b_\xi^\dagger b_\xi \rangle + \sum_i \langle c_i^\dagger c_i \rangle \right\} = 0 . \quad (10.5)$$

This expression shows that the overall change in the number of carriers in the conduction band (and henceforth in the valence band) is equal to the change of the total photon number in the system. This is a very intuitive result, stating that for each created electron-hole pair a photon is destroyed, or vice versa.

Photon-Assisted Polarization

As both the occupation and the photon number depend on the photon-assisted polarization $\langle b^\dagger v^\dagger c \rangle$, one has to establish a differential equation for this quantity as well. By means of Heisenberg's equation of motion and additionally applying the singlet-doublet factorization to the three-particle averages, one finds

$$\begin{aligned}
 i\hbar \frac{\partial}{\partial t} \langle b_\xi^\dagger v_i^\dagger c_j \rangle = & (\varepsilon_j^c - \varepsilon_i^v - \hbar\omega_\xi) \langle b_\xi^\dagger v_i^\dagger c_j \rangle \\
 & + i \sum_{12} g_{21\xi} \left\{ \langle c_2^\dagger c_j \rangle (\delta_{i1} - \langle v_i^\dagger v_1 \rangle) + C_{2ij1}^X \right\} \\
 & + i \sum_{1\xi'} \langle b_\xi^\dagger b_{\xi'} \rangle \left\{ g_{1i\xi'} \langle c_1^\dagger c_j \rangle - g_{j1\xi'} \langle v_i^\dagger v_1 \rangle \right\} \\
 & - \sum_{123} V_{123i} \left\{ \langle b_\xi^\dagger v_1^\dagger c_j \rangle \langle c_2^\dagger c_3 \rangle - \langle b_\xi^\dagger v_1^\dagger c_3 \rangle \langle c_2^\dagger c_j \rangle \right. \\
 & \quad \left. + \langle b_\xi^\dagger v_1^\dagger c_j \rangle \langle v_2^\dagger v_3 \rangle - \langle b_\xi^\dagger v_2^\dagger c_j \rangle \langle v_1^\dagger v_3 \rangle \right\} \\
 & + \sum_{234} V_{j234} \left\{ \langle b_\xi^\dagger v_i^\dagger c_4 \rangle \langle c_2^\dagger c_3 \rangle - \langle b_\xi^\dagger v_i^\dagger c_3 \rangle \langle c_2^\dagger c_4 \rangle \right. \\
 & \quad \left. + \langle b_\xi^\dagger v_i^\dagger c_4 \rangle \langle v_2^\dagger v_3 \rangle - \langle b_\xi^\dagger v_2^\dagger c_4 \rangle \langle v_i^\dagger v_3 \rangle \right\}. \tag{10.6}
 \end{aligned}$$

The first line is generated by the free Hamiltonian H_{carr}^0 of the carriers and the photonic system H_{ph}^0 . It contains the energy difference of the involved unrenormalized conduction- and valence-band states as well as the free energy of the optical mode. The second line constitutes the source term of the photon-assisted polarization and consequently of spontaneous emission. It shows that the photon-assisted polarization is built up as soon as (generalized) population is present in the system. The third line depends on the (generalized) photonic population $\langle b_\xi^\dagger b_{\xi'} \rangle$ and will only be of importance if a cavity or a resonant external field is present. If the photonic environment is the ‘free space’, the term $\langle b_\xi^\dagger b_{\xi'} \rangle$ can be neglected in the incoherent regime. In a cavity, however, this term is responsible for stimulated emission/absorption of photons and will therefore be of great importance in this case. Both the second and the third line originate from the light-matter interaction. The last two sums in Eq. (10.6) stem from the Coulomb interaction. The physics behind these terms will become more transparent in Section 10.2.3 where we specialize the system to a QD with two shells for each type of carrier. Then we will see that the Coulomb terms lead to a renormalization of the single-particle energies and to a coupling of different photon-assisted polarization contributions.

Correlation Functions

In order to fully determine the right-hand side of the differential equation describing the population changes and the evolution of the photon-assisted polarization, one has to determine the correlation C^X , C^c , and C^v . For this, we focus on C^X and comment only briefly on the derivation of equations of motion for C^c and C^v that run along the same lines. To determine the differential equation for C^X , one needs the equations governing $\langle c_i^\dagger v_j^\dagger c_k v_l \rangle$ and $\langle c_i^\dagger v_j^\dagger c_k v_l \rangle_{HF}$. Let us first concentrate on the time evolution generated by the Coulomb interaction. Using Eq. (9.6) and Eq. (9.7) from page 115 we find

$$i\hbar \frac{\partial}{\partial t} \Big|_{H_{Coul}} \langle c_i^\dagger v_j^\dagger c_k v_l \rangle = - \sum_{123} \{ \begin{aligned} & V_{123i} \langle c_1^\dagger (c_2^\dagger c_3 + v_2^\dagger v_3) v_j^\dagger c_k v_l \rangle \\ & + V_{123j} \langle c_i^\dagger v_1^\dagger (c_2^\dagger c_3 + v_2^\dagger v_3) c_k v_l \rangle \\ & - V_{123k}^* \langle c_i^\dagger v_j^\dagger (c_3^\dagger c_2 + v_3^\dagger v_2) c_1 v_l \rangle \\ & - V_{123l}^* \langle c_i^\dagger v_j^\dagger c_k (c_3^\dagger c_2 + v_3^\dagger v_2) v_1 \rangle \end{aligned} \} . \quad (10.7)$$

The eight three-particle averages in the above equation are now factorized according to the singlet-doublet approximation. From Eq. (9.15) we see that in general there are $8 \times 6 = 48$ pure singlet terms. As we consider the incoherent regime, in which the coherent polarizations $\langle v_i^\dagger c_j \rangle$ play no role, only 16 terms remain. Furthermore, there are in general $8 \times 9 = 72$ terms of the form $\langle 1 \rangle \delta \langle 2 \rangle$ in the expansion of Eq. (10.7), of which in the incoherent regime 40 remain.

As the three-particle averages in Eq. (10.7) contain three inner indices, defined by 1, 2, 3, and three outer indices, labeled by latin characters, we can classify each generated $\langle 1 \rangle \delta \langle 2 \rangle$ term according to the number of inner indices present in $\delta \langle 2 \rangle$. There are twelve terms with one, 20 terms with two, and eight terms with three inner indices in the $\delta \langle 2 \rangle$ part. The latter terms cancel exactly the HF-factorized part $\langle c_i^\dagger v_j^\dagger c_k v_l \rangle_{HF} = -\langle c_i^\dagger c_k \rangle \langle v_j^\dagger v_l \rangle$ that need to be subtracted to form a pure correlation, according to the definition (9.11). That such a cancelation is possible can be seen as follows: From the time derivative of a product of the form $\langle 1 \rangle \langle 1 \rangle$ four terms are generated (one from the derivative of each fermion operator). Bearing in mind the explicit form of the time evolution of the carrier operators, as given by Eqs. (9.6) and (9.7), and considering the terms $c^\dagger c$ and $v^\dagger v$ that occur as $(c^\dagger c + v^\dagger v)$ separately, one obtains $4 \times 2 = 8$ terms of the form $\langle 1 \rangle \langle 2 \rangle$. In these terms a summation over three indices in the $\langle 2 \rangle$ part takes place. Finally using $\langle 2 \rangle = \delta \langle 2 \rangle + \langle 1 \rangle \langle 1 \rangle$, yields the same structure of terms from the HF-factorized part as one obtains from the singlet-doublet factorization of the time evolution of $\langle c_i^\dagger v_j^\dagger c_k v_l \rangle$. A close inspection of these two sets of eight terms reveals that they indeed cancel each other. Note that the additional terms of the form $\langle 1 \rangle \langle 1 \rangle \langle 1 \rangle$, as they are generated by the time-evolution of the HF-part in the singlet-doublet approximation, cancel 12 out of the 16 singlet terms arising in the evolution of $\langle c_i^\dagger v_j^\dagger c_k v_l \rangle$.

In the end, one is left only with two different types of terms in the singlet-doublet factorization: Terms that have one inner index in C^X and terms that have two inner indices in C^X . In Section 10.2 a QD with two shells is discussed. Then we will see

that the terms with only one inner index renormalize the single-particle energies, while those with two lead to a coupling of the different correlation matrix elements.

Sorting all the different terms generated by the singlet-doublet factorization of Eq. (10.7) finally leads to

$$\begin{aligned}
 i\hbar \frac{\partial}{\partial t} \Big|_{H_{\text{Coul}}} C_{ijkl}^X = & \\
 - \sum_{1234} V_{1234} \Big\{ & \left[\langle c_i^\dagger c_4 \rangle \langle v_j^\dagger v_3 \rangle (\delta_{1k} - \langle c_1^\dagger c_k \rangle) (\delta_{2l} - \langle v_2^\dagger v_l \rangle) \right. \\
 & - (\delta_{i4} - \langle c_i^\dagger c_4 \rangle) (\delta_{j3} - \langle v_j^\dagger v_3 \rangle) \langle c_1^\dagger c_k \rangle \langle v_2^\dagger v_l \rangle \Big] \\
 & + (\langle v_1^\dagger v_l \rangle \delta_{4j} - \langle v_j^\dagger v_4 \rangle \delta_{1l}) C_{i2k3}^{X+v} - (\langle c_i^\dagger c_4 \rangle \delta_{1k} + \langle c_1^\dagger c_k \rangle \delta_{4i}) C_{2j3l}^{X+c} \\
 & - (\langle v_2^\dagger v_l \rangle \delta_{4i} - \langle c_i^\dagger c_4 \rangle \delta_{l2}) C_{1jk3}^X + (\langle v_j^\dagger v_4 \rangle \delta_{2k} - \langle c_2^\dagger c_k \rangle \delta_{4j}) C_{i13l}^X \\
 & - (\langle c_2^\dagger c_k \rangle \delta_{4i} - \langle c_i^\dagger c_4 \rangle \delta_{k2}) C_{1j3l}^X + (\langle v_j^\dagger v_4 \rangle \delta_{2l} - \langle v_2^\dagger v_l \rangle \delta_{4j}) C_{i1k3}^X \\
 & + (\langle v_3^\dagger v_l \rangle \delta_{4k} + \delta_{3l}(\langle c_4^\dagger c_k \rangle - \delta_{k4})) C_{ij12}^X \\
 & - (\langle c_i^\dagger c_3 \rangle \delta_{4j} + \delta_{3i}(\langle v_4^\dagger v_j \rangle - \delta_{j4})) C_{21kl}^X \\
 & - \delta_{i4} \langle c_1^\dagger c_3 \rangle C_{2jkl}^X - \delta_{j4} \langle v_1^\dagger v_3 \rangle C_{i2kl}^X + \delta_{k1} \langle c_2^\dagger c_4 \rangle C_{ij3l}^X - \delta_{l1} \langle v_2^\dagger v_4 \rangle C_{ijk3}^X \\
 & \left. (\langle c_2^\dagger c_3 \rangle + \langle v_2^\dagger v_3 \rangle) [\delta_{i4} C_{1jkl}^X + \delta_{j4} C_{i1kl}^X - \delta_{k1} C_{ij4l}^X - \delta_{l1} C_{ijk4}^X] \right\}. \quad (10.8)
 \end{aligned}$$

Here the abbreviation $C_{ijkl}^{X+v} = C_{ijkl}^X + C_{ijkl}^c$ and $C_{ijkl}^{X+c} = C_{ijkl}^X + C_{ijkl}^v$ were introduced. The first two lines of the right-hand side constitutes a factorization only in singlet terms, while all the other terms stem from a combination of singlet and doublet correlations.

So far we have only considered the evolution due to the Coulomb interaction. Now the contributions due to the free-carrier Hamiltonian and the light-matter interaction are given. These contribution read, respectively,

$$i\hbar \frac{\partial}{\partial t} \Big|_{H_{\text{carr}}^0} C_{ijkl}^X = -(\varepsilon_i^c + \varepsilon_j^v - \varepsilon_k^c - \varepsilon_l^v) C_{ijkl}^X \quad (10.9)$$

and

$$\begin{aligned}
 i\hbar \frac{\partial}{\partial t} \Big|_{H_D} C_{ijkl}^X = i \sum_{1\xi} \Big\{ & \langle b_\xi^\dagger v_j^\dagger c_k \rangle [g_{1\xi}^* \langle c_i^\dagger c_1 \rangle - g_{i1\xi}^* \langle v_1^\dagger v_l \rangle] \\
 & + \langle b_\xi^\dagger c_i^\dagger v_l \rangle [g_{1j\xi} \langle c_1^\dagger c_k \rangle - g_{k1\xi} \langle v_j^\dagger v_1 \rangle] \Big\}. \quad (10.10)
 \end{aligned}$$

Along the same lines, one can derive equations of motion for C^c and C^v . These equations are even more complicated than the equation for C^X , because in the singlet-doublet expansion of the intraband correlations not so many averages of the form $\langle c_i^\dagger v_j \rangle$, which vanish in the incoherent regime, are generated. As no additional insight is gained from studying the explicit form of the equations of motion for C^c and C^v in the general case, these expression are omitted here. However, they will be discussed for the specialized case in Section 10.2.3.

10.2 Specialization to a Quantum Dot Model

So far the SLE were formulated in a general basis and can now be applied to different systems. The system-dependent parameters are the single-particle energies, the mode frequencies ω_ξ , the Coulomb matrix elements and the dipole-matrix elements that determine the light-matter interaction H_D . Additionally, the underlying symmetry depends on the system: In a quantum well, for which the PL was studied in [143, 144, 153], one has full translational symmetry, whereas in the case of QD system the translational symmetry of the WL is spoiled by the presence of the QDs. To keep the following discussions as simple as possible, we restrict ourselves to QDs that confine two shells for each type of carriers. Such a situation is often met in an experiment and makes the relevant equations more transparent and the numerical evaluation feasible.

We start this section with an analysis of the light-matter interaction matrix elements $g_{ij\xi}$, finding that the matrix elements can, to a good approximation, be taken diagonal $g_{ij\xi} = g_{i\xi} \delta_{ij}$. In Section 10.2.2 the consequences of the circular symmetry of the QDs are analyzed and one finds that off-diagonal contributions $\langle c_i^\dagger c_j \rangle$ with $i \neq j$ vanish. Using these facts, a more transparent interpretation of the various terms of the SLE is possible.

10.2.1 The Light-Matter Interaction Matrix Elements $g_{ij\xi}$

According to Eq. (9.5) the explicit expression of the light-matter interaction matrix elements is given by

$$g_{ij\xi} = \tilde{E}_\xi \int d^3r \psi_i^{c*}(\mathbf{r}) e \mathbf{r} \mathbf{U}_\xi(\mathbf{r}) \psi_j^v(\mathbf{r}),$$

where $\tilde{E}_\xi = \sqrt{\hbar\omega_\xi/2\epsilon\epsilon_0 V}$ and V is the normalization volume. In envelope-function approximation [68, 154] the wave-functions $\psi_i^c(\mathbf{r})$ and $\psi_j^v(\mathbf{r})$ can be decomposed into the envelope parts $\zeta_i^c(\mathbf{r})$ and $\zeta_j^v(\mathbf{r})$, which vary only slightly over a unit cell, and the rapidly oscillating Bloch factor $u_{\mathbf{k}\approx 0}^{c,v}(\mathbf{r})$. From this, one can deduce the approximate expression

$$g_{ij\xi} \approx \tilde{E}_\xi \mathbf{d}_{cv} \int d^3r \zeta_i^{c*}(\mathbf{r}) \mathbf{U}_\xi(\mathbf{r}) \zeta_j^v(\mathbf{r}) \quad (10.11)$$

with the bulk dipole-matrix element \mathbf{d}_{cv} . To keep matters simple, we consider here the case of equal envelopes for the conduction- and valence-band electrons.

For a system containing both localized QD states and delocalized WL states, there are three different cases to be considered: (i) both states $|i\rangle$ and $|j\rangle$ are QD states, (ii) one is a WL and one is a QD state, and (iii) both are WL states. Taking into account that the electromagnetic field is approximately constant over the extent of a QD, one finds for the first case

$$g_{\nu\nu'\xi} \approx \tilde{E}_\xi \mathbf{d}_{cv} \mathbf{U}_\xi(\mathbf{r}_0) \delta_{\nu\nu'} .$$

In this expression \mathbf{r}_0 is the position of the QD and the Kronecker-delta $\delta_{\nu\nu'}$ stems from the overlap of the carrier wave functions. For the second case, the coupling matrix element is zero, because the QD states and the WL states are orthogonal as they are eigenstates of the same single-particle Hamiltonian.

For the third case, we assume that the WL states are plane waves and that the extension of the wave-function perpendicular to the growth direction is negligible. Then one finds

$$g_{\mathbf{k}\mathbf{k}'\xi} \approx \tilde{E}_\xi \mathbf{d}_{cv} \frac{1}{A} \int d^2\rho e^{-i(\mathbf{k}-\mathbf{k}')\rho} \mathbf{U}_\xi(\rho, z_0) = \tilde{E}_\xi \mathbf{d}_{cv} \tilde{\mathbf{U}}_\xi(\mathbf{k} - \mathbf{k}', z_0) . \quad (10.12)$$

Here z_0 is the z -coordinate of the position of the WL plane and $\tilde{\mathbf{U}}_\xi(\mathbf{q}, z_0)$ denotes the Fourier transformed mode function with respect to the x - y plane. As the mode function in real space varies typically only over macroscopic distances, its Fourier transform is strongly peaked around $\mathbf{q} = 0$. In equations defining observable quantities one never encounters the coupling matrix element itself, which could in principle be complex, but always the square of the absolute value. Typical expressions are of the form $\sum_{\mathbf{k}'} |g_{\mathbf{k}\mathbf{k}'\xi}|^2 f(\mathbf{k}')$ with some function $f(\mathbf{k}')$, which varies only slowly with \mathbf{k}' . Using Parseval's theorem [155], which in our situation can be formulated as $\sum_{\mathbf{k}} |\tilde{h}_{\mathbf{k}}|^2 = \frac{1}{A} \int d^2\rho |h(\rho)|^2$, one obtains $\sum_{\mathbf{k}'} |g_{\mathbf{k}\mathbf{k}'\xi}|^2 f(\mathbf{k}') \approx f(\mathbf{k}) \tilde{E}_\xi^2 \frac{1}{A} \int d^2\rho |\mathbf{d}_{cv} U_\xi(\mathbf{p}, z=0)|^2$. Due to this fact and the strong localization of $\tilde{\mathbf{U}}_\xi(\mathbf{q}, z_0)$ around $\mathbf{q} = 0$, one can use to a good approximation instead of Eq. (10.12) the simpler relation

$$g_{\mathbf{k}\mathbf{k}'\xi} \approx \delta_{\mathbf{k},\mathbf{k}'} \tilde{E}_\xi \sqrt{\frac{1}{A} \int d^2\rho |\mathbf{d}_{cv} \mathbf{U}_\xi(\mathbf{p}, z=0)|^2} . \quad (10.13)$$

In the special situation that the modes are those of free space, $\mathbf{U}_\xi(\mathbf{r})$ is proportional to $\mathbf{e}_p(\mathbf{q}) e^{i\mathbf{q}\mathbf{r}}$, and the last term in the previous equation reduces to $|\mathbf{d}_{cv} \mathbf{e}_p(\mathbf{q})|$. In order to check Eq. (10.13), one may rederive the coupling strength and in particular the diagonality, expressed by $\delta_{\mathbf{k},\mathbf{k}'}$, in the case of WL states coupled to free space by inserting the free-space mode directly into Eq. (10.11). Doing so, we readily obtain $g_{\mathbf{k}\mathbf{k}'\xi} \propto \delta_{\mathbf{k},\mathbf{k}'+\mathbf{q}_{||}}$. By neglecting the tiny photon momentum in comparison with the large electron momentum, the component $\mathbf{q}_{||}$ can be dropped and one arrives again at $g_{\mathbf{k}\mathbf{k}'\xi} \propto \delta_{\mathbf{k},\mathbf{k}'}$, which confirms Eq. (10.13).

The three different cases can be summarized as

$$g_{ij\xi} = g_{i\xi} \delta_{ij} \quad (10.14)$$

where i and j denote either WL or QD states. From this expression follows that optical transitions occur only between ‘equal’ states of conduction- and valence-band electrons, that is, for example, between the s -shells and the p -shells or between WL states with equal momentum.

10.2.2 Symmetry Considerations

In this section we investigate the influence of the underlying symmetry of the system. As already mentioned in the introduction, the presence of the QDs destroys the translational symmetry of the WL. However, considering circular symmetric QDs we still have rotational symmetry around the QD axis. Strictly speaking, this statement is only true for a single QD placed on a WL, because any additional QD on the WL plane will destroy this rotational symmetry. Nevertheless, if we assume an ensemble of *randomly* distributed QDs, the rotational symmetry is restored 'on average'¹. This makes it possible to carry over the considerations for a single dot to a QD ensemble.

From the rotational symmetry of the system around the z -axis, it can be deduced that the corresponding second-quantized angular momentum operator $l_{\text{tot}}^z = \sum l_i^{z,c} c_i^\dagger c_i + l_i^{z,v} v_i^\dagger v_i$ commutes with the total Hamiltonian (9.1). Here $l_i^{z,(c,v)}$ is the angular-momentum z -component of the single-particle state $|i\rangle$. This commutation takes place because the angular momentum-operator generates the rotations around the z -axis [70], which leaves the system invariant. Alternatively one can explicitly check the commutation using the symmetry properties of the Coulomb matrix elements $V_{ijkl} \propto \delta_{l_i^z + l_j^z, l_k^z + l_l^z}$ explained in Section 1.2. As the Hamiltonian commutes with the angular momentum operator it can be verified that the commutator

$$[c_i^\dagger c_j, l_{\text{tot}}^z] = -(l_i^{z,c} - l_j^{z,c}) c_i^\dagger c_j$$

holds not only in the Schrödinger but also in the Heisenberg representation. From this one obtains for the time-dependent operator averages calculated in Heisenberg representation,

$$-(l_i^{z,c} - l_j^{z,c}) \langle c_i^\dagger c_j \rangle = \text{Tr}\{\rho_0 [c_i^\dagger c_j, l_{\text{tot}}^z]\} = \text{Tr}\{c_i^\dagger c_j [l_{\text{tot}}^z, \rho_0]\} = 0 . \quad (10.15)$$

Here Tr denotes the trace and the general identity $\text{Tr}\{A[B, C]\} = \text{Tr}\{B[C, A]\}$ was used. Additionally the commutation of the angular-momentum operator with the density operator ρ_0 was assumed. One may ask whether this assumption is a plausible one. In equilibrium it clearly is, as one has $\rho_0 \propto e^{-\beta H}$. Then $[l_{\text{tot}}^z, H] = 0$ immediately gives $[l_{\text{tot}}^z, \rho_0] = 0$. In a more general case the density matrix can be written as $\sum_i p_i |\psi_i\rangle \langle \psi_i|$ with some many-particle states $\{|\psi_i\rangle\}_i$. Commutation of ρ_0 with l_{tot}^z in this situation means that the many-particle states $\{|\psi_i\rangle\}_i$ must all be rotational invariant. This is the case, if one excites the system with an external optical pulse directed along its symmetry axis, because the Hamiltonian describing the evolution of the internal degrees of freedom will not destroy this imposed symmetry.

After this discussion about the validity of the expression, we turn to its consequences. From Eq. (10.15) it immediately follows that

$$\langle c_i^\dagger c_j \rangle = 0 \quad \text{if} \quad l_i^{z,c} \neq l_j^{z,c} , \quad (10.16)$$

¹ How the translational invariance is on average restored in a randomly distributed ensemble of QDs is discussed in Ref. [17].

meaning that if the single-particle states $|i\rangle$ and $|j\rangle$ have different angular momentum l_i^z , the generalized populations $\langle c_i^\dagger c_j \rangle$ are always zero. Using the terminology of annihilation and creation operators one may interpret this as follows: It is only possible to have non-zero expectation values, if the particle being destroyed has the same angular momentum as the particle being created. For a QD confining solely an s - and a p -shell, the states are uniquely defined by their angular momentum so that only the proper populations $\langle c_i^\dagger c_j \rangle$ with $i = j$ can be non-zero.

Along the same lines we can deduce ‘selection rules’ for expectation values containing more than two operators. For example, for the four-operator average $\langle c_i^\dagger c_j^\dagger c_k c_l \rangle$, one finds $\langle c_i^\dagger c_j^\dagger c_k c_l \rangle = \delta_{l_i^z + l_j^z, l_k^z + l_l^z} \langle c_i^\dagger c_j^\dagger c_k c_l \rangle$. This has immediate consequences for the correlation functions as it shows that one has to calculate only a fraction of all possible matrix elements C_{ijkl}^e .

10.2.3 Formulation of the SLE for the Quantum Dot Model

In this section we study the simplifications of the SLE that arise from the diagonality of the light-matter matrix elements and of the symmetry considerations of the previous section. From the latter we recall that one can take $\langle a_i^\dagger a_j \rangle = f_i^a \delta_{ij}$, as all off-diagonal terms $\langle a_i^\dagger a_j \rangle$ with $i \neq j$ describe ‘forbidden’ transitions and remain zero. Therefore in the incoherent regime expectation values of two carrier operators are restricted to populations. Additionally, one can derive $\langle b_\xi^\dagger v_i^\dagger c_j \rangle = \delta_{ij} \langle b_\xi^\dagger v_i^\dagger c_i \rangle$, as the boson operator b_ξ commutes with the total angular momentum operator $l_{\text{tot}}^z = \sum l_i^{z,c} c_i^\dagger c_i + l_i^{z,v} v_i^\dagger v_i$.

Carrier Population and Photon Number

Incorporating the discussed simplifications, we get

$$\begin{aligned} i\hbar \frac{\partial}{\partial t} \langle c_i^\dagger c_i \rangle &= -2i \operatorname{Re} \left\{ \sum_{\xi} g_{i\xi}^* \langle b_\xi^\dagger v_i^\dagger c_i \rangle \right\} \\ &\quad + 2i \operatorname{Im} \left\{ \sum_{234} V_{i234} (C_{2i43}^e - C_{i243}^X) \right\}, \end{aligned} \quad (10.17)$$

for the population dynamics and

$$i\hbar \frac{\partial}{\partial t} \langle b_\xi^\dagger b_\xi \rangle = +2i \operatorname{Re} \left\{ \sum_1 g_{1\xi}^* \langle b_\xi^\dagger v_1^\dagger c_1 \rangle \right\} \quad (10.18)$$

for the photon number.

Photon-Assisted Polarization

Both equations couple to the photon-assisted polarization, which – compared to the general expression of Eq. (10.6) – is now strongly simplified and reads

$$\begin{aligned}
 i\hbar \frac{\partial}{\partial t} \langle b_\xi^\dagger v_i^\dagger c_i \rangle = & (\tilde{\varepsilon}_i^c - \tilde{\varepsilon}_i^v - \hbar\omega_\xi - i\Gamma) \langle b_\xi^\dagger v_i^\dagger c_i \rangle \\
 & + ig_{ii\xi} f_i^c (1 - f_i^v) + i \sum_1 g_{1\xi} C_{1ii1}^X \\
 & + i(f_i^c - f_i^v) \sum_{\xi'} g_{1\xi'} \langle b_\xi^\dagger b_{\xi'} \rangle \\
 & + (f_i^c - f_i^v) \sum_1 V_{i1i1} \langle b_\xi^\dagger v_1^\dagger c_1 \rangle .
 \end{aligned} \tag{10.19}$$

The free evolution in the first line is determined by the Hartree-Fock renormalized energies

$$\begin{aligned}
 \tilde{\varepsilon}_i^c &= \varepsilon_i^c - \sum_1 V_{i1i1} f_1^c + \sum_1 V_{1ii1} (f_1^c + f_1^v - 1) \\
 \tilde{\varepsilon}_i^v &= \varepsilon_i^v - \sum_1 V_{i1i1} (f_1^v - 1) - \sum_1 V_{1ii1} (f_1^c + f_1^v - 1)
 \end{aligned}$$

for the conduction and valence band as well as the resonance frequency ω_ξ of the optical mode ξ . Additionally a phenomenological dephasing Γ , which broadens the spectral lines, was introduced. Note that the inclusion of the ‘–1’ in the terms ‘ $f_1^v - 1$ ’ of the renormalized energies reflects the assumption that the influence of the filled valence band is already included in the band structure calculation. In this case the single-particle energies fulfill $\tilde{\varepsilon}_i^{v,c} = \varepsilon_i^{v,c}$ in the case of a full valence and empty conduction band. Note further that in the case of identical envelopes, the Hartree contribution to the renormalized energies in the evolution of $\langle b_\xi^\dagger v_i^\dagger c_i \rangle$ cancel as only energy differences occur. The source term of spontaneous emission in the second line enters the theory naturally due to the quantization of the light field. The term in the third line represents stimulated emission/absorption, which contributes, for example, if an external field is resonant with the considered transitions or if a resonator provides feedback for the emitted photons. Whether this term describes emission or absorption depends on the sign of the phase-space filling or Pauli blocking factor $(f_i^c - f_i^v) = -(1 - f_i^e - f_i^h)$ and therefore on the excitation conditions. The term in the last line is analogous to the quantum well case, where it gives rise to the excitonic PL below the band gap [156]. Here it introduces the corresponding excitonic resonances for the QD states due to the interband Coulomb exchange interaction.

Correlation Functions

Besides the photon-assisted polarization, the expressions for the equations of motion of the interband correlations as given in Eq. (10.8) reduce considerably for QDs with two shells: First, the fourfold sum of the singlet terms can straightforwardly be evaluated. Secondly, for the terms containing the correlation functions, this sum reduces to a two-fold summation. Thirdly, one can simplify the last two lines of Eq. (10.8), because all the occurring correlation matrix elements contain three outer indices. To see the implied simplification, let us, as an example, consider the term $\sum_{1234} V_{1234} \delta_{i4} \langle c_1^\dagger c_3 \rangle C_{2jkl}^X$, which can be simplified to

$$\sum_{1234} V_{1234} \delta_{i4} \langle c_1^\dagger c_3 \rangle C_{2jkl}^X = \sum_{23} V_{323i} f_3^c C_{2jkl}^X = \left(\sum_3 V_{3i3i} f_3^c \right) C_{ijkl}^X .$$

In the first step we used $\langle c_1^\dagger c_3 \rangle = \delta_{13} f_3^c$ and performed the summation over 1 and 4. In the second step the relation $V_{323i} \propto V_{3i3i} \delta_{i2}$, which is valid because the states can uniquely be identified by their angular momentum, was used and the summation over 2 was performed. The parenthesis is used to underline that these Fock terms, identified by the index order V_{ijij} in the Coulomb matrix element, can be incorporated into a renormalized energy for the single-particle state $|i\rangle$. In addition to the Fock terms, one finds Hartree-renormalization (again identified by the order of the indices in the Coulomb matrix elements) from the last line of Eq. (10.8). Combining these results we obtain for the interband correlations:

$$\begin{aligned} i\hbar \frac{\partial}{\partial t} C_{ijkl}^X &= -(\tilde{\varepsilon}_i^c + \tilde{\varepsilon}_j^v - \tilde{\varepsilon}_k^c - \tilde{\varepsilon}_l^v) C_{ijkl}^X \\ &\quad - V_{klji} [f_k^c f_j^v (1 - f_i^c)(1 - f_l^v) - (1 - f_k^c)(1 - f_j^v) f_i^c f_l^v] \\ &\quad + (f_j^v - f_l^v) \sum_{12} V_{1lj2} (C_{i1k2}^X + C_{i1k2}^c) + (f_i^c - f_k^c) \sum_{12} V_{k12i} (C_{1j2l}^X + C_{1j2l}^v) \\ &\quad + (1 - f_l^v - f_k^c) \sum_{12} V_{kl12} C_{ij21}^X - (1 - f_i^c - f_j^v) \sum_{12} V_{12ji} C_{12kl}^X \\ &\quad + (f_i^c + f_l^v) \sum_{12} V_{1l2i} C_{1jk2}^X - (f_k^c + f_j^v) \sum_{12} V_{k1j2} C_{i12l}^X \\ &\quad + (f_k^c - f_i^c) \sum_{12} V_{k1i2} C_{1j2l}^X + (f_l^v - f_j^v) \sum_{12} V_{1l2j} C_{i1k2}^X \\ &\quad + i \delta_{il} \delta_{jk} \left\{ (f_i^c - f_i^v) \sum_\xi g_{i\xi}^* \langle b_\xi^\dagger v_j^\dagger c_j \rangle + (f_j^c - f_j^v) \left(\sum_\xi g_{j\xi}^* \langle b_\xi^\dagger v_i^\dagger c_i \rangle \right)^* \right\} . \end{aligned} \tag{10.20}$$

Here the first two lines correspond to a calculation of C^X in singlet approximation. A theory restricted to this level was used in [143, 156] for the description of quantum-well luminescence. Note that the singlet factorization of three-particle averages already goes beyond the pure Hartree-Fock approximation, though not consistently. By solving

the equation for the interband correlations on this level in the adiabatic regime and inserting the resulting expression for C_{ijkl}^X into Eq. (10.17), reveals the Boltzmann-like nature of these scattering terms. The terms in the third line can be shown to provide screening according to the Lindhard theory for the Coulomb potential in Eq. (10.19). The following six terms describe Coulomb renormalizations due to scattering between all possible states. Finally, the last line contains the contributions due to the light-matter interaction.

For the intraband correlations one finds:

$$\begin{aligned}
 i\hbar \frac{\partial}{\partial t} C_{ijkl}^c = & - (\tilde{\varepsilon}_i^c + \tilde{\varepsilon}_j^c - \tilde{\varepsilon}_k^c - \tilde{\varepsilon}_l^c) C_{ijkl}^c \\
 & - \left(V_{ijkl}^* - V_{ijlk}^* \right) [(1 - f_i^c)(1 - f_j^c)f_k^c f_l^c - f_i^c f_j^c (1 - f_k^c)(1 - f_l^c)] \\
 & + (f_k^c - f_j^c) \sum_{12} V_{k12j} (C_{i1l2}^c + C_{i1l2}^X) - (f_i^c - f_l^c) \sum_{12} V_{l12i} (C_{j1k2}^c + C_{j1k2}^X) \\
 & - (f_k^c - f_i^c) \sum_{12} V_{k12i} (C_{j1l2}^c + C_{j1l2}^X) + (f_j^c - f_l^c) \sum_{12} V_{l12j} (C_{i1k2}^c + C_{i1k2}^X) \\
 & + (1 - f_l^c - f_k^c) \sum_{12} V_{kl21} C_{ij12}^c - (1 - f_i^c - f_j^c) \sum_{12} V_{12ji} C_{12kl}^c \\
 & - (f_i^c - f_l^c) \sum_{12} V_{l1i2} C_{1jk2}^c + (f_k^c - f_i^c) \sum_{12} V_{1k2i} C_{1j2l}^c \\
 & + (f_k^c - f_j^c) \sum_{12} V_{1k2j} C_{i12l}^c - (f_j^c - f_l^c) \sum_{12} V_{l1j2} C_{i1k2}^c
 \end{aligned} \tag{10.21}$$

and a similar expression for C^v . The interpretation of the individual terms runs in close analogy to the case of the interband correlation functions C^X .

Now that we have established a consistent theory for the evaluation of the PL of semiconductor QDs, we use these equations in the next chapter to investigate the emission into free space. In particular we discuss how correlations influence the emission spectra and the decay behavior.

11 Photoluminescence

In this section the QD emission into ‘free space’ is studied. Strictly speaking, a coupling to the photonic modes of the ‘free space’ is not possible, because QDs are always grown on a substrate and then overgrown to guarantee the three-dimensional carrier confinement. Nevertheless for *unpatterned* structures the modifications of the electromagnetic field are weak, so that we can approximate the modes by plane waves that are solutions for the homogeneous space. In Chapter 12 the luminescence dynamics of QDs in optical resonators, which provide a three-dimensional confinement of the electromagnetic field, will be investigated.

This chapter is organized as follows: First we define the expression for the luminescence spectrum and show how it can be simplified in the case of ‘free space’. Then the adiabatic solution of the SLE in the HF limit is presented. This provides general insight into the structure of the PL spectrum. After this, the influence of correlations is analyzed in Section 11.3. The final Section deals with time-resolved PL. In particular we investigate two limiting cases: the HF-approximation and the two-level approximation. Furthermore we present full numerical results and discuss the role of dephasing of the correlations on the PL dynamics.

11.1 Definition of the Spectrum

We define the time-dependent luminescence spectrum $I(\omega)$ according to [153, 157] and consider the limit of high frequency resolution of a detector to obtain

$$I(\omega) d\omega = \sum_{\substack{\xi \\ \hbar\omega_\xi \in [\hbar\omega, \hbar(\omega+d\omega)]}} \frac{\partial}{\partial t} \langle b_\xi^\dagger b_\xi \rangle . \quad (11.1)$$

This is nothing but the total number of photons generated per unit time having an energy in the interval $[\hbar\omega, \hbar(\omega + d\omega)]$. If the coupling to ‘free space’ is considered, the mode label ξ contains the wave vector \mathbf{q} and the polarization vector $\mathbf{e}_p(\mathbf{q})$ with $p = \pm$ denoting the two possible perpendicular polarizations. In the continuum limit, in which the quantization volume of the electromagnetic field becomes infinite and the energetic spacing between different modes approaches zero, the above summation over \mathbf{q} can be transformed into an integral according to $\frac{1}{V} \sum_{\mathbf{q}} \rightarrow \frac{1}{(2\pi)^3} \int d^3 q$.

To further evaluate the expression of the luminescence spectrum, we proceed by analyzing the total intensity

$$\begin{aligned} I_{\text{tot}} = \int d\omega I(\omega) &= \sum_{\xi} \frac{\partial}{\partial t} \langle b_{\xi}^{\dagger} b_{\xi} \rangle = \sum_{\xi} \frac{2}{\hbar} \text{Re} \sum_i g_{i\xi}^* \langle b_{\xi}^{\dagger} v_i^{\dagger} c_i \rangle \\ &= \frac{2}{\hbar} \text{Re} \sum_i \sum_{\xi} |g_{i\xi}|^2 \widetilde{\langle b_{\xi}^{\dagger} v_i^{\dagger} c_i \rangle}. \end{aligned} \quad (11.2)$$

Here the quantity $\widetilde{g_{i\xi}\langle b_{\xi}^{\dagger} v_i^{\dagger} c_i \rangle} = \langle b_{\xi}^{\dagger} v_i^{\dagger} c_i \rangle$ was introduced and the equation of motion for the photonic population (10.18) was used. By rescaling the photon-assisted polarization with the light-matter coupling, it is obvious that in the actual observable quantity only the modulus square of the coupling matrix elements enters. Another consequence of this rescaling is that the redefined photon-assisted polarization depends only on the photon energy $\hbar\omega = \hbar c |\mathbf{q}|$ and neither on the direction nor on the polarization of the mode ξ . This allows us to perform the part of the summation $\sum_{\xi} |g_{i\xi}|^2$ that runs over the three-dimensional wave vector and the two polarization directions in the way it is usually done in the Wigner-Weisskopf theory of spontaneous emission [145]. Then we can write $\widetilde{\langle b_{\xi}^{\dagger} v_i^{\dagger} c_i \rangle} = \langle b_{\omega}^{\dagger} v_i^{\dagger} c_i \rangle$, where $\omega = cq$ denotes the frequency of the mode and q is the modulus of \mathbf{q} , which reduces the original three-dimensional problem to a one-dimensional one. For the explicit evaluation of the last sum in Eq. (11.2), we consider a general function f that depends only on q , for which we obtain

$$\begin{aligned} \sum_{\xi} |g_{i\xi}|^2 f(q) &\rightarrow \frac{1}{2\epsilon_0\epsilon_r(2\pi)^3} \int d^3 q \hbar c q \sum_{p=\pm} |\mathbf{d}_{cv} \mathbf{e}_p(\mathbf{q})|^2 f(q) \\ &= \frac{\hbar |\mathbf{d}_{cv}|^2}{6\pi^2\epsilon_0\epsilon_r c^3} \int d\omega \omega^3 f\left(\frac{\omega}{c}\right). \end{aligned} \quad (11.3)$$

In the first line the continuum limit was performed and the definition Eq. (9.5) of the light-matter coupling $g_{i\xi}$ was used. To reach the second line we did the following: (i) we used $\sum_{p=\pm} |\mathbf{d}_{cv} \mathbf{e}_p(\mathbf{q})|^2 = |\mathbf{d}_{cv}|^2 \sin^2 \theta$, where θ denotes the angle between the dipole matrix element \mathbf{d}_{cv} and the propagation direction¹ \mathbf{q} , (ii) we employed spherical coordinates, (iii) the resulting angular integrals were carried out, and (iv) the trivial transformation from $|\mathbf{q}|$ to ω was used. With the help of expression (11.3) we find for the photo-luminescence spectrum by identifying $f(q)$ with $\widetilde{\langle b_{\xi}^{\dagger} v_i^{\dagger} c_i \rangle}$

$$I(\omega) = \frac{2}{\hbar} \text{Re} \sum_i |\tilde{g}_{i\omega}|^2 \widetilde{\langle b_{\omega}^{\dagger} v_i^{\dagger} c_i \rangle}. \quad (11.4)$$

Here $|\tilde{g}_{i\omega}|^2 = \frac{\hbar |\mathbf{d}_{cv}|^2 \omega^3}{6\pi^2\epsilon_0\epsilon_r c^3}$ denotes the integrated light-matter interaction matrix-element.

¹ From this relation one can easily see that the number of photons produced per unit time and propagating in the direction \mathbf{q} , $\frac{\partial}{\partial t} \sum_{p=\pm} \langle b_{\mathbf{q}p}^{\dagger} b_{\mathbf{q}p} \rangle$, is proportional to $\sin^2 \theta$. This is in accordance with the far-field pattern of an oscillating dipole known in the context of classical electrodynamics [158].

11.2 Adiabatic Approximation in Hartree-Fock

In this section we investigate the stationary PL spectrum in the HF approximation. This analysis provides insight into the structure of the SLE and will be the basis for the discussion of the PL spectra for the general case in Section 11.3. Only for the sake of a simpler illustration we start by considering the spectrum in the absence of Coulomb interaction. In this way it is possible to obtain directly an analytic expression for the PL spectrum. In a second step we include Coulomb interaction and find that also in this case some general, analytic statements can be made. For the results presented in Section 11.3 none of the simplifying assumptions are made and higher order correlations as well as Coulomb interaction are taken into account.

As an introduction to the problem, we start with the most simple case and neglect Coulomb interaction. By definition, all correlations are neglected in the HF approximation. Therefore the set of equations reduces to Eqs. (10.17) to (10.19), in which additionally all terms containing correlations or Coulomb-matrix elements vanish. Furthermore, the term describing the stimulated emission/absorption can be neglected, because emission into ‘free space’ is considered. Because population changes typically occur on a nanosecond time-scale, the carrier populations can be assumed to be stationary for the evaluation of the spectrum. In this case, the equations evolve into a steady-state solution and we find for the photon-assisted polarization

$$\langle b_\xi^\dagger v_i^\dagger c_i \rangle_{\text{stat}} = - \frac{i g_{i\xi} f_i^c (1 - f_i^v)}{\varepsilon_i^c - \varepsilon_i^v - \hbar\omega_\xi - i\Gamma} . \quad (11.5)$$

Inserting this expression into Eq. (11.4), yields for the luminescence spectrum

$$\begin{aligned} I(\omega) &= \frac{2}{\hbar} \text{Re} \sum_i \frac{-i |\tilde{g}_{i\omega}|^2 f_i^c (1 - f_i^v)}{\varepsilon_i^c - \varepsilon_i^v - \hbar\omega - i\Gamma} \\ &= \frac{2\pi}{\hbar} \sum_i |\tilde{g}_{i\omega}|^2 f_i^c (1 - f_i^v) \delta_\Gamma(\varepsilon_i^c - \varepsilon_i^v - \hbar\omega) \end{aligned} \quad (11.6)$$

where $\delta_\Gamma(E) = \frac{1}{\pi} \frac{\Gamma}{E^2 + \Gamma^2}$ is a broadened δ -function. From this expression it can be inferred that one will observe a PL-spectrum at the transition energies $\varepsilon_i^c - \varepsilon_i^v$ whenever the according conduction-band state is occupied and the corresponding valence-band state is unoccupied. In the *e-h*-picture the factor $f_i^c (1 - f_i^v)$ becomes the product $f_i^e f_i^h$. Consequently, one will observe luminescence from the *s*- and the *p*-shell unless the carrier density and the temperature are so low that the *p*-shell states are unoccupied.

In the presence of Coulomb interaction, the situation is more complicated. Still considering the HF limit and ignoring the term responsible for stimulated emission/absorption, one finds for the steady state solution of the photon-assisted polarization

$$\sum_1 \left\{ (\tilde{\varepsilon}_i^c - \tilde{\varepsilon}_i^v - \hbar\omega - i\Gamma) \delta_{1i} + (f_i^c - f_i^v) V_{i1i1} \right\} \langle b_\xi^\dagger v_1^\dagger c_1 \rangle = -i g_{i\xi} f_i^c (1 - f_i^v) , \quad (11.7)$$

which can more conveniently be expressed as a matrix equation

$$\underline{\underline{M}}(\omega) \underline{\psi} = -i\underline{F} . \quad (11.8)$$

Here the vector $\underline{\psi}$ contains the rescaled photon-assisted polarizations $\widetilde{\langle b_\xi^\dagger v_i^\dagger c_i \rangle}$, the matrix $\underline{\underline{M}}(\omega)$ contains the curly bracket from Eq. (11.7) and the source of spontaneous emission \underline{F} has $f_i^c(1-f_i^v)$ as its components. Note that for given electronic population the matrix $\underline{\underline{M}}(\omega)$ depends only on the mode frequency.

This matrix equation can straightforwardly be solved for each ω by matrix inversion, but no insight into the structure of the solution and the resulting PL spectrum is gained. Therefore, it is more instructive to rewrite the matrix $\underline{\underline{M}}(\omega)$ as $\widetilde{\underline{M}} - (\hbar\omega + i\Gamma)\underline{1}$, where $\widetilde{\underline{M}}$ does not longer depend on the frequency and $\underline{1}$ is the unity matrix. It should be emphasized here that $\widetilde{\underline{M}}$ is in general not hermitian due to the phase-space filling factors $(f_i^c - f_i^v)$ and becomes only hermitian for special situations, like the ground state, for which $f_i^c = 0$ and $f_i^v = 1$. Nevertheless, the matrix $\widetilde{\underline{M}}$ can be diagonalized by the non-unitary matrix S according to $\underline{S}^{-1} \widetilde{\underline{M}} \underline{S} = \underline{D}$ with the diagonal matrix $\underline{D} = \text{diag}(\lambda_1, \lambda_2, \dots, \lambda_n)$. By defining the two vectors $\tilde{\underline{F}} = \underline{S}^{-1} \underline{F}$ and $\tilde{\underline{v}} = \underline{S}^t \underline{1}$ where $\underline{1}$ is a vector with all components being one, the spectrum is given by

$$I(\omega) = \frac{2}{\hbar} \text{Re} \sum_i \tilde{v}_i^t \frac{-i|\tilde{g}_{i\omega}|^2}{\lambda_i - \hbar\omega - i\Gamma} \tilde{F}_i . \quad (11.9)$$

For a real-valued transformation matrix \underline{S} and real eigenvalues λ_i , this equation shows that one can observe PL at the eigenvalues λ_i of the matrix $\widetilde{\underline{M}}$. Note that in the absence of Coulomb interaction (i) $\widetilde{\underline{M}}$ is diagonal with eigenvalues $\lambda_i = \varepsilon_i^c - \varepsilon_i^v$, (ii) $\underline{S} = \underline{1} \Rightarrow \tilde{v}_i = 1$, and (iii) $\tilde{F}_i = f_i^c(1-f_i^v)$, so that Eq. (11.6) is reproduced. Furthermore it can be inferred from Eq. (11.6) that the energetic position λ_i of the luminescence peaks depends in HF-approximation only on the carrier system and not on the light-matter interaction.

If correlations are included, it seems at first glance that the correlation terms can simply be added to the source term in Eq. (11.7) and that one could otherwise proceed as above. This is not the case, however, since in the presence of correlations Eq. (11.7) cannot directly be solved for $\langle b^\dagger v^\dagger c \rangle$, because the correlations C_{ijkl}^X themselves depend on the photon-assisted polarization $\langle b^\dagger v^\dagger c \rangle$, according to the last line in Eq. (10.20). Therefore, the inclusion of the correlation could in principle lead not only to different PL intensities but also to a shift of the emission lines with respect to the eigenvalues λ_i . Despite this fact we did not observe such a energetic shift for the studied parameters.

11.3 Results for Luminescence Spectra

We now present results for the numerical solution of the equations derived in the previous sections. The equations are solved in the time domain using a fourth order Runge-Kutta method. The material parameters are those from Chapter 1 for an InGaAs QD system and a density of QDs on the WL of $3 \cdot 10^{10} \text{ cm}^{-2}$, a bandgap energy of 1.52 eV and the bulk dipole matrix element of GaAs of $9.13 \cdot 10^{-29} \text{ As m}$ is used. We further assume that the excitation involves only carriers with one spin polarization, e.g., due to excitation with circular polarized light. As already mentioned, it is beyond the scope of this thesis to study the dynamics of the carrier generation and relaxation. Since these processes are much faster than the recombination dynamics, a quasi-equilibrium distribution of carriers with given carrier density and temperature is used as an initial state for the calculation.

Initial Conditions for the Correlations

Within such an assumption, the initial values for the correlation functions C^X , C^e , and C^v remain open. For an unexcited system all correlation functions are zero and build up during the carrier generation process according to their equations of motion. Starting a calculation with quasi-equilibrium population and vanishing correlation functions can lead to a too abrupt build-up of correlations, resulting in unphysical oscillations of the correlation matrix elements, which then carry over to the population dynamics.

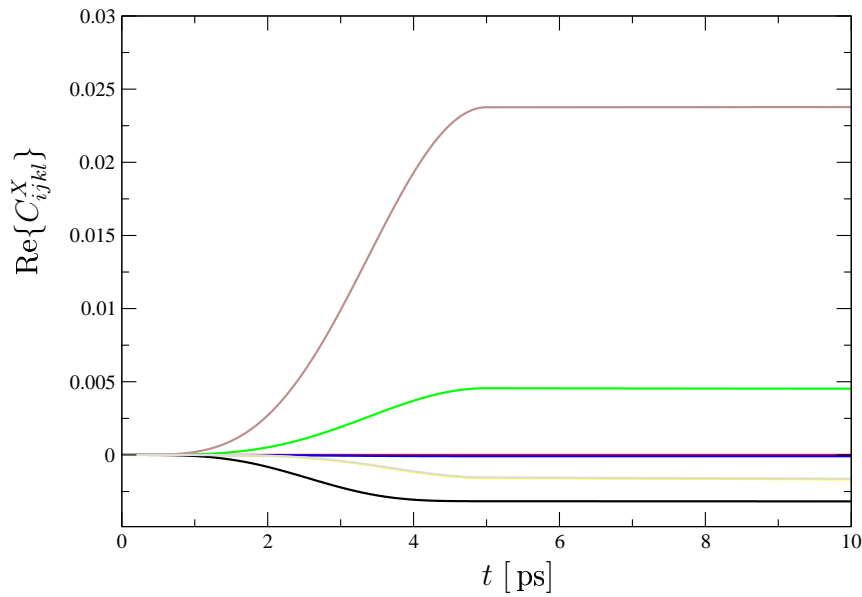


Figure 11.1: Time evolution of the real part of the 3^4 interband correlation matrix elements C_{ijkl}^X . The population is adiabatically switched on over a time interval of 5 ps. Thereafter quasi-stationary solutions for the matrix elements are found. ($n_e = 1.5 \cdot 10^{10} \text{ cm}^{-2}$, $T = 30K$).

To avoid these unphysical results, we numerically determine the initial conditions for the correlation functions from their equations of motion. For this purpose, a separate calculation is performed, in which the carrier populations are adiabatically increased to their equilibrium values. The resulting solutions for the correlations then provide the starting point for the actual time-evolution of the carrier and photon dynamics. The evolution of the real-part of the interband correlation matrix elements during the ramp-up of the population are depicted in Figure 11.1. From the $3^4 = 81$ matrix elements C_{ijkl}^X with $i, j, k, l \in \{0, +1, -1\}$ there are 19 elements that are not equal to zero due to the symmetry constraints discussed in Section 10.2.2. Here, one finds seven different values, of which five can clearly be distinguished in Figure 11.1. For the imaginary parts, one finds after the adiabatic switch-on phase only tiny values. It is important to note that neither the exact form of the ramp-up function nor the time in which the build-up takes place is important. Even for switch-on times as short as 1 ps, one observes only small amplitude oscillations around the values depicted in Figure 11.1. However, for a very abrupt increase $t_{\text{switch}} \ll 1 \text{ ps}$ one finds rapid, large amplitude oscillations for the correlations that then carry over to the population dynamics, leading to additional unphysical peaks in the PL.

Results for the Stationary PL Spectrum

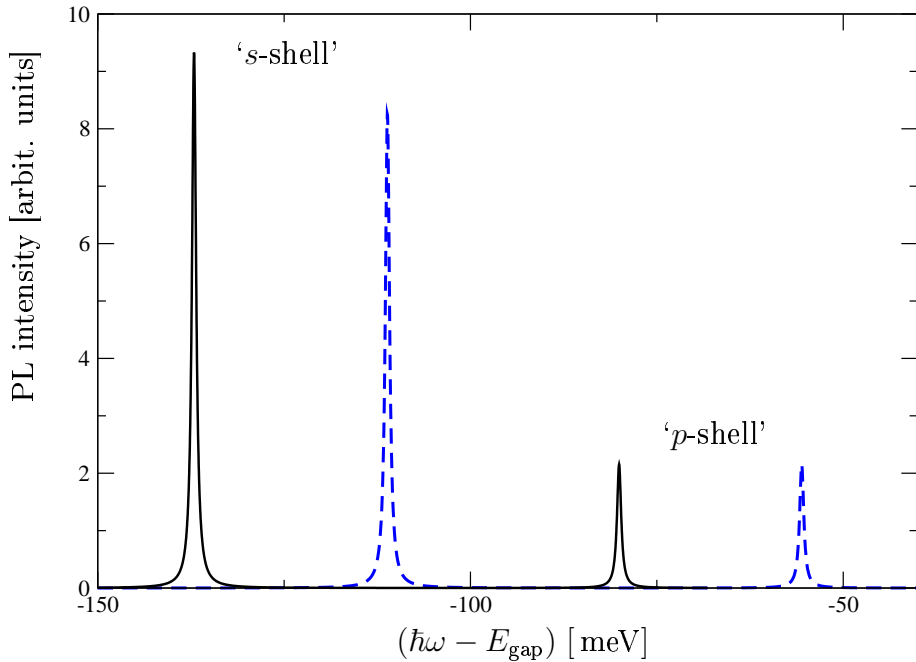


Figure 11.2: Stationary PL spectrum for fixed carrier population. The solid line corresponds to the full calculation. The dashed line gives the result in the absence of Coulomb interaction. ($n_e = 3.0 \cdot 10^{10} \text{ cm}^{-2}$, $T = 200K$).

The PL spectrum in the presence and absence of Coulomb interaction for artificially suppressed population dynamics is plotted in Figure 11.2 for a temperature of $T = 200\text{ K}$ and an initial carrier density of $3.0 \cdot 10^{10}\text{ cm}^{-2}$. Coulomb interaction included and measured relative to the bandgap, the two peaks correspond to the s -shell resonance at about -137 meV and the p -shell transition at about -80 meV . Both peaks are red shifted due to the Coulomb interaction from the non-interacting energies² $\varepsilon_p^c + \varepsilon_p^v = -111\text{ meV}$ and $\varepsilon_s^c + \varepsilon_s^v = -55.5\text{ meV}$, respectively. The different peak heights for the s - and p - shell transitions mainly reflect that the population in the s -shell is higher than the population in the p -shells. An additional enhancement of the s -shell transition line in the presence of Coulomb interaction can be observed.

If one compares the result of a calculation on the singlet-doublet level to those obtained in Hartree-Fock approximation, as depicted in Figure 11.3, it is obvious that the correlations increase the PL intensity slightly but have – if any – only negligible influence on the peak position.

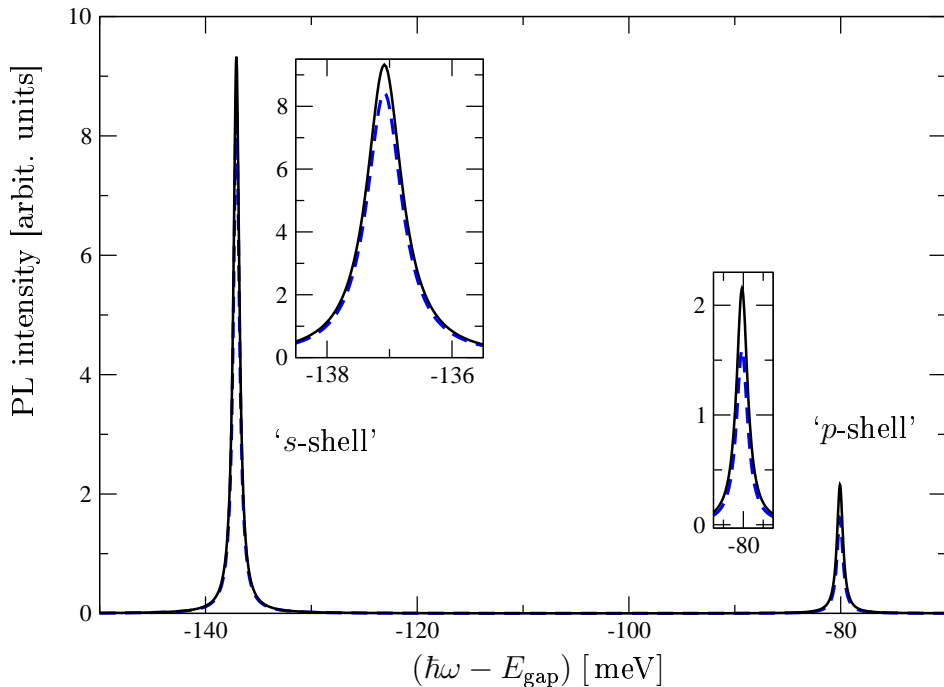


Figure 11.3: Stationary PL spectrum for fixed carrier population. The solid line corresponds to the a calculation including Coulomb interaction and correlations on singlet-doublet level. The dashed line to the Hartree-Fock factorization. The insets are included to allow for a better comparison of the PL intensities. ($n_e = 3.0 \cdot 10^{10}\text{ cm}^{-2}$, $T = 200\text{K}$).

² For a comparison to Part I and II note that in the present part the zero of the energy in each band is defined by the $\mathbf{k} = 0$ wetting layer state. In contrast, the electron and hole energies in the previous parts are measured relative to the bottom of the QD confinement potential.

The previous results were obtained at rather high population densities and elevated temperatures. If one compares these to those depicted in Figure 11.4 and obtained for a weaker carrier density of $1.5 \cdot 10^{10} \text{ cm}^{-2}$ and at a lower temperature $T = 30 \text{ K}$, several features can be observed: Again, the PL at the s -shell is only slightly enhanced by the correlations. In contrast, the p -shell PL of the HF calculation becomes negative, while it remains positive if the correlations are included. Contrary to an absorption spectrum, where a negative peak corresponds to gain, this result is unphysical and an artefact of the HF approximation at low temperatures.

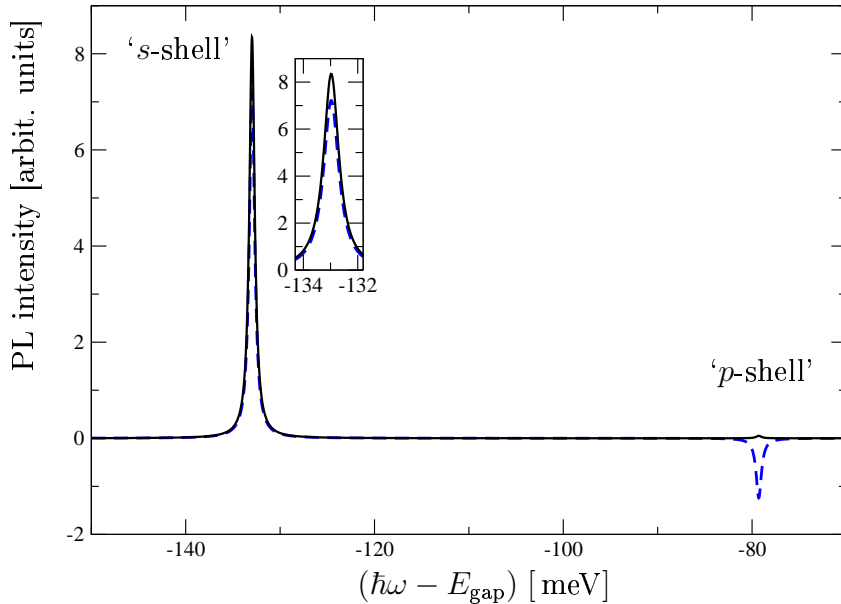


Figure 11.4: Stationary PL spectrum for fixed carrier population. The solid line corresponds to a calculation on singlet-doublet level, the dashed line to the Hartree-Fock factorization. The inset is included to allow for a better comparison of the PL intensities. ($n_e = 1.5 \cdot 10^{10} \text{ cm}^{-2}$, $T = 30 \text{ K}$).

In the absence of Coulomb interaction, it can easily be inferred from Eq. (11.6) that the PL spectrum in HF-approximation is always positive. Including Coulomb interaction, such a statement can no longer be made as the values of \tilde{v}_i and \tilde{F}_i in Eq. (11.9) have to be calculated explicitly. If the correlations are treated on the singlet-doublet level, however, we find that the spectrum remains positive. And it is only in this case that the whole set of equations of motion is truncated consistently, because the photon number itself is already a two-particle average. A mere HF treatment can, therefore, lead to unphysical results for extremely low temperatures. In considering the different contributions to the correlations it is noteworthy that the negative spectrum in the HF-approximation is introduced by the Coulomb interaction, and that it is again the Coulomb-generated terms of the correlations (C^X, C^e, C^v) that correct this artefact. The contribution to the correlation generated by the light-matter interaction play only a negligible role for the stationary PL spectrum.

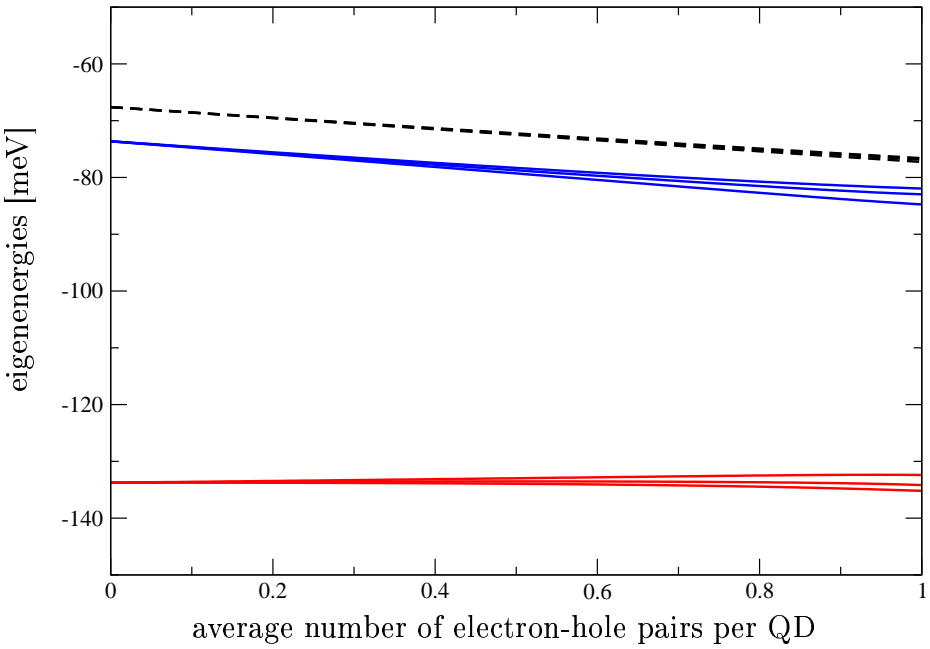


Figure 11.5: Eigenenergies in Hartree-Fock approximation for different temperatures as a function of the average number of electron-hole pairs per QD. The three low-energy solid lines correspond to the position of the s -shell resonance for temperature $T = 30, 70$, and 100 K (from top to bottom). The energetically higher solid lines correspond to the position of the p -shell resonance (this time the temperature varies from bottom to top). The dashed line corresponds to a third eigenvalue that does not show up in the PL.

The weak p -shell PL in Figure 11.4 reveals the low carrier population in this shell. Comparing Figure 11.4 to Figure 11.3, one can observe a small energetic shift of the s - and p -shell. As the energetic position of the peak is practically not altered by the inclusion of correlations, we can investigate the peak position as a function of the average number of carriers in the QD in HF-approximation. The result is shown in Figure 11.5. For negligible population, the eigenenergies derived from the matrix \underline{M} from Eq. (11.8) are found to be at about -133.75 , -73.62 and -67.60 meV. Exactly the same values are obtained using the configuration interaction approach for the absorption spectrum of an initially empty QD as discussed in Section 2.2 of Part I. Furthermore, using the configuration interaction approach, we found that the eigenstate highest in energy has zero oscillator strength. In the approach based on the SLE, one again finds that the corresponding eigenvalue has only an extremely small intensity. With increasing population the energetic position of the s - and p -shell transitions are changed, with a weaker shift for the s -shell than for the p -shell. Such a continuous shift of the eigenenergies cannot be observed in the case of the exact-diagonalization technique, in which one considers only eigenstates with an integer number of electrons and holes. In contrast, by describing the system via the equation of motion technique, averages are performed with respect to a density operator, that allows continuous occupation numbers.

11.4 Results of the Time-Resolved PL

Complementary to the study of the stationary PL spectra, which provides insight into the renormalized energy and the electronic level structure, one can follow the dynamics of the number of emitted photons per unit time. This is known as time-resolved PL and yields information about the carrier dynamics and the photonic environment.

In this section, we study the influence of the correlations on the time-resolved PL and on the corresponding population dynamics. We start by thoroughly analyzing the source term of spontaneous emission. This provides us with a deeper understanding of the decay behavior of the PL in a semiconductor. Then the numerical solutions of the full set of equations are discussed in detail.

In the equation of motion of the photon-assisted polarization (10.19) the source term of spontaneous emission $g_{i\xi}f_i^c(1 - f_i^v) + \sum_1 g_{1\xi}C_{1ii1}^X$ originates from the operator average $\sum_1 g_{1\xi}\langle c_1^\dagger v_1 v_i^\dagger c_i \rangle$. A simplified description is possible if one completely neglects the Coulomb interaction between the charge carriers. Then the source term of spontaneous emission with the four-operator expectation value (resulting from the carrier-photon interaction) can be evaluated in two limiting cases. The first is the Hartree-Fock approximation, in which correlations among the carriers are neglected. The second corresponds to the two-level approximation, in which one assumes that the relevant physics is determined by one confined shell for both the electrons and the holes. The latter limiting case is of particular interest, since two-level models are frequently used for the discussion of QDs in the literature.

PL in the Hartree-Fock Limit

Within the Hartree-Fock approximation, the source term of spontaneous emission is solely determined by the product $f_i^c(1 - f_i^v)$. In the absence of Coulomb interaction one can solve for the stationary solution of the photon-assisted polarization in the case of slowly varying populations, as explained in Section 11.2. Doing so, one obtains for the population changes

$$\begin{aligned} \frac{\partial}{\partial t}f_i^c &= -\frac{2}{\hbar}\operatorname{Re}\sum_\xi\frac{i|g_{i\xi}|^2f_i^c(1-f_i^v)}{\varepsilon_i^c-\varepsilon_i^v-\hbar\omega_\xi-i\Gamma} \\ &= -\frac{f_i^c(1-f_i^v)}{\tau_i}. \end{aligned} \tag{11.10}$$

In going from the first to the second line of the above equation, we performed the ξ summation and found an emission rate $1/\tau_i$, which depends on the electronic states involved in the transition. In the case $\Gamma \rightarrow 0$ the quantity $1/\tau_i$ is nothing but the Wigner-Weisskopf rate of spontaneous emission. From this equation it is obvious that the decay of the population f_i^c is non-exponential, unless f_i^v is held constant by some mechanism, like background doping. Furthermore, the rate of decay depends on the

carrier density and is higher for larger population. This behavior carries over to the PL, as for each recombined conduction-band electron a photon is created, see Eq. (10.5). In an experiment one would therefore expect from Eq. (11.10) to observe a decay rate that will strongly depend on the initial excitation of the system. Due to the non-exponential PL decay a simple decay rate cannot be used to characterize the PL dynamics. This might appear surprising, since from a two-level atom an exponential decay behavior is known. Let us therefore consider this two-level approximation as the second limiting case.

PL in the Two-Level Approximation

Carrier indices are dropped as they are not needed if one restricts the population dynamics to one confined electron and hole level. In the de-excited (excited) state for this two-level system the electron is in the valence- (conduction-) band state. For the two spin polarizations, which are decoupled in the absence of Coulomb interaction, the excitation processes then involve only a single electron. This has a significant consequence for the evaluation of the source term of spontaneous emission. Within the two-level approximation, the successive application of more than one annihilation or creation operator always yields zero, so that the source term $\langle c^\dagger v v^\dagger c \rangle$ reduces to f^c . If we proceed with this altered source term along the lines discussed above, one obtains instead of Eq. (11.10) the following expression:

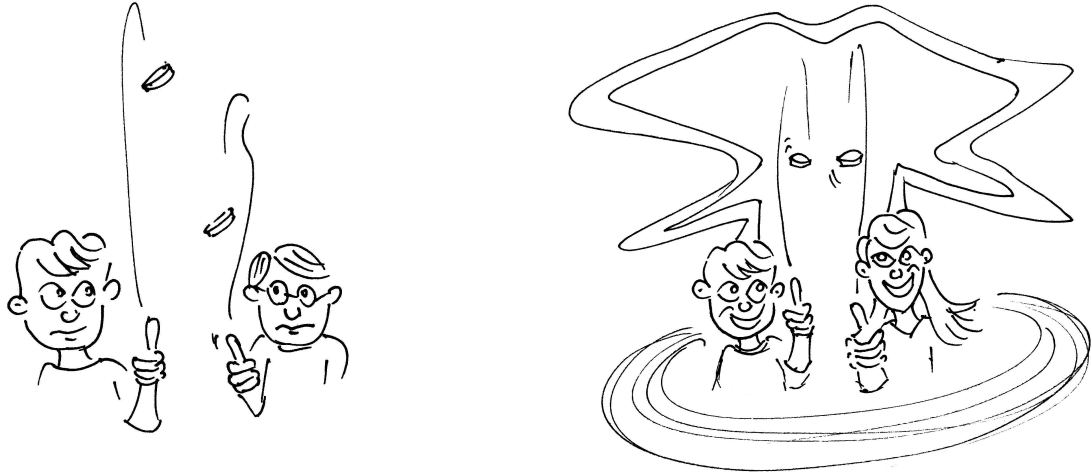
$$\frac{\partial}{\partial t} f^c = -\frac{f^c}{\tau}. \quad (11.11)$$

This clearly corresponds to the exponential decay behavior known from the two-level system.

Discussion of the Two Limiting Cases

From this analysis we deduce that the exponential decay within the two-level approximation stems from the fact, that the excitation of a QD conduction-band carrier is rigidly linked to the absence of a QD valence-band carrier. In the electron-hole picture, this corresponds to a fully correlated electron-hole pair: whenever an electron is present, a hole is present, and if no electron is present neither is a hole. On the operator level this is expressed as $c^\dagger v v^\dagger c = c^\dagger c$ or, more conveniently, in the electron-hole picture as $\hat{n}_e \hat{n}_h = \hat{n}_e$, where \hat{n}_e and \hat{n}_h denote the occupation number operator for the electrons and holes, respectively. In a semiconductor, however, many carriers are present and the correlations are subject to scattering and dephasing processes and must therefore be explicitly calculated.

Only in the case of a fully correlated electron-hole pair the expectation value of the product of operators $\hat{n}_e \hat{n}_h$ is equal to the expectation value of the single operator \hat{n}_e . In the case of fully uncorrelated carriers the relation $\langle \hat{n}_e \hat{n}_h \rangle = \langle \hat{n}_e \rangle \langle \hat{n}_h \rangle$ holds. These



n_E	n_H	$n_E n_H$	p
0	0	0	1/4
0	1	0	1/4
1	0	0	1/4
1	1	1	1/4

n_E	n_H	$n_E n_H$	p
0	0	0	1/2
1	1	1	1/2

$\left. \begin{array}{l} \langle n_E \rangle = 1/2 \\ \langle n_H \rangle = 1/2 \\ \langle n_E n_H \rangle = 1/4 \end{array} \right\} \Rightarrow \langle n_E n_H \rangle = \langle n_E \rangle \langle n_H \rangle$
 $\left. \begin{array}{l} \langle n_E \rangle = 1/2 \\ \langle n_H \rangle = 1/2 \\ \langle n_E n_H \rangle = 1/2 \end{array} \right\} \Rightarrow \langle n_E n_H \rangle = \langle n_E \rangle$

Figure 11.6: How correlation affects the average $\langle n_E n_H \rangle$: The results of Emil and Henrik (left), which are fully uncorrelated, show: $\langle n_E n_H \rangle = \langle n_E \rangle \langle n_H \rangle$. In contrast, the fully correlated results of Emil and Hendrike (right), obey $\langle n_E n_H \rangle = \langle n_E \rangle$. Please note that the drawing does not reflect the authors view of an uncorrelated/correlated electron-hole pair and is solely meant as an illustration.

two facts might be illustrated by considering Figure 11.6. While this artist's perception hits the heart of the problem, it should of course not be taken completely seriously. On the left side Emil and Hendrik throw coins. The results and the corresponding probabilities are listed in the table underneath. Because the results of their throws are completely uncorrelated one finds $\langle n_e n_h \rangle = \langle n_e \rangle \langle n_h \rangle$. On the right side Emil tries his luck with Hendrike. By means of some curious link between the two, the results are always identical, as shown in the corresponding table. In this case one indeed finds $\langle n_e n_h \rangle = \langle n_e \rangle$. For the avid reader we like to point out that we have developed yet another tutorial description of the problem, which can be found in Ref. [159].

It is instructive to check whether the main result of the two-level approximation, namely that the source of spontaneous emission is given by f^c alone, can be reproduced by a

calculation on singlet-doublet level. To this end, we study the equations of motion for the correlations in the absence of Coulomb interaction and consider only an s -shell. In this situation we can omit all carrier indices. Doing so, we obtain from Eq. (10.21) for the intraband correlations $\frac{\partial}{\partial t}C^e \propto C^e$, which yields $C^e(t) = 0$ due to the initial conditions. Using Eq. (10.20), we can deduce for the interband correlation

$$i\hbar \frac{\partial}{\partial t}C^X = 2i\text{Re}\left\{(f^c - f^v) \sum_{\xi} g_{\xi}^* \langle b_{\xi}^{\dagger} v^{\dagger} c \rangle\right\} .$$

From this one can directly infer that C^X is purely real-valued. As a consequence, $\frac{\partial}{\partial t}f^c$ is fully determined by $\langle b^{\dagger} v^{\dagger} c \rangle$. Explicitly one obtains from Eq. (10.17)

$$i\hbar \frac{\partial}{\partial t}f^c = -2i\text{Re}\left\{\sum_{\xi} g_{\xi}^* \langle b_{\xi}^{\dagger} v^{\dagger} c \rangle\right\} .$$

Using this equation and the relation $\frac{\partial}{\partial t}f^c = -\frac{\partial}{\partial t}f^v$ for the populations, we find for the correlations $\frac{\partial}{\partial t}C^X = \frac{\partial}{\partial t}(f^c f^v)$ with the solution $C^X = f^c f^v + \text{const.}$ For the initially unexcited system ($f^c = 0, f^v = 1, C^X = 0$) we therefore deduce $C^X = f^c f^v$. Inserting this in the source term $g_{\xi}\{f^c(1-f^v) + C^X\}$ of the photon-assisted polarization, finally leads us – as anticipated – to the source $g_{\xi}f^c$. This analysis shows that a factorization on singlet-doublet level is able to reproduce the exact results known from the very special situation of a two-level approximation in the case of a single shell and in the absence of Coulomb interaction.

Numerical Results

After investigating the two special cases of a fully uncorrelated system and the two-level approximation, we now present full numerical results of the SLE including Coulomb interaction, correlations and several shells. The evolution of the time-resolved PL is shown in Figure 11.7. Again, the initial carrier density is taken to be $1.5 \cdot 10^{10} \text{ cm}^{-2}$. For the solid line all correlations up to the singlet-doublet level have been included. The result of a calculation in the Hartree-Fock approximation, which corresponds to uncorrelated carriers, is shown as a dashed line. In this case, the decay is clearly non-exponential, which is in accordance with Eq. (11.10). Comparing these two results, it is obvious that carriers are strongly correlated on the singlet-doublet level. However, our approach so far does not account for any kind of dephasing of the correlations. One physical mechanism for such a dephasing is phonon scattering. Hoyer et al. have studied phonon scattering on a microscopic level for a quantum-well system [144, 150]. They have shown that dephasing of correlations is indeed provided, although this enters only via higher-order triplet terms. Extensions beyond the singlet-doublet factorization are not within the scope of this thesis. Nevertheless, we can account for the main features of phonon scattering, which is dephasing of correlations and relaxation of the carrier population towards thermal equilibrium at the lattice temperature, on a phenomenological level. A constant dephasing term $-i\gamma C_{ijkl}^X$ is added on the right hand

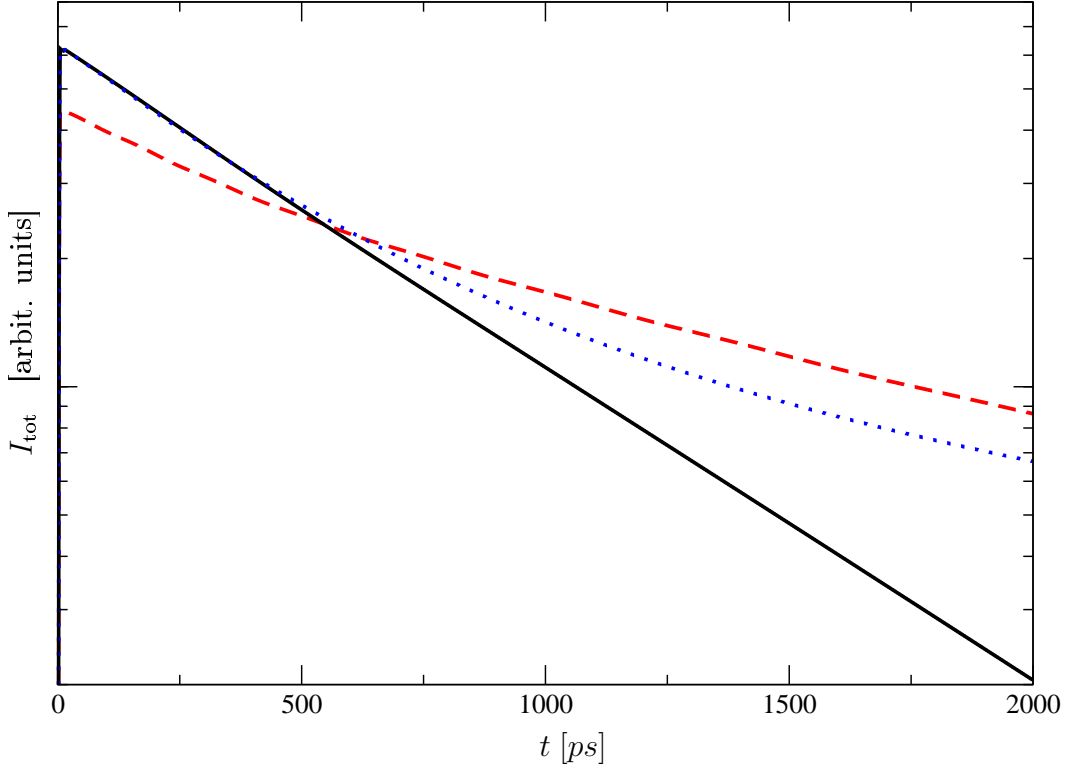


Figure 11.7: Time-resolved photo-luminescence. Solid line: calculation on singlet-doublet level without dephasing. Dashed line: HF result. Dotted line: calculation on singlet-doublet level with dephasing via phonons $\gamma = 0.001 \text{ meV}$, $\tau_{\text{relax}} = 1 \text{ ps}$.

side of Eq. (10.20) and the scattering is treated within relaxation-time approximation by introducing an additional term to Eq. (10.17)

$$\frac{\partial}{\partial t} f_i^{c,v} \Big|_{\text{relax}} = -\frac{f_i^{c,v} - F_i^{c,v}(T)}{\tau_{\text{relax}}^{c,v}}, \quad (11.12)$$

where $F_i^{c,v}(T)$ is a Fermi-Dirac distribution at temperature T , evaluated for every timestep at the present carrier density. For the relaxation times typical values of 1 ps for electrons and holes are taken [18]. Note that the dynamics is rather insensitive to the exact value of these relaxation times. Hoyer et al. have also shown that a constant dephasing causes unphysical heating of the system. However, this effect is only weak for a small value for the dephasing and, additionally, the scattering term (11.12) counteracts the heating. We find $\gamma = 0.001 \text{ meV}$ to already weaken the correlations drastically so that a non-exponential signature of the decay is regained on longer timescales. The result of this calculation can be seen as dotted line in Figure 11.7.

Clearly such a phenomenological treatment of the dephasing via phonons cannot cover all sorts of phonon effects, such as, e.g., the spectral side-bands known from an interaction of the QD carriers with the continuum of acoustic phonons [62, 160]. For this,

a microscopic description of the electron-phonon interaction would be necessary, which is left for future work. Here the important point is that *any* kind of dephasing of the correlations does lead to deviations from an exponential decay.

After this discussion of the time-resolved PL dynamics for unpatterned substrates, we study in the next chapter how the emission properties of a system of QDs is changed by embedding them in an optical microcavity. We start with an analysis of the theoretical problem and then compare the calculated results to recent experimental findings.

12 Photoluminescence in a Microcavity

In the preceding chapter we have discussed a situation in which the QDs couple to the modes of ‘free space’. In some aspects even more interesting is the case in which the QD system is embedded in a cavity. The investigation of the PL dynamics in this situation will be the topic of the present chapter. We start with some general remarks about how a cavity can affect the emission properties. In particular the decay in two-level approximation is discussed and the Purcell effect is introduced. Then results for an ensemble of identical QDs is presented and the influence of correlations on the PL decay is studied in Section 12.2. Subsequent to this, results for an ensemble of inhomogeneously broadened QDs that couple to the modes of the microcavity are analyzed in Section 12.3 and are compared to recent experiments in Section 12.4.

12.1 Basic Considerations

In this section we give a general overview about the changes that arise due to the alteration of the photonic environment. First of all a electromagnetic field can build up in the presence of a microcavity so that stimulated emission and absorption can become important. Therefore the corresponding term in the photon-assisted polarization must explicitly be considered. Secondly, the energy of the QD transition is now of paramount importance, because only those QDs, which are tuned to the cavity resonance, can strongly participate in the carrier-photon dynamics. This statement, which is rather intuitive, will become clearer later on. In contrast to this sensitivity to the QD transition energy in a cavity, the coupling between the electromagnetic field and the QD transition in ‘free space’ is rather insensitive to small variations of the transition energies, because the emitters couple to an entire continuum of modes with a smooth optical density of states. Thirdly, the position of the QDs in the cavity plays an important role for the light-matter interaction. In Section 9.1 the general expression of the coupling matrix elements was derived:

$$g_{\nu\xi} \approx \tilde{E}_\xi \mathbf{d}_{cv} \mathbf{U}_\xi(\mathbf{r}_0) . \quad (12.1)$$

This equation reveals that the coupling strength is zero if the QD is placed in a node of the mode function \mathbf{U}_ξ . Furthermore it shows that the orientation of the dipole matrix element \mathbf{d}_{cv} relative to the mode function is of great importance. This dependence of the light-matter interaction on the spatial position of the QD and the orientation of the

dipole of the electronic transition in case of a microcavity is in strong contrast to the coupling to the modes in ‘free space’. In the latter case it does not matter where the QD is placed, as the space is homogeneous, nor how the QD dipole is oriented, because of the space isotropy.

In addition to these changes, the physically interesting and actual observable quantity is not the number of photons generated, but the number of photons leaving the cavity per unit time. In what follows we choose to model the cavity losses by means of complex frequencies $\bar{\omega}_\xi = \omega_\xi - i\frac{\kappa_\xi}{2}$, where the real part contains the energetic position of the cavity resonance and the imaginary part determines the loss rate for the cavity mode ξ . Therefore, in the equations of motion all mode frequencies have to be replaced by $\bar{\omega}_\xi$ if the time derivative of b_ξ is taken and by its complex conjugate $\bar{\omega}_\xi^*$ if the time derivative of b_ξ^\dagger is performed. Without any source that additionally feeds or decreases the photon number, one obtains for the *free* evolution of the photon number an exponential decay $\langle b_\xi^\dagger b_\xi \rangle(t) = \langle b_\xi^\dagger b_\xi \rangle(0)e^{-\kappa_\xi t}$. In an experiment, the cavity loss or the finite lifetime of a photon in the cavity shows up as a broadening $\Delta\omega_\xi = \kappa_\xi$ of the cavity resonance. In addition to the resonant modes, which are characterized by their high quality factor $Q = \omega_0/\Delta\omega$, there exists a continuum of leaky modes. These leaky modes are characterized by extremely short cavity lifetimes and correspondingly low quality factors.

Besides the dimensionless quality factor Q , which is a measure for the spectral width of the cavity resonance, often the so-called *Purcell factor* F_P is introduced to characterize a cavity [2,30]. This quantity is – as we will see – a measure of how strong the spontaneous emission is altered by the presence of the cavity. For a given cavity resonance ξ the Purcell factor is defined as

$$F_P = \frac{3}{4\pi^2} \frac{Q_\xi \lambda_\xi^3}{V_{\text{eff},\xi}} , \quad (12.2)$$

where λ_ξ is the wavelength of the cavity resonance, $V_{\text{eff},\xi} = \int d^3r \frac{|\mathbf{U}_\xi(\mathbf{r})|^2}{|\mathbf{U}_\xi^{\max}|^2}$ is the effective mode volume, and $|\mathbf{U}_\xi|_{\max}^2$ denotes the maximum value of $|\mathbf{U}_\xi(\mathbf{r})|^2$. With these definitions one can rewrite the coupling strength (12.1) as

$$|g_{\nu\xi}|^2 = \frac{\hbar^2 \omega_\xi}{\tau^{\text{WW}}(\omega_\xi)} \frac{1}{4} \frac{F_P}{Q} \frac{|\mathbf{U}_Q(\mathbf{r}_0)|^2}{|\mathbf{U}_Q^{\max}|^2} \cos(\phi_p) , \quad (12.3)$$

where $\tau^{\text{WW}}(\omega_\xi)$ denotes the Wigner-Weisskopf rate of spontaneous emission at the frequency ω_ξ in a homogeneous medium with refractive index n and ϕ_p is the angle between the local electromagnetic field vector and the dipole matrix element. From this expression it can be inferred that the light-matter interaction is maximal if the QD is positioned in the field maximum and the dipole is parallel or anti-parallel to the local electromagnetic field. In this case the last two factors in the above equation become unity.

In order to get a deeper insight into the physical meaning of the Purcell factor, we consider the coupling of a QD to a *single* mode in *two-level* approximation for a situation

in which stimulated emission/absorption can be neglected. To keep the discussion as simple as possible, we additionally neglect the influence of Coulomb interaction. In the two-level approximation the electronic indices can be dropped for clarity. The same is true for the mode label as only one single modes is considered. In this case, one finds that the SLE reduce to the following set of coupled differential equations:

$$\begin{aligned}\frac{d}{dt}f &= -\frac{2}{\hbar}\text{Re}\{g^*\langle b^\dagger v^\dagger c \rangle\}, \\ \frac{d}{dt}\langle b^\dagger b \rangle &= -\kappa\langle b^\dagger b \rangle + \frac{2}{\hbar}\text{Re}\{g^*\langle b^\dagger v^\dagger c \rangle\}, \\ \frac{d}{dt}\langle b^\dagger v^\dagger c \rangle &= -i(\varepsilon^c - \varepsilon^v - h\omega_c - i\frac{\hbar\kappa}{2})\langle b^\dagger v^\dagger c \rangle + gf.\end{aligned}\quad (12.4)$$

The first line describes the population changes due to the photon-assisted polarization. The second line gives the dynamics of the photonic population which is determined by the cavity losses (first term) and the photon-assisted polarization (second term). The third line constitutes the equation of motion for the photon-assisted polarization. In addition to the free part, which is damped by the cavity losses, it contains the source term in the two-level approximation. Solving the last line of Eq. (12.4) in the stationary regime, yields $\langle b^\dagger v^\dagger c \rangle = -igf/(\varepsilon^c - \varepsilon^v - h\omega - i\hbar\kappa/2)$. If one assumes that the number of photons in the cavity has already increased to its stationary value, in which the number of photons produced per unit time is balanced exactly by the cavity losses, one finds $\langle b^\dagger b \rangle = \frac{1}{\kappa}\text{Re}\{g^*\langle b^\dagger v^\dagger c \rangle\}$. Combining these two expressions yields

$$\langle b^\dagger b \rangle(t) = f(t) \frac{1}{\kappa} \frac{2}{\hbar} \text{Im} \left\{ \frac{|g|^2}{\varepsilon^c - \varepsilon^v - h\omega - i\frac{\hbar\kappa}{2}} \right\}. \quad (12.5)$$

This expression is valid in the adiabatic regime, in which the photonic and electronic population change only slowly. From the last factor of the expression one can deduce that only a QD with a transition energy close to the cavity resonance will strongly participate in the emission dynamics. By combining all the time-independent quantities into a single constant C , we can use Eq. (12.5) in the form $\langle b^\dagger b \rangle(t) = Cf(t)$ to combine the first two lines of Eq. (12.4). In this way one obtains

$$(1 + C)\frac{d}{dt}f = -\kappa Cf. \quad (12.6)$$

From this equation one immediately deduces an exponential decay of the population in the two-level approximation. But how is this decay time changed with respect to the time constant of the homogeneous medium? For $C \ll 1$ the decay time $\tau^{\text{spon. cav.}}$ is simply given by $1/\kappa C$. This can further be evaluated to¹

¹ Here $C \ll 1$ was assumed. The reader may well ask if this is justified in a typical experiment? To answer this question we rewrite C as $C \approx \frac{1}{\kappa \tau^{\text{spon. cav.}}} \leq \frac{F_p}{\kappa \tau^{\text{WW}}} = \frac{F_p Q}{\omega_0 \tau^{\text{WW}}}$. While the quantity $\omega_0 \tau^{\text{WW}}$ is typically of the order of 10^6 , the product $F_p Q$ is for micropillars normally of the order of 10^4 [30, 38, 161], so that $C \ll 1$ is indeed valid.

$$\frac{1}{\tau^{\text{spon. cav.}}} = \frac{F_P}{\tau^{\text{WW}}} \frac{(\frac{\hbar\kappa}{2})^2}{(\varepsilon^c - \varepsilon^v - h\omega)^2 + (\frac{\hbar\kappa}{2})^2} \frac{|\mathbf{U}_Q(\mathbf{r}_0)|^2}{|\mathbf{U}_Q^{\max}|^2} \cos(\phi_p) . \quad (12.7)$$

In Figure 12.1 the three last factors of Eq. (12.7) that determine the decay time in two-level approximation are depicted. For an emitter that (i) is tuned exactly to the cavity resonance, (ii) is placed in the field maximum, and (iii) has its dipole-moment oriented along the local electromagnetic field, the decay is fastest. The corresponding decay time is – compared to the decay time τ^{WW} observed in a homogenous medium – increased or decreased by the Purcell factor. For a Purcell factor larger than one, the spontaneous emission is enhanced. In the case of $F_P < 1$ spontaneous emission is reduced. Clearly, a generic QD, which is not optimally tuned to the cavity resonance and has a mismatch in the optimal position and orientation, can easily show a spontaneous decay time well above the one found for ‘free space’.

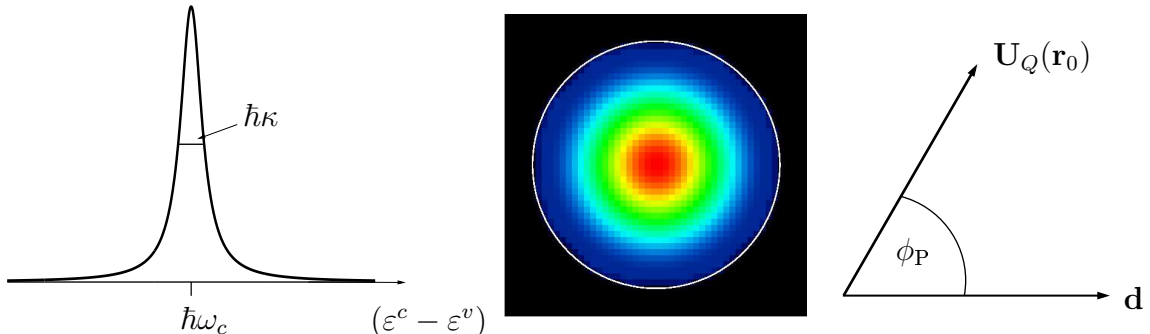


Figure 12.1: Visualization of the three factors that determine, next to the Purcell factor, the decay time in two-level approximation: The detuning of the transition with respect to the cavity resonance, the position of the QD in the cavity (a transverse mode pattern is shown), and the orientation matching between the local electromagnetic field and the dipole moment.

12.2 Ensemble of Identical QDs Coupled to a Single Mode

Before proceeding to the problem of an entire ensemble of different QDs and different cavity modes in the next section, we discuss the case of ‘identical’ QDs. What we mean with ‘identical’ is that all the dots are assumed to have the same light-matter coupling matrix elements and the same transition energy, which is tuned for this section on resonance with the fundamental cavity mode. Despite being rather artificial, it provides us with important insight into the luminescence dynamics of an ensemble of QDs, for which the stimulated emission/absorption term is important and the carrier dynamics of the individual QDs are coupled to each other via the photonic field. For a more realistic description that at least qualitatively accounts for the fluctuations of the individual QD

properties, effective parameters for the Purcell factor and the dot density are assumed in this section. In the next section, these ensemble properties are treated more thoroughly. To gain deeper insight into the alteration of the spontaneous emission dynamics due to the presence of a cavity, in a first step, we artificially switch the terms responsible for the stimulated emission/absorption off and analyze the influence of the correlation contributions on the dynamics. In a second step, we study the decay dynamics in the presence of the stimulated terms. In this case, we will see that the overall shape of the decay is not altered by the inclusion of the doublet correlations. This observation allows us to restrict the analysis in Section 12.3 to the singlet level and makes it possible to investigate the PL dynamics of an inhomogeneously broadened ensemble of QDs that couples to several cavity modes.

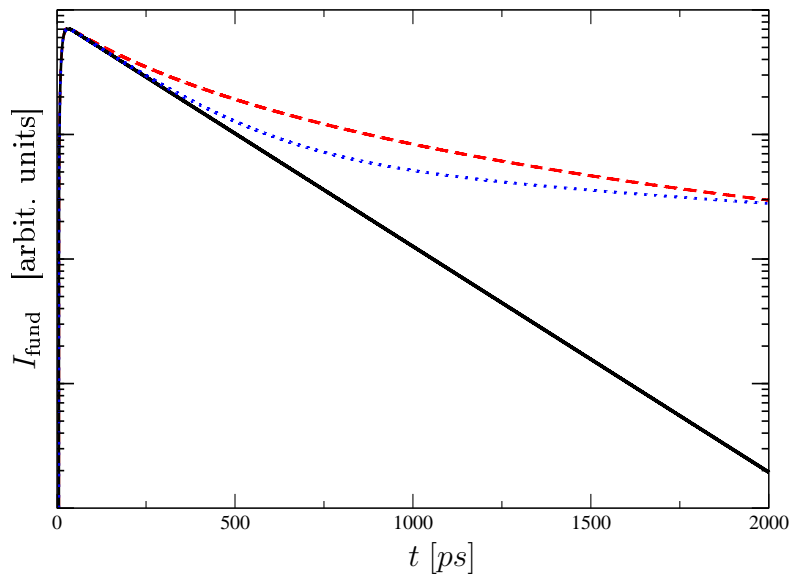


Figure 12.2: Time resolved PL of the fundamental mode. The stimulated emission/absorption term as well as Coulomb interaction was artificially switched off to allow for a better comparison to ‘free space’. Solid line: calculation on singlet-doublet level without dephasing. Dashed line: HF result. Dotted line: Results on singlet-doublet level with phenomenological dephasing as described in Section 11.4 with $\gamma = 0.001$ meV and $\tau_{\text{relax}} = 1$ ps.

As mentioned above, we will start our analysis with a situation in which we *artificially* switch off the term responsible for stimulated emission/absorption. Because the QD-transition shifts slightly with the average number of carriers, as outlined in Section 11.3, it is in principle possible that the QD-transition energy detunes somewhat from the cavity resonance. To allow for a better comparison to the situation encountered for QDs coupled to the modes of the ‘free space’, in which a small detuning has practically no influence on the emission dynamics, the QD transition energy is held constant throughout this subsection. This is achieved by studying the PL dynamics in the absence of Coulomb interaction. The result of a calculation on singlet-doublet level without dephasing of the correlation is shown in Figure 12.2. For this figure a maximal

light-matter coupling was assumed, i.e., the emitters are placed in the field maximum and have their dipole moment directed along the local electromagnetic field. In analogy to the situation in free space, which is depicted in Figure 11.7 on page 148, one obtains in this special situation an exponential decay of the PL signal. By comparing these two results one finds, however, that the decay time in the cavity is drastically shortened due to the Purcell factor of the cavity. This is in accordance with Eq. (12.7) that was deduced for the ideal case of the two-level approximation.

If we again include the phenomenological dephasing as discussed in Section 11.4, we find strong deviations from the exponential decay as the interband correlation are weakened. With increasing time the PL intensity including singlet-doublet terms and dephasing approaches the HF result.

In summary, if one artificially turns off the stimulated emission/absorption terms, one obtains in a cavity overall the same result as in ‘free space’. The main difference is the shortening of the decay time due to the altered local density of states seen by the emitters and described by the Purcell factor.

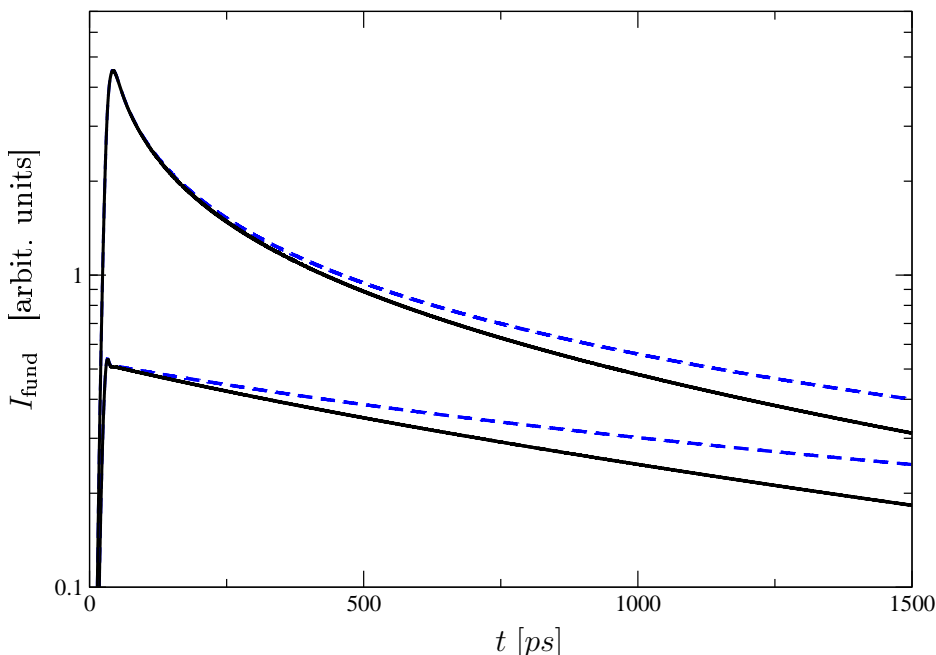


Figure 12.3: Time resolved PL of the fundamental mode. Results on singlet-doublet level without dephasing (solid lines) and on HF-level (dashed lines) for two different initial densities: $n_e = n_h = 2 \cdot 10^9 \text{ cm}^{-2}$ (lower curve) and $n_e = n_h = 3 \cdot 10^9 \text{ cm}^{-2}$ (upper curve). A Purcell factor of 0.52 and an effective QD density of $n_{QD} = 3 \cdot 10^9 \text{ cm}^{-2}$ is used. In the presence of the feedback provided by the cavity the influence of the doublet correlations are clearly reduced even without dephasing.

If the terms describing stimulated emission/absorption are included, we find that the correlations on doublet level produce – even without dephasing – only small changes to

the dynamics obtained on HF level, see Figure 12.2. The results are depicted for two different sets of parameters and in each case with and without doublet correlations.

On a first glance the lower curves may appear to be rather exponential. But this is the case only because the overall decay is, for these parameters, weak on the plotted time span. As a consequence, the curvature is only small. The overall shape of the decay is not altered by the inclusion of the doublet correlation and the deviations between the two curves are small *even without dephasing*. Therefore we neglect the effect of the doublet correlations, which would be additionally reduced due to dephasing of the correlation, for the following ensemble calculations. In this case, it is additionally feasible to incorporate the WL-states in our analysis and verify our previous statement, that the influence of the WL states on the photon dynamics is small at low temperatures.

12.3 Inhomogeneously Broadened Ensemble of QDs Coupled to Several Cavity Modes

In this section the PL dynamics of an inhomogeneously broadened ensemble of QDs coupling to several cavity modes, as well as to a continuum of leaky modes, is investigated. We start with a description of how the ensemble properties of the QDs are treated. Then details about the modeling of the optical modes are given. Thereafter the results of the PL dynamics for different pillar sizes and different initial carrier densities are presented. These results are then compared to recent experimental findings [139] in Section 12.4.

Theoretical Model

The various QDs in a cavity have in general all different transition energies due to the size fluctuations and different dipole-orientations. Furthermore individual QDs experience different local electromagnetic fields. In a typical experimental situation, with an areal density of QDs of the order of 10^{10} to 10^{11} cm^{-2} and a pillar diameter in the μm -range, up to several thousand QDs interact with the light field. Clearly it is not feasible to resolve all the different QDs individually in a numerical simulation that typically spans nanoseconds. On the other hand, the description of the ensemble used in the previous section does not reflect the physical reality. As a good compromise several hundred ‘prototypical’ QDs are considered and each of these dots is assigned a fraction of the total QD density.

In a typical experiment, one collects the out-coupled light only in a small frequency interval, so that it is reasonable to restrict the analysis to the fundamental and some lower excited cavity modes. Due to the inhomogeneous broadening present in a QD ensemble, it is therefore possible to work with an effective density of QDs with transition energies close to the relevant cavity modes. For the following, we assume this effective density to be $3 \cdot 10^9 \text{ cm}^{-2}$ distributed over an energy interval of approximately 1.5 meV.

In addition to the transition energy, each of the prototypical QD is characterized by a light-matter coupling matrix element. As discussed at the beginning of this chapter, the coupling strength is influenced by the orientation of the dipole and the position of the dot in the cavity. For this we assume that each dipole orientation in the QD-plane occurs with the same probability [162]. The form of the transverse mode-pattern together with resonance frequency ω_ξ^{res} is calculated for each cavity resonance using a three-dimensional transfer-matrix approach [161, 163]. The modeling of the variation of the different local electromagnetic fields is greatly simplified by the fact that the modulus of the mode profile $|\mathbf{U}_\xi(\mathbf{r})|$ depends in the QD-plane only on the radial distance ρ from the pillar axis [161, 163]. Therefore it is sufficient to use a one-dimensional distribution function to account for the different spatial positions of the QDs in the cavity.

The quality-factors Q_ξ for the different resonant modes ξ are obtained from experimental results [139]. They enter the analysis via the complex frequency $\omega_\xi = \omega_\xi^{\text{res}}(1 - \frac{i}{2Q})$, where they describe the loss rate. In the following, the coupling between different modes is neglected, so that $\langle b_\xi^\dagger b_{\xi'} \rangle \approx \delta_{\xi\xi'} \langle b_\xi^\dagger b_\xi \rangle$. Besides the resonant modes, which are characterized by their large Q -values and pronounced peak structures in a transmission spectrum, there exists a background contribution formed by the continuum of leaky modes. In order to include the influence of these leaky modes, it is assumed that the background contribution consists of a fraction of the continuum of modes of the ‘free space’. The size of this fraction can be estimated by counting the plane waves that (i) either reach the sidewalls of the micropillar in an angle smaller than the critical angle of total internal reflection (as these waves will not be reflected by the sidewalls, they will leave the cavity), or (ii) have a momentum component $k_{||}$ along the pillar axis that lies outside the stopband of the distributed Bragg reflector (DBR) and can therefore escape from the cavity². Further details can be found in Appendix D.

Numerical Results

The numerical results for the inhomogeneously broadened ensemble of QDs that couple to several cavity modes as well as the continuum of leaky modes are shown in Figure 12.4 and Figure 12.5. The numerical evaluation for an entire ensemble of QDs over such a long time-scale is computationally very expensive and parameter studies are only feasible if one solves the photon-assisted polarization in the adiabatic approximation³. For simplicity, we assume that the QDs are initially equally populated according to the Fermi-Dirac distribution of the QD energetically at the center of the ensemble.

² A DBR has a high reflectivity only in a finite frequency range, the so-called stop band. Outside this range the mirror is more or less transparent [164].

³ As discussed already in Section 11.2, in this approximation the photon-assisted polarization follows the population adiabatically. The reduction in computer time stems from the possibility of increasing the timestep in the Runge-Kutta algorithm by typically a factor of 100. As the adiabatic procedure requires a matrix inversion (or a diagonalization), this method only pays off in the case of many QDs.

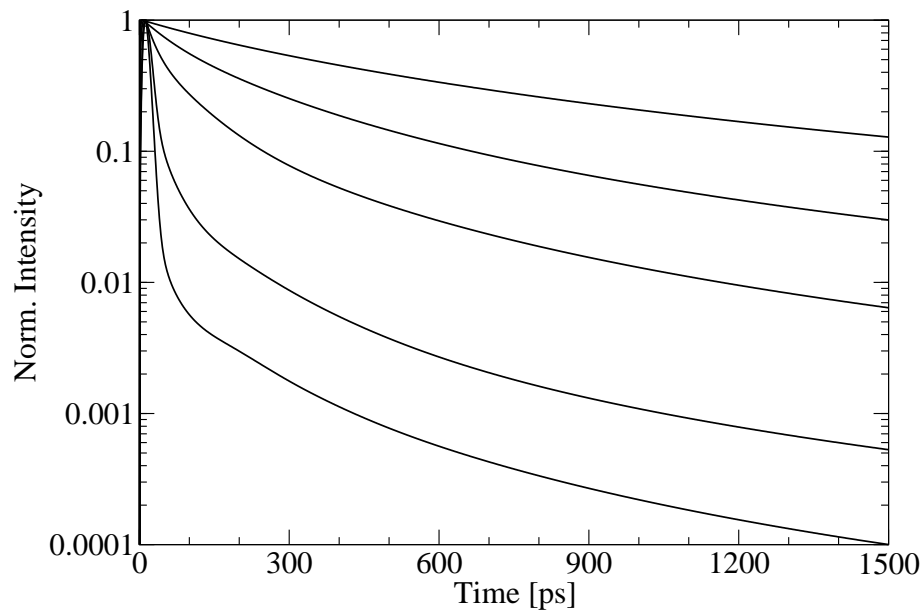


Figure 12.4: Calculated photoluminescence for an ensemble of QDs in a $6 \mu\text{m}$ diameter pillar microcavity with initial carrier densities from $1 \times 10^9 \text{ cm}^{-2}$ to $5 \times 10^9 \text{ cm}^{-2}$ in equidistant steps from top to bottom. For better comparison the results are normalized.

In Figure 12.4 the number of photons leaving the fundamental mode per unit time is shown for different initial carrier densities. This corresponds to a variation of the excitation power in an experiment. The non-exponential decay of the PL and the strong dependence of the decay rate on the initial population is evident. Both features can be understood by considering the source term of spontaneous emission in the HF-limit: $f_i^e f_i^h$. A detailed discussion of how this source term leads to an non-exponential decay was already given in Section 11.4. The same argumentation applies to the density-dependence because only a source term linear in the population leads to a decay that does not depend on the initial population. Any non-linear source term generates a density dependent decay. Another source for a density dependent decay arises in a cavity as for highly populated systems stimulated emission becomes important and can efficiently deplete the system.

In the next section the theoretical results are compared to those of recent experiments [139]. The microscopic analysis of the PL based on the SLE describes an ideal situation. Therefore it is impossible to reach full quantitative accordance between the experimental and theoretical findings. However, by adjusting the light-matter coupling, one obtains an overall good agreement between theory and experiment. To this end, we used for the dipole-matrix element twice the value known for GaAs *bulk* material. Such an adjustment is acceptable as the precise value of the dipole-matrix element of the QD transition is not known and depends on the form of the QD and on strain fields inside the dot. Additionally, the value is influenced by intermixing of different bands and by the composition profile that is not precisely known.

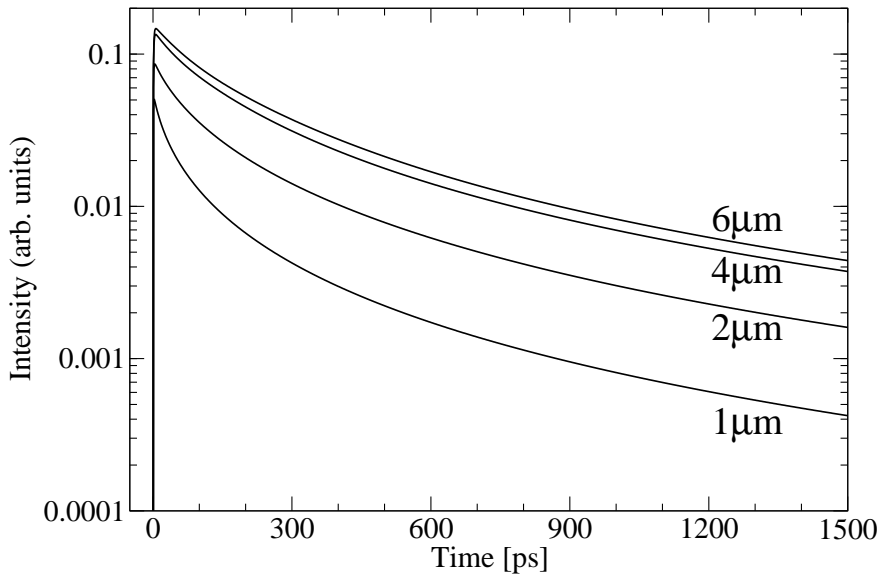


Figure 12.5: Calculated photoluminescence of QDs in a pillar microcavity with various diameters for an initial carrier density of $2 \times 10^9 \text{ cm}^{-2}$.

The calculated PL for fixed initial carrier density but varying diameters of the micropillar cavity is displayed in Figure 12.5. For all pillar diameters a clear non-exponential decay can be observed. The different heights of the curves can mainly be attributed to the fact that in a larger pillar more carriers take part in the recombination dynamics. The smaller pillars show a faster decay in connection with a larger Purcell factor: The reduction of the effective mode volume for smaller pillar sizes overcompensates the reduction of the quality factor observed with decreasing pillar size. This results in an enhanced Purcell factor $F_P \propto Q/V_{\text{eff}}$ for the smaller cavities. Nevertheless, it is impossible to read off the Purcell-factor from the calculated decay curves due to the non-exponential character of the curves.

Visualization of the mode structure

In an experiment one can use a charged coupled device (CCD) camera image to obtain an overview about the modes structure in a certain microcavity [161, 163]. To this end, a microscope objective is focussed on a certain section of the micropillar and the signal emitted from this region is collected. By resolving this signal spectrally and detecting it with a CCD camera, one obtains information on both the spatial mode pattern and the resonance frequencies. Similar information can be obtained from a theoretical analysis. In Figure 12.6 the energy is depicted along the horizontal axis and along the vertical axis the transverse mode pattern in radial direction is shown. The intensity is encoded in the color (blue: weak signal, red: strong signal). Modes at four different resonance frequencies can be identified. The leftmost mode corresponds to the fundamental mode

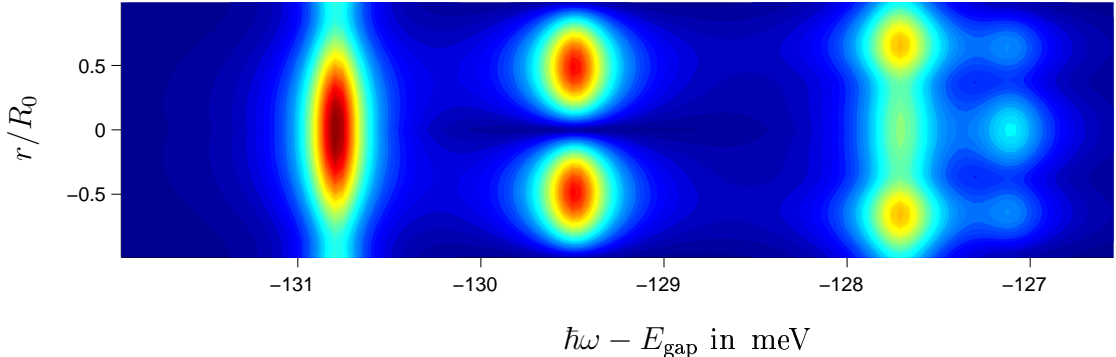


Figure 12.6: (color online) Combined information about the transverse mode pattern and the carrier-photon system: Transition energies are shown along the horizontal axis. Along the vertical the transverse mode pattern is shown. The intensity, which is proportional to the number of photons with a certain energy, is encoded in color.

and is most strongly illuminated by the QDs, because the center frequency of the ensemble is tuned exactly to this resonance. The horizontal extension of this mode is determined by the frequency-broadening due to the cavity lifetime and is, therefore, directly related to quality-factor Q_ξ of the mode. The fundamental mode is followed to the right by excited modes. While the first excited mode is still strongly illuminated, the intensity decreases for the higher excited modes, as less QDs lie energetically close. Note that the third peak actually consists out of two different types of modes: one with a node and one with a maximum at the center. The former mode is much stronger illuminated. This can be mainly attributed to the fact that for a constant areal QD density, a higher number of QDs can interact with a mode having its maxima at $\rho \neq 0$.

12.4 Experimental Results

In the following we present experiments performed by Schwab et al. in the group of Prof. Manfred Bayer in Dortmund and Mohamed Benyoucef and Prof. Peter Michler in Stuttgart [139]. The experimental results are obtained by time-resolved PL measurements on InGaAs/GaAs QDs in GaAs-based pillar microcavities. Using μ -PL, the emission of individual pillars is analyzed after excitation of the QDs with a short laser pulse energetically in or above the WL-resonance. For more details on the experimental setup see Ref. [139].

The left panel of Figure 12.7 shows typical results for the PL of a given micropillar as a function of time for different excitation power densities. For the decay of the signal over the first order of magnitude in the intensity, the deviation from an exponential decay is rather weak. Therefore straight lines have been added to extract a decay time for this initial decay. However, following the decay on a longer time-scale and over a

larger intensity-scale clearly reveals a non-exponential character, which shows that the description of the PL dynamics by a simple decay time is not possible. Maybe even more important, the estimated decay rates continuously decrease with decreasing excitation power density. This behavior was found from the weakest pumping, which still made a clear recording of the PL signal possible (and was well below the laser threshold), up to the laser threshold.

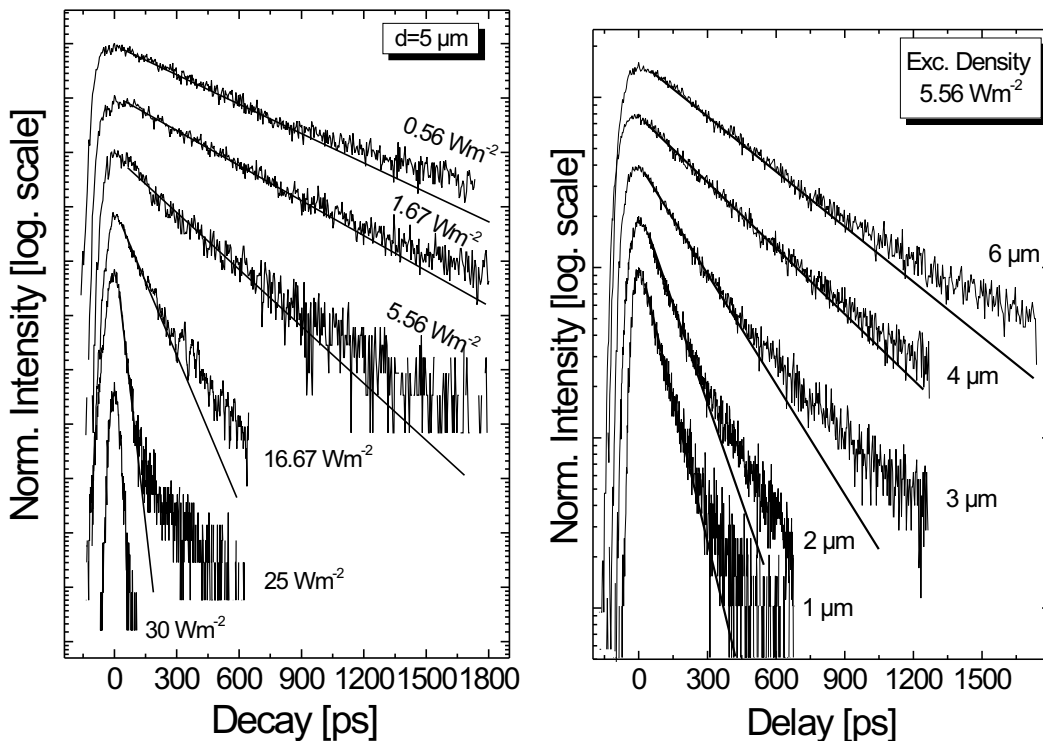


Figure 12.7: Measured PL decay for one pillar but different excitation densities (left panel) and different pillar diameter but fixed excitation density (right panel). For the power series (left) a pillar with a diameter of $5\text{ }\mu\text{m}$ was used. The decay times corresponding to single exponential fits (shown by the solid lines) are, from top to bottom, 550 ps, 475 ps, 265 ps, 120 ps, 30 ps, and 20 ps. For the diameter series (right) pillars with different diameters are excited with a power density of 5.5 W m^{-2} . The decay times, corresponding to the single exponential fits, are, from top to bottom: 400 ps, 315 ps, 200 ps, 110 ps, and 80 ps. For clarity, the different PL traces have been shifted vertically relative to each other.

Additional measurements were performed on a series of different micropillars. For all resulting curves shown in the right panel of Figure 12.7, the same low excitation-power density was used to make sure that one is below the laser threshold. The faster decay for decreasing pillar diameter is a consequence of the Purcell effect.

All these features are well reproduced by our analysis based on the semiconductor luminescence equations as discussed in the preceding section: There we found that the decay is clearly non-exponential and that the decay rate strongly varies with the initial carrier density. Additionally we found that the decay is faster for smaller pillars in connection with the Purcell factor. The deviations of the measured from the calculated results close to time $t = 0$ and in particular the somewhat slower raise of the PL signal observed in the experiment, can be attributed partially to the fact that the optical carrier generation process was not modeled and that the experimental setup has only a finite time resolution. Furthermore, a direct one-to-one comparison of, for example, the power series is complicated by the fact that the carrier density generated in the QD sample depends in a nonlinear manner on the pulse intensity due to saturation effects. Here, we do not want to quantify these optical nonlinearities and the subsequent carrier relaxation, which would be needed to connect experimental pump intensities directly to the resulting carrier densities. Instead, we focus on the physics of the recombination dynamics that yields a non-exponential decay and emphasize the strong dependence of the time-resolved PL decay on the carrier density in the system.

Alternative explanations for the non-exponential character of the decay should be addressed. For example, it is frequently argued, that the non-exponential decay observed in PL measurements stems from a superposition of many exponential PL signals of various emitters with different decay times due to a different light-matter coupling strength. To rule out this explanation an ensemble of *identical* QDs was studied in Section 12.2 and a clear non-exponential decay behavior was found even though all the QDs were modeled to have identical light-matter coupling strength. Additionally, a superposition of a series of exponential decays would not show the discussed decay-time shortening with increasing excitation power density.

Additional alternatives for the origin of the non-exponential decay, which could be important in other experiments, are ruled out by a variety of further experimental studies [139]. For example, coupling of bright and dark exciton states via spin-flip processes has been suggested as origin for the non-exponential character [89]. If feeding of the spin-bright exciton reservoir from the reservoir of dark excitons were important, two time-scales would be relevant: the decay time of the bright excitons and a slower time-scale on which the dark exciton would convert into bright excitons via a spin-flip. From the study of a QD reference sample it was concluded that dark exciton states cannot be thought of as origin of the non-exponential decay. Further explanations, like effects of charged exciton complexes formed due to unintentional background doping, or the influence of non-radiative decay channels, such as traps at the etched cavity sidewalls, are as well ruled out by additional experiments [138, 139].

In summary, the experimental findings are well described by our microscopic theory based on the SLE. In particular the non-exponential decay as well as the strong dependence of the decay dynamics on the excitation density that occurs even below the laser threshold is well reproduced. Furthermore, alternative explanations for the non-exponential decay dynamics can be ruled out for the present case in part by our theoretical analysis and in part by experiments.

Part IV

Summary and Outlook

Different aspects of the electronic and optical properties of semiconductor QDs have been investigated in this thesis. Using the full configuration interaction method, it is possible to solve the problem of few charge carriers in the discrete states of a given confinement potential without further approximations. In Part I, we solved in this way the challenging problem of finding all eigenenergies and eigenstates for up to twelve electron-hole pairs for the InGaAs system. The resulting multi-exciton spectra were analyzed in detail and comparisons with previous results and interpretations in the literature were made. In order to obtain a more intuitive picture for the rather complicated spectra, we used a description based on a diagonal Hamiltonian, which was derived by taking into account the relative importance of various interaction matrix elements. The limitation of this approach was discussed and the more sophisticated ‘adiabatic Hamiltonian’ was introduced. Using this improved description, it was in particular possible to gain deeper insight into the intriguing stability of the emission from an open shell, which is called ‘hidden symmetry’ property. Additionally, we studied the emission from charged exciton complexes and helped to identify the different emission lines in recent experimental spectra.

The electronic and optical properties of nitride QDs were investigated in Part II using lens-shaped InN/GaN quantum dots as an example. Employing a tight-binding model, we found an exactly degenerate single-particle p -shell and identified the C_{3v} -symmetry of the underlying wurtzite lattice as the source of this degeneracy. This finding is in particular intriguing in view of recent discussions in the literature about the p -shell degeneracy in zinc-blende QDs. Based on the microscopically determined single-particle wave function, the dipole and Coulomb matrix elements were evaluated. These matrix elements served as input parameters for configuration interaction calculations and allowed us to determine the optical spectra. This enabled us to predict a dark exciton and biexciton ground state for small dots – a rather surprising result that is confirmed by careful symmetry considerations. In strong contrast to more conventional III-V systems, the emission from nitride-based QDs is dominated by ‘skew’ excitons, so that totally different multi-exciton spectra arise. For larger QDs, we found that the strong internal electric field can reverse the energetic order of the hole states, which results in a bright exciton and biexciton ground state. However, the oscillator strength is strongly reduced in these structures due to the quantum confined Stark effect. By restricting the analysis to the two energetically lowest shells for each carrier, a semi-analytic description of the optical properties was possible, leading to a deeper insight into the origin of the various emission lines.

In Part III the photoluminescence (PL) dynamics of a QD system was investigated. To this end, we used Heisenberg's equation of motion for the various operator averages of interest. The encountered hierarchy problem, which is entailed on the one hand by the carrier-carrier interaction and on the other hand by the interaction of the carriers with the quantized light field, is truncated unambiguously using the cluster expansion scheme. The resulting semiconductor luminescence equations (SLE) including correlations up to the singlet-doublet level were discussed in detail. In particular, we studied the influence of correlations on the PL dynamics for QDs either coupled to the modes of 'free space' or embedded in a microcavity. In the first case, the two limiting cases of uncorrelated carriers, leading to a non-exponential decay, and fully-correlated carriers in two-level approximation, leading to an exponential decay, were investigated. For QDs embedded in a microcavity, a detailed comparison of our theoretical results based on the SLE and recent PL experiment were given. From our numerical analysis of the SLE for the QD system we conclude that the lack of full correlation between the carriers is responsible for the non-exponential and excitation-density dependent decay, indicating that approaches based on atomic models fail to describe the photoluminescence dynamics in this case and that a full semiconductor treatment is required for the explanation of recent experimental results.

Extension of the present work can proceed in several directions. For example, we could use the developed schemes to investigate the multi-exciton spectra in QD molecules. As the number of confined states in such coupled QD structures grows rapidly and the symmetry is, at least in laterally coupled QDs [165], strongly reduced, it may turn out to be necessary to restrict the many-particle basis to 'single' or 'double' excited states. A truncation of the many-particle basis has been used by others to study the multi-exciton emission of single QDs, see, for example Refs. [45, 49]. The validity of such a truncation could be tested by comparing it to the QD containing three shells that was treated in this thesis without further approximation. While the analysis of QD molecules would be interesting for both the group-III arsenide and nitride systems, to date a comparison with experimental findings seems more realistic for the former case. For the nitrides, at first, a comparison of our predictions for single QDs to experiments would be beneficial.

Regarding the emission dynamics of QDs, an inclusion of higher-order correlations to study the photon statistics of QDs embedded in a optical cavity is desired. With increasing coupling efficiency of the spontaneous emission into the laser mode, one approaches the limit of thresholdless lasing. Therefore, a clear indicator for the transition from thermal light, below the threshold, to the laser regime is needed. Such a indicator is given by the second-order correlation function $g^2(\tau)$ of the photon number [166]. Promising results in this direction have already been obtained in our group [133] and are currently further investigated.

Appendix

A Construction of the Hamiltonian Matrix

To construct the Hamiltonian matrix, three different parts of the Hamiltonian need to be considered: (i) the non-interacting part (ii) the part describing the electron-electron and hole-hole Coulomb interaction and (iii) the one containing the electron-hole Coulomb interaction.

The central quantities to be considered are the matrix elements

$$\langle \phi_\alpha | H | \phi_\beta \rangle \quad (\text{A.1})$$

where the uncorrelated basis states $|\phi_i\rangle$ are of the form

$$|\phi\rangle = \prod_{\substack{i \\ \sum_i n_i^e = N_e}} (e_i^\dagger)^{n_i^e} \prod_{\substack{j \\ \sum_j n_j^h = N_h}} (h_j^\dagger)^{n_j^h} |0\rangle \quad . \quad (\text{A.2})$$

Here \prod denotes an *ordered* product. As the carrier operators do not commute, such an ordering is necessary to uniquely define the states $|\phi\rangle$. To this end, one sorts the single-particle states in an arbitrary way and then creates the particles in Eq. (A.2) according to this order.

(i) Let us first consider the single-particle Hamiltonian H_0^e for the electrons

$$H_0^e = \sum_i \varepsilon_i e_i^\dagger e_i \quad .$$

Constructing the matrix elements in this case is straightforward as the uncorrelated basis states are eigenfunctions of the free Hamiltonian. One obtains

$$\langle \phi_\alpha | H_0^e | \phi_\beta \rangle = \sum_i \varepsilon_i n_i^e(\alpha) \langle \phi_\alpha | \phi_\beta \rangle = \delta_{\alpha,\beta} \sum_i \varepsilon_i n_i(\alpha)$$

with $n_i^e(\alpha) = 1$, if the electron single-particle state $|i\rangle$ is occupied in the Slater state $|\phi_\alpha\rangle$, and $n_i^e(\alpha) = 0$, otherwise. A similar expression is obtained for the corresponding equations for H_0^h .

(ii) The case of the electron-electron and hole-hole interaction is more complicated. As both cases can be treated in full analogy, only the case of the electron-electron interaction will be discussed. The corresponding Hamiltonian has the form

$$H_{ee} = \frac{1}{2} \sum_{ijkl} V_{ij,kl} e_i^\dagger e_j^\dagger e_k e_l .$$

Since H_{ee} does not act on the hole states one may write the desired matrix elements (A.1) as

$$\langle \phi_\alpha | H_{ee} | \phi_\beta \rangle = \langle \phi_\alpha^h | \phi_\beta^h \rangle \langle \phi_\alpha^e | H_{ee} | \phi_\beta^e \rangle ,$$

where $|\phi^\lambda\rangle$ with $\lambda \in \{e, h\}$ is of the form

$$|\phi^\lambda\rangle = \prod_{\substack{i \\ \sum_i n_i^\lambda = N_\lambda}} (a_{i,\lambda}^\dagger)^{n_i^\lambda} |0\rangle .$$

As the Hamiltonian H_{ee} annihilates two particles, one in state $|k\rangle$ and one in state $|l\rangle$, and creates two particles, one in $|i\rangle$ and one in $|j\rangle$, it is easy to see that $\langle \phi_\alpha^e | H_{ee} | \phi_\beta^e \rangle$ is zero if the many-particle states $|\phi_\alpha^e\rangle$ and $|\phi_\beta^e\rangle$ differ by more than two occupied single-particle states. Denoting the number of single-particle states by which the two basis states differ N_{diff}^e , one has four different cases:

1. $N_{\text{diff}}^e = 0$:

In this case we have $|\phi_\alpha^e\rangle = |\phi_\beta^e\rangle$. As these states are uncorrelated Slater states we can immediately apply Wick's theorem and find:

$$\langle \phi_\alpha^e | H_{ee} | \phi_\alpha^e \rangle = \frac{1}{2} \sum_{i,j} n_i^e(\phi_\alpha) n_j^e(\phi_\alpha) (V_{ij,ji} - V_{ij,ij}) .$$

2. $N_{\text{diff}}^e = 1$:

As the two states differ only in the occupation of one single-particle state one may express the two states $|\phi_\alpha^e\rangle$ and $|\phi_\beta^e\rangle$ as being created from a common state $|\bar{\phi}^e\rangle$ by the application of one creation operator

$$\begin{aligned} |\phi_\alpha^e\rangle &= (-1)^{P_{\bar{\alpha}}} e_{\bar{\alpha}}^+ |\bar{\phi}^e\rangle , \\ |\phi_\beta^e\rangle &= (-1)^{P_{\bar{\beta}}} e_{\bar{\beta}}^+ |\bar{\phi}^e\rangle . \end{aligned} \quad (\text{A.3})$$

The label $\bar{\alpha}$ refers to the single-particle state that is occupied in $|\phi_\alpha^e\rangle$ but not in $|\bar{\phi}^e\rangle$. Similarly $\bar{\beta}$ refers to the single-particle state occupied in $|\phi_\beta^e\rangle$ but not in $|\bar{\phi}^e\rangle$. The sign depends on how many transpositions of the ordered creation operators are necessary to achieve this representation. With the states of Eq. (A.3) we can write

$$\begin{aligned} \langle \phi_\alpha^e | H_{ee} | \phi_\beta^e \rangle &= (-1)^{P_\alpha + P_\beta} \frac{1}{2} \sum_{ijkl} V_{ij,kl} \langle \bar{\phi}^e | e_{\bar{\alpha}} e_i^\dagger e_j^\dagger e_k e_l e_{\bar{\beta}}^+ | \bar{\phi}^e \rangle \\ &= (-1)^{P_\alpha + P_\beta} \sum_i n_i^e(\phi_\alpha) (V_{\bar{\alpha}i,i\bar{\beta}} - V_{i\bar{\alpha},i\bar{\beta}}) . \end{aligned}$$

To get from the first to the second line of the previous equation, once again Wick's theorem and the fact $\alpha \neq \beta$ was used.

3. $N_{\text{diff}}^e = 2$:

If the two basis states differ in the occupation of two single-particle states one can write these states as

$$\begin{aligned} |\phi_\alpha^e\rangle &= (-1)^{P_{\bar{\alpha}_1, \bar{\alpha}_2}} e_{\bar{\alpha}_1}^+ e_{\bar{\alpha}_2}^+ |\bar{\phi}^e\rangle, \\ |\phi_\beta^e\rangle &= (-1)^{P_{\bar{\beta}_1, \bar{\beta}_2}} e_{\bar{\beta}_1}^+ e_{\bar{\beta}_2}^+ |\bar{\phi}^e\rangle. \end{aligned}$$

Again, by virtue of Wicks theorem we obtain in this case

$$\langle \phi_\alpha^e | H_{ee} | \phi_\beta^e \rangle = (-1)^{P_\alpha + P_\beta} (V_{\bar{\alpha}_1 \bar{\alpha}_2, \bar{\beta}_2, \bar{\beta}_2} - V_{\bar{\alpha}_1 \bar{\alpha}_2, \bar{\beta}_1, \bar{\beta}_2}) .$$

4. $N_{\text{diff}}^e > 2$:

As already mentioned, one obtains in this case simply:

$$\langle \phi_\alpha^e | H_{ee} | \phi_\alpha^e \rangle = 0 .$$

(iii) Let us finally consider the case of the electron-hole interaction with its Hamiltonian

$$H_{eh} = \sum_{ijkl} V_{ij,kl} h_i^\dagger e_j^\dagger e_k h_l .$$

In this case the elements of the Hamiltonian matrix can be cast into

$$\langle \phi_\alpha | H_{eh} | \phi_\beta \rangle = \sum_{ijkl} V_{ij,kl} \langle \phi_\alpha^e | e_j^\dagger e_k | \phi_\beta^e \rangle \langle \phi_\alpha^h | h_i^\dagger h_l | \phi_\beta^h \rangle .$$

Once one has established the rules for the matrix elements $\langle \phi_\alpha^e | e_j^\dagger e_k | \phi_\beta^e \rangle$ one can immediately calculate the desired matrix elements for the electron-hole interaction. For such matrix elements, three cases have to be distinguished:

1. $N_{\text{diff}}^e = 0$:

In this case one readily finds:

$$\langle \phi_\alpha^e | e_j^\dagger e_k | \phi_\beta^e \rangle = \delta_{j,k} n_j^e(\phi_\alpha) .$$

2. $N_{\text{diff}}^e = 1$:

Expressing $|\phi_\alpha^e\rangle$ and $|\phi_\beta^e\rangle$ as above in terms of $|\bar{\phi}^e\rangle$ we find:

$$\langle \phi_\alpha^e | e_j^\dagger e_k | \phi_\beta^e \rangle = (-1)^{P_\alpha + P_\beta} \delta_{j,\bar{\alpha}} \delta_{k,\bar{\beta}} .$$

3. $N_{\text{diff}}^e > 1$:

As the operator combination $e_j^\dagger e_k$ can at most interchange one particle one has:

$$\langle \phi_\alpha^e | e_j^\dagger e_k | \phi_\beta^e \rangle = 0 .$$

And similarly for the holes.

Equipped with this knowledge one may now set out and find an efficient numerical implementation of these rules.

B Spin and Band Symmetries

Let us first consider the commutation of the total spin operators in a one-component electron gas. In this case the z -component, and the raising and lowering operators of the total electronic spin are, respectively, given by

$$\begin{aligned} S_z &= \frac{1}{2} \sum_i (a_{i\uparrow}^\dagger a_{i\uparrow} - a_{i\downarrow}^\dagger a_{i\downarrow}), \\ S_+ &= \sum_i a_{i\uparrow}^\dagger a_{i\downarrow}, \\ S_- &= \sum_i a_{i\downarrow}^\dagger a_{i\uparrow}. \end{aligned} \quad (\text{B.1})$$

If one considers now operators of the form

$$\sum_\sigma a_{i\sigma}^\dagger a_{j\sigma} , \quad (\text{B.2})$$

one can readily verify that these operators commute with all the spin operators. This commutation only holds because the summation over *both* spin states is performed in Eq. (B.2). By rewriting the Hamiltonian of the electron gas

$$\begin{aligned} H &= \sum_{i\sigma} \varepsilon_i a_{i\sigma}^\dagger a_{i\sigma} + \frac{1}{2} \sum_{ijkl} V_{ijkl} a_{i\sigma}^\dagger a_{j\sigma'}^\dagger a_{k\sigma'} a_{l\sigma} \\ &= \sum_i \varepsilon_i \left(\sum_\sigma a_{i\sigma}^\dagger a_{i\sigma} \right) + \sum_{ijkl} V_{ijkl} \left[\left(\sum_\sigma a_{i\sigma}^\dagger a_{l\sigma} \right) \left(\sum_{\sigma'} a_{j\sigma'}^\dagger a_{k\sigma'} \right) - \delta_{lj} \left(\sum_\sigma a_{i\sigma}^\dagger a_{k\sigma} \right) \right] \end{aligned} \quad (\text{B.3})$$

one observes that the total Hamiltonian commutes with the total spin operators. This happens because neither the Coulomb matrix elements V_{ijkl} nor the single-particle energies depend on spin so that they do not interfere with the spin summation. Along the same lines one can prove for the Hamiltonian (1.1) from page 7 that both the total spin of the electrons as well as the total spin of the holes are separately good quantum numbers. This relies on the fact that (i) the operators of the form Eq. (B.2) with the indices i and j now labeling states within the same band will commute with the spin operators in Eq. (B.1) even if the summation is restricted to one band and (ii) the two-band Hamiltonian can again be rewritten in the form (B.3) where each occurring summation of the form $\sum_\sigma a_{i\sigma}^\dagger a_{k\sigma}$ contains only states from one band.

The Hamiltonian that describes the Coulomb interaction in the *c-v*-picture reads

$$H_{\text{Coul}}^{\text{cv}} = \frac{1}{2} \sum_{\substack{ijkl \\ \sigma\sigma' \\ \lambda\lambda'}} V_{i\sigma\lambda, j\sigma'\lambda', k\sigma'\lambda', l\sigma\lambda} a_{i\lambda\sigma}^\dagger a_{j\lambda'\sigma'}^\dagger a_{k\lambda'\sigma'} a_{l\lambda\sigma} \quad (\text{B.4})$$

where λ, λ' label the bands and σ, σ' denote the spin indices. In the case of equal envelope wave functions for the conduction- and valence-band electrons, the Coulomb

matrix elements are band independent: $V_{i\sigma\lambda,j\sigma'\lambda',k\sigma'\lambda',l\sigma\lambda} = V_{i\sigma,j\sigma',k\sigma',l\sigma}$. In the previous paragraph we explained the consequences of the Coulomb matrix elements being spin independent. This was responsible for the commutation of the Hamiltonian with the spin operators (B.1) for the total spin as well as for the conduction and valence band carriers separately. As the band-indices enter Eq. (B.4) in exactly the same way as the spin indices, one expects that in the case of identical envelopes similar commutation relations hold for quantities in which the spin degree of freedom is replaced by the band-index. Conventionally, this is done by identifying c with \uparrow and v with \downarrow . Indeed, one can prove along the lines detailed above for the spin operators that for equal envelopes for the valence- and conduction-band electrons the operators

$$\begin{aligned}\tilde{S}_z &= \frac{1}{2} \sum_i (a_{i,c}^\dagger a_{i,c} - a_{i,v}^\dagger a_{i,v}) =: \mathcal{P}_z, \\ \tilde{S}_+ &= \sum_i a_{i,c}^\dagger a_{i,v} = \mathcal{P}^\dagger, \\ \tilde{S}_- &= \sum_i a_{i,v}^\dagger a_{i,c} = \mathcal{P}\end{aligned}$$

all commute with the Hamiltonian Eq. (B.4). This is the case as the Coulomb matrix elements do not depend on the band index: $V_{i\sigma\lambda,j\sigma'\lambda',k\sigma'\lambda',l\sigma\lambda} = V_{i\sigma,j\sigma',k\sigma',l\sigma}$. In the above equations \mathcal{P} denotes the interband dipole operator in the c - v -picture.

While $[H_{\text{Coul}}^{cv}, \mathcal{P}] = 0$, the free part $H_0^{cv} = \sum_i \varepsilon_i^c a_{i,c}^\dagger a_{i,c} + \sum_i \varepsilon_i^v a_{i,v}^\dagger a_{i,v}$ does only commute with \mathcal{P} in the very special situation of $\varepsilon_i^c = \varepsilon_i^v$. Because only then the single-particle energies are band-independent. In the general situation we can rewrite the free part as

$$H_0^{cv} = \sum_i \frac{\varepsilon_i^c + \varepsilon_i^v}{2} (a_{i,c}^\dagger a_{i,c} + a_{i,v}^\dagger a_{i,v}) + \sum_i \frac{\varepsilon_i^c - \varepsilon_i^v}{2} (a_{i,c}^\dagger a_{i,c} - a_{i,v}^\dagger a_{i,v}) .$$

In this expression the first part commutes with \mathcal{P}_z , \mathcal{P}^\dagger , and \mathcal{P} while the second does not. However, if $\varepsilon_i^c - \varepsilon_i^v$ is constant, as it is in the case of a single, degenerate shell, we can rewrite the last term as $(\varepsilon_i^c - \varepsilon_i^v)\mathcal{P}_z$. From this one can deduce for a single, degenerate shell

$$[H^{cv}, \mathcal{P}] = [H_{\text{Coul}}^{cv} + H_0^{cv}, \mathcal{P}] = [H_0^{cv}, \mathcal{P}] = (\varepsilon_i^c - \varepsilon_i^v)[\mathcal{P}_z, \mathcal{P}] = -(\varepsilon_i^c - \varepsilon_i^v)\mathcal{P} .$$

In the above equation we have used in the last step the usual commutation relations for spin operators [70].

This is quite an amazing result as it states, together with the discussion in Section 3.2, that one always obtains an exact eigenstate of the interacting system by repeated application of \mathcal{P} on the vacuum state and that the energy of this eigenstate increases linearly with the number of excitons [44, 80]. At first glance, it is even more amazing that it is not the Coulomb interaction that entails this increase of energy with the number of excitons but the free Hamiltonian. But this can be made plausible if one takes a closer look at the assumption of identical envelopes [80]. In this case the Coulomb

interaction does not depend on the band index, that is, $V_{ijkl}^{\lambda\lambda'} = V_{ijkl}$ irrespective of the band index $\lambda \in c, v$. Therefore it does – for the Coulomb interaction – not matter whether the electron is in the conduction or in the valence band. The only energy difference comes from promoting the valence-band electron above the gap. This is in full analogy to a spin system in which the interaction between the carriers does *not* depend on spin. In such a situation the spin configurations are, without an external magnetic field, degenerate and a spin flip does not change the energies. If a constant homogeneous external magnetic field is present the analogy between the exciton system and the spin system can be further extended as in this situation the energy of the spin system depends linearly on the number of flipped spins.

Note that in the electron-hole picture the free energies ε^h and ε^e contain Hartree-Fock renormalization due to the full valence band. These renormalization terms can spoil the discussed result as a degenerate shell in the electron-hole picture does not necessarily mean a degenerate shell in the conduction-valence band picture, because different individual states are in general differently renormalized. For an isolated *s*-or *p*-shell, however, the individual states will be identically renormalized, so that we can conclude: $\{\varepsilon_i^h\}_i$ and $\{\varepsilon_i^e\}_i$ degenerate $\rightarrow \{\varepsilon_i^c\}_i$ and $\{\varepsilon_i^v\}_i$ degenerate \rightarrow ‘hidden symmetry’ commutation relation fulfilled. Deviations from this picture, as observed in a full calculation procedure in Chapter 2, stem from the fact that the *p*-shell cannot be considered as being decoupled from other shells. Additionally, while the restriction to a single, degenerate shell reproduces the remarkable stability of the *p*-shell emission lines, only the inclusion of the *s*-shell within the adiabatic Hamiltonian produces an energy value that is in good quantitative agreement with the full calculation.

C Rotation and Time-Reversal

In this appendix we give an alternative proof of the existence of energetically degenerate states for a lens-shaped QD crystallized in the wurtzite phase. We compare this structure on the one hand to the case of a QD grown in a zinc-blende structure and on the other hand to a disk-like QD. For this additional proof of the results in Section 7.1, we consider only the allowed rotations of the symmetry group and utilize additionally the so-called *time-reversal* operator \mathcal{K} , which is an anti-linear operator⁴. As we will detail in the following one can in this situation deduce a degeneracy even though these operators commute with each other *and* the Hamiltonian.

Let us consider the case of a general symmetry operation T such that $T^n = 1$, where n denotes the smallest integer for which unity is reached. (For the here considered cases these operators will be the rotations around the z -axis, but more general operators are possible.) The eigenvalues λ of this operator are given by the n -order roots of unity,

⁴ In contrast to a linear operator A that does not affect the coefficients of a linear combination, that is, $A(\alpha|\psi\rangle + \beta|\phi\rangle) = \alpha A|\psi\rangle + \beta A|\phi\rangle$, one has for an antilinear operator [126]: $A(\alpha|\psi\rangle + \beta|\phi\rangle) = \alpha^* A|\psi\rangle + \beta^* A|\phi\rangle$.

$\lambda = e^{i\frac{2\pi}{n}m}$, with $m = 0, 1, \dots, n - 1$. For $n > 2$ some of these eigenvalues are necessarily complex. Let us furthermore consider the time inversion operator \mathcal{K} , defined in spatial representation via the action $\mathcal{K}\psi(\mathbf{r}) = \psi^*(\mathbf{r})$. In case of a real-valued potential the commutator $[H, \mathcal{K}] = 0$ holds. Using the definition of the action of the symmetry operation T on the wave function, namely, $T\psi(\mathbf{r}) = \psi(T^{-1}\mathbf{r})$, one has additionally

$$\mathcal{K}T\psi(\mathbf{r}) = \mathcal{K}\psi(T^{-1}\mathbf{r}) = \psi^*(T^{-1}\mathbf{r}) = T\psi^*(\mathbf{r}) = T\mathcal{K}\psi(\mathbf{r}) , \quad (\text{C.1})$$

which shows the commutation of the operators \mathcal{K} and T . At a first glance it seems that the three operators H , T , and \mathcal{K} are most unsuited to discuss degeneracies, as these operators all commute. Therefore a statement about degeneracies along the lines presented in Section 7.1 is not possible. Nevertheless such a statement can be achieved by considering a state $\phi(\mathbf{r})$ that is a common eigenstate of H and T with energy E and eigenvalue λ having non-vanishing imaginary part, respectively. As outlined above such states exist for $n > 2$. In this case the following relations are readily verified $H(\mathcal{K}\phi(\mathbf{r})) = \mathcal{K}(H\phi(\mathbf{r})) = E(\mathcal{K}\phi(\mathbf{r}))$ and $T(\mathcal{K}\phi(\mathbf{r})) = \mathcal{K}(T\phi(\mathbf{r})) = \lambda^*(\mathcal{K}\phi(\mathbf{r}))$. As $\lambda^* \neq \lambda$ this shows that the two states $\phi(\mathbf{r})$ and $\mathcal{K}\phi(\mathbf{r})$ are really two different states that have the same energy. From this we deduce that in the case of a symmetry operator T with $T^n = 1$ a real-valued potential leads to the existence of degenerate eigenstates for $n > 2$. That this is not in contradiction with the commutation of the three operators stems from the fact that the proof of a common eigenbasis for commuting operators uses the linearity of the operators, while \mathcal{K} is antilinear.

How is this now linked to the degeneracy of the QD states? The connection is established when identifying the operator T with the rotation R by an angle $\frac{2\pi}{3}$ around the z -axis for the wurtzite QD discussed above. In this case one obtains $n = 3$ and therefore degenerate states. (For a schematic of the different dots and the corresponding symmetries see Figure 7.5 on page 74.) In the case of a pyramidal or lens-shaped QD in a zinc-blende phase the improper rotation IC_{4z} of the underlying lattice is removed. Instead one has only a C_{2z} rotation in the presence of the QD, as the dot destroys the inversion-symmetry. But a C_{2z} symmetry, leading to $n = 2$, is not rich enough to predict a degeneracy from the above argument. If one considers a disk-like QD in zinc-blende phase, the full IC_{4z} rotation is present. This yields $n = 4$, from which we predict a degeneracy in accordance with the discussion of Refs. [121].

D Leaky Modes

Besides the resonant modes, which are characterized by their large Q -values and pronounced peak structure in a transmission spectrum, there exists a background contribution formed by the continuum of leaky modes. In order to include the influence of these leaky modes, we assume that the background contribution constitutes a fraction of the continuum of modes of free space. The size of this fraction can be estimated by counting the plane waves that (i) either reach the sidewalls of the micropillar in an angle smaller than the critical angle α_i of total internal reflection (as these waves are not reflected

by the sidewalls, they leave the cavity), or (ii) have a momentum component $k_{||}$ along the pillar axis that lies outside the stopband of the DBR⁵. For a given frequency ω , the last case defines two critical angles $\alpha_{s1}(\omega)$ and $\alpha_{s2}(\omega)$, see Figure D.1. All plane waves with an angle α outside the interval $[\alpha_{s1}, \alpha_{s2}]$ will leave the cavity. As all emitters

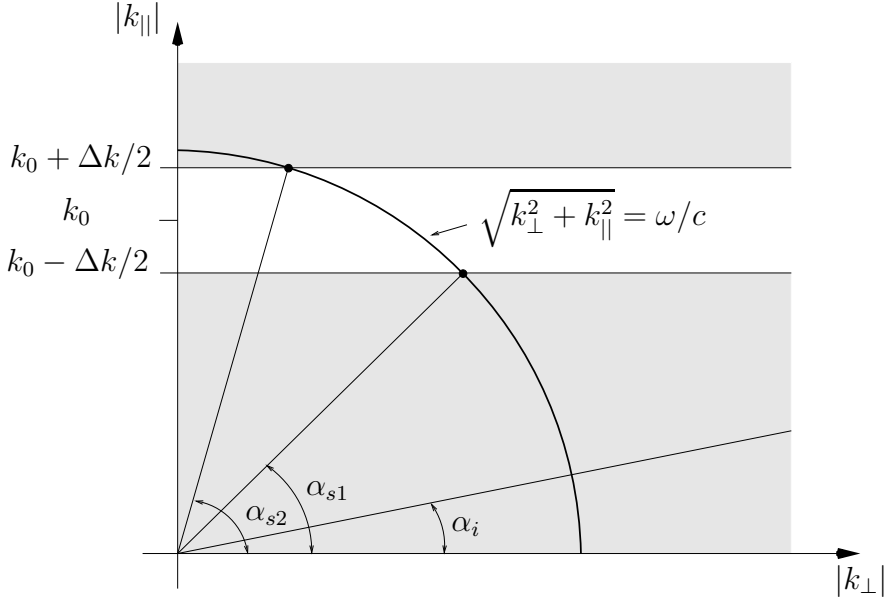


Figure D.1: All waves characterized by $(|k_{\perp}|, |k_{||}|)$ -values that lie below the line defined by the critical angle α_i of total internal reflection can leave the cavity, as they are not reflected from the lateral boundaries. Those specified by $(|k_{\perp}|, |k_{||}|)$ -values in the shaded areas can leave the cavity as they have a $|k_{||}|$ -components that does *not* lie within the stopband of the DBR. For a given photonic frequency (defined by the circle) the latter condition defines the two angles α_{s1} and α_{s2} .

have frequencies around the fundamental cavity mode, which is to first approximation at the center ω_0 of the stopband, and the angles α_{s1} and α_{s2} depend only weakly on ω , we can take these angles as constant. The actual values for these angles are then calculated for $\omega_0 = ck_0$. In this case the circle defined by $k_{\perp}^2 + k_{||}^2 = \omega_0^2/c^2$ runs through the point $(0, k_0)$ and intersects therefore only with the lower shaded area in Figure D.1. Consequently we can set α_{s2} to $\frac{\pi}{2}$. For the other angle one can infer from Figure D.1 $\alpha_{s1} = \arcsin \frac{k_0 - \Delta k/2}{k_0}$. For typical parameters of an AlAs/GaAs DBR one has $\alpha_{s1} > \alpha_i$, so that the leakage-channel defined by α_i , which is provided by the absence of total internal reflection, does not yield additional leaking modes. In summary, we deduce that all plane waves characterized by an angle between 0 and α_{s1} will leave the cavity. In terms of propagation directions this means that all wave forming an angle between

⁵ A DBR has a high reflectivity only in a finite frequency range, the so-called stop band. Outside this range the mirror is more or less transparent [164].

$\frac{\pi}{2} - \alpha_{s1}$ and $\frac{\pi}{2}$ with the pillar axis, will contribute to the leaky modes.

If we sum now over all the plane waves leaving the cavity, we can determine an effective light-matter coupling matrix element $|\tilde{g}_{\omega i}^{\text{leaky}}|^2$ that only depends on the energy of the transition. This runs in close analogy to the lines discussed in the case of ‘free space’ in Section 11.1. The only difference is that in the present situation only a certain amount of all plane waves contributes. Assuming that the dipole-moment lies within the QD-plane [162], we finally obtain

$$|\tilde{g}_{\omega i}^{\text{leaky}}|^2 = \zeta |\tilde{g}_{\omega i}|^2 , \quad (\text{D.1})$$

where the fraction ζ is given by $\frac{3}{4} \sin(\alpha_{s1}) + \frac{1}{4} \sin^3(\alpha_{s1})$. For $k_0 \gg \Delta k/2$ this can be approximated by $1 - \frac{3}{4} \frac{\Delta k}{k}$. From this expression it can be inferred, that for a vanishing stop-band width Δk the fraction of leaky modes goes to unity. This is a physically very intuitive result as in this case the DBRs are transparent for all the frequencies. Using the estimate for the relative spectral width of the stop band $\frac{\Delta \lambda}{\lambda_0} \approx \frac{1}{\pi} \frac{n_1^2 - n_2^2}{n_1 n_2}$ given in Ref. [164] one obtains for a typical AlAs/GaAs DBR a fraction ζ of approximately 90%. This value is in very good agreement with the experimental finding reported in Ref. [36, 167] and close to the estimate used in Ref. [38]. The fact that photons in a leaky mode will leave the cavity is taken into account by a loss-rate κ_{leaky} , which is much larger than those of a resonant mode. Note that the exact value of this loss-rate is only of minor importance for the emission dynamics.

E Numerical Methods

The numerical methods employed for the evaluation of integrals, diagonalization of matrices, solution of systems of linear equations, and the calculation of the time evolution of a set of differential equations are well documented in the literature. For the sake of completeness, we will briefly comment on some aspects of the subject and direct the reader to appropriate references.

Evaluation of Coulomb Matrix Elements

For the evaluation of the Coulomb matrix elements, several cases have to be distinguished, according to how many of the four involved states are QD and how many are WL states. Details can be found in Ref. [168].

If one is solely interested in the Coulomb interaction between the localized states, one can evaluate the interaction matrix elements analytically in the case of two-dimensional harmonic oscillator wave functions and vanishing lateral extension $L_z \rightarrow 0$ in growth direction [44, 152, 169]. For a finite extension L_z , a one-dimensional integral remains [168, 169], which can – as the remaining integrand has no singularity – straightforwardly be integrated.

Evaluating an integral $\int_a^b f(x)dx \approx \sum_i f(x_i)\Delta x$ using equidistant grid points and equal weights for each point turns out to be rather ineffective. Instead, one better rewrites the integral in the more general form $\sum_i w_i f(x_i)$ with carefully chosen weighting factors $\{w_i\}$ and grid points $\{x_i\}$ [170]. In general, more integration points should be used in regions where the function $f(x)$ varies more rapidly, for example, near an (integrable) singularity. For most of our applications, the following sets of grid points and weighting factors turned out to be well suited:

$$\begin{aligned} x_i &= \frac{1}{2\pi} \left[\frac{2\pi}{N+1} i - \sin\left(\frac{2\pi}{N+1} i\right) \right] (b-a) + a, \\ w_i &= \frac{1}{2\pi} \left[1 - \cos\left(\frac{2\pi}{N+1} i\right) \right] \frac{b-a}{N+1}. \end{aligned} \quad (\text{E.1})$$

where the integer i runs from 1 to N . Note that with this choice the points $\{x_i\}$ become denser near the endpoints a and b of the interval, but never actually reach these points.

In the case that only delocalized WL states are involved, one encounters integrals of the form $I(k) = \int dk' V(k, k') f(k')$ with $V(k, k')$ being singular for $k = k'$. In this case it is worth rewriting the integral in the form

$$I(k) = \int dk' V(k, k') [f(k') - f(k) \alpha(k, k')] + f(k) \int dk' V(k, k') \alpha(k, k') , \quad (\text{E.2})$$

where an arbitrary function $\alpha(k, k')$ fulfilling $\alpha(k, k) = 1$ is introduced. While here the first part is regular and can therefore readily be numerically integrated, the singular part is moved to the second term. The advantage of this representation is that the singular part is now independent of the function $f(k)$, so that it can be evaluated once and for all using a large number of grid points. In some cases, it is even possible to choose the function $\alpha(k, k')$ such that the singular part can be calculated analytically [171].

Matrix Diagonalization

The quest for highly efficient diagonalization algorithms for a general eigenvalue problem is still an active research field. Nevertheless there exist already several code-libraries that contain reliable and rather efficient implementations for special eigenvalue problems, like, real and symmetric matrices. We chose to employ the wide-spread LAPACK library [172]. More specifically we used the ‘dsyev’-routine [172] for finding all eigenvectors and eigenvalues of the real and symmetric matrices encountered in Part I and Part II of this thesis. This algorithm is based on a QR -factorization, for an introduction to this topic see Ref. [170].

Unfortunately, it is not sufficient to calculate just a few of the energetically lowest eigenstates, because *any* eigenstates of the $(N_X - 1)$ -exciton problem can occur as a final state in an emission spectrum. Therefore, more specialized, considerably faster and less memory consuming algorithms that focus only on a couple of eigenvalues cannot be used in the present case. As a consequence, the memory demand can become extremely

high, so that the calculation of the multi-exciton emission spectra in the presence of a d -shell was only made possible at the supercomputer ‘JUMP’ at the Forschungszentrum Jülich with its huge shared-memory architecture [91].

Integration of Differential Equations

Heisenberg’s equation of motion technique employed in Part III leads to a coupled set of equations of the form

$$\frac{d}{dt}y(t) = f[y(t), t] \quad \text{with } y(t=0) = y_0,$$

where the high-dimensional vector $y(t)$ contains the populations, correlations, etc. at time t . In the most simple approach, one approximates the differential quotient by its finite difference value $\Delta y/\Delta t$. In this way, one finds

$$y(t + \Delta t) = y(t) + f[y(t), t]\Delta t + \mathcal{O}[(\Delta t)^2], \quad (\text{E.3})$$

which shows that the error is quadratic in the time differences Δt . Therefore, one needs in general extremely small Δt to obtain reasonable results and it turns out that this algorithm is still numerically quite unstable.

A scheme that allows for larger time steps and is by far more stable, is given by the fourth order Runge-Kutta method [170]. In our case stable results are obtained for typical time steps of the order of $\Delta t = 1$ fs. To follow the PL dynamics on a nanosecond time scale, one needs approximately 10^6 time steps. This number of time-steps can be reduced by a factor of roughly 100 in the adiabatic regime, as already discussed in Chapter 12. The price to be paid is that one needs in this case to solve a set of linear equations, which can be time-consuming and, therefore, pays off only for large sets of coupled equations. To solve the set of linear equations, we use the so-called Gauß algorithm [170].

Bibliography

- [1] G. Stix. *Little Big Science*. Sci. Am. p. 32 (2001).
- [2] J. M. Gerard and B. Gayral. *Strong Purcell effect for InAs quantum boxes in three-dimensional solid-state microcavities*. J. Light Wave Tech. **17**, 2089 (1999).
- [3] P. Michler, A. Kiraz, C. Becher, W. V. Schoenfeld, P. M. Petroff, L. Zhang, E. Hu, and A. Imamoglu. *A Quantum Dot Single-Photon Turnstile Device*. Science **290**, 2282 (2000).
- [4] C. Santori, M. Pelton, G. Solomon, Y. Dale, and Y. Yamamoto. *Triggered Single Photons from a Quantum Dot*. Phys. Rev. Lett. **86**, 1502 (2001).
- [5] J. P. Reithmaier and A. Forchel. *Semiconductor Quantum Dots*. IEEE Circuits and Devices Magazine **19**, 24 (2003).
- [6] D. Bouwmeester, A. Ekert, and A. Zeilinger (Eds.). *The Physics of Quantum Information* (Springer, Berlin, 2000).
- [7] A. Zrenner, E. Beham, S. Stufler, F. Findeis, M. Bichler, and G. Abstreiter. *Coherent properties of a two-level system based on a quantum-dot photodiode*. Nature **418**, 612 (2002).
- [8] F. Rossi. *The Excitonic Quantum Computer*. IEEE Trans. Nanotechnology **3**, 165 (2004).
- [9] L. P. Kouwenhoven, D. G. Austing, and S. Tarucha. *Few-electron Quantum Dots*. Rep. Prog. Phys. **64**, 701 (2001).
- [10] E. Dekel, D. Gershoni, E. Ehrenfreund, D. Spektor, J. M. Garcia, and P. M. Petroff. *Multiexciton Spectroscopy of a Single Self-Assembled Quantum Dot*. Phys. Rev. Lett. **80**, 4991 (1998).
- [11] L. Landin, M. S. Miller, M.-E. Pistol, C. E. Pryor, and L. Samuelson. *Optical Studies of Individual InAs Quantum Dots in GaAs: Few-Particle Effects*. Science **280**, 262 (1998).
- [12] M. Bayer, O. Stern, P. Hawrylak, S. Fafard, and A. Forchel. *Hidden symmetries in the energy levels of excitonic 'artificial atoms'*. Nature **405**, 923 (2000).
- [13] R. Nötzel. *Self-organized growth of quantum-dot structures*. Semicond. Sci. Technol. **11**, 1365 (1996).

Bibliography

- [14] K. Jacobi. *Atomic structure of InAs quantum dots on GaAs*. Progress in Surface Science **71**, 185 (2003).
- [15] J. Stangl, V. Holy, and G. Bauer. *Structural properties of self-organized semiconductor nanostructures*. Rev. Mod. Phys. **76**, 725 (2004).
- [16] S. Fafard, Z. R. Wasilewski, C. Ni. Allen, D. Picard, M. Spanner, J. P. McCaffrey, and P. G. Piva. *Manipulating the energy levels of semiconductor quantum dots*. Phys. Rev. B **59**, 15368 (1999).
- [17] T. R. Nielsen, P. Gartner, and F. Jahnke. *Many-body theory of carrier capture and relaxation in semiconductor quantum-dot lasers*. Phys. Rev. B **69**, 235314 (2004).
- [18] J. Seebeck, T. R. Nielsen, P. Gartner, and F. Jahnke. *Polarons in semiconductor quantum-dots and their role in the quantum kinetics of carrier relaxation*. Phys. Rev. B **71**, 125327 (2005).
- [19] R. K. Jain and M. Stroh. *Zooming in and out with quantum dots*. Nature Biotechnology **22**, 959 (2004).
- [20] D. Bertram and Horst Weller. *Zwischen Molekül und Festkörper*. Physik Journal **1**, 47 (2002).
- [21] H. Schweizer, M. Jetter, and F. Scholz. *Quantum-Dot Lasers*. In: *Single Quantum Dots: Fundamentals, Applications, and New Concepts* (edited by P. Michler), pp. 185–235 (Springer, Berlin, 2003).
- [22] Y. Shen, C. S. Friend, Y Jiang, D. Jakubczyk, J. Swiatkiewicz, and P. N. Prasad. *Nanophotonics: Interactions, Materials, and Applications*. J. Phys. Chem. B **104**, 7577 (2000).
- [23] I. Vurgaftman and J. R. Meyer. *Band parameters for nitrogen-containing semiconductors*. J. Appl. Phys. **94**, 3675 (2003).
- [24] F. A. Ponce and D. P. Bour. *Nitride-based semiconductors for blue and green light-emitting devices*. Nature **386**, 351 (1997).
- [25] S. Nakamura, T. Mukai, and M. Senoh. *Candela-class high-brightness InGaN/AlGaN double-heterostructure blue-light-emitting diodes*. Appl. Phys. Lett. **64**, 1687 (1994).
- [26] S. Nakamura. *The Roles of Structural Imperfections in InGaN-Based Blue Light-Emitting Diodes and Laser Diodes*. Science **281**, 956 (1998).
- [27] J.-Y. Marzin, J.-M. Gerard, A. Izraël, D. Barrier, and G. Bastard. *Photoluminescence of Single InAs Quantum Dots Obtained by Self-Organized Growth on GaAs*. Phys. Rev. Lett. **73**, 716 (1994).
- [28] W.-H. Chang, H.-S. Chang, W.-Y. Chen, T. M. Hsu, T.-P. Hsieh, J.-I. Chyi, and N.-T. Yeh. *Optical control of the exciton charge states of single quantum dots via impurity levels*. Phys. Rev. B **72**, 233302 (2005).

- [29] E. Dekel, D. Gershoni, E. Ehrenfreund, J. M. Garcia, and P. M. Petroff. *Carrier-Carrier correlations in an optically excited single semiconductor quantum dot*. Phys. Rev. B **61**, 11009 (2000).
- [30] K. J. Vahala. *Optical microcavities*. Nature **424**, 839 (2003).
- [31] C. Weisbuch, H. Benisty, and R. Houdre. *Overview of fundamentals and applications of electrons, excitons and photons in confined structures*. J. Luminescence **85**, 271 (2000).
- [32] J. P. Reithmaier, G. Sek, A. Löffler, C. Hofmann, S. Kuhn, S. Reitzenstein, L. V. Keldysh, V. D. Kulakovskii, T. L. Reinicke, and A. Forchel. *Strong coupling in a single quantum dot-semiconductor microcavity system*. Nature **432**, 197 (2004).
- [33] T. Yoshie, A. Scherer, J. Hendrickson, G. Khitrova, H. M. Gibbs, G. Rupper, C. Ell, O. B. Shchekin, and D. G. Deppe. *Vacuum Rabi splitting with a single quantum dot in a photonic crystal nanocavity*. Nature **432**, 200 (2004).
- [34] E. Peter, P. Senellart, D. Martrou, A. Lemaitre, J. Hours, J. M. Gerard, and J. Bloch. *Exciton-Photon Strong-Coupling Regime for a Single Quantum Dot Embedded in a Microcavity*. Phys. Rev. Lett. **95**, 067401 (2005).
- [35] G. S. Solomon, M. Pelton, and Y. Yamamoto. *Single-mode Spontaneous Emission from a Single Quantum Dot in a Three-Dimensional Microcavity*. Phys. Rev. Lett. **86**, 3903 (2001).
- [36] M. Bayer, T. L. Reinecke, F. Weidner, A. Larionov, A. McDonald, and A. Forchel. *Inhibition and Enhancement of the Spontaneous Emission of Quantum Dots in Structured Microresonators*. Phys. Rev. Lett. **86**, 3168 (2001).
- [37] P. Lodahl, A. F. van Driel, I. S. Nikolaev, A. Irman, K. Overgaag, Daniel Vanmaekelbergh, and W. L. Vos. *Controlling the dynamics of spontaneous emission from quantum dots by photonic crystals*. Nature **430**, 654 (2004).
- [38] J. M. Gerard, B. Sermage, B. Gayral, B. Legrand, E. Costard, and V. Thierry-Mieg. *Enhanced Spontaneous Emission by Quantum Boxes in a Monolithic Optical Microcavity*. Phys. Rev. Lett. **81**, 1110 (1998).
- [39] P. Michler. *Single Quantum Dots: Fundamentals, Applications, and New Concepts*. Topics in Applied Physics (Springer, Berlin, 2003).
- [40] S. Raymond, S. Studenikin, A. Sachrajda, Z. Wasilewski, S. J. Cheng, W. Sheng, P. Hawrylak, A. Babinski, M. Potemski, G. Ortner, and M. Bayer. *Excitonic Energy Shell Structure of Self-Assembled InGaAs/GaAs Quantum Dots*. Phys. Rev. Lett. **92**, 187402 (2004).
- [41] E. Moreau, I. Robert, J. M. Gerard, I. Abram, L. Manin, and V. Thierry-Mieg. *Single-mode solid-state single photon source based on isolated quantum dots in pillar microcavities*. Appl. Phys. Lett. **79**, 2865 (2001).
- [42] R. M. Stevenson, R. J. Young, P. Atkinson, K. Cooper, D. A. Ritchie, and A. J. Shields. *A semiconductor source of triggered entangled photon pairs*. Nature **439**, 179 (2006).

Bibliography

- [43] A. Barenco and M. A. Dupertuis. *Quantum many-body states of excitons in a small quantum dot.* Phys. Rev. B **52**, 2766 (1995).
- [44] P. Hawrylak. *Excitonic artificial atoms: Engineering optical properties of quantum dots.* Phys. Rev. B **60**, 5597 (1999).
- [45] U. Hohenester and E. Molinari. *Role of Coulomb Correlations in the Optical Spectra of Semiconductor Quantum dots.* phys. stat. sol. (b) **221**, 19 (2000).
- [46] A. Franceschetti, A. Williamson, and A. Zunger. *Addition Spectra of Quantum Dots: the Role of Dielectric Mismatch.* J. Phys. Chem. B **104**, 3398 (2000).
- [47] M. Braskén, M. Lindberg, D. Sundholm, and J. Olsen. *Spatial carrier-carrier correlations in strain-induced quantum dots.* Phys. Rev. B **64**, 035312 (2001).
- [48] G. Bester, S. Nair, and A. Zunger. *Pseudopotential calculation of the excitonic fine structure of million-atom self-assembled $In_{1-x}Ga_xAs/GaAs$ quantum dots.* Phys. Rev. B **67**, 161306 (2003).
- [49] W. Sheng, S.-J. Cheng, and P. Hawrylak. *Multiband theory of multi-exciton complexes in self-assembled quantum dots.* Phys. Rev. B **71**, 035316 (2005).
- [50] S. V. Nair and Y. Masumoto. *Coulomb effects in the optical spectra of highly excited semiconductor quantum dots.* J. Lumin. **87-89**, 438 (2000).
- [51] O. Stier, R. Heitz, A. Schliwa, and D. Bimberg. *Shape and Composition Effects on Excitons and Biexcitons in Quantum Dots.* phys. status solidi (a) **190**, 477 (2002).
- [52] S. Rodt, A. Schliwa, K. Potschke, F. Guffarth, and D. Bimberg. *Correlation of structural and few-particle properties of self-organized $InAs/GaAs$ quantum dots.* Phys. Rev. B **71**, 155325 (2005).
- [53] G. Bester and A. Zunger. *Compositional and size-dependent spectroscopic shifts in charged self-assembled $In_xGa_{1-x}As/GaAs$ quantum dots.* Phys. Rev. B **68**, 073309 (2003).
- [54] S. M. Ulrich, M. Benyoucef, P. Michler, N. Baer, P. Gartner, F. Janke, H. Kurtze, M. Schwab, M. Bayer, S. Fafard, Z. Wasilewski, and A. Forchel. *Correlated photon-pair emission from a charged single quantum dot.* Phys. Rev. B **71**, 235328 (2005).
- [55] U. Merkt, J. Huser, and M. Wagner. *Energy spectra of two electrons in a harmonic quantum dot.* Phys. Rev. B **43**, 7320 (1991).
- [56] A. Wojs and P. Hawrylak. *Exciton-Exciton Interactions in highly excited quantum dots in a magnetic field.* Solid State Commun. **100**, 487 (1996).
- [57] A. Wojs, P. Hawrylak, S. Fafard, and L. Jacak. *Electronic structure and magneto-optics of self-assembled quantum dots.* Phys. Rev. B **54**, 5604 (1996).
- [58] P. Hawrylak, G. A. Narvaez, M. Bayer, and A. Forchel. *Excitonic Absorption in a Quantum Dot.* Phys. Rev. Lett. **85** (2000).

- [59] N. H. Quang, S. Ohnuma, and A. Natori. *Charged magnetoexcitons in parabolic quantum dots*. Phys. Rev. B **62**, 12955 (2000).
- [60] H. C. Schneider, W. W. Chow, and S. W. Koch. *Many-body effects in the gain spectra of highly excited quantum-dot lasers*. Phys. Rev. B **64**, 115315 (2001).
- [61] S. M. Reimann and M. Manninen. *Electronic structure of quantum dots*. Rev. Mod. Phys. **74**, 1283 (2002).
- [62] B. Krummheuer, V. M. Axt, and T. Kuhn. *Theory of pure dephasing and the resulting absorption line shape in semiconductor quantum dots*. Phys. Rev. B **65**, 195313 (2002).
- [63] C. P. Garcia, V. Pellegrini, A. Pinczuk, M. Rontani, G. Goldoni, E. Molinari, B. S. Dennis, L. N. Pfeiffer, and K. W. West. *Evidence of Correlation in Spin Excitations of Few-Electron Quantum Dots*. Phys. Rev. Lett. **95**, 266806 (2005).
- [64] F. Qu and P. Hawrylak. *Magnetic exchange interactions in quantum dots containing electrons and magnetic ions*. Phys. Rev. Lett. **95**, 217206 (2005).
- [65] P. S. Zory. *Quantum Well Lasers* (Academic Press, Boston, 1993).
- [66] R. Blossey and A. Lorke. *Wetting droplet instability and quantum ring formation*. Phys. Rev. E **65**, 021603 (2002).
- [67] C. Cohen-Tannoudji, B. Diu, and F. Laloë. *Quantum Mechanics, Volume I* (John Wiley, New York, 1992).
- [68] H. Haug and S. W. Koch. *Quantum Theory of the Optical and Electronic Properties of Semiconductors* (World Scientific, Singapore, 1993).
- [69] S. Schulz, S. Schumacher, and G. Czycholl. *Tight-binding model for semiconductor quantum dots with a wurtzite crystal structure: From one-particle properties to Coulomb correlations and optical spectra*. Phys. Rev. B **73** (2006).
- [70] F. Schwabl. *Quantenmechanik* (Springer, Heidelberg, 1998).
- [71] G. Czycholl. *Theoretische Festkörperphysik* (Vieweg, Braunschweig/Wiesbaden, 2000).
- [72] H. Kamada, H. Gotoh, H. Ando, J. Temmyo, and T. Tamamura. *Spin-selective excitation spectroscopy of excitons and biexcitons in $In_xGa_{1-x}As$ quantum disks: Suppression of the spin-flip process in semiconductor zero-dimensional systems*. Phys. Rev. B **60**, 5604 (1999).
- [73] A. Hartmann, Y. Ducommun, E. Kapon, U. Hohenester, and E. Molinari. *Few-Particle Effects in Semiconductor Quantum Dots: Observation of Multicharged Excitons*. Phys. Rev. Lett. **84**, 5648 (2000).
- [74] A. Kuther, M. Bayer, A. Forchel, A. Gorbunov, V. B. Timofeev, F. Schäfer, and J. P. Reithmaier. *Zeeman splitting of excitons and biexcitons in single $InGaAs/GaAs$ self-assembled quantum dots*. Phys. Rev. B **58**, R7509 (1998).
- [75] A. Zrenner. *A close look on single quantum dots*. J. Chem. Phys. **112**, 7790 (2000).

Bibliography

- [76] F. Findeis, A. Zrenner, G. Böhm, and G. Abstreiter. *Optical spectroscopy on a single InGaAs/GaAs quantum dot in the few-exciton limit.* Solid State Commun. **114**, 227 (2000).
- [77] J. Shumway, A. Franceschetti, and A. Zunger. *Correlation versus mean-field contributions to excitons, multiexcitons, and charging energies in semiconductor quantum dots.* Phys. Rev. B **63**, 155316 (2001).
- [78] P. Hawrylak and A. Wojs. *Electronic structure and optical properties of self-assembled quantum dots.* Semicond. Sci. Technol. **11**, 1516 (1996).
- [79] P. Hawrylak. *Hidden symmetry and correlated states of electrons and holes in quantum dots.* Solid State Commun. **127**, 793 (2003).
- [80] D. Paquet, T. M. Rice, and K. Ueda. *Two-dimensional electron-hole fluid in a strong perpendicular magnetic field: Exciton Bose condensate or maximum density two-dimensional droplet.* Phys. Rev. B **32**, 5208 (1985).
- [81] A. H. MacDonald and E. H. Rezayi. *Fractional Quantum Hall effect in a two-dimensional electron-hole fluid.* Phys. Rev. B **42**, 3224 (1990).
- [82] Ph. Lelong and G. Bastard. *Binding energies of excitons and charged excitons in GaAs/Ga(In)As quantum dots.* Solid State Commun. **98**, 819 (1996).
- [83] G. A. Narvaez and P. Hawrylak. *Effects of electron-electron interactions on excitonic absorption in charged self-assembled quantum dots.* Phys. Rev. B **61**, 13753 (2000).
- [84] M. Bayer, G. Ortner, O. Stern, A. Kuther, A. Forchel A.A. Gorbunov, P. Hawrylak, S. Fafard, K. Hinzer, T. L. Reinecke, S. N. Walck, J. P. Reithmaier, F. Klopf, F. Schäfer, and G. W. Bryant. *Fine structure of neutral and charged excitons in self-assembled In(Ga)As/(Al)GaAs quantum dots.* Phys. Rev. B **65**, 195315 (2002).
- [85] M. C. Troparevsky and A. Franceschetti. *Radiative recombination of charged excitons and multiexcitons in CdSe quantum dots.* Appl. Phys. Lett. **87**, 263115 (2005).
- [86] R. J. Warburton, C. Schäflein, D. Haft, F. Bickel, A. Lorke, K. Karrai, J. M. Garcia, W. Schoenfeld, and P. M. Petroff. *Optical emission from a charge-tunable quantum ring.* Nature **405**, 926 (2000).
- [87] S. M. Ulrich, M. Benyoucef, P. Michler, J. Wiersig, N. Baer, P. Gartner, F. Jahnke, M. Schwab, H. Kurtze, R. Oulton, M. Bayer, S. Fafard, Z. Wasilewski, and A. Forchel. *Single-Photon And Photon Pair Emission From Individual (In,Ga)As Quantum Dots.* Proceedings of: 27th International Conference on the Physics of Semiconductors - ICPS-27 **1**, 661 (2005).
- [88] R. Hanbury Brown and R.Q. Twiss. *Correlation between photons in two coherent beams of light.* Nature **177**, 27 (1956).
- [89] B. Patton, W. Langbein, and U. Woggon. *Trion, biexciton, and exciton dynamics in single self-assembled CdSe quantum dots.* Phys. Rev. B **68**, 125316 (2003).

- [90] A. S. Chaves and H. Chacham. *Negative photoconductivity in semiconductor heterostructures*. Appl. Phys. Lett. **66**, 727 (1995).
- [91] <http://jumpdoc.fz-juelich.de>.
- [92] H. Morkoc, A. Neogi, and M. Kuball. *Growth Structure, and Optical Properties of III-Nitride Quantum Dots*. Mat. Res. Soc. Symp. Proc. **799** (2004).
- [93] F. Bernardini, V. Fiorentini, and D. Vanderbilt. *Spontaneous polarization and piezoelectric constants of III-V nitrides*. Phys. Rev. B **56**, R10024 (1997).
- [94] H. Morkoc. *Nitride Semiconductors and Devices* (Springer, Heidelberg, 1999).
- [95] J. Wu, W. Walukiewicz, K. M. Yu, J. W. Ager III, E. E. Haller, H. Lu, W. J. Schaff, Y. Saito, and Y. Nanishi. *Unusual properties of the fundamental band gap of InN*. Appl. Phys. Lett. **80**, 3967 (2002).
- [96] E. Dekel, D. Gershoni, E. Ehrenfreund, D. Spektor, J.M. Garcia, and P. M. Petroff. *Optical spectroscopy of a single self-assembled quantum dot*. Physica E **2**, 694 (1998).
- [97] S. De Rinaldis, I. D'Amico, and F. Rossi. *Intrinsic electric field effects on few-particle interactions in coupled GaN quantum dots*. Phys. Rev. B **69**, 235316 (2004).
- [98] J.-J. Shi. *Exciton states and interband optical transitions in InGaN quantum dots*. Solid State Commun. **124**, 341 (2002).
- [99] S. De Rinaldis, I. D'Amico, and F. Rossi. *Exciton-exciton interaction engineering in coupled GaN quantum dots*. Appl. Phys. Lett. **81**, 4236 (2002).
- [100] R. W. Martin and K. P. O'Donnell. *Calculation of Optical Transition Energies for Self-Formed InGaN Quantum Dots*. phys. stat. sol (b) **216**, 441 (1999).
- [101] U. Hohenester, R. Di Felice, E. Molinari, and F. Rossi. *Optical spectra of nitride quantum dots: Quantum confinement and electron hole coupling*. Appl. Phys. Lett. **75**, 3449 (1999).
- [102] F. Widmann, J. Simon, B. Daudin, G. Feuillet, J. L. Rouviere, N. T. Pelekanos, and G. Fishman. *Blue-light emission from GaN self-assembled quantum dots due to giant piezoelectric effect*. Phys. Rev. B **58**, R15989 (1998).
- [103] A. D. Andreev and E. P. O'Reilly. *Optical transitions and radiative lifetime in GaN/AlN self-organized quantum dots*. Appl. Phys. Lett. **79**, 521 (2001).
- [104] J.-J. Shi and Z.-Z. Gan. *Effects of piezoelectricity and spontaneous polarization on localized excitons in self-formed InGaN quantum dots*. J. Appl. Phys. **94**, 407 (2003).
- [105] A. Bagga, P. K. Chattopadhyay, and S. Ghosh. *Dark and bright excitonic states in nitride quantum dots*. Phys. Rev. B **71**, 115327 (2005).
- [106] S. Schulz and G. Czycholl. *Electronic states in nitride semiconductor quantum dots: A tight-binding approach*. to appear (2006).

Bibliography

- [107] C. M. Goringe, D. R. Bowler, and E. Hernandez. *Tight-binding modelling of materials*. Rep. Prog. Phys. **60**, 14447 (1997).
- [108] G. Klimeck, F. Oyafuso, T.B. Boykin, R.C. Bowen, and P. v. Allmen. *Development of a Nanoelectronic 3-D (NEMO 3-D) Simulator for Multimillion Atom Simulations and Its Application to Alloyed Quantum Dots*. CMES **3**, 601 (2002).
- [109] J. C. Slater and G. F. Koster. *Simplified LCAO Method for the Periodic Potential Problem*. Phys. Rev. **94**, 1498 (1954).
- [110] S.-H. Wei and A. Zunger. *Valence band splittings and band offsets of AlN, GaN, and InN*. Appl. Phys. Lett. **69**, 2719 (1996).
- [111] A. Kobayashi, O. F. Sankey, S. M. Volz, and J. D. Dow. *Semiempirical tight-binding band structures of wurtzite semiconductors: AlN, CdS, CdSe, ZnS, and ZnO*. Phys. Rev. B **28**, 935 (1983).
- [112] D. Fritsch, H. Schmidt, and M. Grundmann. *Band dispersion relations of zinc-blende and wurtzite InN*. Phys. Rev. B **69**, 165204 (2004).
- [113] G. L. Zhao, D. Bagayoko, and T. D. Williams. *Local-density-approximation prediction of electronic properties of GaN, Si, C, and RuO₂*. Phys. Rev. B **60**, 1563 (1999).
- [114] F. D. Sala, A. D. Carlo, P. Lugli, F. Bernardini, V. Fiorentini, R. Scholz, and J. M. Jancu. *Free-carrier screening of polarization fields in wurtzite GaN/InGaN laser structures*. Appl. Phys. Lett. **74**, 2002 (1999).
- [115] T. Saito and Y. Arakawa. *Electronic structure of piezoelectric In_{0.2}Ga_{0.8}N quantum dots in GaN calculated using a tight-binding method*. Physica E (Amsterdam) **15**, 169 (2002).
- [116] S. J. Sun and Y. C. Chang. *Modeling self-assembled quantum dots by effective bond-orbital method*. Phys. Rev. B **62**, 13631 (2000).
- [117] J. C. Slater. *Atomic Shielding Constants*. Phys. Rev. **36**, 57 (1930).
- [118] S. Lee, J. Kim, L. Jönsson, J. W. Wilkins, G. W. Bryant, and G. Klimeck. *Many-body levels of optically excited and multiply charged InAs nanocrystals modeled by semiempirical tight binding*. Phys. Rev. B **66**, 235307 (2002).
- [119] J. P. Elliott and P. G. Davber. *Symmetry in Physics, Volume 1 and 2* (The Macmillian Press LTD, London, 1979).
- [120] T. Inui, Y. Tanabe, and Y. Onodera. *Group theory and its applications in physics* (Springer, Heidelberg, 1990).
- [121] G. Bester and A. Zunger. *Cylindrically shaped zinc-blende semiconductor quantum dots do not have cylindrical symmetry: Atomistic symmetry, atomic relaxation, and piezoelectric effects*. Phys. Rev. B **71**, 045318 (2005).
- [122] S. Schulz and G. Czycholl. *Tight-Binding model for semiconductor nanostructures*. Phys. Rev. B **72**, 165317 (2005).

- [123] J. F. Cornwell. *Group Theory and Electronic Energy Bands in Solids* (North-Holland Publishing Company, Amsterdam, 1969).
- [124] A. D. Andreev and E. P. O'Reilly. *Theory of the electronic structure of GaN/AlN hexagonal quantum dots*. Phys. Rev. B **62**, 15851 (2000).
- [125] V. A. Fonoberov and A. A. Balandin. *Excitonic properties of strained wurtzite and zinc-blende GaN/Al_xGa_{1-x}N quantum dots*. J. Appl. Phys. **94**, 7178 (2003).
- [126] A. S. Davydov. *Quantum mechanics* (Pergamon Press, Oxford, 1965).
- [127] M. Nirmal, D. J. Norris, M. Kuno, M. G. Bawendi, A. L. Efros, and M. Rosen. *Observation of the "Dark Exciton" in CdSe Quantum Dots*. Phys. Rev. Lett. **75**, 3728 (1995).
- [128] D. Morris, N. Perret, and S. Fafard. *Carrier energy relaxation by means of Auger processes in InAs/GaAs self-assembled quantum dots*. Appl. Phys. Lett. **75**, 3593 (1999).
- [129] H. Walther. *Generation of photons on demand using cavity quantum electrodynamics*. Ann. Phys. **14**, 7 (2005).
- [130] B. Gayral, J. M. Gerard, A. Lemaitre, C. Dupuis, L. Manin, and J. L. Pelouard. *High-Q wet-etched GaAs microdisks containing InAs quantum boxes*. Applied Physics Letters **75**, 1908 (1999).
- [131] B. Ohnesorge, M. Bayer, A. Forchel, J. P. Reithmeier, N. A. Gippius, and S.G. Tikhodeev. *Enhancement of spontaneous emission rates by three-dimensional photon confinement in Bragg microcavities*. Phys. Rev. B **56**, R4370 (1997).
- [132] C. J. M. Smith, H. Benisty, D. Labilloy, U. Oesterle, R. Houdre, T.F. Krauss, R.M. De La Rue, and C. Weisbuch. *Near-infrared microcavities confined by two-dimensional photonic bandgap crystals*. Electron. Lett. **35**, 228 (1999).
- [133] S.M. Ulrich, C. Gies, J. Wiersig, S. Reitzenstein, C. Hofmann, A. Löffler, A. Forchel, F. Jahnke, and P. Michler. *Photon statistics of semiconductor microcavity lasers*. submitted (2006).
- [134] X. Fan, M. C. Lonergan, Y. Zhang, and H. Wang. *Enhancement of spontaneous emission rates by three-dimensional photon confinement in Bragg microcavities*. Phys. Rev. B **64**, 115310 (2001).
- [135] W. Fang, J. Y. Xu, A. Yamilov, H. Cao, Y. Ma, S. T. Ho, and G. S. Solomon. *Large enhancement of spontaneous emission rates of InAs quantum dots in GaAs microdisks*. Optics Letters **27**, 948 (2002).
- [136] I. L. Krestnikov, N. N. Ledentsov, A. Hoffmann, D. Bimberg, A. V. Sakharnov, W. V. Lundin, A. S. Tsatsul'nikov, A.F. Usikov, Zh. I. Alferov, Yu. G. Musikhin, and D. Gerthsen. *Quantum dot origin of luminescence in InGaN-GaN structures*. Phys. Rev. B **66**, 155310 (2002).

Bibliography

- [137] R. A. Oliver, G. A. D. Briggs, M. J. Kappers, C. J. Humphreys, S. Yasin, J. H. Rice, J. D. Smith, and R. A. Taylor. *InGaN quantum dots grown by metalorganic vapor phase epitaxy employing a post-growth nitrogen anneal*. Appl. Phys. Lett. **83**, 755 (2003).
- [138] M. Schwab, T. Auer, T. Berstermann, and M. Bayer. *private communication* (2005).
- [139] M. Schwab, H. Kurtze, T. Auer, T. Berstermann, M. Bayer, J. Wiersig, N. Baer, C. Gies, F. Jahnke, M. Benyoucef, P. Michler, J. P. Reithmaier, and A. Forchel. *Radiative emission dynamics of quantum dots in a single cavity micropillar*. submitted (2005).
- [140] M. Kira, F. Jahnke, and S. W. Koch. *Microscopic Theory of Excitonic Signatures in Semiconductor Photoluminescence*. Phys. Rev. Lett. **81**, 3263 (1998).
- [141] M. Kira, F. Jahnke, W. Hoyer, and S. W. Koch. *Quantum Theory of Spontaneous Emission and Coherent Effects in Semiconductor Microstructures*. Prog. Quant. Electr. **23**, 189 (1999).
- [142] J. Fricke. *Transport equations including many-particle correlations for an arbitrary quantum system: A general formalism*. Ann. Phys. **252**, 479 (1996).
- [143] F. Jahnke, M. Kira, W. Hoyer, and S. W. Koch. *Influence of Correlation Effects on the Excitonic Semiconductor Photoluminescence*. phys. stat. sol (b) **221**, 189 (2000).
- [144] W. Hoyer, M. Kira, and S.W. Koch. *Influence of Coulomb and phonon interaction on the exciton formation dynamics in semiconductor heterostructures*. Phys. Rev. B **67**, 155113 (2003).
- [145] P. Meystre and M. Sargent III. *Elements of Quantum Optics* (Springer, Berlin, 1999).
- [146] V. M. Axt and S. Mukamel. *Nonlinear optics of semiconductor and molecular nanosstructures; a common perspective*. Rev. Mod. Phys. **70**, 145 (1998).
- [147] G. Khitrova, H. M. Gibbs, F. Jahnke, M. Kira, and S. W. Koch. *Nonlinear optics of normal-mode-coupling semiconductor microcavities*. Rev. Mod. Phys. **71**, 1591 (1999).
- [148] W. Schäfer and M. Wegener. *Semiconductor Optics and Transport Phenomena* (Springer, Heidelberg, 2002).
- [149] A. L. Fetter and J. D. Walecka. *Quantum theory of many-particle systems* (Dover Publications, Inc, New York, 2003).
- [150] W. Hoyer. *Quantentheorie zu Exzitonbildung und Photolumineszenz in Halbleitern*. Ph.D. thesis, Universität Marburg, Germany (2002).
- [151] S. W. Koch, M. Kira, and T. Meier. *Correlation effects in the excitonic optical properties of semiconductors*. J. Opt. B: Quantum Semiclass. Opt. **3**, R29 (2001).
- [152] T. Feldtmann, L. Schneebeli, M. Kira, and S. W. Koch. *Quantum theory of light emission from a semiconductor quantum dot*. Phys. Rev. B **73**, 155319 (2006).
- [153] M. Kira, F. Jahnke, W. Hoyer, and S. W. Koch. *Quantum Theory of Spontaneous Emission and Coherent Effects in Semiconductor Microstructures*. Prog. Quant. Electr. **23**, 189 (1999).

- [154] G. Bastard. *Wave mechanics applied to semi-conductor heterostructures* (John Wiley, New York, 1992).
- [155] P. M. Morse and H. Feshbach. *Methods of Theoretical Physics* (McGraw-Hill, New York, 1953).
- [156] M. Kira, F. Jahnke, and S. W. Koch. *Quantum Theory of Secondary Emission in Optically Excited Semiconductor Quantum Wells*. Phys. Rev. Lett. **82**, 3544 (1999).
- [157] J. H. Eberly and K. Wódkiewicz. *The time-dependent physical spectrum of light*. J. Opt. Soc. Am. **67**, 1252 (1977).
- [158] J. D. Jackson. *Classical Electrodynamics* (John Wiley, New York, 1975).
- [159] J. Wiersig, C. Gies, N. Baer, and F. Jahnke. *Intrinsic non-exponential decay of time-resolved photoluminescence from semiconductor quantum dots*. submitted (2006).
- [160] K. J. Ahn, J. Förstner, and A. Knorr. *Resonance fluorescence of semiconductor quantum dots: Signatures of the electron-phonon interaction*. Phys. Rev. B **71**, 153309 (2005).
- [161] H. Lohmeyer, K. Sebald, C. Kruse, R. Kröger, J. Gutowski, D. Hommel, J. Wiersig, N. Baer, and F. Jahnke. *Confined optical modes in monolithic II-VI pillar microcavities*. Appl. Phys. Lett. **88**, 051101 (2006).
- [162] K. L. Silverman, R. P. Mirin, S. T. Cundiff, and A. G. Norman. *Direct measurement of polarization resolved transition dipole moment in InGaAs/GaAs quantum dots*. Appl. Phys. Lett. **82**, 4552 (2003).
- [163] M. Benyoucef, S.M. Ulrich, P. Michler, J. Wiersig, F. Jahnke, and A. Forchel. *Enhanced correlated photon pair emission from a pillar microcavity*. New J. Phys. **6**, 91 (2004).
- [164] C. Wilmsen, H. Temkin, and L. A. Coldren. *Enhancement of Spontaneous Emission in Microcavities*. Cambridge studies in Modern Optics (Cambridge University Press, 1999).
- [165] G. J. Beirne, C. Hermannstadter, L. Wang, A. Rastelli, O. G. Schmidt, and P. Michler. *Quantum Light Emission of Two Lateral Tunnel-Coupled (In,Ga)As/GaAs Quantum Dots Controlled by a Tunable Static Electric Field*. Phys. Rev. Lett. **96**, 137401 (2006).
- [166] R. Jin, D. Boggavarapu, M. Sargent, P. Meystre, H. M. Gibbs, and G. Khitrova. *Photon-number correlations near the threshold of microcavity lasers in the weak-coupling regime*. Phys. Rev. A **49**, 4038 (1994).
- [167] M. Bayer, A. Forchel, T. L. Reinecke, P. A. Knipp, and S. Rudin. *Confinement of Light in Microresonators for Controlling Light-Matter Interaction*. phys. stat. sol. (a) **191**, 3 (2002).
- [168] T. Nielsen. *Carrier-Carrier and Carrier-Phonon Scattering in Self-Assembled Quantum Dots*. Ph.D. thesis, Universität Bremen, Germany (2005).
- [169] N. Baer. *Optische Eigenschaften von Halbleiter-Quantenpunkten*. Diploma thesis, Universität Bremen, Germany (2003).

Bibliography

- [170] William H. Press, Brian P. Flannery, Saul A. Teukolsky, and William T. Vetterling. *Numerical Recipes: The Art of Scientific Computing* (Cambridge University Press, Cambridge (UK) and New York, 1986), 1st edition.
- [171] S. Schumacher. *Polariton Propagation and Coherent Many-Particle Effects in Semiconductor Heterostructures*. Ph.D. thesis, Universität Bremen, Germany (2005).
- [172] E. Anderson, Z. Bai, C. Bischof, S. Blackford, J. Demmel, J. Dongarra, J. Du Croz, A. Greenbaum, S. Hammarling, A. McKenney, and D. Sorensen. *LAPACK Users' Guide* (Society for Industrial and Applied Mathematics, Philadelphia, PA, 1999), third edition.

List of Publications

- N. Baer, P. Gartner, and F. Jahnke. *Coulomb Effects in Semiconductor Quantum Dots*. Eur. Phys. J. B **42**. 231 (2004).
- S. M. Ulrich, M. Benyoucef, P. Michler, N. Baer, P. Gartner, F. Jahnke, M. Schwab, H. Kurtze, M. Bayer, S. Fafard, Z. Wasilewski, and A. Forchel. *Correlated photon-pair emission from a charged single quantum dot*. Phys. Rev. B **71**. 235328 (2005).
- N. Baer, J. Wiersig, P. Gartner, F. Jahnke, M. Benyoucef, S. M. Ulrich, P. Michler, and A. Forchel. *Optical properties of semiconductor quantum dots and pillar microcavities*. Proceedings of the ICPS-27 **1**. 725 (2005).
- S. M. Ulrich, M. Benyoucef, P. Michler, J. Wiersig, N. Baer, P. Gartner, F. Jahnke, M. Schwab, H. Kurtze, R. Oulton, M. Bayer, S. Fafard, Z. Wasilewski, and A. Forchel. *Single-Photon And Photon Pair Emission From Individual (In,Ga)As Quantum Dots*. Proceedings of the ICPS-27 **1**. 661 (2005).
- N. Baer, S. Schulz, S. Schumacher, P. Gartner, G. Czycholl, and F. Jahnke. *Optical properties of self-organized wurtzite InN/GaN quantum dots: A combined atomistic tight-binding and full configuration interaction calculation*. Appl. Phys. Lett. **23**. 231114 (2005).
- H. Lohmeyer, K. Sebald, J. Gutowski, C. Kruse, D. Hommel, J. Wiersig, N. Baer, and F. Jahnke. *Efficient coupling into confined optical modes of ZnSe-based pillar microcavities*. phys. stat. sol. (b) **243**. 844 (2006).
- H. Lohmeyer, K. Sebald, C. Kruse, R. Kröger, J. Wiersig, N. Baer, F. Jahnke, J. Gutowski, and D. Hommel. *Confined optical modes in monolithic II-VI pillar microcavities*. Appl. Phys. Lett. **88**. 051101 (2006).
- N. Baer, C. Gies, J. Wiersig, and F. Jahnke. *Luminescence of a Semiconductor Quantum Dot System*, Eur. Phys. J. B, **50**, 411 (2006)
- C. Gies, N. Baer, J. Wiersig, and F. Jahnke. *Microscopic Theory of Quantum Dot Luminescence Spectra*. phys. stat. sol. (c), **3**, 2385 (2006).
- M. Schwab, H. Kurtze, T. Auer, T. Berstermann, M. Bayer, J. Wiersig, N. Baer, C. Gies, F. Jahnke, M. Benyoucef, P. Michler, J. P. Reithmaier, and A. Forchel. *Radiative emission dynamics of quantum dots in a single cavity micropillar*. Phys. Rev. B **74**. 045323 (2006).
- J. Wiersig, C. Gies, N. Baer, and F. Jahnke. *Intrinsic non-exponential decay of time-resolved photoluminescence from semiconductor quantum dots*. Adv. in Solid State Phys. (2006), accepted.

- S. Schulz, N. Baer, S. Schumacher, P. Gartner, F. Jahnke ,and G. Czycholl. *Microscopic tight-binding description for electronic and optical properties of InN/GaN quantum dots.* (2006), submitted.

List of Selected Conference Contributions

- N. Baer, P. Gartner, and F. Jahnke. *Coulomb Effects in the Optical Spectra of Semiconductor Quantum Dots*. Workshop of the DFG-Research Group ‘Quantum Optics in Semiconductor Nanostructures’, Bremen (2003).
- J. Wiersig, N. Baer, P. Gartner, F. Jahnke, M. Benyoucef, S. M. Ulrich, and P. Michler. *Optical Properties of Semiconductor Microcavity Pillars*. DPG-Frühjahrstagung des Arbeitskreises Festkörperphysik, Regensburg (2004).
- N. Baer, P. Gartner, and F. Jahnke. *Coulomb Effects in the Optical Spectra of Semiconductor Quantum Dots*. DPG-Frühjahrstagung des Arbeitskreises Festkörperphysik, Regensburg (2004).
- J. Wiersig, N. Baer, P. Gartner, F. Jahnke, M. Benyoucef, S. M. Ulrich, P. Michler, and A. Forchel. *Optical Properties of Semiconductor Microcavity Pillars*. Workshop of the DFG-Research Group ‘Quantum Optics in Semiconductor Nanostructures’, Rügen (2004).
- N. Baer, P. Gartner, and F. Jahnke. *Theoretical Investigation of Multi-Exciton Spectra of Semiconductor Quantum Dots*. Workshop of the DFG-Research Group ‘Quantum Optics in Semiconductor Nanostructures’, Rügen (2004).
- J. Wiersig, N. Baer, P. Gartner, F. Jahnke, M. Benyoucef, S.M. Ulrich, P. Michler, and A. Forchel. *Optical Modes of Semiconductor Micropillars: a Theory-Experiment Comparison*. CLEO/IQEC, San Francisco (2004).
- N. Baer, J. Wiersig, P. Gartner, F. Jahnke, M. Benyoucef, S.M. Ulrich, P. Michler, and A. Forchel. *Optical properties of semiconductor quantum dots and pillar microcavities*. ICPS-27, Flagstaff (2004).
- S. M. Ulrich, M. Benyoucef, P. Michler, N. Baer, P. Gartner, F. Jahnke, M. Schwab, H. Kurtze, M. Bayer, S. Fafard, and Z. Wasilewski. *Single-photon and photon pair emission from individual (In,Ga)As quantum dots*. ICPS-27, Flagstaff (2004).
- J. Wiersig, T. Aschenbrenner, N. Baer, M. Lorke, P. Gartner, F. Jahnke, M. Benyoucef, P. Michler, M. Schwab, H. Kurtze, M. Bayer, A. Forchel. *Microscopic Theory of Photoluminescence from Semiconductor Quantum Dots in Microcavities*. CLEO/IQEC, Baltimore (2005).
- N. Baer, J. Wiersig, P. Gartner, F. Jahnke, M. Benyoucef, S.M. Ulrich, P. Michler, and A. Forchel. *Investigation of the optical mode structure in pillar microcavities*. DPG-Frühjahrstagung des Arbeitskreises Festkörperphysik, Berlin (2005).
- N. Baer, J. Wiersig, P. Gartner, F. Jahnke, M. Benyoucef, S.M. Ulrich, P. Michler, and A. Forchel. *Optical properties of semiconductor quantum dots and pillar microcavities*. BaCaTeC-Summer School, Würzburg (2005).

- H. Lohmeyer, K. Sebald, J. Gutowski, C. Kruse, D. Hommel, J. Wiersig, N. Baer, and F. Jahnke. *Efficient Coupling into Confined Optical Modes of ZnSe-based Pillar Microcavities*. 12th International Conference on II-VI Compounds, Warsaw (2005)
- S. Schulz, N. Baer, S. Schumacher, P. Gartner, G. Czycholl, and F. Jahnke. *Optical and electronic properties of self-organized wurtzite InN/GaN quantum dots*. DPG-Frühjahrstagung des Arbeitskreises Festkörperphysik, Dresden (2006).
- N. Baer, S. Schulz, S. Schumacher, P. Gartner, G. Czycholl, and F. Jahnke. *Engineering the multi-exciton spectra in wurtzite InN/GaN quantum dots*. DPG-Frühjahrstagung des Arbeitskreises Festkörperphysik, Dresden (2006).
- C. Gies, J. Wiersig, N. Baer, and F. Jahnke. *Theory of Photoluminescence for Semiconductor Quantum Dots*. DPG-Frühjahrstagung des Arbeitskreises Festkörperphysik, Dresden (2006).
- F. Jahnke, J. Wiersig, N. Baer, C. Gies. *Theory of optical properties for quantum dots in microcavities*. DPG-Frühjahrstagung des Arbeitskreises Festkörperphysik, Dresden (2006).
- J. Wiersig, N. Baer, C. Gies, F. Jahnke, M. Schwab, H. Kurtze, M. Bayer, M. Benyoucef, P. Michler, and A. Forchel. *Radiative emission dynamics of quantum dots in a single cavity micropillar*. Noeks8, Münster (2006).
- T. Auer, M. Schwab, H. Kurtze, M. Bayer, J. Wiersig, N. Baer, C. Gies, F. Jahnke, V. Stavarache, D. Reuter, and A. Wieck. *Dependence of the radiative emission dynamics of quantum dots on e-h correlations*. Noeks8, Münster (2006).
- S. Schulz, N. Baer, S. Schumacher, P. Gartner, F. Jahnke ,and G. Czycholl. *Microscopic tight-binding description for electronic and optical properties of InN/GaN quantum dots*. Semiconductor Quantum Dots: Fourth International Conference, Chamonix-Mont Blanc (2006).
- S. Schumacher, N. Baer, S. Schulz, P. Gartner, G. Czycholl, and F. Jahnke. *Electronic and Optical Properties of Self-Assembled InN/GaN Quantum Dots*. CLEO/IQEC, Long Beach (2006).
- C. Kruse, A. Gust, H. Lohmeyer, K. Sebald, J. Gutowski, J. Wiersig, N. Baer, F. Jahnke and D. Hommel. *Towards a quantum dot based single photon emitter operating at room temperature*. ICPS-28, Wien (2006).

Danksagung

Als Erstes möchte ich Herrn Prof. Dr. Frank Jahnke für die gute Betreuung und Unterstützung beim Erstellen dieser Arbeit und der damit verbundenen Mühe danken.

Paul Gartner danke ich ganz herzlich für die vielen erhellenden Diskussionen – insbesondere zu den Teilen I und II dieser Arbeit – die von Zeit zu Zeit auch den Rahmen der theoretischen Physik verließen.

Jan Wiersig danke ich für die freundliche und fruchtbare Zusammenarbeit, insbesondere bezüglich Teil III dieser Arbeit.

Prof. Dr. Gerd Czycholl danke ich für die bereitwillige Übernahme des Zweitgutachtens.

Ein ganz besonderer Dank geht an meine Freunde, Kollegen und Koautoren Stefan Schumacher, Stefan Schulz und Christopher Gies für die Unterstützung und die vielen gelungenen Freizeitaktivitäten.

Des Weiteren danke ich Jan Seebeck und Torben Nielsen, sowie allen anderen (ehemaligen) Mitgliedern der AG Jahnke und AG Czycholl für dieses und jenes.

Zu guter Letzt bedanke ich mich ganz herzlich bei meiner Freundin Ivona, die mich stetig unterstützt, begleitet und ertragen hat und der beste Ausgleich neben der vielen Arbeit war.
